



HAL
open science

La caractérisation du sous-sol et des structures du génie civil : une approche combinant imagerie optique, géophysique et modélisation numérique

Raphaël Antoine

► To cite this version:

Raphaël Antoine. La caractérisation du sous-sol et des structures du génie civil : une approche combinant imagerie optique, géophysique et modélisation numérique. Interfaces continentales, environnement. Université de Rouen Normandie, 2022. tel-04682378

HAL Id: tel-04682378

<https://hal.science/tel-04682378v1>

Submitted on 30 Aug 2024

HAL is a multi-disciplinary open access archive for the deposit and dissemination of scientific research documents, whether they are published or not. The documents may come from teaching and research institutions in France or abroad, or from public or private research centers.

L'archive ouverte pluridisciplinaire **HAL**, est destinée au dépôt et à la diffusion de documents scientifiques de niveau recherche, publiés ou non, émanant des établissements d'enseignement et de recherche français ou étrangers, des laboratoires publics ou privés.



Normandie Université

MEMOIRE

Pour obtenir le diplôme de l'Habilitation à Diriger des Recherches

Sciences de l'Univers

Préparé au sein du Laboratoire de Morphodynamique Continentale et Côtière

La caractérisation du sous-sol et des structures du génie civil : une approche combinant imagerie optique, géophysique et modélisation numérique

**Présenté et soutenu par
Raphaël ANTOINE**

HDR soutenue publiquement le 16 décembre 2022 devant le jury composé de

Yu Jun Cui	Directeur de Recherche du Développement Durable, Ecole Nationale des Ponts et Chaussées	Examineur
Luminita Danaila	Professeur des Universités, Université Rouen- Normandie	Examineur
Anne Davaille	Directrice de Recherche CNRS, Laboratoire FAST	Rapporteur
Alain Tabbagh	Professeur émérite de Sorbonne Université	Examineur
Stéphane Jacquemoud	Directeur de recherche CNRS, Institut de Physique du Globe de Paris	Rapporteur
Marc Pierrot-Deseilligny	Directeur de recherche du Développement Durable, Ecole Nationale des Sciences Géographiques	Examineur
Michel Rabinowicz	Professeur émérite de l'Université Paul Sabatier	Examineur
Géraldine Villain	Ingénieure Divisionnaire des Travaux Publics de l'Etat, Université Gustave Eiffel	Rapporteur

Sommaire

1 Démarche scientifique	1
1.1 Une formation initiale conjuguant physique et géologie	1
1.2 Contexte de mon poste et positionnement scientifique	1
1.2.1 Contexte de mon poste	1
1.2.2 Positionnement scientifique	3
1.3 Des collaborations nationales et internationales	3
1.4 Une activité portant sur l'ensemble des facettes du métier de chercheur . .	4
2 Curriculum vitæ détaillé	6
2.1 Etat civil	6
2.2 Diplômes et titres	6
2.3 Déroulement de carrière	6
2.4 Identification des domaines de compétence et d'études	7
2.5 Formation complémentaire	7
2.6 Production Scientifique	7
2.7 Enseignement et formation à la Recherche	8
2.8 Activité d'expertise, de valorisation et de transfert	11
2.9 Activité internationale	12
2.10 Activité d'administration et d'animation de la Recherche	13
2.11 Rayonnement scientifique et diffusion de l'information et de la culture scientifique	14
3 Activité de recherche	17
3.1 Imagerie optique et géophysique appliquée à la caractérisation des milieux .	17
3.1.1 Un début de carrière en volcanologie planétaire	17
3.1.2 A la recherche de l'eau dans les zones arides et les volcans	19
3.1.3 Vers la caractérisation des structures du génie civil	24
3.2 Modélisation 3D pour les géosciences	27
3.3 Le drone, un moyen d'observation révolutionnaire	32
4 Projet de recherche	35
4.0.1 Caractérisation physique des milieux	35
4.0.2 Développement de méthodologie d'observations et de traitement de données	42
4.0.3 Développement de prototypes et de moyen de recueil de données . . .	44
4.0.4 Perspectives stratégiques et scientifiques	45
5 Annexe : publications scientifiques représentatives de mon parcours	47
5.1 Tired à part Thermal infrared image analysis of a quiescent cone on Piton de la Fournaise volcano : Evidence of convective air flow within an uncon- solidated soil (Journal of Volcanology and Geothermal Research	47
5.2 Subsurface Hydrology of the Lake Chad Basin from Convection Modelling and Observations (Survey in Geophysics)	65
5.3 Permeability and voids influence on the thermal signal, as inferred by mul- titemporal UAV-based infrared and visible images (Journal of Hydrology) . .	98
5.4 3D assessment of an underground mine pillar by combination of photo- grammetric and geoelectric methods (Geophysics)	116
5.5 Geoscientists in the Sky : Unmanned Aerial Vehicles Responding to Geo- hazards (Survey in Geophysics)	128
6 Démarche scientifique	168
6.1 Une formation initiale conjuguant physique et géologie	168
6.2 Contexte de mon poste et positionnement scientifique	168
6.2.1 Contexte de mon poste	168
6.2.2 Positionnement scientifique	170

6.3 Des collaborations nationales et internationales	170
6.4 Une activité portant sur l'ensemble des facettes du métier de chercheur . .	171
7 Projet de recherche	173
7.0.1 Caractérisation physique des milieux	173
7.0.2 Développement de méthodologie d'observations et de traitement de données	180
7.0.3 Développement de prototypes et de moyen de recueil de données . . .	182
7.0.4 Perspectives stratégiques et scientifiques	183
Références	194

1 Démarche scientifique

Cette section est dédiée à la présentation de ma démarche scientifique, qui constitue la colonne vertébrale de mon travail de chercheur. Après avoir décrit ma formation initiale, mon parcours de recherche est présenté en le positionnant dans le contexte de mon établissement. Ce parcours est guidé par un questionnement scientifique dont je décris l'ensemble des aspects, ainsi que les axes de recherche que j'ai mis en place pour y répondre. Enfin, mon positionnement scientifique est exposé au regard de cette activité.

1.1 Une formation initiale conjuguant physique et géologie

Après trois années d'études en mathématiques et physique, je me suis tourné vers les sciences de la Terre et l'exploration planétaire. J'ai intégré la Licence 3 de sciences de la Terre et de l'Univers de l'Université de Toulouse en 2002, au sein de laquelle j'ai acquis des connaissances en géologie et planétologie. Mon contact avec la recherche a été initié lors de mon stage de Master 1. J'ai ainsi participé à une mission de terrain financée par mes soins sur le volcan Piton de la Fournaise à l'Île de la Réunion, dans le cadre du programme ACI CATNAT¹. Cette première expédition scientifique, qui demeure un souvenir fabuleux et formateur, fut le point de départ de mon parcours scientifique, forgé par diverses expériences en France et au Japon :

- En 2003-2004 : un stage de Master 1 dans lequel j'ai travaillé sur les données thermiques issus de thermocouples implantés dans le sol volcanique de la Plaine des Sables (Piton de la Fournaise, Île de La Réunion) ;
- En 2004-2005 : un stage de Master 2 sur l'étude locale des circulations d'air et d'eau dans le sol d'un cône volcanique inactif du Piton de la Fournaise (Formica Leo). J'ai découvert la modélisation numérique des processus de convection en milieu poreux dans ce stage ;
- En 2006-2009 : une thèse en co-direction entre l'Université Paul Sabatier et l'Université de La Réunion. Celle-ci étend l'étude des écoulements convectifs d'air et d'eau à l'ensemble du Piton de la Fournaise et à une zone volcanique récente de la planète Mars à partir d'observations optiques, géophysiques et de la modélisation numérique des circulations en milieu poreux ;
- En 2008 : un séjour d'un mois à l'Université de Tokyo en tant que bénéficiaire d'une bourse internationale de l'Université de Toulouse. Ce séjour a permis d'initier mes relations avec l'Université de Tokyo (professeur Kei Kurita) ;
- En 2009-2011 : deux années de post-doctorat à l'Earthquake Research Institute de l'Université de Tokyo sur invitation du professeur Kei Kurita en tant que lauréat du programme franco-japonais CNRS-JSPS². J'y ai étudié la dynamique de la convection en milieu poreux en conditions expérimentales.

1.2 Contexte de mon poste et positionnement scientifique

1.2.1 Contexte de mon poste

En 2011, j'ai réussi le concours de chargé de recherche en géophysique appliquée du Ministère de la Transition Écologique et Solidaire (MTES) et affecté au CETE³ Normandie-Centre, devenu Cerema⁴ en 2014. Il s'agit d'un établissement tourné vers l'appui scientifique et technique aux politiques publiques, placé sous la double tutelle du MTES et du Ministère de la cohésion des territoires et des relations avec les collectivités territoriales. Le Cerema est issu de la fusion de plusieurs centres d'ingénierie publique (CETE,

1. Programme Actions Concertées Incitatives 1999-2004 "Prévention des catastrophes Naturelles"

2. Japan Society for the Promotion of Science

3. Centre d'Étude Technique de l'Équipement

4. Centre d'Études et d'Expertise sur les Risques, l'Environnement, la Mobilité et l'Aménagement

CERTU⁵, CETMEF⁶ et SETRA⁷). Bien qu'étant un centre tourné vers l'ingénierie, l'établissement a été reconnu acteur de la recherche nationale par la loi de programmation de la recherche en 2021. L'équipe ENDSUM⁸ a été créée au 1er janvier 2018. Son objectif principal est le développement de méthodes de caractérisation et de diagnostic non destructives des sols et des ouvrages. En effet, les techniques actuelles (tels que les forages) ne délivrent souvent que des résultats ponctuels, onéreux et destructifs des structures et matériaux impliqués. L'enjeu est donc de mettre à disposition des gestionnaires des techniques et outils de diagnostic et de contrôle non invasifs, si possible à grand rendement, à faibles coûts et améliorant l'efficacité des procédures d'inspection et de suivi.

Au sein d'ENDSUM, j'ai poursuivi le développement de mon projet initié en thèse en tentant de répondre à la question scientifique suivante : **Peut-on caractériser le sous-sol et les structures du génie civil en combinant données d'imagerie optiques, géophysiques et modélisation numérique** ? Je me focalise notamment sur l'étude du lien entre phénomènes de surface et profonds (notamment hydrodynamiques), en utilisant une combinaison originale de données associant données de terrain (méthodes électriques, radar géologique, potentiels spontanés), aéroportés (infrarouge thermique, visible), satellitaires (infrarouge thermique, visible, accélérométriques) et modélisation (transferts de chaleur et de masse en milieu poreux, inversion électrique). Cette question centrale m'a amené à construire un parcours qui repose sur l'étude d'objets et de processus variés et qui ont des échelles spatiales et temporelles très différentes. Au Cerema, mes applications se sont enrichies en s'étendant au génie civil, à l'archéologie ou aux sciences pour l'ingénieur. J'ai pu analyser les données de nombreux capteurs, qu'ils soient embarqués depuis l'orbite, aéroportés ou déployés au sol (caméras, matériels géophysiques). La diversité et le volume important de ces observations m'a poussé à faire évoluer ma méthodologie initiale, en développant des outils permettant de combiner ou fusionner ces données spatialisées et les modèles. Cette approche s'est avérée très efficace au fil des années pour 1) mieux comprendre les phénomènes hydrogéologiques ou électriques en jeu dans les sols, 2) mieux contraindre certains traitements géométriques ou géophysiques (inversion...) et 3) fournir des outils de visualisation et d'analyse intuitifs. Mes recherches posent des questions diverses, qu'elles soient de nature scientifique ou technique, qui sont liées :

- au domaine spectral étudié. Peut-on utiliser l'infrarouge thermique, afin de caractériser des écoulements souterrains ou des structures dans les sols ? Cela sous-entend notamment de comprendre 1) comment l'eau circule dans les milieux et 2) comment se font les échanges aéro-hydro-thermiques entre la subsurface et l'atmosphère.
- au volume d'observations acquises. Quelles méthodes utiliser pour combiner/fusionner des données de télédétection, géophysiques et géométriques afin de faciliter et d'enrichir l'interprétation des données ?
- à l'avènement de nouveaux modes d'observation. Peut-on utiliser les drones comme vecteurs d'observation fiables, robustes et à bas coût pour des auscultations à grand rendement ?

Afin de répondre à ces questions, mes recherches sont structurées selon les trois axes de recherche d'ENDSUM, nourris par les remontées de terrain du Cerema, ainsi que par mes interactions avec des établissements et universités au niveau national et international : 1) la caractérisation physique et géométrique des milieux (section 3.1) ; 2) le développement de méthodologies d'observation et de traitement de données (section 3.2) et 3) le développement de prototypes et de moyens de mesure (section 3.3).

5. Centre d'études sur les réseaux, les transports, l'urbanisme et les constructions publiques

6. Centre d'études techniques, maritimes et fluviales

7. Service d'études sur les transports, les routes et leurs aménagements

8. Évaluation Non Destructive des Structures et des Matériaux

1.2.2 Positionnement scientifique

A l'interface entre la physique et les sciences de la Terre, mon investissement est à l'image de ce que j'aime faire :

- réaliser/analyser des observations et concevoir des modèles pour comprendre des phénomènes physiques ;
- Explorer des domaines scientifiques variés et créer de la connaissance pluridisciplinaire ;
- Développer des méthodologies ayant vocation à irriguer l'ingénierie ;
- en étant au Cerema, pouvoir réaliser des expertises pour les collectivités, au plus proche des besoins des concitoyens ;
- pouvoir interagir quotidiennement en relation avec des techniciens et ingénieurs de disciplines diverses.

Mon positionnement scientifique me semble relativement singulier dans le paysage international. De ma formation initiale en physique et géologie a découlé une thèse en géophysique et télédétection appliquée à la volcanologie planétaire, et une carrière en cohérence avec cette orientation pluridisciplinaire. Ce profil me permet de communiquer avec des scientifiques de plusieurs communautés, voire d'être de plus en plus en mesure de les fédérer (géologie, géotechnique, géophysique, télédétection, mathématiques appliquées). Les contributions personnelles issues de ces collaborations sont diversifiées, allant du pilotage de la collecte de données (en géophysique de subsurface ou en télédétection) à la réalisation de modèles numériques permettant d'expliquer les observations (modélisation directe hydro-thermique ou inversion électrique). Mon expérience dans les processus de convection en milieu poreux me permet par ailleurs de développer des idées originales faisant le lien entre températures de surface, phénomènes géophysiques et hydrogéologiques. Du point de vue thématique, mes publications scientifiques peuvent donc aussi bien traiter d'interactions sol-atmosphère, de phénomènes de subsurface, que d'interactions fluide-roche. Enfin, étant télépilote de drone depuis 2016, je maîtrise l'ensemble de la chaîne acquisition-traitement-interprétation pour les observations issues de ce vecteur. A titre d'exemple, cette compétence me permet aujourd'hui de participer au programme de gestion du littoral Ouest Africain (WACA⁹) afin de faire monter en compétence les équipes africaines sur l'usage des drones pour l'observation du littoral.

1.3 Des collaborations nationales et internationales

La diversité de mes thématiques de recherche fait que de nombreuses collaborations se sont développées au niveau national et international, donnant lieu à une participation à des projets et/ou à des publications scientifiques communes. D'abord, j'ai toujours su garder le réseau issu de ma thèse, constitué du GET¹⁰ (Michel Rabinowicz), de l'IPGP¹¹ (Fabrice Fontaine), le Laboratoire Géosciences Réunion (Anthony Finizola) et le laboratoire Magma et Volcans de l'Université Clermont-Auvergne (Lydie Gailler). Ces partenariats ont donné lieu à divers projets CNES (projets TOSCA), ANR (projet Slide4Volc), européens (7^{ème} PCRD Medsurv) et internationaux (Huayruro) et à l'encadrement de Cécile Mézon et de Téodolina Lopez en tant que doctorante et post-doctorante pendant plusieurs années. Avec mon intégration au Cerema, mes liens avec d'autres établissements se sont développés comme avec l'UGE¹² (Yannick Fargier, Sergio Palma Lopes et Jean-Luc Sorin) et l'ENPC¹³ (Yu-Jun Cui). Ces collaborations ont donné lieu à plusieurs travaux publiés, ainsi qu'au projet FUI national Didro (2016-2019). Ce projet a marqué le début de la montée en compétence de l'équipe ENDSUM Rouen sur les drones et m'a permis d'encadrer Marion Tanguy en tant que post-doctorante. Au niveau régional, je

9. <https://www.wacaprogram.org/fr>

10. Laboratoire Géosciences Environnement Toulouse

11. Institut de Physique du Globe de Paris

12. Université Gustave Eiffel

13. Ecole des Ponts Paris Tech

possède des liens étroits avec le laboratoire M2C ¹⁴ (Fayçal Rejiba et Abdel Jardani), le laboratoire IDEES ¹⁵ de Caen (Olivier Maquaire et Stéphane Costa), le Laboratoire de Mathématique de l'INSA de Rouen (Carole Le Guyader) et le Laboratoire de Mathématiques Raphaël Sale (LMRS) de l'Université de Rouen Normandie. Ces liens ont donné lieu à deux projets régionaux sur l'observation des falaises (TéléDÉTAC et Defhy3geo), à la thèse d'Azziz Saley, de Georges EDDE et à l'encadrement de trois post-doctorants : Imen Hassen, Sam Taoum et Thomas Junique.

Enfin, mes relations internationales ont été initiées grâce à mon post-doctorat à l'Université de Tokyo. Mes liens avec Anthony Finizola de l'Université de la Réunion ont permis une collaboration de plusieurs années avec Tullio Ricci de l'INGV ¹⁶ dans le cadre de la thèse de Cécile Mézon, mais aussi dans le cadre des projets d'imagerie électrique grande profondeur du Vésuve et de l'Etna (projet Medsurv). Par ailleurs, j'ai réalisé quatre séjours à l'Ingemmet ¹⁷ au Pérou entre 2015 et 2018 avec Anthony Finizola, soit un total cumulé de 6 mois en tant que chercheur invité dans le cadre du projet archéologique Huayruro ¹⁸. Depuis ma thèse en 2009, j'ai donc passé 2 ans et demi dans des instituts étrangers afin de mener des travaux collaboratifs. Enfin, depuis 2020, nous avons formé un consortium franco-chinois avec l'ENPC, la Northwest Agriculture and Forestry University (Heijun Hu), Zhengzhu University (Weikang Song), Cardiff University (Ni An) et le pôle "applications satellitaires" du Cerema (Téodolina Lopez) afin de d'étudier le lien entre données satellitaires, données géotechniques et géophysiques en milieu aride. Plusieurs articles sont en cours de rédaction sur cette thématique.

1.4 Une activité portant sur l'ensemble des facettes du métier de chercheur

Cet investissement constant dans plusieurs domaines me permet aujourd'hui de présenter à l'Habilitation à Diriger des Recherches un dossier attestant de diverses facettes du métier de chercheur qui seront détaillées en section 2 :

- 26 publications en premier auteur ou co-auteur en revues internationales à comité de lecture, donnant un h-index de 8 (référencement Scopus),
- deux chapitres d'ouvrage,
- quatre conférences invitées,
- 45 congrès internationaux avec actes,
- 15 communications avec actes en congrès national,
- 13 rapports de recherche,
- neuf rapports d'expertise.

J'ai co-encadré quatre thèses et ai participé à l'encadrement de quatre chercheurs post-doctoraux et de nombreux étudiants, du niveau prépa/DUT au niveau Master 2. Je porte actuellement un projet pour la Région Normandie en 2022, ainsi qu'un contrat d'expertise pour la ville de La Rochelle. J'ai été responsable de workpackages dans un projet industriel (FUI) et un projet international (franco-péruvien). Enfin, j'ai participé à 12 projets régionaux, nationaux ou internationaux.

En terme d'activité collective, je suis responsable-adjoint de l'équipe ENDSUM du Cerema Normandie-Centre (1DR, 1CR, 4 chargés d'études, 1 à 4 thèses ou post-doctorats par an et 1 à 5 stagiaires par an). Je m'investis pour ma communauté scientifique depuis 2014 en tant qu'élu à la Comeval ¹⁹ et membre de son bureau national. Il s'agit de l'équivalent du CoNRS au MTES. Depuis 2022, je suis nommé au Conseil Scientifique du Patrimoine Naturel de Normandie du fait de mes travaux en hydrogéologie. Enfin, mes travaux sont ponctués par une valorisation très importante à destination de la po-

14. Laboratoire de Morphodynamique Continental et Côtière de l'Université Rouen Normandie

15. Laboratoire Identité et Différenciation de l'Espace, de l'Environnement et des Sociétés

16. Istituto Nazionale di Geofisica e Vulcanologia

17. Instituto Geológico, Minero y Metalúrgico

18. Acronyme du projet franco-péruvien "Las civilizaciones olvidadas del volcan HUAYnaputina y les grand Retos del futURO"

19. COMmission nationale d'EVALuation des Chercheurs du Ministère de l'écologie

pulation, sous forme d'articles, d'interviews ou de films réalisés en collaboration avec la société de production 4scienceprod et les médias locaux/nationaux.

Après avoir présenté mon Curriculum Vitae détaillé dans la section suivante, mon mémoire se focalisera sur mes différents axes de recherche, afin de présenter les points saillants de mon activité scientifique. Finalement, je terminerai par le développement de mon projet de recherche pour les années à venir.

2 Curriculum vitæ détaillé

2.1 Etat civil

Nom : ANTOINE

Prénom : Raphael

Date de naissance : 23/02/1981

Corps, grade et ancienneté : Chargé de Recherche du Développement Durable depuis Novembre 2011

Organisme d'affectation : Cerema

Dates d'affectation dans l'organisme et l'unité : Novembre 2011

Téléphone : 02.35.68.90.53 **Télécopie** : 02.35.68.81.88

E-Mail : raphael.antoine@cerema.fr

Adresse professionnelle : Cerema, Direction Territoriale Normandie-Centre (Dter NC)
Equipe de Recherche ENDSUM
10, chemin de la Poudrière
CS 90245 - F-76121
Le Grand-Quevilly Cedex

[Lien base de données Scopus](#) et [Lien Google Scholar](#)

2.2 Diplômes et titres

2006-2009 Doctorat de l'Université de Toulouse, spécialité Géophysique.

Titre : Etude et modélisation des écoulements d'air et d'eau dans le Piton de la Fournaise et Cerberus Fossae (Mars). Directeur de thèse : Michel Rabinowicz, co-directeur : Patrick Bachèlery, co-encadrant : David Baratoux. Collaboration entre le Laboratoire Dynamique Terrestre et Planétaire (UMR 5562) et le Laboratoire Géosciences Réunion (UMR 7154).

2004-2005 Master 2 Sciences de la Terre et des Planètes Solides (STPS), Université Paul Sabatier, Toulouse. Stage de 6 mois au Laboratoire Dynamique Terrestre et Planétaire.

2003-2004 Master 1 de Sciences de la Terre et de l'Univers, spécialité Géophysique, Université Paul Sabatier, Toulouse. Stage de 4 mois au Laboratoire Dynamique Terrestre et Planétaire.

2002-2003 Licence 3 de Sciences de la Terre et de l'Univers, Université Paul Sabatier, Toulouse.

2001-2002 Licence 3 de Physique, Université Paul Sabatier, Toulouse.

2000-2001 DEUG de Sciences de la Matière, Université de La Réunion, Ile de la Réunion.

1999-2000 Classes Préparatoires Mathématiques Physique Sciences de l'Ingénieur, Lycée Leconte de Lisle, Ile de la Réunion.

2.3 Déroulement de carrière

2018- Chargé de recherche de Classe Normale en géophysique de subsurface. Adjoint au chef de groupe Evaluation Non Destructive des Structures et des Matériaux (ENDSUM) sur le site de Rouen.

2017 Création et management de l'équipe inter-département "DRONES", composée de 4 télépilotes, dont moi.

- 2015-2018** Chargé de Recherche de première classe en géophysique de subsurface. Equipe Electromagnétisme Appliquée - Laboratoire Régional de Rouen, Centre d'Etude et d'Expertise sur le Risques, l'Environnement, la mobilité et l'Amenagement (Cerema), Direction Territoriale Normandie-Centre.
- 2014-2015** Chargé de Recherche de seconde classe en géophysique de subsurface. Equipe Electromagnétisme Appliquée - Laboratoire Régional de Rouen, Cerema.
- 2011-2014** Chargé de Recherche de seconde classe en géophysique de subsurface. Equipe Electromagnétisme Appliquée - Laboratoire Régional des Ponts et Chaussées (LRPC), Centre d'Etude Technique de l'Equipement (CETE).
- 2011** Qualification aux fonctions de Maître de Conférence en 2010, section 35.
- 2009-2011** Post-doctorat. Titulaire d'une bourse post-doc CNRS-JSPS (Japan Society for the Promotion of Science) de 2 ans à l'Earthquake Research Institute de l'Université de Tokyo, sur invitation du professeur Kei Kurita. Sujet : Étude expérimentale et numérique des phénomènes convectifs et électriques en milieu poreux.
- 2005-2006** Trois mois de CDD en tant qu'Ingénieur sismique. Total, Pau.

2.4 Identification des domaines de compétence et d'études

Domaines de compétence : STU2 (Géophysique, géotechnique, géodésie, physique de l'atmosphère) et STU3 (Physique et mécanique des sols, sismique, mécanique des roches, géologie, géothermie)

Mots clé(s) associé(s) au(x) domaine(s) de compétences : Imagerie géophysique, Télédétection, Modélisation, Fluides, Interactions sol-atmosphère

2.5 Formation complémentaire

2015 : Qualification au télépilotage de drone (brevet théorique d'ULM + formation pratique), dans le cadre de mon activité de recherche.

2019 : Qualification au vol "hors vue" pour opérer les drones à 1 km de distance.

Langues

Français, Anglais, Espagnol (courant), Japonais (académique).

2.6 Production Scientifique

	Code	Nombre total
Article dans revue à comité de lecture répertoriée dans les BDI JCR, Scopus, ERIH, HCRES	ACL	26
Article dans revue à comité de lecture non répertoriée dans les BDI JCR, Scopus, ERIH, AEREL	ACLN	1
Ouvrage scientifique ou chapitre	OS	2
Conférence invitée dans un congrès international ou national	INV	4
Communications dans un congrès international	ACTI	47
Communications dans un congrès national	ACTN	8
Rapport de recherche	RAPP	12
Rapport d'expertise	RAPP-EX	8

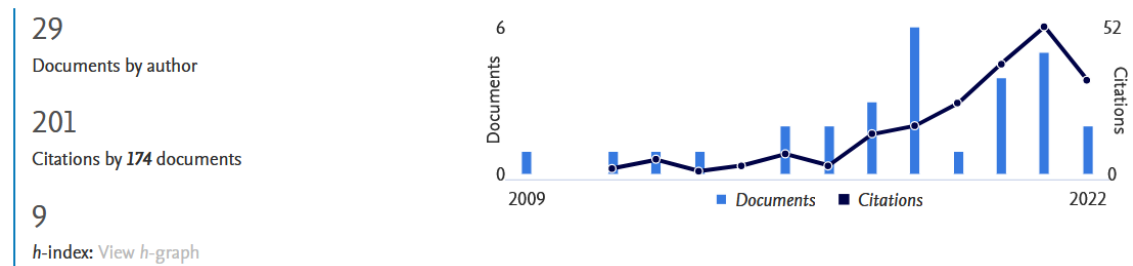


FIGURE 1 – Métrique Scopus.

2.7 Enseignement et formation à la Recherche

Enseignement

Prévue pour octobre 2022 Formation continue sur les méthodologies d'observation du littoral par drone au Sénégal (ville de Saint Louis) pour 16h (programme franco-africain WACA-BAR).

Avril 2022 Formation continue interministérielle sur les méthodologies d'observation du littoral par drone en République Démocratique de Sao Tomé-et-Principe (40h) (programme franco-africain WACA-BAR). La formation a réuni des stagiaires de divers horizons : ministères de l'Environnement et de l'agriculture, capitainerie du port, service météorologique et service d'incendie et de secours. La formation a porté sur une introduction à la télédétection avec focus sur les drones, la photogrammétrie appliquée à l'observation du littoral et les techniques d'acquisition.

2021- Avec Loic Gourmelen et Pascal Leger du Cerema, nous avons été à l'initiative de la mise en place de la formation continue « les drones pour l'observation des territoires » à destination des personnels du MTES et des collectivités. [Description de la formation ici](#)

Nous avons conçu complètement la formation, dont l'offre n'existait pas et qui contient trois modules :

- Module 1, Découverte des drones (16h) : connaissance des applications possibles en lien avec les politiques publiques, limites de l'usage de drones, principaux aspects réglementaires.
- Module 2, Entreprendre une activité drone (16h) : présentation de l'écosystème professionnel du drone et des usages privilégiés, définition du besoin d'utilisation du drone et des données produites, chiffrage des coûts, appréhension des impacts concrets de l'activité.
- Module 3, Acquisition et traitement des données issues du drone (16h) : présentation des différents capteurs pour l'acquisition de données, introduction à la télédétection visible et infrarouge thermique, traitements photogrammétriques multi-spectraux, manipulation de modèles 3D pour différentes applications (notion de combinaison et de fusion de données).

J'interviens dans le Module 2 pour 8h et dans le Module 3 pour 16h.

2018-2019 16h de cours magistraux en télédétection appliquée au drone + 8h de travaux pratiques sur le terrain (Master de l'Ecole d'ingénieur en génie civil de l'Université de Puno, Pérou).

2016-2017 16h de cours magistraux en télédétection appliquée au drone + 4h de travaux pratiques sur le terrain (Master en géophysique de l'Université San Augustin, Arequipa, Pérou).

2010-2011 Heat and Mass Transfer in Porous Media, Master 2 in Earth Sciences, Université de Tokyo, Cours + Travaux Dirigés (24h ETD).

2008-2009 Attaché d'Enseignement et de Recherche (demi contrat), Université Paul Sabatier. Plus de 130h d'ETD sur l'année. Stage de terrain en géophysique de subsurface appliquée à l'archéologie, Montans (Master 1 STU). Stage de terrain en géologie structurale, Ile de Groix (Master 1 STU). Travaux Pratiques en télédétection satellitaire (Master 1 STU).

2006-2008 Vacations, Université Paul Sabatier. 75h effectives, soit 70h ETD/an, Université Paul Sabatier. Travaux Dirigés en Sédimentologie (Licence 3 STU). Travaux pratiques en Sédimentologie (Licence 3 STU). Travaux d'Initiative Personnelle Encadrés (Licence 1 Sciences de l'Environnement).

Thèses

2022-2025 Encadrement de la thèse de Georges Edde intitulée "Étude des écoulements d'air et d'eau dans des cavités souterraines à partir de la modélisation numérique et de données de télédétection". Thèse financée par le Cerema. Directeur de thèse : Ionut Danaïla (50 %), Encadrement : Raphael Antoine (50 %). Je deviendrai co-directeur de thèse après l'obtention de l'HDR. Début de la thèse : Octobre 2022

2021-2024 Encadrement de la thèse de Diego Navarro intitulée "Localisation de drones par méthodes UWB, optique et accélérométrie en contexte de GPS dégradé et mesures radar sur ouvrage". Thèse financée par le Cerema dans le cadre du projet ROAD-AI avec l'Inria. Directeur de thèse : Ezio Malis, Inria (50 %), Encadrement : Raphael Antoine (50 %). Je deviendrai co-directeur de la thèse après l'obtention de l'HDR. Début de la thèse : Octobre 2021.

2014-2018 Azziz Saley a soutenu sa thèse en Décembre 2018 à l'Université de Rouen. Titre de la thèse : «Tomographie hydraulique des milieux poreux hétérogènes à partir de traçage thermique : approches expérimentales », Directeur de thèse : Jean-Paul Dupont (20 %), Co-direction : Abdel Jardani (40 %), Encadrement : Raphael Antoine (40 %)

2013-2017 Cécile Mézon a soutenu sa thèse en Janvier 2017 à l'Université Paris-Sorbonne. Titre de la thèse : "« Caractérisation des circulations thermo-convectives à l'échelle d'une zone fracturée par méthodes géophysiques et numériques ». Directeur de thèse : Anthony Finizola (33 %), Co-directeur de thèse : Pierre Adler (33 %), Encadrant : Raphael ANTOINE, encadrement à 33 %.

Post-doctorats

2023-2025 Encadrement prévu d'un post-doctorat à 50 % avec Carole Le Guyader (Insa de Rouen) dans le cadre du projet Defhy3geo. Sujet : Détection semi automatique de la fissuration sur les falaises de Normandie par fusion de données thermiques et visibles. Début : janvier 2023 ;

2023-2024 Encadrement prévu d'un post-doctorat à 33 % avec Ioana Ciotir et Antoine Tonnoir (Insa de Rouen) dans le cadre du projet Defhy3geo. Sujet : Modélisation numérique des écoulements dans la falaise de Sainte-Marguerite-sur-mer. Début : janvier 2023 ;

2022-2024 Encadrement à 50 % avec Cyrille Fauchard du post-doctorat de Thomas Junique dans le cadre du projet Defhy3geo. Sujet : Observations géophysiques et par drone des sites des Vaches Noires (14) et de de Sainte Marguerite-sur-mer avec application à l'hydrologie de ces falaises (76). Début : juin 2022 ;

2017-2019 Encadrement de Sam Taoum sur le développement d'un nouveau code d'inversion électrique 3D intégrant des topographies complexes avec application à l'imagerie géophysique des falaises des Vaches Noires (projet Région Télédétac). Encadrement à 25 % avec Cyrille Fauchard (ENDSUM), Antoine Tonnoir (INSA Rouen) et Yannick Fargier (UGE).

2017-2019 Encadrement de Imen Assen sur la modélisation géologique 3D et hydrologique des falaises des Vaches Noires (projet Télédétac). Encadrement à 50 % avec Cyrille Fauchard.

2012-2019 Encadrement de Téodolina Lopez à 50 % avec Michel Rabinowicz (Laboratoire Géosciences Environnement, Toulouse) dans le cadre de divers projets (notamment TOSCA CNES) durant 7 ans sur l'étude hydrologique de zones arides (Tchad, Algérie, Mongolie intérieure).

Etudiants pré-doctorat

2021-2022 Georges EDDE (Master 2 nanomatériaux, Université Libanaise, Beyrouth) : Étude numérique des écoulements d'air et d'eau dans une cavité souterraine possédant un puit ouvert. Encadrement à 33 % avec Hyam Abboud (Université Libanaise, Beyrouth) et Ionut Danaïla (Université de Rouen-Normandie).

2021-2022 Olivier Thérain (DUT Génie Civil, IUT du Havre) : Détermination de la précision de modèles photogrammétriques en fonction du nombre de cibles posées au sol. Encadrement à 50 % avec Vincent Guilbert.

2020-2021 Ayoub Rabeh (première année du cursus ingénieur de l'INSA de Rouen en mathématiques appliquées). Sujet : Influence du sol et de la végétation sur les températures de surface mesurées par drone : application au glissement des Vaches Noires. Encadrement à 50 % avec Philippe Foucher.

2020-2021 Arthur Leconte (seconde année DUT Mesures Physiques, Mont Saint Aignan). Sujet : Utilisation du code d'inversion PyLGRIM pour l'imagerie électrique 3D d'un terril en combustion interne. Encadrement à 50 % avec Vincent Guilbert.
Martin Dumoulin (seconde année DUT Mesures Physiques, Mont Saint Aignan). Sujet : Utilisation d'un prototype d'imageur électrique en conditions expérimentales (50 % avec Vincent Guilbert).

2019-2020 Astrid Legrand (DUT Mesures Physiques) : Imagerie électrique sur un champ d'Éoliennes. Encadrement à 50 % avec Vincent Guilbert.

Sarah Desfontaines (CPGE MPSI, Lycée Corneille). Sujet : Imagerie électrique d'une zone côtière, théorie et expérimentation en laboratoire. Encadrement à 100 %.

2018-2019 Ayoub Saydy (Master 2 GEHYD de l'Université de Normandie. Sujet : « Imagerie électrique sur pilier de carrière ». Encadrement à 50 % avec Cyrille Fauchard.

2017-2018 Kamila Azzoug (Master 2 Science de la Terre et des Planètes, parcours Terre et Géorressources, Université de Toulouse). Sujet : « Apport des données infrarouges thermiques pour comprendre l'évolution hydrogéologique en contexte sismique ». Encadrement à 50 % avec Téolodolina Lopez de l'ISSI de Bern (Suisse).

Melissa Pragassam (dernière année à Polytech Sorbonne, spécialité Sciences de la Terre). Sujet : « Hydrogéologie de la carrière de Saint-Martin-Le-Noeud à partir de données acquises dans l'infrarouge thermique et géophysiques ». Encadrement à 50 % avec Cyrille Fauchard.

2016-2017 Adrien Lebeau (dernière année du parcours Mathématiques Appliquées de l'INSA de Rouen). Sujet : « Détection automatique d'anomalies thermiques par méthodes neuronales. Encadrement à 50 % avec Carole Le Guyader de l'INSA de Rouen.

Encadrement de TPE : Tidjan Diallo (CPGE PCSI, Lycée d'Evreux. Sujet : imagerie électrique 3D d'une cavité souterraine par méthode électrique, Travail Personnel Encadré des classes préparatoire PC du Lycée Corneille (Rouen), encadrement à 50 % avec Vincent Guilbert.

2015-2016 Encadrement de TPE : Rémi Agricola/Emma Bely/Paco Iglesias/Milan Reigner (CPGE BCPST, Lycée Corneille). Sujet : Modélisation 3D pour l'étude des relations entre le système karstique de Caumont et la micro-topographie de surface,

Normandie, Travail Personnel Encadré en classes préparatoire BCPST, encadrement à 100 %.

2013-2014 Azziz Djibrilasalley (dernière année à Polytech Sorbonne, spécialité Sciences de la Terre). Sujet : Mesures géophysiques pour l'imagerie de subsurface de l'abbaye Notre Dame du Bec (27). Encadrement à 50 % avec Cyrille Fauchard.

2012-2013 Hassen Baoueb (Master 2 Sciences de l'eau, parcours hydrologie, risques, environnement). Sujet : Combinaison des approches hydrogéophysiques et thermiques pour l'identification des points d'infiltration rapide des eaux dans le contexte karstique de la Haute-Normandie. Encadrement à 50 % avec Abdel Jardani.

Paul Lethuillier (seconde année DUT Mesures Physiques). Sujet : Photogrammétrie appliquée aux Sciences de la Terre et au Génie Civil. Encadrement à 100 %.

2010-2011 Hiroshi Matsuoka (Master 2 Earth and Planetary Science, Université de Tokyo). Sujet : Caractérisation d'un panache thermique et des potentiels électriques associés en milieu poreux expérimental. Encadrement à 50 % avec Kei Kurita.

2.8 Activité d'expertise, de valorisation et de transfert

J'ai coordonné ou participé à 13 projets régionaux/nationaux/industriels/internes depuis 2009.

- trois projets région
- six projets nationaux
- deux projets industriels
- quatre projets de recherche interne ou participation à un programme de recherche

Projets Région

2022-2025 Porteur du projet Région RIN Tremplin DEFHY3GEO sur la caractérisation de la fracturation des falaises de Normandie (Evaluation par l'ANR) (885 k€). Consortium Cerema/M2C/INSA Rouen/LETG Caen.

2019-2022 Partenaire du projet Région RIN FONDEOL sur la caractérisation des interactions entre fondations d'éoliennes on-shore et leur environnement. Consortium Université Le Havre Normandie/INSA Rouen/Cerema/Université Franche-Comté.

2017-2019 Partenaire du projet Région RIN TELEDETAC (caractérisation de glissement de terrain grâce à la télédétection). Montant alloué à l'équipe : 200 k€. Coconsortium Cerema/INSA Rouen/LETG Caen. Ce projet a donné lieu à quatre articles de rang A ([44], [50], [52], [54], [58])

Projets nationaux

2022-2024 Partenaire du projet ANR Scan4volc dont l'objectif est d'imager le système hydrothermal du volcan Piton de la Fournaise à partir de mesures géophysiques et drone. Montant alloué à l'équipe : 10 k€. Porteuse : Lydie Gailler, Physicien adjointe Observatoire de Physique du Globe de Clermont-Ferrand. Consortium : Université Clermont-Auvergne/IPGP/Université Savoie Mont Blanc/Cerema.

2016-2019 Partenaire du projet ANR Slidevolc (caractérisation thermique d'un glissement de flanc en domaine volcanique. Montant alloué à l'équipe : 10 k€. Université Clermont-Auvergne/IPGP/Université Savoie Mont Blanc/Cerema. Ce projet a été valorisé dans un article de rang A [47].

2018-2019 Partenaire du Projet INSU EC2CO [99]. Consortium Cerema/Université Paris-Sorbonne.

2013-2016 Partenaire du projet CNES-TOSCA « THERSYA » sur la faisabilité d'utilisation de l'infrarouge thermique embarqué pour la caractérisation des ressources en eau autour du lac Tchad (obtention d'un postdoc). Consortium GET Toulouse/Cerema. Ce projet a donné lieu à deux articles de rang A ([36], [43]).

2012-2014 Partenaire du projet de recherche TERREAU (financement d'un post-doctorat par le RTRA STAE²⁰ de Toulouse). Consortium GET Toulouse/Cerema.

2007-2010 Partenaire de l'ANR Volcarisk durant ma thèse. Financement : 10 k€ par an pour du fonctionnement et des frais de mission. Le projet a été valorisé dans deux articles de rang A ([31], [38]). Consortium LDTP/CEREGE/IPGP/Université de Clermont-Ferrand.

Projets en partenariat avec des industriels

2014-2016 Partenaire du projet de recherche pour un grand industriel portuaire (montant : 100 k€). Consortium Cerema/Altran/Geolite/Geocarta. Le projet a donné lieu à une publication de rang A [49].

2016-2019 Responsable de deux workpackages « Observations multi-spectrales » et « étude expérimentale digue » dans le cadre du projet FUI DiDRO (Développement d'un démonstrateur drone pour le diagnostic, la surveillance des digues et l'intervention en cas de crise). Montant du projet : 2.7 M€. Consortium Ifsttar/inrae/Cerema/Ign/Geomatys/Survey Copter/Atechsys. Ce projet a donné lieu à plusieurs communications [126], [113], dont 1 internationale [47].

Programmes nationaux et opérations de recherche internes Cerema

2021- Participation au montage du défi quadriennal Cerema-Inria ROAD-AI portant sur les thématiques de l'acquisition de données géophysiques par tandem de drones et sur la fusion de données de la surface terrestre grâce à des données issues des drones et des satellites. Il s'agit d'un projet quadriennal avec mise en commun de financements de la part du Cerema et de l'Inria (2 thèses + 1 post-doctorat + 1 ingénieurs d'étude), dont la thèse de Diego Navarro. [Description du projet ici](#).

2013-2018 Responsable du projet de recherche interne HYDROGEO (financé par la DGPR et DGALN à hauteur de 80 k€ à 100 k€ euros/an).

2012-2016 Partenaire de l'opération de Recherche PRECAS financée par l'IFSTTAR (2012-2016). Tâche : Caractérisation thermique et géophysique (méthodes électriques) de cavités souterraines naturelles et anthropiques.

2012-2016 Partenaire de l'opération de Recherche DOFEAS financée par l'IFSTTAR (2012-2016). Tâche : Caractérisation de zones de perméabilité élevées dans les digues à partir de méthodes thermiques et géophysique. Modélisation des écoulements et des potentiels électriques dans ces structures. Le projet a donné lieu à une publication de rang A ([35]).

2.9 Activité internationale

Participation à des projets internationaux

2022 Participation à la rédaction du projet européen ECO4BRIDGE dans le cadre du CALL-HORIZON-CL5 portant sur le contrôle non destructif d'ouvrage d'art. Consortium BAM (Allemagne), BOKU (Autriche), WUST (Belgique), UNIZA (Slovaquie), CEREMA (France).

2019-2023 Participation au projet franco-africain WACA qui est un programme d'investissement de résilience des zones côtières en Afrique de l'ouest. Ce projet intervient dans six pays africains (Mauritanie, Sénégal, Bénin, Togo, Côte d'Ivoire, Sao Tomé-et-Principe) pour mettre en place des stratégies de veille et de lutte contre l'érosion côtière. Le projet WACA financé par la Banque Mondiale soutient techniquement les pays dans la mise en œuvre de leurs plans de travail. J'interviens dans ce programme en tant que formateur pour faire monter en compétences les pays sur la mise en œuvre des drones pour l'observation du littoral. [Description du projet ici](#).

20. Fondation Sciences et Technologie pour l'Aéronautique et l'Espace

- 2020-2023** Partenaire du projet européen Interreg POLDER2C's (<https://polder2cs.eu/>) Adaptation des ouvrages hydrauliques au changement climatique [ACL3]. Consortium France, Belgique, Hollande et Grande Bretagne. Dans ce cadre, collaboration étroite avec le Department of Mobility and Public Works belge ([51]). [Description du projet ici](#).
- 2017-2019** Partenaire du projet européen SAFER-LC project, H2020, CORDIS Europa ([128]). [Description du projet ici](#).
- 2016-2019** Responsable du work-package « Observations géophysiques » dans le cadre du projet franco-péruvien Huayruro (financé par l'équivalent de l'ANR au Pérou CONCYTEC, 120000 \$, ([53]). Consortium IPGP/Ingemmet/Igp/Cerema/Université Clermont-Auvergne.
- 2013-2016** Partenaire du projet européen MEDSUV « MEDiterranean SUPersites Volcanoes » - 7th Framework Programme on Research, Technological Development and Demonstration ([74], [82]). [Description du projet ici](#).

Collaborations internationales suivies

- Depuis 2020** En partenariat avec Yu-Jun Cui de l'ENPC, constitution d'une équipe franco-chinoise dans le cadre de mes travaux en hydrologie en Afrique (Lac Tchad) et en Mongolie (Désert du Badain Jaran). L'objectif des travaux est de faire le lien entre données satellite, données géotechniques et hydrologiques. Le consortium est constitué de Heijun Hu (Northwest Agriculture and Forestry University, Xianyang, Chine), de Weikang Song (Zhengzhu University, Chine), de Ni An (Cardiff University), de Téodolina Lopez (Pole Satellitaire de Toulouse, Cerema) et de Yu-Jun Cui (ENPC). La collaboration a déjà fait l'objet d'un papier soumis ([57]) et d'une communication en congrès international ([94]). Nous cherchons en ce moment à donner un cadre à cette collaboration fructueuse.
- 2016** - Collaboration internationale suivie avec l'INGEMMET et l'IGP du Pérou, notamment autour du projet franco-péruvien Huayruro, qui a donné lieu à la rédaction de plusieurs actes et d'un article de rang A ([53]).
- 2013**- Collaborations pérennes avec l'INGV de Rome et notamment Tullio Ricci, chercheur au département de Géophysique de l'institut. Cette collaboration a permis le financement par EIFER de la thèse de Cécile Mézon et la réalisation de missions d'envergure à Stromboli, sur le Vésuve et l'Etna (dans le cadre du projet MED-SURV).

2.10 Activité d'administration et d'animation de la Recherche

Direction de laboratoire ou d'équipes, gestion de personnel

- Janvier 2021** - responsable-adjoint de l'équipe ENDSUM-Rouen, intégré au nouveau département Géosciences et Infrastructures (DGI) de la Direction Territoriale Normandie-Centre :
- représentation du Chef de groupe et intérim en cas d'absence ;
 - management de quatre chargés d'études scientifiques/chargés d'essai, ainsi que du personnel non permanent (ingénieurs, étudiants, stagiaires, vacataires) ;
 - suivi fonctionnel et financier des activités du groupe
 - participation aux instances décisionnelles et aux groupes de travail ;
 - contribution à la définition de la stratégie de positionnement en matière de recherche en géophysique ;
 - participation à l'activité opérationnelle du département ;
 - participation aux actions de formation du groupe.
- Depuis 2018** Responsable Axe 1 de l'équipe ENDSUM : « Caractérisation physique et géométrique des sols et des matériaux ».

Depuis 2016 À l'initiative de l'équipe inter-département DRONE, dont la mission est de mettre en œuvre des drones dans le cadre de projets de recherche et d'activités opérationnelles du Cerema Normandie-Centre. Cette équipe a été créée en 2016 pour intervenir dans le cadre d'applications variées (risques naturels, aménagement, ouvrages ou infrastructures). Mon rôle consiste en :

- la définition de la stratégie scientifique et opérationnelle de l'équipe ;
- le suivi fonctionnel et financier de l'activité de l'équipe ;
- le management de quatre télé pilotes.

Animation de réseau

Depuis 2020, je m'implique beaucoup dans l'animation de la communauté Drone du MTES. L'objectif de cette communauté est de mettre en relation l'ensemble des acteurs du drone présents au MTE (établissements publics et de recherche, services déconcentrés notamment) afin de 1) partager leurs connaissances sur l'usage de ces outils et des méthodologies de traitements de données et 2) homogénéiser les pratiques concernant les drones volants dans le cadre de la réglementation aéronautique européenne mise en place début 2021.

Participation à des instances en lien avec la vie des chercheurs ou des établissements.

2019-2023 Membre élu du bureau de la Commission nationale d'Évaluation des Chercheurs du MTES (Comeval). Cette commission a pour mission d'évaluer et de recruter les chercheurs des établissements sous tutelle du ministère de l'Écologie (UGE, ENPC, ENTPE, IGN, ENSG, Cerema, Météo-France, ESTB et ENSM) ;

2014-2018 Premier mandat en tant que membre élu à la Comeval ;

2017 Membre du Comité Scientifique des Projets de Thèse du Cerema.

2.11 Rayonnement scientifique et diffusion de l'information et de la culture scientifique

Participation à des réseaux de recherche

Participation au réseau d'observation DYNALIT (OSU) ;

Participation au réseau national PIREN-SEINE ;

Participation au réseau régional Normandie Aerospace.

Participation à des comités éditoriaux et expertise d'articles

Je participe régulièrement aux reviews de différentes revues de rang A, parmi lesquelles : - Scientific Data (Nature.com, IF : 4.19), Near Surface Geophysics (1.2), Journal of Geophysical Research (IF : 3.4), Engineering Geology (IF : 1.7), Advances in Geosciences (IF=0.8).

Organisation de colloques ou de journée scientifiques

2019 à 2022 Participation au comité d'organisation du colloque « Usage des drones pour l'appui aux territoires » ouvertes aux établissements publics du ministère et aux collectivités. Dans ce cadre, organisateur de la session « Drone pour la Recherche et l'Innovation ». [URL du colloque ici](#)

Participation à des comités scientifiques, d'évaluation

2022-2027 Membre nommé au Conseil Scientifique Régional du Patrimoine Naturel de Normandie (CSRPN). Cette instance, placée auprès du Préfet de région et du Président du Conseil Régional, peut être consultée pour des questions relatives à la connaissance, la conservation et la gestion du patrimoine naturel régional. Le CSRPN a également la capacité de s'autosaisir. Le CSRPN rend des avis et pour cela il s'appuie sur des commissions thématiques et territoriales.

- inventaire et conservation du patrimoine naturel régional,
- classement et gestion des réserves naturelles nationales et régionales, autorisations portant sur des espèces protégées,
- proposition de listes régionales d'espèces protégées,
- mise en œuvre du réseau Natura 2000,
- volet général du Système d'Information sur la Nature et les Paysages.

2020 Evaluation scientifique du projet franco-singapourien BIPOS. Session ANR AAPG2020.

Activités d'expertise

2011 Depuis 2011, de nombreuses expertises ont été réalisées pour le compte de collectivités ou de services déconcentrés.

Activités de vulgarisation

Communications sur le projet Région Defhy3geo :

- [Article de presse sur les mesures réalisées sur la falaise de Sainte-Marguerite-sur-Mer en septembre 2022.](#)
- [Vidéo sur les mesures de Sainte-Marguerite-sur-Mer.](#)

Communications sur le projet franco-africain WACA :

- [Article du Cerema sur la mission Sao Tome et Principe](#)

Communications françaises sur le projet Huayruro :

- [Interview dans la série de films "Volcanologues du bout du monde"](#)
- [Une du journal quotidien Paris -Normandie](#)
- [Interview dans l'émission Un jour en France sur France Bleu national](#)
- [Nombreux articles et films sur le projet diffusés sur le site de la société de production 4scienceprod](#)
- [Prix du meilleur film scientifique pour Huayruro lors du congrès Cities on Volcanoes 9 qui a eu lieu en 2016 au Chili](#)

Communications péruviennes sur le projet Huayruro :

- [Communiqué de presse sur la visite du président de la République du Pérou sur le site du projet](#)
- [Page de l'Ingemmet sur le projet](#)
- [Page internet sur l'impact du projet Huayruro sur le tourisme](#)
- [Article d'inforegion.pe](#)
- [Article du quotidien national La Republica](#)
- [Article du site Andina.pe](#)

Communications sur le projet Didro (projet FUI) :

- [Explication du concept de Didro lors des Assises Nationales des Risques Naturels 2016](#)
- [Film de présentation du projet réalisé par la Compagnie Nationale du Rhône](#)
- [Article du Pôle Safe Cluster sur le projet](#)

Communications sur l'imagerie électrique profonde de l'Etna (Projet européen MED-SURV) :

- [Film de 26 minutes sur l'expédition Etna](#)
- [Reportage de la chaine italienne RAI italienne sur l'expédition](#)
- [Article du Cerema sur le projet](#)

Communications sur les projets TERREAU et THERSYA (projets CNES) :

- [Article du site Earth Observations \(NASA\) sur notre travail sur le lac Tchad](#)
- Communications sur le projet interne HYDROGEO :
- [Article de la Voix du Nord sur la mission d'imagerie géophysique du terril en combustion interne d'Haveluy \(Hauts de France\)](#)

3 Activité de recherche

Les cycles d'évolution de notre planète, les variations de sa morphologie, les fluctuations océanographiques et climatiques sont intimement liés aux processus profonds, quelle que soit l'échelle de temps et d'espace considérées. Les surfaces continentales interagissent avec l'atmosphère et l'océan, ce qui induit des modifications qui conditionnent notre activité anthropique. Caractériser notre planète Terre passe donc par la compréhension de ce lien entre phénomènes profonds et de surface, qui nécessite une approche multi-disciplinaire et multi-échelle. C'est ce qui m'anime en tant que chercheur depuis une dizaine d'années maintenant. La thématique principale de mes recherches porte sur la caractérisation du sous-sol et des structures du génie civil à partir de données de surface et profondes. Je m'intéresse plus particulièrement aux phénomènes intervenant entre le premier kilomètre de profondeur et la surface. Mes travaux sont tournés vers les risques naturels (étude de systèmes volcaniques, falaises, cavités souterraines), les ressources en eau (notamment en milieu aride) et la caractérisation d'ouvrages (ponts, routes, digues). Pour ce faire, j'utilise des outils d'imagerie optique (satellitaire, aéroporté, sol dans le visible et l'infrarouge), des méthodes géophysiques (méthodes électriques, radar) et la modélisation numérique (physique des écoulements en milieu poreux, inversion géophysique et photogrammétrique). Ces outils permettent de faire le lien entre les processus de surface observées à différentes échelles de temps et d'espace et des phénomènes plus profonds (notamment hydrodynamiques). Dans cette section, je présente mon parcours de recherche en trois parties consacrées à la caractérisation des milieux, aux méthodologies que j'ai développées et aux moyens de mesures que j'ai pu mettre en place.

3.1 Imagerie optique et géophysique appliquée à la caractérisation des milieux

3.1.1 Un début de carrière en volcanologie planétaire

Ma thèse a consisté à caractériser les échanges entre les sols volcaniques et l'atmosphère en contexte planétaire. Celle-ci s'est focalisée d'abord sur le volcan Piton de la Fournaise (Ile de La Réunion) et plus particulièrement sur le cratère inactif Formica Leo, pour lequel une suspicion d'anomalie thermique existait déjà. Pour documenter ce signal thermique et le relier aux interactions sol-atmosphère à l'échelle du cône, j'ai développé une méthodologie basée sur l'utilisation conjointe de plusieurs outils :

- des caméras exploitant les longueurs d'onde de l'infrarouge thermique et du visible pour observer les températures et l'état de surface ;
- des méthodes géophysiques (Imagerie de résistivité électrique ou IRE, potentiel spontané ou PS, microgravimétrie, radar) pour caractériser la structure du cratère Formica Leo ;
- des données micro-météorologiques (anémométrie ultrasonique) pour quantifier les vitesses et direction des entrées/sorties d'air dans le sol ;
- la modélisation numérique des écoulements convectifs en milieu poreux ;
- des données géologiques disponibles dans la littérature ou obtenues sur le terrain.

Cette approche a permis de montrer que dans un contexte volcanique constitué de matériaux non consolidés (scories, sables, cendres) et/ou fissurés, les échanges avec l'atmosphère sont induits au premier ordre par une ventilation convective de l'air humide à l'intérieur du milieu poreux [31]-[33]. Dans le cône inactif Formica Leo, ces circulations génèrent une anomalie thermique de 4 à 5°C, observable en surface et qui est la conséquence d'un réchauffement ou d'un refroidissement du milieu. L'air atmosphérique froid est aspiré par le fond des cratères (au nombre de deux dans Formica Leo), en les refroidissant pendant la nuit. Celui-ci se réchauffe dans le milieu poreux grâce au gradient géothermique du volcan, remonte les pentes stratifiées pendant un quart de journée, puis ressort plus chaud de quelques degrés au niveau des crêtes des cratères, créant ainsi un véritable effet cheminée. Les gradients de température observés en sur-

face sont induits par un transfert de chaleur efficace, évalué à jusqu'à dix fois le flux conductif dans ces zones (200 mW m^{-2}). Ce phénomène est rendu possible grâce aux vitesses du fluide élevées (de l'ordre de 10^{-3} m s^{-1} à 10^{-2} m s^{-1}) dans le milieu perméable, constitué de lapilli et de bombes volcaniques de diamètre pluri-centimétriques (perméabilités estimées de 10^{-8} m^2 à 10^{-5} m^2 , correspondant à des tailles de grains/blocs de 10^{-2} m à 10^{-1} m). L'anomalie de température observée sur Formica Leo a d'abord été suggérée, puis documentée grâce à une caméra thermique. Elle a par la suite été confirmée par des mesures de température à 30 cm de profondeur. L'air aspiré dans le fond des cratères a par ailleurs pu être observée grâce à un anémomètre ultrasonique 3D prêté par Météo France et posé sur la surface. Cela montre à quel point les techniques de télédétection combinées à la modélisation numérique peuvent être puissantes pour étudier les échanges sol-atmosphère. Enfin, cette circulation d'air à l'intérieur des cratères induit des processus électriques très intéressants et qui sont rarement mis en évidence en milieu non saturé. En effet, des anomalies de potentiel spontané atteignant 300 mV et corrélées aux anomalies thermiques se développent sur quelques dizaines de mètres. J'explique cette observation par la circulation d'air humide dans le réseau poreux, venant draguer des ions des films d'eau présents autour des grains.

Si de nombreuses études ont par le passé traité de ces échanges entre le sol et l'atmosphère [18], jamais à notre connaissance une anomalie thermique de faible ampleur n'avait été caractérisée de façon aussi complète sur un volcan. Au fil de ma thèse, je me suis servi du cône Formica Leo comme d'un véritable laboratoire à ciel ouvert, ce qui m'a permis de développer et d'éprouver mes outils d'observation et de modélisation et de bien cerner les phénomènes en jeu. Je me suis ensuite appuyé sur ces connaissances pour étendre mon étude à l'ensemble du Piton de la Fournaise et une zone volcanique récente de Mars, Cerberus Fossae. Dans le cas du Piton de la Fournaise, je propose qu'à l'instar de Formica Leo 1) l'air froid entrant à la base du cône terminal 2) se réchauffe et remonte à l'intérieur des couches stratifiées perméables pour 3) ressortir plus chaud autour du cratère sommital de Dolomieu, avec une différence de température observée de $10\text{-}15^\circ\text{C}$ par rapport à l'air atmosphérique. La figure 2 présente le concept de cette circulation à grande échelle dans le Piton de la Fournaise. Il est à noter que plusieurs sorties d'air ont été détectées autour du cratère sommital Dolomieu entre 2007 et 2012, avec des vitesses de sorties pouvant avoisiner les 10^{-1} m s^{-1} en période calme (sans vent) [69]. Ce modèle impliquant des écoulements pluri-kilométriques dans un milieu poreux non consolidé ou fracturé a déjà été proposé par plusieurs auteurs sur des volcans ou dans la zone de stockage nucléaire souterraine expérimentale de Yucca Mountain dans le Nevada aux Etats-Unis ([6], [8]-[10]).

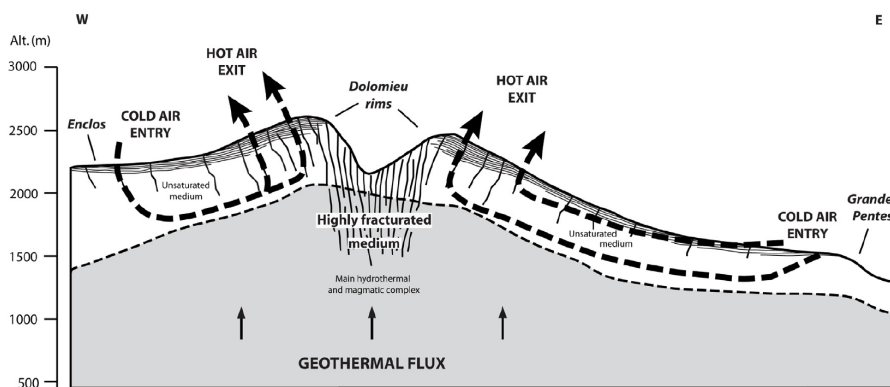


FIGURE 2 – Modèle conceptuel des circulations d'air internes dans le Piton de la Fournaise obtenu à partir de données de terrain au sommet du volcan et de la théorie de la convection [38].

Sur la planète Mars, de nombreuses anomalies thermiques ont été retrouvées ces

dernières années à l'intérieur de zones d'effondrement appelées pit craters, dont certaines de 50°C [21]. Mes travaux ont montré, qu'à l'instar de la Terre, des phénomènes de convection d'air atmosphérique (du CO_2 en l'occurrence) sont possibles dans des sols perméables de la planète. Encore plus que pour la Terre, de fortes perméabilités sont nécessaires pour un transfert de chaleur efficace permettant l'apparition d'une anomalie thermique en surface, du fait de la faible capacité calorifique de l'atmosphère martienne (au moins 10^{-6} m^2 , correspondant à un diamètre de blocs de 10^{-1} m). Ces transferts semblent possibles dans des pierriers tels que ceux des fractures pluri-kilométriques de Cerberus Fossae [32] ou à l'intérieur de pit craters du volcan Tharsis Mons [33]. Ces résultats sont appuyés par les travaux récents de [21] sur l'influence de la géométrie des pits craters d'Arsia Mons sur leurs températures de surface. Ils permettent de jeter un regard nouveau sur les processus d'échanges entre la subsurface et l'atmosphère en contexte planétaire. Ces interactions peuvent en effet être particulièrement dynamiques dans les milieux poreux perméables, transporter du gaz en profondeur et participer au façonnement du champ thermique de surface. Enfin, la détection indirecte des entrées/sorties via les températures de surface ouvre une nouvelle voie pour appréhender la perméabilité du milieu qui permet une circulation efficace du fluide.

3.1.2 A la recherche de l'eau dans les zones arides et les volcans

Après cette expérience en contexte planétaire, je me suis intéressé à l'hydrologie des zones arides (sur financements CNES), en collaboration avec le GET²¹, l'ISSI²² de Bern (Suisse) et le laboratoire Hydrosience Montpellier. La possibilité d'utiliser des données thermiques pour la localisation de nappes d'eau peu profondes a été évoquée dans les années 70 ([1], [3]). Ces résultats montrent que les nappes souterraines se comportent comme des puits de chaleur en été et comme des sources de chaleur en hiver, car les eaux souterraines ont une inertie thermique intra-annuelle plus forte que les eaux de surface [16]. Une étude réalisée par [11] a montré une corrélation entre les températures obtenues à partir des données dans l'infrarouge thermique du satellite METEOSAT, et des anomalies piézométriques de la nappe libre du Quaternaire dans le bassin du lac Tchad. Celles-ci correspondent à des dômes -avec une profondeur de $\approx 10 \text{ m}$ sous la surface- et dépressions piézométriques fermés -avec une profondeur de $\approx 60 \text{ m}$. Nous avons complété cette étude grâce à des observations satellitaires, géologiques et la modélisation numérique des circulations dans le bassin ([36], [43]). Bien que performants, les codes de convection "in house" utilisés dans les précédentes études ne permettaient pas de modéliser les circulations sous le lac Tchad du fait de la géométrie du bassin sédimentaire. J'ai donc pris l'initiative de réaliser les simulations via le logiciel commercial Comsol Multiphysics utilisant la méthode des éléments finis et plus flexible pour la résolution des EDP en milieu complexe. Cette étude a favorisé des développements notables en modélisation numérique 2D par rapport à mes travaux précédents, avec notamment la prise en compte de la géométrie des couches sédimentaires et de leurs caractéristiques physiques en fonction de la température (conductivité thermique effective, viscosité, ou coefficient d'expansion thermique ou encore perméabilité anisotrope). Les résultats montrent qu'il existe un courant d'eau convectif à grande échelle (plusieurs dizaines de kilomètres) dans le bassin sédimentaire du Lac Tchad et qui implique plusieurs couches géologiques, comme le montre le champ de température de la figure 3. Une multitude de petites cellules convectives est présente dans la couche de grès en base du bassin, induisant une descente de fluide sous le Kadzell et une remontée à droite de la figure sous le Kanem. Les dépressions et dômes piézométriques sont donc liées respectivement à la présence d'un courant convectif descendant (sous le Kadzell) et ascendant (sous le Kanem). Cette circulation induit une baisse de température au niveau du courant descendant (flux de chaleur de 40 mW m^{-2}), alors que le flux montant réchauffe la surface de 5 à 10°C en générant un flux de plus de 100 mW m^{-2} , important pour la région. Avec ceux de [11], ces travaux mettent en exergue l'influence

21. Laboratoire Géosciences Environnement Toulouse

22. International Space Science Institute

1) des variations spatiales de conductivité thermique dans le bassin pour la génération de la convection, 2) de la perméabilité des couches et de la présence de discontinuités structurales (failles) dans la migration des fluides vers la surface et 3) de la topographie à l'intérieur du bassin qui facilite la circulation.

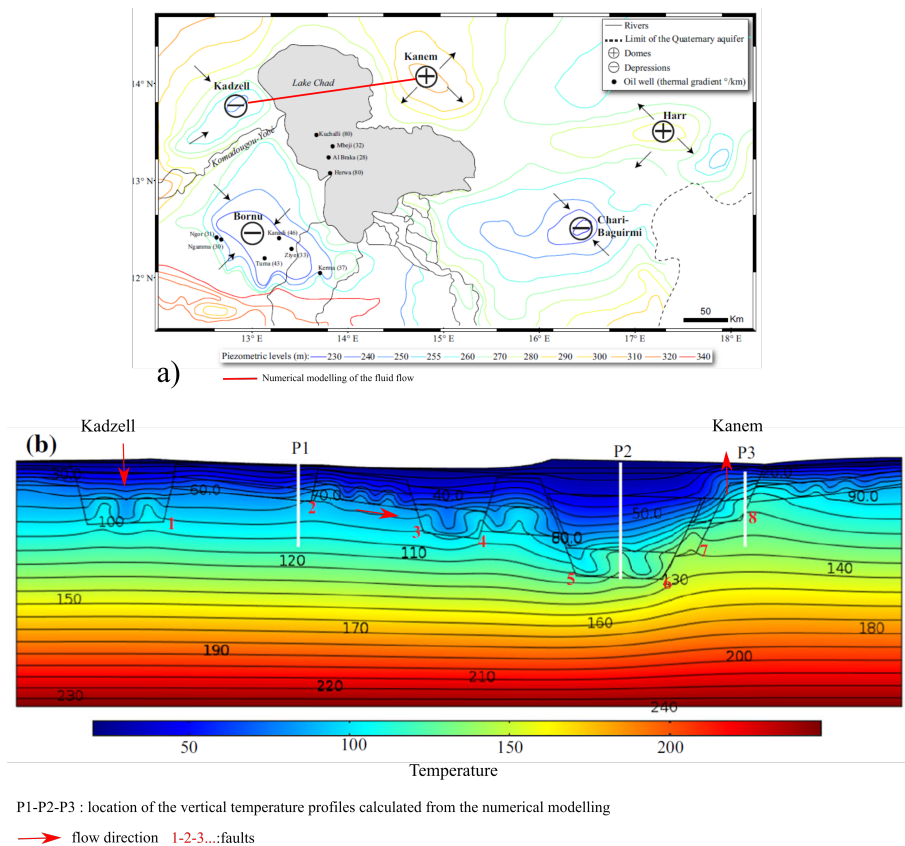


FIGURE 3 – Simulation numérique de la température à l'intérieur du bassin du lac Tchad présentant la morphologie de la circulation convective d'eau dans les couches géologiques les plus perméables [36].

Ces écoulements profonds impliquent des phénomènes similaires à ceux présents dans les systèmes hydrothermaux des volcans. Ces processus ont pu être indirectement caractérisés grâce à l'imagerie géophysique, et notamment aux mesures électriques basse fréquence, dont j'ai contribué à la mise en œuvre grâce à des projets menés par Anthony Finizola du Laboratoire Géosciences Réunion sur le Vésuve, l'Etna ou encore le Stromboli entre 2014 et 2018 ([74], [85], [87], [45], [107]). Plusieurs missions de grande ampleur (financées grâce au projet du 7^{eme} PCRD Medsuv) ont permis d'établir les premières inversions d'IRE à grande profondeur de ces systèmes (≈ 900 m sur l'Etna). Elles ont été complétées par des mesures de potentiels spontanés, de CO₂ et de températures à 30 cm de profondeur, donnant des informations sur l'hydrodynamique du système hydrothermal. Au delà de l'important défi technique que représentent ces expéditions sur le terrain (une vingtaine de personnes pendant 20 jours), le déploiement de mesures de résistivité grande profondeur a permis de caractériser la présence de fluides hydrothermaux à une échelle pluri-kilométrique sur l'Etna et le Vésuve, en relation avec les discontinuités structurales des édifices (failles, fissuration). La figure 4 présente une compilation de données de terrain obtenues sur le Vésuve sur six kilomètres de distance. Elle met en évidence la corrélation entre plusieurs types de données (température, potentiels spontanés) et une zones conductrice (visible sur la carte de résistivité électrique) permettant de localiser le système hydrothermal du volcan. Elle

montre aussi l'influence des discontinuités structurales (failles, fractures...) liées au cratère de 1906 et accueillant potentiellement des circulations de fluides sur les données de températures, de potentiels spontanés et de résistivité électrique.

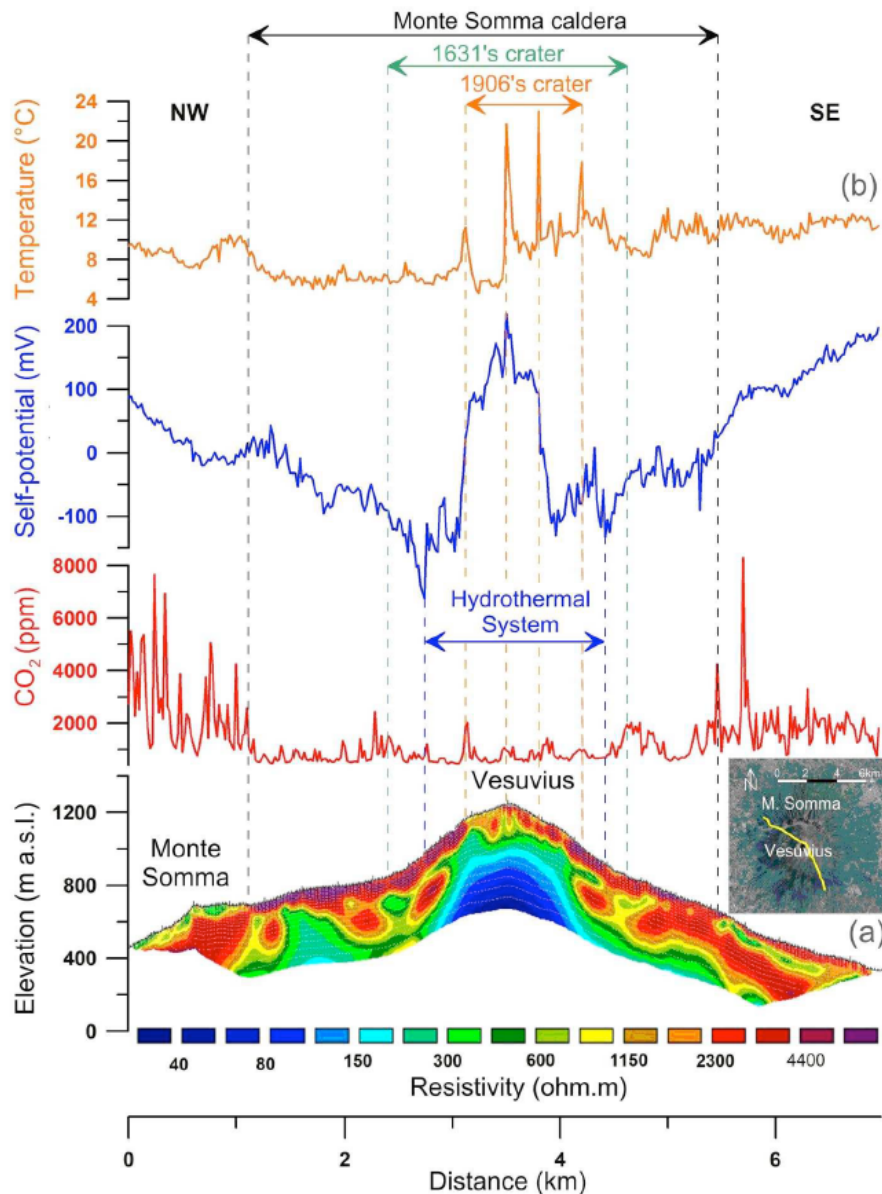


FIGURE 4 – a) Localisation du profil géoelectrique de 7 km de long traversant le Vésuve; (b) De haut en bas : Tomographie de résistivité électrique, potentiels électriques, Température à 30 cm de profondeur et concentration de CO₂ le long du profil NO-SE montré en a) [107].

A une échelle plus petite (hectométrique), la thèse de Cécile Mezon (financée par EDF R&D) s'est focalisée sur la caractérisation des circulations de fluides dans une zone fracturée du sommet du système hydrothermal du volcan Stromboli (Pizzo) grâce à ces méthodes, ainsi que sur le développement d'un modèle convectif en présence de fractures ([81], [86], [45]). L'objet étudié dans cette thèse est la remontée hydrothermale située au niveau de la limite supérieure de l'effondrement de Rina Grande, au sommet du volcan Stromboli. L'approche géophysique de sub-surface comprend une cartographie spatiale (à l'échelle métrique) en IRE, PS et température et un suivi tempo-

rel des signaux PS et thermique. La cartographie spatiale nous renseigne sur l'extension spatiale du système hydrothermal grâce à l'IRE 3D et le caractère actif des circulations (méthodes PS et température). Le traitement des données de surveillance montre qu'une relation linéaire lie le signal thermique et le signal PS, une relation qui ne peut être purement thermo-électrique. Le jeu de données temporel met l'accent sur la dynamique du système convectif et notamment la probable dépendance de la vigueur du système convectif avec les variations saisonnières de température atmosphérique. Le second volet vise à quantifier l'énergie évacuée par des systèmes thermo-convectifs à l'aide d'une approche numérique. Cette approche géophysique met en évidence le fait que les zones endommagées telles que des limites structurales favorisent la circulation des fluides hydrothermaux. Ceci s'explique par le fait que fractures, failles ouvertes, zones d'altération etc. changent à petite échelle la perméabilité du milieu. L'approche numérique se focalise sur la simulation 3D de l'écoulement et du transfert de chaleur dans des milieux poreux fracturés. Le travail s'est basé sur un code d'écoulement en milieux poreux fracturé pré-existant dans l'équipe de Pierre Adler de Sorbonne Université. Ce code a été adapté afin de résoudre le problème thermique. L'étude théorique vise à quantifier l'influence des paramètres du réseau de fractures sur l'énergie dissipée. L'influence de la densité de fractures, de la transmissivité de fractures et l'anisotropie du réseau de fractures sont évaluées. L'étude compare également les flux de chaleur dégagés par des modèles où les fractures sont insérées de manière discrète avec des modèles homogènes et de même propriétés macroscopiques (approche effective). Les résultats montrent que la validité de l'approche effective est fortement dépendante des paramètres du réseau de fracture (figure 5). Enfin, à l'échelle du laboratoire, j'ai pu faire le lien entre températures du milieu et écoulements d'eau en condition expérimentales. J'ai notamment pu 1) caractériser l'évolution d'un panache convectif d'eau en milieu poreux déclenché par chauffage par le bas grâce à des thermocouples et des mesures de potentiels électriques dans le cadre de mon post-doctorat à l'Université de Tokyo [66] et 2) proposer une méthode de quantification de la perméabilité d'un milieu poreux grâce à l'envoi d'un pulse d'eau chaude dans le cadre de la thèse d'Azziz Saley [37]. Ces travaux ont été réalisées avec des laboratoires divers comme le LGSR²³, l'INGV²⁴, le Volcano Research Center de l'Université de Tokyo ou le Laboratoire M2C de l'Université de Rouen.

23. Laboratoire Géoscience Environnement de La Réunion

24. Institut National de Géophysique et de Volcanologie

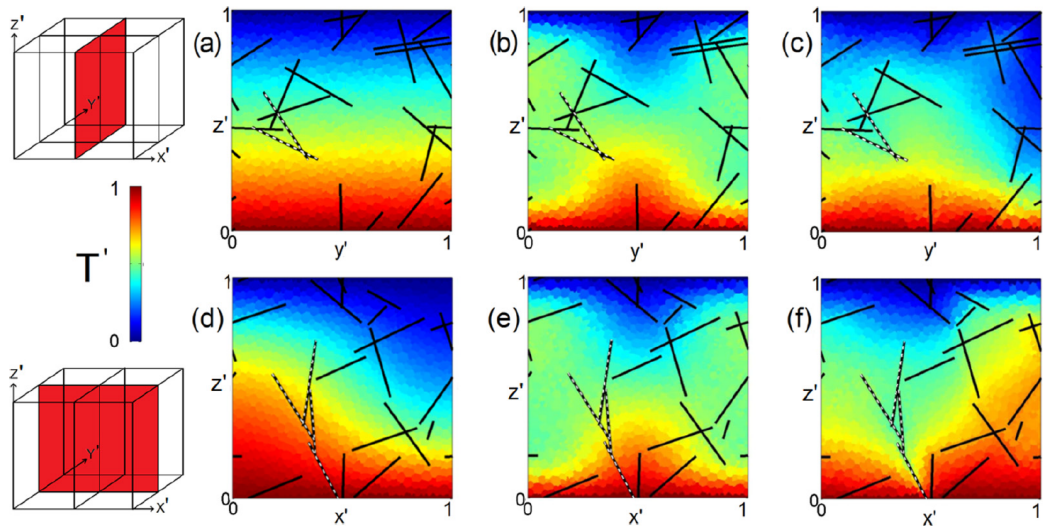


FIGURE 5 – Champ de température stationnaire simulé pour deux plans verticaux orthogonaux verticaux pour trois transmissivités de fracture adimensionnées différentes (a), (d) $\sigma'=0.1$; (b), (e) 1; et (c), (f) 5. Simulations réalisées pour une densité de fracture par unité de volume adimensionnée $\rho'=4$ et un nombre de Rayleigh $Ra=41.5$ [45].

3.1.3 Vers la caractérisation des structures du génie civil

Ces études en science de la Terre ont apporté des connaissances solides que j'utilise pour la caractérisation de structures du génie civil. Les expertises à laquelle je participe régulièrement au Cerema sont tout à fait propices à ces travaux. En 2014, j'ai mené une étude sur deux quais de Haropa Port Le Havre mettant en évidence i) des dépressions de surface au droit de cavités souterraines grâce à la modélisation 3D photogrammétrique par drone et ii) des anomalies thermiques de 2 à 4°C observées sur les flancs de ces dépressions, grâce à un suivi temporel réalisé par une caméra thermique embarquée [49]. Ces observations montrent des zones froides apparaissant pendant la journée sur les flancs des dépressions avec des contrastes maximums en milieu d'après-midi. Après avoir étudié l'influence potentielle des propriétés de surface (inertie thermique, émissivité, albedo), de la micro-topographie des quais et de la présence de cavités souterraine sur le champ thermique, j'explique cette corrélation entre température et déformations par une infiltration d'eau météorique. Ce processus est plus efficace (i.e. une vitesse de Darcy plus élevée) au niveau des flancs des dépressions qui sont en extension mécanique et donc plus perméables (via des fissures) que leurs centres. Dans ces zones, la pluie induit une anomalie thermique capable de se maintenir pendant plusieurs heures, voire plusieurs jours par rapport aux zones saines comme le montre les travaux expérimentaux de [2]. Ces contrastes sont alors détectables grâce à un suivi temporel par caméra thermique. Il est à noter que les seules méthodes ayant apporté des résultats dans cette étude sont les techniques optiques, les observations géophysiques (électromagnétiques et radar géologique 3D) étant inexploitable du fait de la présence d'armatures dans les quais générant un bruit important dans les signaux. En l'absence de ces perturbations électromagnétiques, les fortes perméabilités peuvent aussi induire des signaux remarquables dans les données obtenues par radar. En 2014, j'ai dirigé une expertise utilisant le radar géologique sur une digue de protection contre les inondations localisées à Saint Firmin dans le Loiret (45). Ces mesures ont mis en évidence des contrastes de permittivité diélectriques importants, liées à des zones remaniées ou de porosité élevée dans la digue et sujettes à des fuites. L'originalité de l'étude réside dans la combinaison d'une méthode géophysique et d'une méthode hydraulique afin de mettre en évidence des zones de fuites. Elle montre la relation qualitative entre les signaux radar, la perméabilité du milieu mesurée grâce au système PERMEAFOR [15] et les observations de fuites en pied de digue ([129], [109], [35]). Du point de vue opérationnel, l'étude géophysique permet ainsi de compléter les observations visuelles réalisées par les gestionnaires sur le terrain et d'optimiser le diagnostic de l'ouvrage. Par ailleurs, ces travaux valorisent le Perméafor au niveau international, outil développé par l'UGE et le Cerema et donnant accès à des informations directes sur les perméabilités de la subsurface.

La caractérisation des structures du génie civil passe aussi par l'imagerie du bâti ancien, notamment en archéologie. Ces dernières années ont été l'occasion de caractériser de nombreux sites patrimoniaux ou archéologiques en France ou à l'international ([68], [34], [41], [53]). Deux projets présentent un intérêt particulièrement important dans ma vie de chercheur. Le premier est l'Abbaye du Bec Hellouin (Eure, 27), pour laquelle j'ai participé aux mesures radar et électriques, et où nous avons découvert par hasard l'emplacement de l'église romane originelle [41]. Le second est le projet franco-péruvien Huayruro, que j'ai intégré grâce aux résultats du Bec Hellouin. L'objectif est de mettre en évidence l'importance culturelle et touristique de vestiges Incas dans la région de Moquegua (sud Pérou) au travers d'études en histoire, géologie, géophysique, archéologie et paléoclimatologie [53]. Ces villages ont été enfouis lors de l'explosion gigantesque du volcan péruvien Huaynaputina en l'an 1600. Cette explosion est une des plus importantes qu'ait connue la planète ces cinq cents dernières années. Ayant produit plusieurs km³ de cendres et des coulées pyroclastiques recouvrant une trentaine de villages Incas, cette explosion a abaissé la température de la Terre de 1.2°C. Le projet, mené par Anthony Finizola en collaboration avec l'Ingemmet et l'IGP²⁵ péruviens a eu un impact national

25. Institut de Géophysique du Pérou

au Pérou : Huayruro a été proclamé d'intérêt régional par la Région de Moquegua et présenté au congrès (l'équivalent du parlement français) en 2018. Dans ce projet, j'ai participé au déploiement de méthodes radar, électromagnétique (EM31), magnétique, visible et infrarouge thermique pour la cartographie des vestiges, dont une synthèse est fournie sur la figure 6. Notre investissement est allé au-delà de la géophysique, avec une implication active dans la valorisation géologique, historique et touristique du site. Enfin, ces périodes passées au Pérou ont été l'occasion d'un investissement important dans l'enseignement prodigué dans plusieurs universités, ainsi que dans la formation des chercheurs/ingénieurs aux techniques géophysiques et embarquées sur drone.

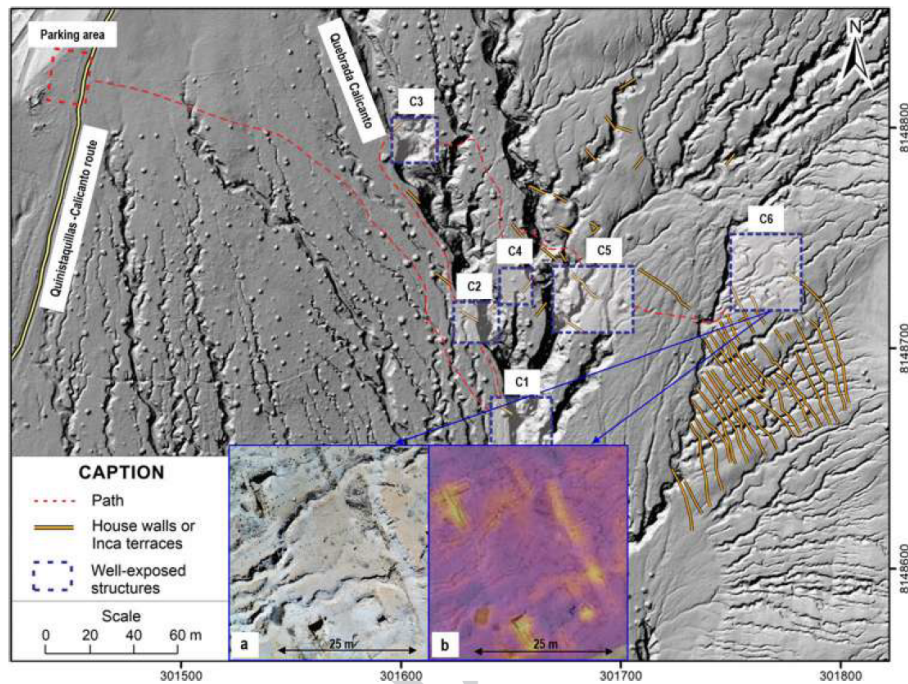


FIGURE 6 – Modèle ombré (8.27 cm/pixel) montrant la zone archéologique de Calicanto étudiée dans le cadre du projet Huayruro. Les vestiges enterrés ou semi-enterrés détectés grâce à l'infrarouge thermique et au radar géologique sont replacés sur la carte. L'image a) montre une vue de drone d'un bâtiment semi-enterré. L'image b) montre le même bâtiment détecté grâce à une caméra thermique à bas coût FLIR One branchée sur smartphone et embarquée sur le drone [53].

Tiré-à-part ACL35 : Permeability and voids influence on the thermal signal, as inferred by multitemporal UAV-based infrared and visible images. *Journal of Hydrology, Rang Q1, IF=5.7.*

3.2 Modélisation 3D pour les géosciences

La nécessité de prise en compte de la troisième dimension a très tôt été sous-jacente dans mes travaux. Les signaux thermiques et géophysiques peuvent être dépendants de la géométrie de surface, notamment dans le cas des volcans, des falaises, des glissements de terrain ou des ouvrages du génie civil. La convection thermique naturelle est notamment dépendante de la morphologie 3D de l'environnement. Cette dernière peut en effet contrôler le déclenchement de la convection, la faciliter, influencer sa structure (nombre et dimension des cellules) et/ou son amplitude ([10], [38], [27]). En imagerie géophysique, l'absence de prise en compte de la topographie dans les inversions électriques peut mener à des résultats inexploitablement dans le cas de topographies complexes [105]. Par ailleurs, la prise en compte d'une topographie a minima juste au voisinage des électrodes de mesure peut induire des artefacts et donc à une mauvaise interprétation des résultats, du fait de la résolution imprécise du problème direct. Au début de mon parcours de recherche, les modèles 3D de terrain permettant de documenter l'influence de la topographie sur le signal thermique et géophysique étaient difficiles à obtenir, voire n'existaient pas. En effet, le coût des données était élevé et les résolutions s'avéraient souvent insuffisantes pour les études. Les codes numériques permettant de réaliser des simulations prenant en compte des variations de la topographie étaient aussi difficiles à obtenir.

Peu après mon recrutement, la méthode photogrammétrique a été introduite au laboratoire, ouvrant la voie à la réalisation de Modèles Numériques de Terrain (MNT) à bas coût. Cette technique exploite les lois de l'optique pour calculer la localisation de la prise de photo et ainsi reconstituer une surface en trois dimensions à partir de photographies. Une image constitue un enregistrement plan et déformé de l'environnement. Pour reconstruire notre environnement tridimensionnel, il faut au moins deux images prises de deux points de vue différents et procéder par intersection. Ce principe est analogue au fonctionnement de notre système visuel qui nous permet d'appréhender notre environnement en relief, par nos deux yeux : c'est la stéréovision. Deux images prises dans des conditions semblables à celles de la vision humaine (dont les points de vue sont parallèles mais décalés dans l'espace) forment un couple qui permet de retrouver la sensation de relief par photogrammétrie. Aujourd'hui, le traitement simultané de centaines de photographies grâce aux logiciels photogrammétriques permet de reconstituer en 3D un objet géologique en quelques heures, objectif encore impensable il y a une quinzaine d'années.

Étant données les potentialités majeures de cette méthode, je me suis formé à l'acquisition et au traitement de données photogrammétriques, dans le but d'implémenter cet outil dans les études thermiques et géophysiques. En 2013, nous avons intégré les résultats d'inversion électrique 2D et de données radar dans un pont²⁶ reconstitué en 3D pour faciliter sa restauration ([34], [111], [59]). Dans cet article, tout en participant à l'acquisition et à l'interprétation des données, j'ai pu combiner l'ensemble de ces observations dans un seul et même modèle 3D. Ce travail a été réalisé en collaboration avec Julien Lacogne (alors architecte au Cerema) et dont un des résultats obtenu grâce au logiciel gratuit Google Sketchup est présenté dans la figure 7. Elle permet de préciser la distribution verticale et latérale de résistivité dans le pont et son environnement proche en relation avec les deux sondages réalisés sur le site. Combinées aux données radar et à l'inspection de l'ouvrage, ces résultats ont facilité la localisation des pathologies du pont (décompressions, déjointements de pierres, présence de racines d'arbres...) pour optimiser sa restauration, mais aussi pour mieux le replacer dans son contexte morpho-fluvial et archéologique [60]. Dans cette étude, les inversions électriques ont été réalisées en deux dimensions avant d'être intégrées dans un modèle géométrique du pont tridimensionnel. Une seconde publication [39] va plus loin en combinant photogrammétrie et tomographie 3D afin 1) d'obtenir une image de l'intérieur d'un pilier de carrière en réalisant des ceintures d'électrodes à trois endroits différents, 2) de décrire l'influence de la résolution du modèle photogrammétrique sur les inversions et 3) faire

26. Le Pont de Coq, classé aux monuments historiques et situé près de Ménéval (Seine-Maritime, 76)

le lien entre ces résultats et la présence de zones à forte teneur en eau. Dans ce cas, le problème direct est résolu en prenant en compte directement le modèle maillé photogrammétrique. Ces travaux ont été menés avec Yannick Fargier de l'Université Gustave Eiffel.

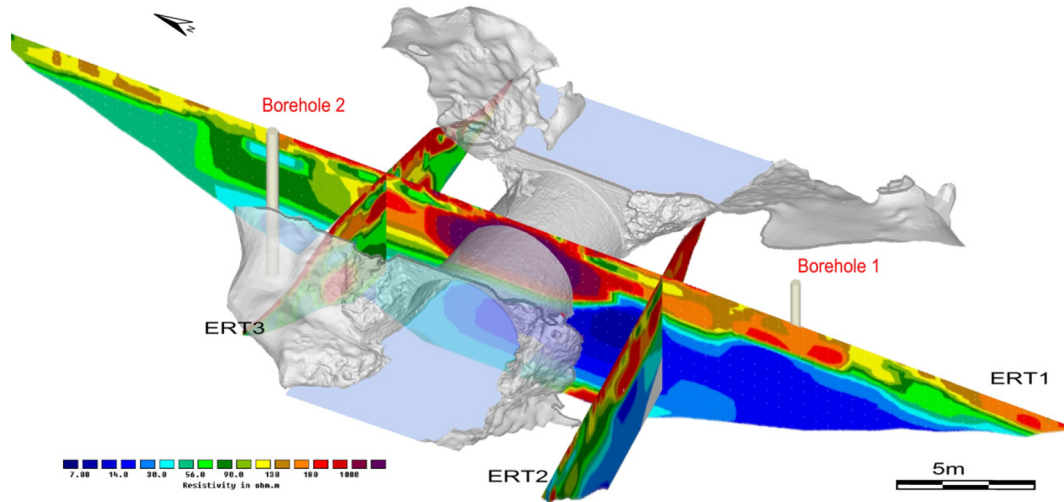


FIGURE 7 – Combinaison des observations photogrammétriques et des résultats d'inversion électrique 2D pour le Pont de Coq [34].

Les difficultés rencontrées pour inverser ces profils électriques avec des logiciels classiques (souvent payants) nous ont naturellement amené à développer un nouveau code d'inversion électrique open-source capable de traiter les données acquises dans des zones à topographies complexes. En effet, les codes d'inversion 3D actuellement disponibles sont soit payants, soit ils ne sont pas optimisés pour des inversions prenant en compte ce type de géométrie. PyLGRIM (Python Language-based Geoelectrical Resistivity Imaging and Modeling) a été écrit par Antoine Tonnoir du LMI²⁷, en collaboration avec Yannick Fargier, Cyrille Fauchard (Cerema) et moi-même dans le cadre du projet région TélédéTAC²⁸. Implémenté en éléments finis, le code prend en compte n'importe quel nuage de points issu de campagnes photogrammétriques ou LiDAR pour le problème direct et d'inverser les mesures en 3D [58]. Par ailleurs, il est tout à fait possible d'intégrer dans les inversions des profils orientés de façon arbitraire et qui prennent en compte le géoréférencement des électrodes. Enfin, le problème direct est optimisé grâce à des conditions aux limites originales (éléments infinis) permettant de réduire la taille du maillage et donc les temps de calcul, particulièrement longs pour ce genre de géométrie (de l'ordre de plusieurs jours sur un ordinateur possédant un processeur Core i9 avec 64 Go de RAM et une carte graphique de 11 Go). Actuellement, je participe à la définition des fonctionnalités métier de cet outil, à sa validation scientifique et à la rédaction du premier article le présentant.

Comme précisée en début de cette section, les températures de surface peuvent elles aussi être modulées de façon importante par les variations de pente de la surface observée ([4], [5]). En particulier, la topographie détermine :

- la distribution de rayonnement incident ;
- la variabilité des pentes et des orientations des surfaces ;
- la génération de zones d'ombre ;
- la proportion de ciel α dans laquelle émet un point présent au niveau de la surface. Le refroidissement est en effet contrôlé par les échanges d'énergie entre la surface et les parois des vallées/crêtes vues par un point de cette surface [4].

27. Laboratoire de Mathématiques de l'INSA de Rouen

28. projet Région Normandie "TELEDEtection par drone du TrAit de Côte", porté par Cyrille Fauchard

Plus cet angle est petit, moins la surface voit de ciel, et plus celle-ci retarde son refroidissement par rapport à une surface plane ou le sommet d'une crête [31]. La surface pourra alors apparaître plusieurs degrés plus chaude que la surface plane pendant la nuit ;

- le déclenchement de la convection et son amplitude quand ce phénomène est présent.

Face à l'influence de ces variations de pente sur le signal thermique, j'ai développé une méthodologie permettant de générer des cartes de température en trois dimensions. J'ai eu l'idée d'appliquer la méthode photogrammétrique aux données d'imagerie acquises dans l'infrarouge thermique. Cette technique permet d'obtenir l'information de température directement en 3D sur le modèle. En effet, de la même façon qu'une caméra visible, une caméra thermique possède un objectif avec une focale bien déterminé et un capteur matriciel et donc un modèle optique rendant possible la stéréovision. A l'instar de la photogrammétrie dans le visible, le résultat est un modèle 3D mais dont le pixel est une température, obtenu à partir d'images thermiques orientées avec un certain taux de recouvrement (au moins 70 % en longitudinal et 30 pourcent en latéral). L'obtention de cartes de températures en trois dimensions que j'appelle "thermogrammétriques" permet ainsi de caractériser spatialement les températures de surface en fonction de la topographie du terrain (cassures de pentes, etc...). Fusionné aux données visibles 3D, l'influence du type de sol (grossier, fin, consolidé ou non) et de la végétation sur le signal thermique peuvent être aussi appréhendés. La figure 8 montre la richesse des informations obtenues en présence d'un modèle 3D visible couplé à un modèle thermogrammétrique dans le cas du glissement littoral des Vaches Noires [50]. *In fine*, la méthodologie mise en place facilitera la détection de signaux thermiques (par exemple associée à l'eau) non induits par les propriétés intrinsèques de la surface ou par la végétation. Ce travail est réalisé en collaboration avec Vincent Guilbert, technicien dans l'équipe ENDSUM.

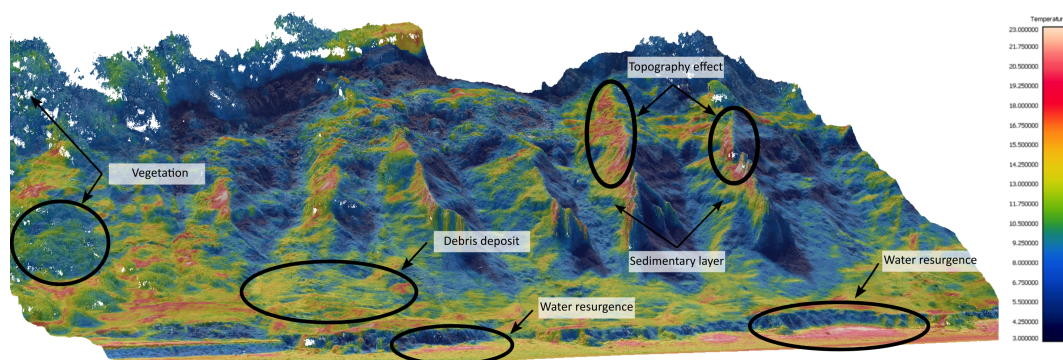


FIGURE 8 – Modèle 3D de température du glissement des Vaches Noires obtenu en été et fusionné au modèle acquis dans le visible [50]. Les deux acquisitions ont été réalisées simultanément grâce à un drone.

Mes projets proposent aujourd'hui des méthodologies combinant/fusionnant plusieurs types de données d'imagerie optiques et géophysiques sur des glissements littoraux (Vaches Noires), des falaises de craie (Sainte-Marguerite-mer), des volcans (Etna, Vésuve, Stromboli) ou des ouvrages actuels ou anciens ([71], [47], [50], [51], [54]). Ces modèles peuvent contenir des nuages de points 3D reconstituant la surface observée, des cartes de température de surface tridimensionnelles, des orthophotographies, des cartes de différences de hauteur pour le suivi diachronique des milieux et bien sûr des données géophysiques (imagerie électrique, électromagnétique, polarisation spontanée ou radar). Enfin, les modèles sont réalisés avec des outils de visualisation et d'analyse open-source (Paraview, Cloud Compare, Meshlab, QGIS...) et très souvent interfacés avec Python. Ces travaux sont menés en collaboration étroite avec Cyrille Fauchard,

directeur de l'équipe, Vincent Guilbert et Cyril Ledun, techniciens à ENDSUM.

La combinaison de différents types de données dans un seul et même modèle constitue une avancée majeure par rapport à mes travaux de début de carrière. Au fil du temps, je me suis rendu compte qu'elle améliore considérablement nos interprétations : 1) les inversions géophysiques sont mieux contraintes pour des géométries complexes [105]; 2) cet outil permet de mieux caractériser les phénomènes en jeu du fait d'une meilleure spatialisation de l'information et 3) il rend les résultats beaucoup plus lisibles pour les gestionnaires. En ce sens, ces travaux facilitent la diffusion des résultats de géophysique de subsurface et de télédétection au plus grand nombre. Aujourd'hui, ce savoir-faire est utile aux projets d'expertise de l'équipe (pour le compte des collectivités et du tissu industriel) et est transféré dans les services opérationnels du Cerema. Les connaissances acquises en photogrammétrie ont fait l'objet de plusieurs formations en interne pour les ingénieurs/techniciens s'occupant d'ouvrages ou de risques naturels. Ces transferts concourent à l'enrichissement des études pour la caractérisation ou le suivi d'ouvrages et d'infrastructures. La figure 9 présente un résultat issu de ces transferts opérationnels dans le cadre d'un phare. Il s'agit d'une carte de différence de distance obtenue par comparaison entre deux modèles photogrammétriques à un an d'intervalle. Celle-ci met en évidence un gonflement central important et rapide au niveau de la structure. Ce type de rendu montre les potentialités de cette méthodologie pour la réalisation de diagnostic de l'ensemble de l'ouvrage avec une précision de quelques centimètres et cela sans intervenir physiquement.

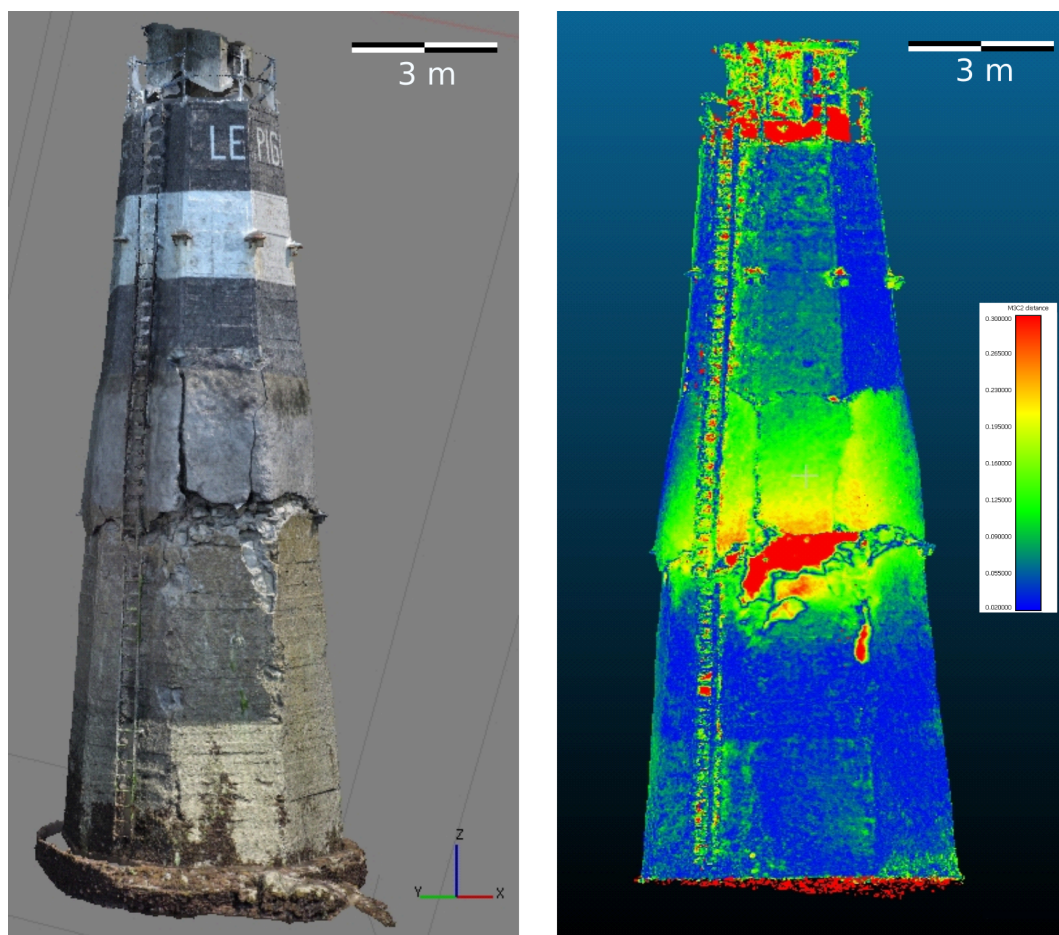


FIGURE 9 – A gauche : modèle photogrammétrique de la tourelle du Pignon obtenu grâce à des prises de vue circulaires par bateau ; à droite : carte de distance montrant l'évolution de la tourelle de Pignon située au large des îles Chausey (50) entre 2018 et 2019. Elle est issue de la comparaison entre deux modèles 3D de l'ouvrage grâce au logiciel Cloud Compare. Cette carte a été obtenue par le Département Mobilité, Sécurité Ouvrages d'arts (DMSOA) du Cerema Normandie-Centre.

3.3 Le drone, un moyen d'observation révolutionnaire

Le drone volant ouvre l'accès à des observations optiques et/ou géophysiques de manière autonome. Depuis cinq ans, ce système est en plein essor dans de nombreux domaines, du fait de sa flexibilité, de sa miniaturisation rapide et de son coût abordable [47]. Cependant, il s'avère très exigeant en terme de rigueur d'acquisition, de réglementation et de maintenance. Dès mon arrivée au Cerema, je me suis naturellement tourné vers ce système d'acquisition afin de réaliser des observations à petite échelle. J'ai donc monté une collaboration avec Jean-Luc Sorin, ingénieur d'étude à l'Ifsttar²⁹ et pionnier dans l'acquisition de données par drone. J'utilisais les données acquises dans le visible et l'infrarouge thermique pour réaliser des observations optiques sur le site karstique de Bouville (76) comportant de nombreuses dolines³⁰ et pour traquer les résurgences d'eau sur le glissement des Vaches Noires dans le Calvados (figure 8) ([50], [54]). Ces premières observations ont par exemple été à la base des réflexions qui ont mené à la thèse expérimentale d'Aziz Saley sur le traçage des écoulements en milieu poreux par méthode infrarouge thermique [37] avec le laboratoire M2C de l'Université de Rouen (Jean-Paul Dupont et Abdel Jardani).

Cette expérience, encore rare en 2012, a permis l'émergence de projets structurants tels que celui mené avec Haropa Port Le Havre sur l'étude du lien entre présence de cavités souterraines et données optiques [49]. N'étant pas formés au pilotage au Cerema, nous avons alors demandé à une société privée de réaliser les mesures au-dessus des structures. Par la suite, le projet national DiDRO (2015-2018) coordonné par Jean-luc Sorin a été labellisé par trois pôles de compétitivité. Celui-ci a favorisé le développement de l'activité au laboratoire en investissant dans du matériel (vecteur, caméra haute résolution), et dans la formation de l'équipe au traitement de données 3D et au télépilotage ([96], [47], figure 10). L'objectif de DiDRO était de développer un démonstrateur drone capable 1) de mener des opérations d'observation lors de l'entretien des digues afin de faciliter le travail des techniciens de terrain et 2) d'intervenir en cas d'inondations (surveillance des zones proches de la rupture et aide au sauvetage). Dans ce projet, j'étais responsable des tâches "Observations multi-spectrales" et "cibles GPS dérivantes". DiDRO a permis de combiner plusieurs types de données de surface afin d'observer finement la géométrie des ouvrages, voire de quantifier leur déformation (LiDAR et capteur photogrammétrique), de caractériser le type de végétation présent (via le proche infrarouge) et de réaliser des tests de détection de fuites à partir de mesures thermiques. Dans ce cadre, j'ai exploité le drone gros porteur de Didro afin de tester les systèmes embarqués, j'ai monté les expérimentations pour la détection de fuites dans les flancs de digues en eau et j'ai collaboré avec la société Geomatys pour la valorisation des données 3D thermiques obtenus. La figure 11 montre les drones utilisés dans le cadre de DiDRO, tous permettant d'embarquer plusieurs capteurs et sélectionnés pour leur fiabilité. Ces deux types de drones (multicoptère et hélicoptère) possèdent des autonomies allant de 30 min à 2h. Ils sont par ailleurs flexibles, permettant d'opérer des plans de vols automatiques préalablement conçus au laboratoire ou des vols stationnaires afin d'observer l'évolution d'une scène. Ils sont donc particulièrement intéressants pour le diagnostic d'ouvrage régulier.

29. Institut français des sciences et technologies des transports, de l'aménagement et des réseaux. Il a fusionné avec l'université Paris-Est Marne-la-Vallée pour créer l'Université Gustave-Eiffel.

30. Forme caractéristique d'érosion des systèmes calcaire en contexte karstique.

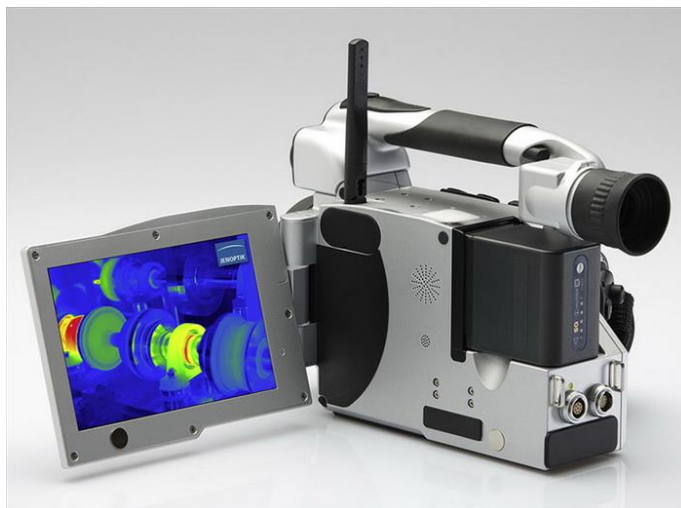


FIGURE 10 – Caméra thermique haute résolution Jenoptik Variocam HD800 (1024*768 pixel), achetée dans le cadre du projet DiDRO et embarquée sur les drones de l'équipe.

DiDRO a mis en exergue les potentialités du drone pour la surveillance de dizaines de milliers de kilomètres de digues aujourd'hui vieillissantes en France. A vocation industriel (financé par BPI France), il fait aujourd'hui l'objet de réflexions sur la mise en place d'un service autour des résultats obtenus. Il est à noter qu'avec le projet polonais SAFEDAM, ce projet fait partie des efforts nationaux visant à offrir une solution drone pour les digues, dans une période où la fréquence des événements extrême est de plus en plus importante. Par la suite, les projets région TéléDETAC (2017-2019) et européens POLDER2Cs ont permis à l'équipe de renforcer ses compétences dans cette thématique qui allie aujourd'hui acquisition, traitement des données et interprétation des résultats ([51], [54]).

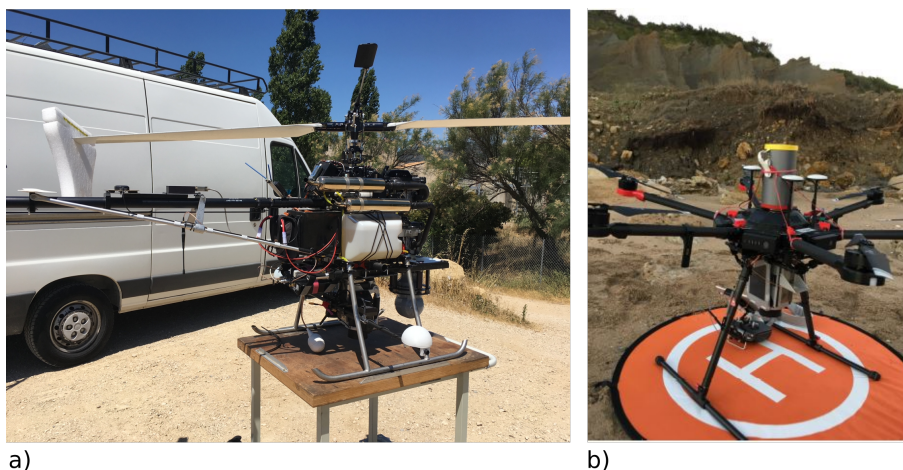


FIGURE 11 – a) Drone hélicoptère multi-capteur de la société Survey Copter utilisé dans le cadre de DiDRO. Le système embarque un capteur optique visible et infrarouge développé par l'IGN, la caméra thermique haute résolution de l'équipe, un LiDAR et une caméra thermique de surveillance. Il peut soulever jusqu'à 16 kg de matériel ; b) Drone hexacoptère acheté dans le cadre de DiDRO, embarquant un capteur visible ainsi que la caméra thermique haute résolution. Il peut embarquer jusqu'à 6 kg de charge utile.

En parallèle de ces travaux, avec Julien Lacogne et Cyrille Fauchard, j'ai impulsé

la mise en place d'un groupe de pilotes inter-département au Cerema Normandie-Centre dès 2015, dans un contexte réglementaire national encore balbutiant pour les drones. Celle-ci a mis en place 1) l'ensemble des protocoles nécessaires pour le déploiement de nos drones dans le respect de cette réglementation et 2) l'instrumentation permettant de réaliser des mesures de qualité en vol. Ces aspects sont traités avec l'aide de Bruno Beaucamp, technicien à ENDSUM Rouen. L'équipe drone mène aussi bien des acquisitions à des fins de recherche que d'ingénierie, dont certaines expertises sur plusieurs années pour le compte de collectivités comme La Rochelle [136]. Elle figure parmi les équipes pionnières du Cerema dans cette thématique et illustre bien le caractère complémentaire entre la recherche et l'ingénierie au Cerema : une recherche nourrie par le terrain et une ingénierie irriguée par la recherche. Aujourd'hui, je participe à l'animation du réseau drone du Ministère de l'Ecologie, que le Cerema a contribué à mettre en place en 2019 en relation avec le CGDD³¹ (<https://www.cerema.fr/fr/evenements/drones-en-appui-des-territoires>). En outre, j'ai participé à la mise en place d'une formation continue en trois modules sur l'usage des drones pour les territoires labellisée en 2021 par le Cerema. Cette expérience me conduit aujourd'hui à monter des formations continues au niveau international, comme l'atteste la formation inter-ministérielle que j'ai prodiguée à Sao-Tome-et-Principe en mai 2022, dans le cadre du projet WACA³² (figure 12). Elle m'a enfin conduit à la publication de [47], qui a été l'occasion de réunir des scientifiques français de domaines différents pour réaliser une des premières synthèses de l'emploi des drones pour les risques naturels au niveau international.



FIGURE 12 – Vol de drone dans le cadre de la formation continue sur l'observation du littoral à Sao-Tomé-et-Principe.

31. Commissariat Général au Développement Durable.

32. Formation continue sur l'observation du littoral par drone. WACA est le programme de gestion du littoral ouest Africain.

4 Projet de recherche

Fort de l'expérience acquise suite à ces travaux ancrés dans la communauté académique et la recherche appliquée, j'envisage les thématiques suivantes afin de continuer à promouvoir l'utilisation conjointe de données optiques, géophysiques et de modélisation à toutes les échelles.

4.0.1 Caractérisation physique des milieux

Je souhaite poursuivre mes investigations sur l'origine des anomalies thermiques dans les bassins sédimentaires. Un sujet qui me tient particulièrement à cœur est l'accès à l'eau. A l'échelle mondiale, les eaux souterraines constituent le principal réservoir d'eau douce disponible (96,7 %). Les événements hydro-météorologiques extrêmes associés au changement climatique, telles que les sécheresses et les inondations, deviennent plus fréquents et affectent la disponibilité de l'eau. En conséquence, 38 % de la population mondiale sera exposée au stress hydrique en 2025, contre 9 % en 2008. À l'échelle régionale, l'épuisement des eaux souterraines a de graves répercussions sur la société, l'économie et l'environnement [20]. L'impact de la sécheresse sur les régions (semi-)arides est considérable : accès limité aux eaux souterraines propres, problèmes sanitaires et instabilités sociales notamment pour les aquifères transfrontaliers. En effet, les régions (semi-)arides représentent ≈ 30 % de la surface de la Terre où les nappes constituent une ressource importante en eau douce ; faiblement renouvelable car l'apport en eau est souvent très localisé, mais exploitable (e.g., [19]). Le Programme des Nations unies pour le développement (PNUE) prévoit une diminution des précipitations de 5 à 15 % dans la plupart des zones désertiques du monde. Étant donné l'importance croissante de ces ressources en eau spécifiques dans le monde, il est essentiel que tous les efforts soient faits pour trouver, gérer et préserver ces ressources fragiles. Le développement de méthodologies permettant de déterminer la présence de nappe dans ces zones et de suivre son évolution est donc fondamental pour la stabilité des zones arides. Ce projet vise à explorer la présence de la nappe et à étudier son évolution en utilisant une combinaison de données satellitaires, de mesures *in situ* et de modélisation numérique. Nos principales hypothèses de recherche sont les suivantes : 1) les nouvelles avancées dans la recherche satellitaire et les études d'interaction sol-atmosphère montrent qu'une nappe phréatique peut influencer l'hydrologie et le comportement thermique de la surface dans certaines zones arides [36] et 2) étant donné la première hypothèse, la combinaison des mesures *in situ* avec les données satellitaires peut aider à explorer l'aquifère.

Les mesures seront effectuées dans le désert de Badain Jaran (BJD) en Mongolie intérieure (figure 21), qui possède les plus hautes dunes immuables du monde (jusqu'à 400 m) et où la présence d'un système aquifère dans les sédiments sableux du Quaternaire et les grès du Néogène-Crétacé est bien décrite [24]. Cet aquifère s'exprime en surface par la présence de lacs permanents entre les dunes, mais la teneur en eau peut encore être très élevée à une altitude de 100 m sur les dunes. Les fluctuations saisonnières du lac sont inférieures à 0,5 m, en raison de la décharge quasi-stable des eaux souterraines (et probablement d'une alimentation permanente). De nombreux travaux ont été réalisés pour caractériser l'origine des eaux souterraines alimentant les lacs, la connexion hydrologique entre le BJD et le bassin de la rivière Heihe (HRB), la recharge par infiltration et les caractéristiques géochimiques des eaux. Récemment, un effet d'îlot de chaleur a été décrit par [26] sur la région des lacs. Ils proposent que cet excès de chaleur atmosphérique est principalement lié à la chaleur transportée par l'aquifère profond. Les nouvelles observations satellitaires Landsat et ASTER recueillies par notre équipe soutiennent clairement cette hypothèse en révélant la présence d'anomalies thermiques de surface à grande échelle, quotidiennes et saisonnières, sur le BJD, où les régions autour des lacs sont $\approx 5^\circ\text{C}$ plus chaudes le jour et la nuit (figure 22). Ces observations suggèrent que la nappe phréatique affecte la température du sol. Elles font du BJD un laboratoire original à grande échelle adapté à l'utilisation de données

satellitaires et *in situ* pour étudier le lien entre la nappe phréatique et la surface. Ce projet fait l'objet d'une soumission à l'ANR et fait intervenir l'ENPC (Yu-Jun Cui), l'IGN (Pierre-Louis Frison) et le Cerema (Téodolina Lopez).



FIGURE 13 – Photographie du désert du Badain Jaran avec vue sur les dunes immuables et les lacs permanents (crédit photo ©chinadiscovery.com).

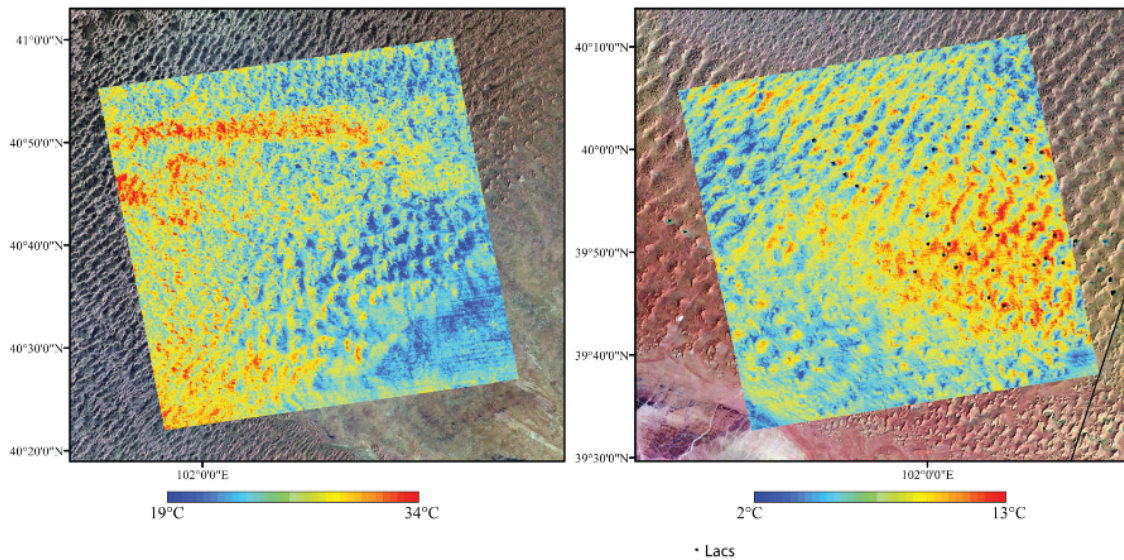


FIGURE 14 – Carte de température de jour et de nuit de la zone désertique du Badain Jaran. Certaines zones sableuses sont chaudes de jour comme de nuit et probablement associées à la nappe présente dans les sables du quaternaire, alimentée par des eaux profondes. Les lacs sont signalés par des étoiles.

Au Sahel, [36] a montré qu'une anomalie thermique peut être générée par des circulations convectives d'eau sous le Lac Tchad du fait de variations spatiales de conductivité thermique dans le bassin sédimentaire et de la présence de topographie dans les couches sédimentaires. Il est aussi bien connu que des anomalies de température

peuvent apparaître juste avant des séismes importants à l'aplomb de certains bassins sédimentaires [14]. Ces anomalies thermiques chaudes pouvant couvrir une superficie allant jusqu'à 100 000 km² ont été observées depuis une vingtaine d'années avant des séismes de magnitude supérieure à 5. Nous nous attachons plus particulièrement à étudier les anomalies thermiques qui se sont développées environ 20 jours avant le séisme de Boumerdès qui a touché l'Algérie le 21 Mai 2003 ($M_w \approx 6,9$), comme le montre la figure 23. Le but de l'étude est de comprendre les processus hydro-tectoniques à l'oeuvre pour générer de telles anomalies avant un séisme, en tenant compte du contexte géologique particulier de la région algérienne. En reposant sur les hypothèses déjà existantes, nous proposons que le développement des anomalies thermiques avant le séisme de Boumerdès est induit par un relâchement catastrophique d'eau souterraine vers la surface. Ce relâchement est contrôlé par la combinaison d'un phénomène de compaction des argiles et du cycle de déshydratation-hydratation d'une couche épaisse et profonde d'argile (un mélange de smectite et d'illite) [42]. Cette combinaison de phénomènes provoque des changements dans 1) la perméabilité verticale de la séquence sédimentaire et 2) la quantité d'eau arrivant en surface et apportant de l'énergie par condensation dans la zone. La combinaison originale d'analyse de séries temporelles de température de surface (obtenues par les capteurs thermiques à bord des satellites MODIS - Moderate Resolution Imaging Spectroradiometer), des données de précipitations (TRMM) et des estimations du stock d'eau continental (GRACE) avec des données géologiques et géophysiques (gravimétrie et tomographie sismique) permettrait de proposer une vision alternative d'un sujet peu étudié jusqu'alors. Ce sujet pourrait avoir un impact fort sur la compréhension de la physique des séismes lents et donc permettre d'améliorer la compréhension 1) de l'évolution des bassins sédimentaires en contexte de compression tectonique et 2) proposer dans le futur un outil de détection pour les très gros séismes à partir des données gratuites américaines telles que les données MODIS mais aussi en reposant sur les nouvelles constellations Copernicus comme les données Sentinel-3, la nouvelle mission TRISHNA et la future mission LSTM (Land Surface Temperature Monitoring). Ces travaux sont réalisés en collaboration avec Téodolina Lopez du Cerema de Toulouse et Michel Rabinowicz du GET.

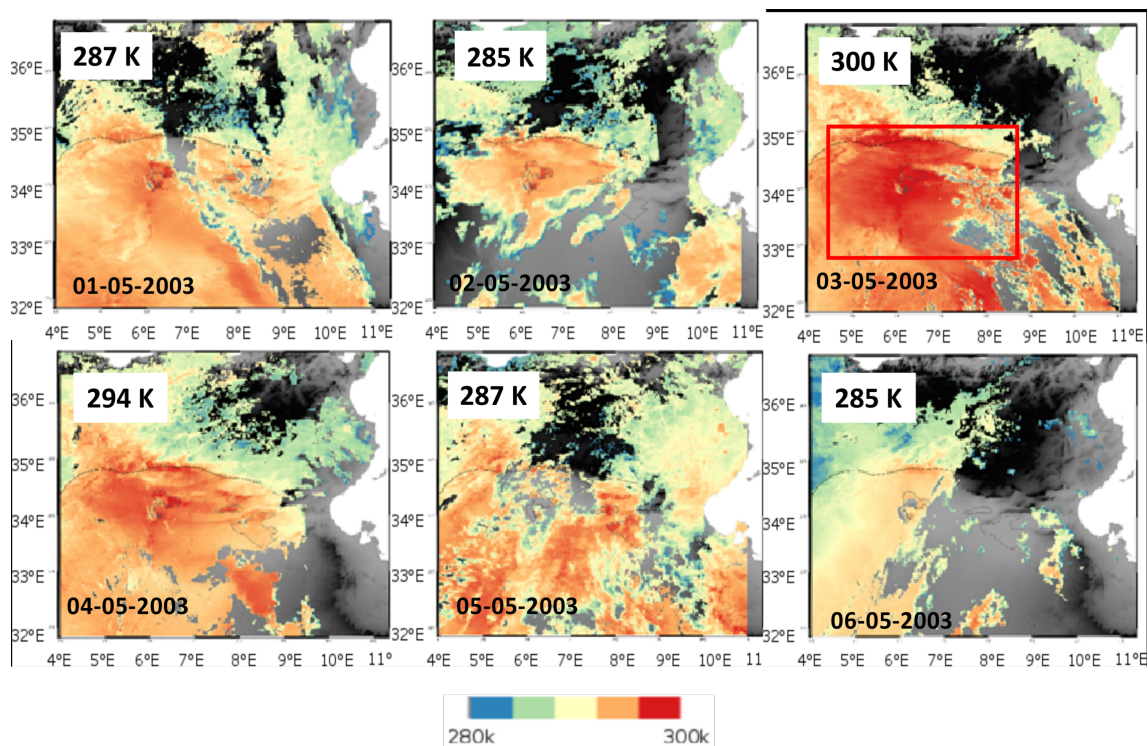


FIGURE 15 – Évolution de la température de nuit quelques jours avant le séisme de Bourmedès qui a eu lieu le 21 mai 2003. Noter le réchauffement important de la zone le 03 mai 2003. L'objectif de ce projet est d'expliquer comment une telle anomalie thermique peut être générée dans une zone aride avant un séisme.

L'eau joue un rôle prépondérant dans l'érosion des falaises. A l'ouest du bassin sédimentaire parisien, les falaises de craie et de marnes de Normandie subissent une ablation continue avec des conséquences pouvant être importante pour le bâti littoral. Si les caractéristiques mécaniques des falaises littorales de Normandie sont connues, les interactions falaises/eaux continentales/eaux marines (dont la connaissance est primordiale pour les études de stabilité) sont moins bien décrites. En particulier, les mécanismes de transfert de l'eau météorique à travers la falaise depuis le plateau limoneux jusqu'au platier carbonaté restent à préciser. Le projet Région Normandie Defhy3geo qui a commencé au 1^{er} janvier 2022 vise à établir un modèle hydrologique de certaines falaises de Normandie (badlands littorales des Vaches Noires et falaise de craie de Sainte-Marguerite-sur-Mer) à partir de données optiques, géophysiques, géologiques et la modélisation numérique. Le projet implique un consortium constitué des Laboratoire M2C, IDEES, le LMI et le Cerema. Dans ce cadre, les premiers modèles des Vaches Noires combinant modèle infrarouge (obtenu avant le lever du soleil en hiver) et imagerie électriques 3D (obtenue grâce au code PYLGRIM) ont pu être réalisés, comme le montre la figure 24. Le calcul d'inversion 3D incorporant six profils électriques longitudinaux et transversaux a été fait en donnant plus de poids aux variations verticales de résistivité, ce qui permet de bien décrire le milieu tabulaire composé de marnes, d'argile et de calcaire constituant le glissement des Vaches Noires. Ces résultats montrent bien le lien entre la présence de zones conductrices à l'intérieur de la structure (soulignées par des tirets blancs sur la figure 24) et des sorties d'eau (11-12°C observées en hiver) à deux altitudes différentes sur le glissement. Dans ce cas, l'eau est détectée par la caméra thermique, car la température du sol est proche de 0°C en février. La végétation est de même plus chaude que le sol au petit matin (mais à peu près à la même température que les sorties d'eau), du fait de l'arrêt de l'évapotranspiration pendant la nuit. Ces zones de résurgences sont localisées dans des cassures de pentes de la falaise et sont le lieu de

coulées de boue importantes, dont la mise en place semble à certains moments décorrélée des épisodes de précipitations [56]. Je souhaite m'investir dans la compréhension de la génération de ces coulées de boue, événements qui conditionnent l'érosion du littoral des Vaches Noires et le recul du trait de côte dans cette région. En particulier, le lien entre les écoulements et le comportement rhéologique des marnes (constitué d'argiles et de calcaire) à l'intérieur du plateau en dehors des événements dits saisonniers me paraît intéressant à investiguer. Il est connu que la rhéologie des argiles dépend du volume de liquide interstitiel dans les pores. Lorsque ce volume atteint un certain seuil (appelé seuil de consolidation allant de 26% à 47%, dépendant du type d'argile), les grains ne sont plus en contact, peuvent glisser dans la suspension boueuse et s'écouler au niveau du glissement [42]. Les mécanismes à l'origine de la migration, de la concentration de l'eau et de la séparation de la boue de ces argiles (générées par la compaction) restent à décrire et c'est ce que je veux m'atteler à faire dans les années à venir. Si ce mécanisme est présent dans le plateau, l'extraction de boue devrait alors se traduire par une subsidence locale. Des travaux récents de TU Delft montrent qu'il semble possible de détecter des variations verticales associées au retrait-gonflement des argiles à partir de données InSAR ([17], [22]). Je souhaite donc tester l'apport potentiel de données interférométriques fournies par le satellite Sentinel 1 pour répondre aux questions suivantes 1) Peut-on observer des variations verticales de hauteur saisonnière du plateau du fait de l'humidification/compaction des argiles dans le milieu?; 2) Peut-on détecter des phénomènes de subsidence du fait de l'expulsion de matière à l'intérieur du plateau? et 3) si oui, existe-t-il des phénomènes de subsidence intra-saisonniers non corrélés aux événements pluvieux? Ces données disponibles via l'European Ground Motion Service (<https://egms.land.copernicus.eu/>) seront complétées par des mesures réalisées au GPS et photogrammétriques, des observations infrarouge, des mesures *in situ* de teneur en eau jusqu'à 1 m de profondeur dans le sol, des mesures géophysiques et météorologiques.

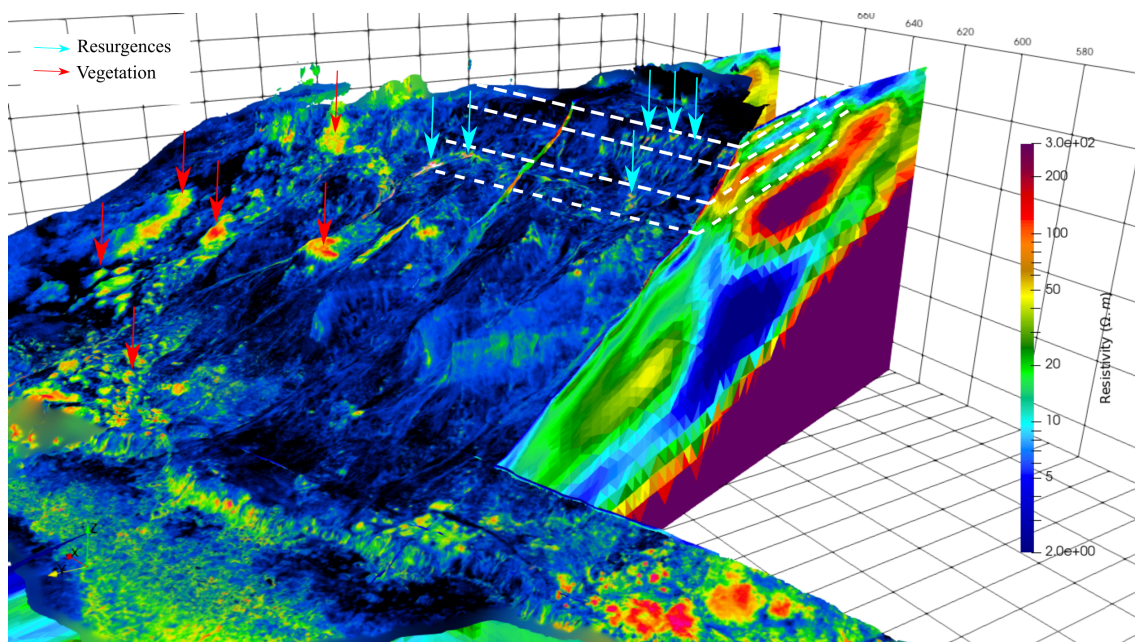


FIGURE 16 – Modèle de température 3D des Vaches Noires obtenu en hiver combiné au résultats d'imagerie électrique pour six profils inversés ensemble. Les flèches rouges et vertes localisent les résurgences d'eau et la végétation, respectivement.

Enfin, à petite échelle, je souhaite continuer à promouvoir l'utilisation de l'infrarouge thermique pour les risques associés aux cavités. Les déstabilisations des cavités souter-

raines constituent un aléa important pour l'aménagement du territoire. En Normandie, des dizaines de milliers de cavités anthropiques (appelées marnières) ont été creusées (au XIXe siècle) pour l'extraction de la craie servant à l'amendement des sols. Celles-ci se distinguent d'autres cavités artificielles par un volume réduit par rapport à leur profondeur (jusqu'à 50 m) et par le fait qu'elles sont souvent oubliées, ignorées ou mal localisées. Les marnières sont reliées à la surface par un puits de diamètre métrique souvent mal rebouché et recouvert de sol agricole (figure 25). L'effondrement de ces objets, souvent brutal et parfois léthal, est un réel problème en Normandie et constitue une préoccupation majeure pour les pouvoirs publics et les citoyens [25]. Leur détection est donc primordiale, en particulier du fait du réchauffement climatique, dont les manifestations de plus en plus fréquentes peuvent accélérer les effondrements. Dans les années 2000, des données thermiques aériennes ont permis de détecter la signature thermique de surface de puits de plusieurs marnières (figure 26), faisant apparaître cette méthode comme prometteuse, mais sans en comprendre les mécanismes à l'origine de ces observations [12].

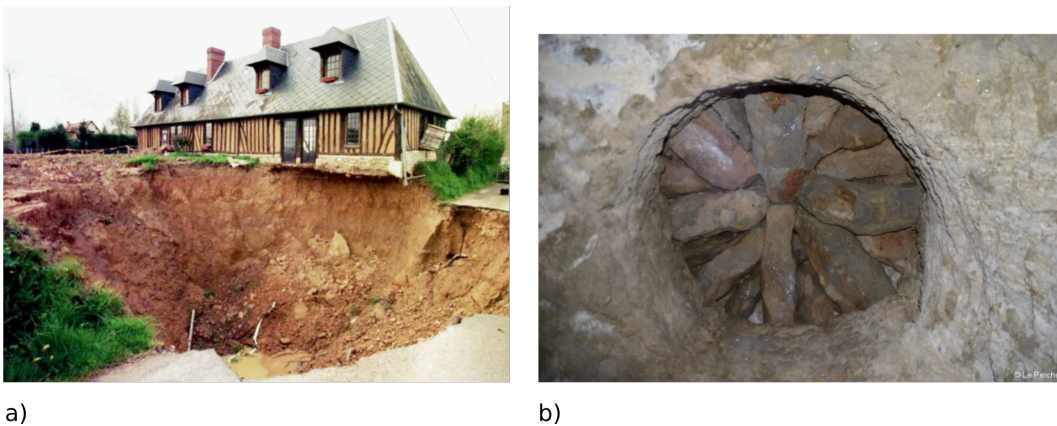


FIGURE 17 – a) Photographie d'un effondrement de marnière en Normandie et b) Photographie d'un puits bouché par des galets prise de l'intérieur de la marnière et montrant une perméabilité très importante.

Les travaux que j'ai menés sur les cavités souterraines à partir de 2015 mettent en évidence le lien potentiel entre températures et déformations de surface [49]. Ces subsidences sont souvent générées à un stade avancé de la migration de la cavité vers la surface [49]. Je souhaite donc me focaliser sur leur détection précoce, en me basant sur la caractérisation quantitative des échanges d'air et d'eau entre les marnières et l'atmosphère. L'objectif est de modéliser les circulations convectives et les transferts de chaleur en 3D dans ces objets pour comprendre comment sont générées les anomalies thermiques observées en surface. Pour un milieu fluide (e.g. vide), le nombre de Rayleigh Ra donnant la vigueur de la convection est donnée par la formule suivante :

$$Ra = \frac{g\alpha H^3 \Delta T}{\nu \kappa} \quad (1)$$

avec g , l'accélération de la gravité (9.81 m s^{-2}); α le coefficient d'expansion thermique du fluide ($3.7 \cdot 10^{-4} \text{ K}^{-1}$); H la hauteur de la cavité (2 m), ΔT la différence de température entre le haut et le bas de la cavité (1 K); ν la viscosité du fluide ($2 \cdot 10^{-5} \text{ Pa s}$) et κ la diffusivité thermique du fluide ($2 \cdot 10^{-5} \text{ m}^2 \text{ s}$). Ainsi, en prenant en compte ces valeurs pour une cavité totalement vide, le nombre de Rayleigh Ra est d'environ $3 \cdot 10^9$, donc très largement au dessus du nombre de Rayleigh critique (10^3). Cette valeur montre que la convection peut être extrêmement active dans ce milieu avec la création de plusieurs cellules comme l'atteste les résultats obtenus pour la marnière de Barcq (figure 26). La topographie réaliste de la cavité a été obtenue par photogrammétrie avec des photos

acquises par le groupe Risques Naturels du Cerema de Rouen. Il est à noter que cette valeur calculée de Ra constitue plutôt un maximum pour les modèles, car les marnières intègre un milieu poreux, qui diminue drastiquement ce nombre. Nous comparerons ces modèles aux observations thermiques et géophysiques obtenues sur plusieurs sites en Normandie. La thèse de Georges EDDE qui débutera au dernier trimestre 2022 portera sur cette thématique. La thèse permettra de répondre aux questions suivantes :

- Quelles doivent être les caractéristiques du sol pour que de la convection d'air se déclenche dans des cavités souterraines et interagissent avec l'atmosphère ?
- Comment se font les interactions entre le rayonnement de surface, par définition évolutif, et le système convectif ?
- Quelles sont les anomalies de température générées en surface par ces circulations d'air ?
- Quelles sont les modifications du champ thermique lorsque de l'eau est ajoutée au système ?

Le projet sera réalisé en collaboration avec Ionut Danaila de l'Université de Rouen Normandie. Le code 3D du LMRS écrit en éléments finis est capable de décrire des phénomènes de convection en milieu "fluide" (vide) et en milieu poreux. Il permettra donc de s'adapter aux configurations géologiques complexes rencontrées dans ces marnières. Une collaboration pourra être par ailleurs développée avec le BRGM qui possède des données géophysiques récentes de plusieurs sites en Normandie.

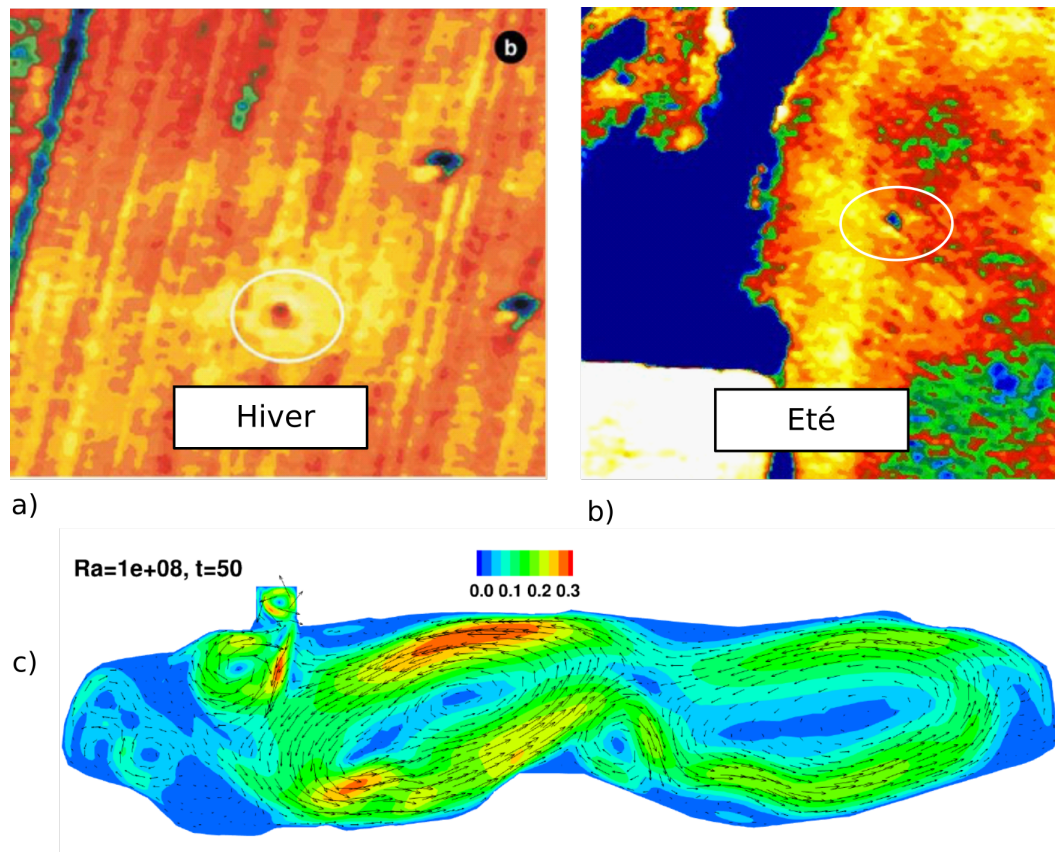


FIGURE 18 – a) Anomalie thermique au droit d'un puits invisible en surface générée en hiver (contraste de 2 à 4°C entre le puits et l'encaissant), b) anomalie thermique induite en été (même type de contraste) et c) Champ de vitesse 2D adimensionné de l'air issu du couplage entre l'équation de Navier-Stokes et de la chaleur pour un nombre de Rayleigh de 10^8 sous FreeFEM++. Il montre la formation de plusieurs cellules de convection dans une marnière refroidie par le haut et ayant un puits non bouché (connecté à l'atmosphère). La cavité est la marnière de Barcq. Sa morphologie est réaliste, ayant été obtenue par photogrammétrie. Résultats obtenus pendant le stage de Georges EDDE.

4.0.2 Développement de méthodologie d'observations et de traitement de données

Le développement d'outils de détection des puits de marnières me semble particulièrement primordial pour la région Normandie. La thèse de Georges EDDE se concentrera sur la compréhension du comportement thermique des structures grâce à la modélisation numérique et à la confrontation de ces modèles à des observations thermiques, géologiques et géophysiques (disponibles dans la bibliographie historique des laboratoires des Ponts et Chaussées et plus récemment suite à nos mesures). Elle décrira les configurations optimales géologiques, météorologiques et temporelles favorisant la génération des anomalies thermiques, mettra en exergue les avantages et les limitations de l'infrarouge thermique et finalement permettra de définir les premiers contours d'une méthodologie de détection. Il n'existe en ce moment aucune méthode à grand rendement capable de détecter ces petits objets, notamment en contexte de couverture argileuse. La micro-gravimétrie, seul outil capable de détecter des défauts de masse dans les sols a certes fait de gros progrès (sensibilité multipliée par 10 en 20 ans), mais elle n'est pas adaptée pour le grand rendement du fait des temps d'acquisition longs en chaque point. Le drone (et l'avion) sont des outils capables de faire du grand rendement (10 min/Ha pour le drone) et permettent de plus l'emport de plusieurs capteurs complémentaires.

Même si la thèse menait à une capacité de détection de 10 % à 20 % des marnières grâce à l'infrarouge thermique, cela constituerait une avancée considérable et un vivier de plusieurs dizaines de milliers de cavités à traiter. Enfin, les résultats obtenus dans ce cadre pourront servir à d'autres types de cavités comme les catiches du Nord de la France, les carrières possédant des fontis ou même les dolines naturelles interagissant avec l'atmosphère.

La détection visuelle de singularités thermiques, qu'elles soient associées à des puits de cavités souterraines ou à des circulations d'eau est très fastidieuse, sinon impossible à réaliser lorsque l'on parcourt des surfaces importantes. Dans toutes nos études, la détection de ces signaux nécessite l'intervention humaine, en comparant données acquises dans l'infrarouge, le visible et des observations météorologiques. Elle requiert souvent une analyse dynamique (saisonnnière et/ou journalière) afin de détecter l'anomalie à proprement dit. Dans les prochaines années, je souhaite m'investir dans la détection de ces signaux à partir de méthodologies de classification automatiques. Les falaises des Vaches Noires constituent un terrain de jeu idéal pour tester différentes méthodes de détection des résurgences d'eau. Un premier stage réalisé en 2021 en collaboration avec Philippe Foucher (Endsum Strasbourg) a permis de montrer qu'il est tout à fait possible de détecter automatiquement les anomalies thermiques associées aux sorties d'eau sans végétation présentées sur la figure 24. Cette détection se base sur le fait que les sorties d'eau et la végétation sont chauds par rapport au sol en hiver. L'orthoimage thermique possède donc deux classes qui sont les zones chaudes et froides. Pour supprimer la contribution thermique de la végétation et ne détecter que les sorties d'eau, on effectue une classification de la végétation et du sol nu sur les données visibles (obtenue à partir du nuage de point dense). La soustraction des deux orthoimages classifiées fournit alors la localisation des résurgences d'eau, comme le montre la figure 27.

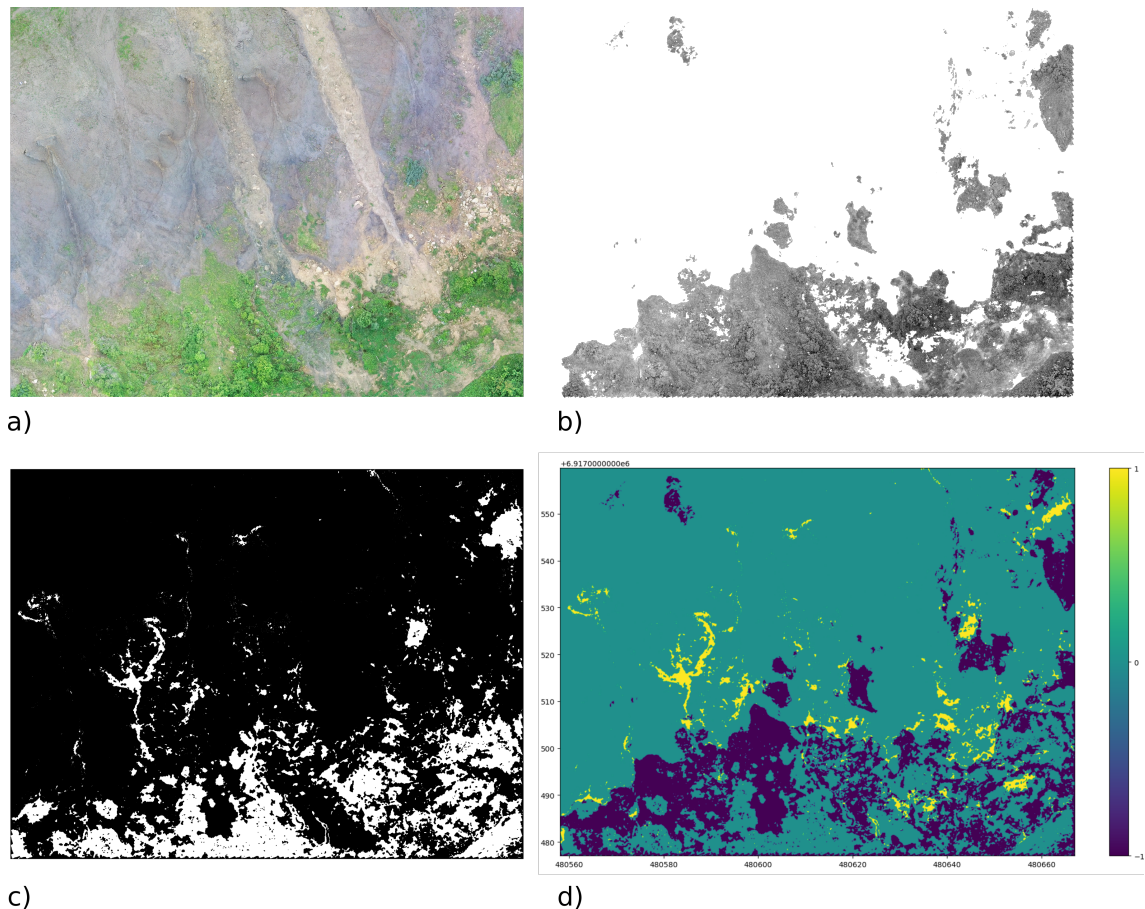


FIGURE 19 – a) orthoimage visible d'une zone des Vaches Noires ; b) classification de la végétation sur l'orthoimage visible ; c) orthoimage binarisée montrant les zones chaudes et froides sur l'orthoimage thermique et d) résultat de la soustraction entre les orthoimages thermiques et visible classifiées. Le chiffre 1 (jaune) signifie qu'on a de l'eau chaude s'écoulant sur un sol nu ; le chiffre 0 (vert) signifie que la végétation est chaude ou que le sol nu est froid et le chiffre -1 (violet) signifie qu'une partie de la végétation est froide. La détection se fait donc grâce à la localisation de la valeur 1.

4.0.3 Développement de prototypes et de moyen de recueil de données

Si les caméras sont classiquement utilisées sur les drones, j'envisage pour les années à venir de m'investir dans l'emploi de l'imagerie géophysique embarquée. Le matériel géophysique est par définition relativement fastidieux à mettre en oeuvre notamment dans les zones avec de la topographie marquée. Par conséquent, les observations géophysiques réalisées grâce à un drone obéissant à un plan de vol automatisé sont en plein développement et prennent de l'ampleur. Les méthodes magnétiques [28], électromagnétiques basse fréquence [23] et géoradar [30] sont maintenant commercialisées sur ces systèmes et de nouvelles méthodologies comme la gravimétrie quantique embarquée sont en cours de développement [29]. Dans le cadre de Defhy3geo, j'ai fait l'acquisition d'un radar géologique embarqué possédant trois fréquences (75 MHz, 120 MHz, 200 MHz) et présenté sur la figure 28. Celui-ci est couplé à un système d'asservissement laser maintenant le drone à une hauteur constante par rapport au sol, ce qui facilite le traitement de l'arrivée directe de l'onde dans l'air. Cette combinaison d'outils permettra de réaliser des mesures radar dans des environnements inaccessibles pour un opérateur. Elle ouvrira une nouvelle voie de recherche exploitant ce type de données dans des environnements divers (infrastructures, piles de ponts, digues, etc...) et apportera

son lot de nouvelles méthodologies pour les équipes opérationnelles du Cerema. Nous prévoyons par exemple des essais de faisabilité au droit des falaises verticales de craie de Sainte-Marguerite-sur-Mer qui font entre dix et vingt mètres de hauteur. La profondeur d'investigation pour un tel matériau avoisine les dix mètres de profondeur. Dans le cas de ce type de scans verticaux, un des challenges majeurs réside dans le fait de localiser correctement la mesure sur la paroi. C'est l'objectif de la thèse de Diego Navarro démarrée fin 2021 dans le cadre du Défi INRIA-Cerema en collaboration avec Ezio Malis de l'équipe ACENTAURI de l'INRIA. Celle-ci permettra de fournir une méthodologie de positionnement du drone et de la mesure (notamment lorsque les données GPS sont manquantes) grâce à la fusion de données multi-modales issues 1) de la centrale inertielle de navigation (IMU) permettant d'avoir les accélérations de l'appareil ; 2) d'une ou plusieurs caméras par odométrie visuelle et 3) d'un LiDAR grâce à la technique du Simultaneous Localisation and Mapping - SLAM). Les résultats de cette thèse permettront d'envisager à l'avenir des investigations géophysiques sur parois d'ouvrages (piles de ponts par exemple) jusqu'ici très difficiles à exécuter et finalement d'enrichir le diagnostic de ces objets.



FIGURE 20 – Photographie du nouveau drone DJI M300 RTK embarquant un radar RADSYS Zond Aero Low Frequency disponible à ENDSUM Rouen (crédits photo UGCS).

4.0.4 Perspectives stratégiques et scientifiques

Ce mémoire présente mon parcours académique et de recherche. Il montre comment j'ai adapté les connaissances acquises à l'environnement de travail du Cerema qui possède une forte spécificité appliquée. Il montre aussi finalement les fortes interactions entre tous mes domaines d'études et c'est ce qui explique mon intérêt pour toutes les échelles d'observations et la pluri-disciplinarité depuis le début de ma carrière. Ma pluri-disciplinarité s'est forgée grâce à un réseau solide de laboratoires et d'écoles que j'ai su développé et pérenniser depuis mon recrutement. Ces expériences m'ont permis d'intégrer de nombreux projets de recherche nationaux et internationaux permettant des investissements importants, de me former à de nouvelles techniques ou de travailler avec de jeunes chercheurs. Cette implication se concrétise par des publications de rang A, une stabilité de l'équipe et de ses personnels permanents et par une attracti-

tivité croissante pour des chercheurs de disciplines différentes (origines des doctorant(e)s et postdoctorant(e)s variée e.g. géophysiciens, géologues, automaticiens et mathématiciens). L'obtention de l'HDR me permettra de m'impliquer dans des directions de thèses et de rayonner plus largement au niveau national/international. Ce diplôme sera par ailleurs une grande reconnaissance de mon travail et de ma persévérance qui me permet aujourd'hui de présenter un dossier équilibré entre production scientifique, activité d'encadrement/formation, de valorisation et collective. La création de l'équipe ENDSUM est le fruit d'un travail en commun que peu de chercheurs de ma génération vivent. Cet exercice à la fois exigeant et motivant doit permettre de pérenniser l'équipe et ses thématiques de recherche, tout en offrant un cadre de travail adéquat aux jeunes chercheurs et aux personnels permanents. Je souhaite que l'obtention de l'HDR puisse contribuer à son renforcement et à son développement dans les années à venir.

Du point de vue scientifique, mes études montrent bien que les échanges sol-atmosphère sont rencontrés dans divers contextes géologiques (et même planétaires) et peuvent être caractérisés en utilisant les outils que je développe depuis une dizaine d'années. Ces échanges influencent de façon fondamentale la couche limite atmosphérique via les transferts hydriques et thermiques, ce qui affecte la circulation atmosphérique. Ces interactions jouent donc un rôle important dans la modélisation météorologique. Dans les années à venir, je souhaite porter cette thématique et les enseignements issus de mes travaux au niveau international. Cette activité pourrait prendre la forme de la création d'un groupement de recherche rassemblant les acteurs de différents domaines disciplinaires (géologues, géophysiciens, atmosphériciens...) et travaillant sur la compréhension, la modélisation et la prédiction des interactions sol-atmosphère en lien avec les phénomènes météorologiques.

5 Annexe : publications scientifiques représentatives de mon parcours

- 5.1 Tired à part Thermal infrared image analysis of a quiescent cone on Piton de la Fournaise volcano : Evidence of convective air flow within an unconsolidated soil (Journal of Volcanology and Geothermal Research**



Thermal infrared image analysis of a quiescent cone on Piton de la Fournaise volcano: Evidence of convective air flow within an unconsolidated soil

R. Antoine^{a,*}, D. Baratoux^a, M. Rabinowicz^a, F. Fontaine^b, P. Bachèlery^c,
T. Staudacher^d, G. Saracco^e, A. Finizola^c

^a Observatoire Midi-Pyrénées, UMR 5562 CNRS, Laboratoire Dynamique Terrestre et Planétaire, Université Toulouse III, Toulouse, France

^b Institut de Physique du Globe, Equipe Géosciences Marines, Paris, France

^c Géosciences Réunion, UMR 7154 CNRS, Faculté des Sciences et Technologies, Université de la Réunion, St Denis, Ile de La Réunion, France

^d Observatoire Volcanologique du Piton de La Fournaise, Insitut de Physique du Globe de Paris, Ile de la Réunion, France

^e Centre Européen de Recherche et d'Enseignement des Géosciences de l'Environnement UMR 6635 CNSR, Aix-en-Provence, France

ARTICLE INFO

Article history:

Received 6 December 2007

Accepted 12 December 2008

Available online 24 December 2008

Keywords:

infrared
volcanology
Reunion Island
porous media
convection

ABSTRACT

We report on the detection of air convection with infrared thermal images for two quasi-circular craters, 20 m and 40 m wide, forming the volcanically inactive cone of Formica Leo (Reunion Island). The thermal images have been acquired from an infrared camera at regular time intervals during a complete diurnal cycle. During the night and at dawn, we observe that the rims are warmer than the centers of the craters. The conductivity contrast of the highly porous soils filling the craters and their 30° slopes are unable to explain the systematic temperature drop from rim to centers. We suggest that this signal could be attributed to air convection with gas entering the highly permeable soil at the center of each crater, then flowing upslope along the bottom of the soil layer, before exiting it along the crater rims. To quantify this process, we present a two-dimensional numerical modelling of air convection in a sloped volcanic soil with a surface temperature evolving between day and night. This convection depends on a unique dimensionless equivalent Rayleigh number Ra_{eq} which is the product of the standard Rayleigh number with the volumetric heat capacity ratio of the air and the soil. The convective flow is unsteady: during some periods, the convective flow is entirely confined within the soil, and at other times air enters the crater at its center and exits it at the rim crests. When $Ra_{eq} = 6000$, a value likely compatible with the soil permeability and the geothermal heat flux, a very strong transient cold air plume occasionally develops along the center of the crater. The interval of time between two plumes only depends on the thermal fluctuations within the top boundary layer of the convective cell, and thus is not contrasted by the diurnal cycle. The detachment of a cold plume can occur at any time, after few days of quiescence, and lasts several hours. During the whole convective cycle, the rim to center temperature drop persists and has an amplitude and a shape having an excellent agreement with that found in the IR-images. This work constitutes a preliminary step to explore the deep thermal structure of the active caldera of Bory-Dolomieu and could help to improve the understanding of volcanic hazards of the Reunion volcano.

© 2009 Elsevier B.V. All rights reserved.

1. Introduction

In 2001, a helicopter flyby was done just before sunrise over Enclos Fouqué, the caldera of Piton de la Fournaise (Fig. 1). IR images were acquired during the flyby and striking observations were found at a small volcanically inactive scoria cone, Formica Leo. This 250 years-old ellipsoidal structure (major axis: 115 m, minor axis: 80 m) is composed of 2 unconsolidated and highly eroded subcircular craters (Fig. 2). The South East crater is 40 m in diameter and 15 m deep. The North West crater is smaller and shallower measuring 22 m in

diameter and 5 m deep. Fine lapillis ($d \approx 0.5$ cm) cover the rims of each crater (Fig. 3a). Their inner and outer flanks are covered by coarse lapillis ($d \approx 5$ cm) and the slopes are near the 30° angle of repose. The bottoms of both craters are filled with aggregates – highly porous assemblage of the fine lapillis – which are $d \approx 10$ cm size blocks (Fig. 3b). Some parts of the external flanks are deeply incised by erosion. Finally, some zones on the internal flanks are filled with highly permeable scorias locally covered by fine lapillis (Fig. 2b). The whole Formica Leo structure is embayed within a flat and highly fissured platform of massive basalts (Fig. 2a and b) sparsely covered with lapillis.

IR data have usually been used to discriminate geological facies (Myers et al., 1969; Sabins, 1969; Rowan et al., 1970; Watson, 1973, 1975). However, a first examination of Formica Leo IR images revealed

* Corresponding author. Tel.: +33 0561333024.

E-mail address: antoine@ntp.obs-mip.fr (R. Antoine).

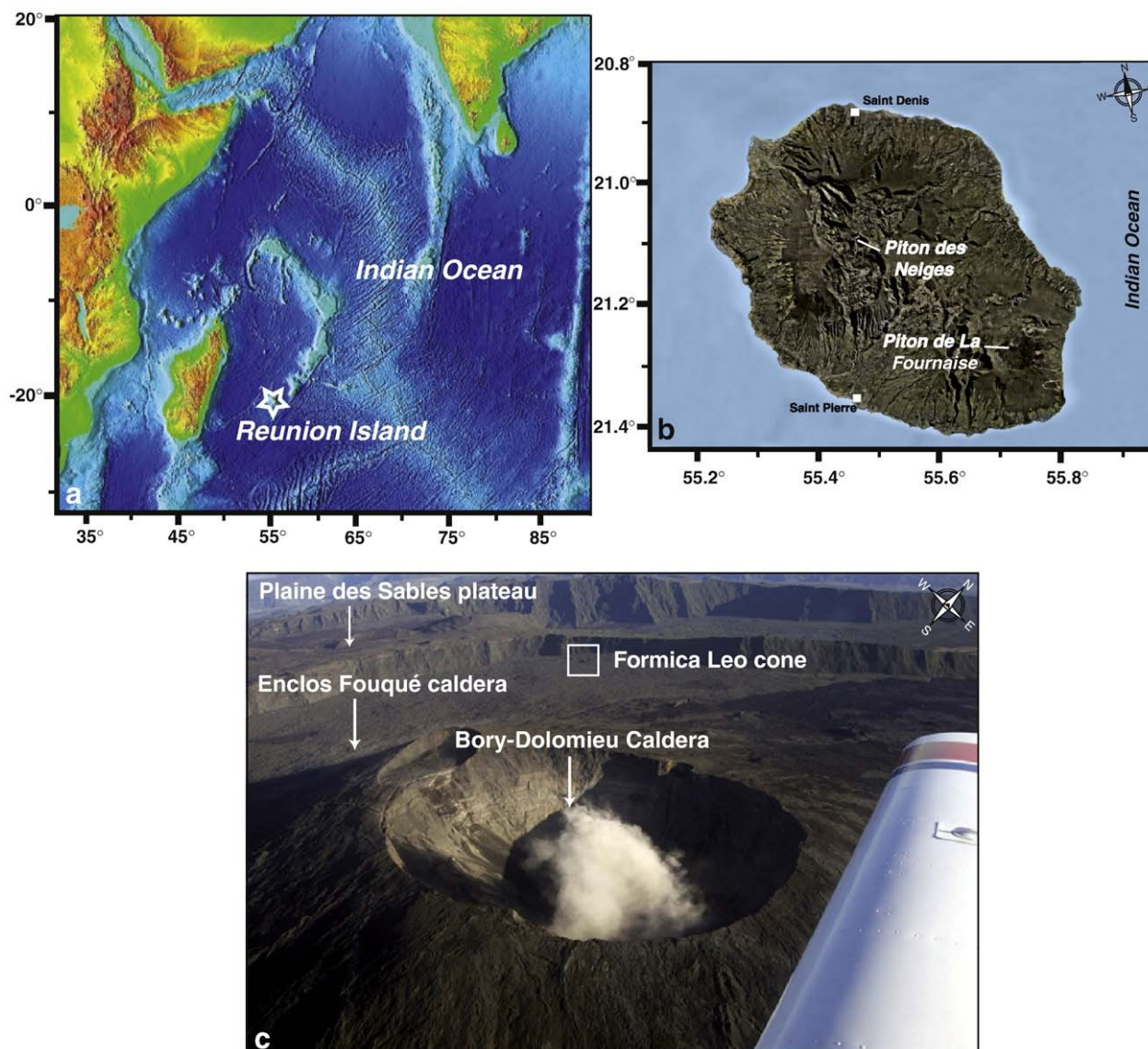


Fig. 1. a) Location of Reunion Island and b) Piton des Neiges and Piton de La Fournaise volcanoes; c) Aerial view of Piton de La Fournaise volcano and location of Plaine des Sables plateau, Enclos Fouqué caldera, Bory–Dolomieu summit and Formica Leo cone study site (photo taken by Frédéric Caillé).

temperature patterns in apparent contradiction with the variations of thermal surface properties. At this preliminary stage, a possible link with subsurface thermal processes was suggested. Between eruptions, the heat of the volcano is partly lost by conduction and advection through fumerolles, hot springs or phreatomagmatic events. The high temperatures associated to these areas are easily detected and mapped from a single thermal image. The evolution of the activity can be recorded by weekly, monthly or yearly observations. Outside of these areas, heat is also discharged to a lesser extent and is more difficult to detect. Indeed, the temperature perturbations remain in the range of the diurnal surface temperature variations. The detection of this heat flow is thus not possible from a single thermal image, and only few experiments have been done with such objectives (Bonneville et al., 1985; Brivio et al., 1989).

To overcome this problem, we obtained repeated field observations during one diurnal cycle and conducted thermal modelling of the surface and subsurface heat transport. In Section 2, we present IR images of Formica Leo acquired over several days as well as the procedure to separate the contribution of the diurnal cycle based on the evolution of these temperature fields. We estimate the thermal

diffusivity and porosity of Formica Leo soil from thermal data acquired with ground probes in Plaine Des Sables inactive area, a flat surface of Piton de la Fournaise volcano, with a similar soil granulometry to Formica Leo (Section 1). Then, we evaluate the influence of the cone topography on the surface temperatures (Section 4). These studies show that the observed rim to crater center temperature contrast is opposite to that induced by the topography and at least 5 °C to 10 °C too large to be attributed to surface properties.

Since the soil at Formica Leo is clearly saturated with air, the subsurface heat transport can only be attributed to convective porous air flow. In Section 5, we present a numerical model of this convection within an inclined rectangular box approximating the geometry of the porous media below the surface of the crater. The numerical model takes into account the physical properties of the soil, the topography and the diurnal evolution of temperature. The model easily explains the observed temperature contrast between the rim crest and the craters centers at Formica Leo. To scale the model, we compare measured subsurface temperatures across the South East crater with predicted ones. Finally, a comparison between computed and observed Darcy velocities of the flow using anemometry is presented.

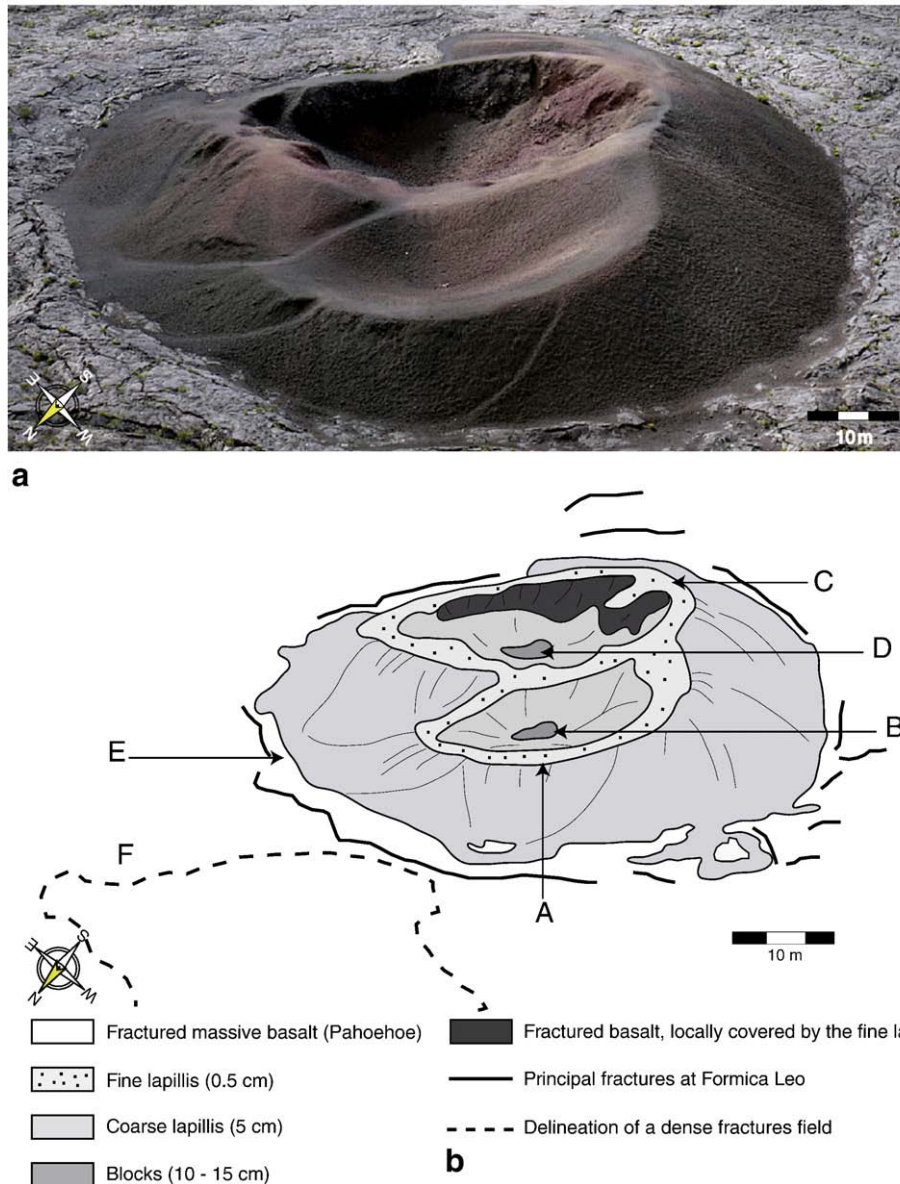


Fig. 2. a) Formica Leo cone and its surroundings. The picture is taken from the rim crest of Enclos Fouqué. b) Map of the different classes of material of Formica Leo: A,B sites are located on the rim crest and on the bottom of the NW crater, respectively; C,D sites are located on the rim crest and on the bottom of the SE crater, respectively; E, F zones are outside Formica Leo on the flat plateau of Enclos Fouqué. This plateau is composed of fine lapillis from Formica Leo in E, and massive basalt in F.

This cross check between observations and modelling allows us to definitively demonstrate that the heat steadily provided by the volcano is actively transported by a porous air convective flow within Formica Leo. In the last section of the paper, we consider possible consequences of these processes on the general heat transport in the whole structure, particularly the Bory Dolomieu caldera.

2. Infrared data and their processing

The infrared survey was conducted in 2006, from April, 24th, 6 p.m. to April, 25th, noon. A camera was placed along Enclos Fouqué rim (Fig. 2) at a height of 100 m above Formica Leo approximately 150 m away, optimizing both the resolution and the angle of view amongst the possible observation points. The sky was partly cloudy and the wind was weak. We used a digital FLIR ThermaCam PM 695 camera owned by the *Observatoire Volcanologique du Piton de la Fournaise*. The instrument uses an uncooled microbolometer technology to measure radiations in the range of 7.5 to 13 μm . The surface temperatures measured by the camera

are corrected from the effects of the relative humidity of the air, the ambient temperature, the distance and emissivity of the target using the empirical relationships provided by FLIR.

The emissivity spectrum of basalts is provided by the Arizona State University (Christensen et al., 2000) (Fig. 4). In the wavelength domain of the camera, the average emissivity is 0.95. Depending on the surface roughness, grain size, and possible contamination by other material (dust coating), this emissivity could drop down to 0.85. Thus, a value of 0.90 ± 0.05 was adopted in this study, leading to an uncertainty of temperature ≤ 0.5 °C. The relative uncertainty is expected to be considerably lower than this value, especially when comparing temperatures within the 2 Formica Leo craters where a relatively homogeneous surface of basaltic scorias is found. However, complication may arise from the effects of topography or viewing angles. Because of the angle of view of our camera, the temperatures might be affected by the non-Lambertian behavior of the surfaces (Coret et al., 2004). However the temperature variations around the cone does not appear to be related to the variations of the emergence angle in the images

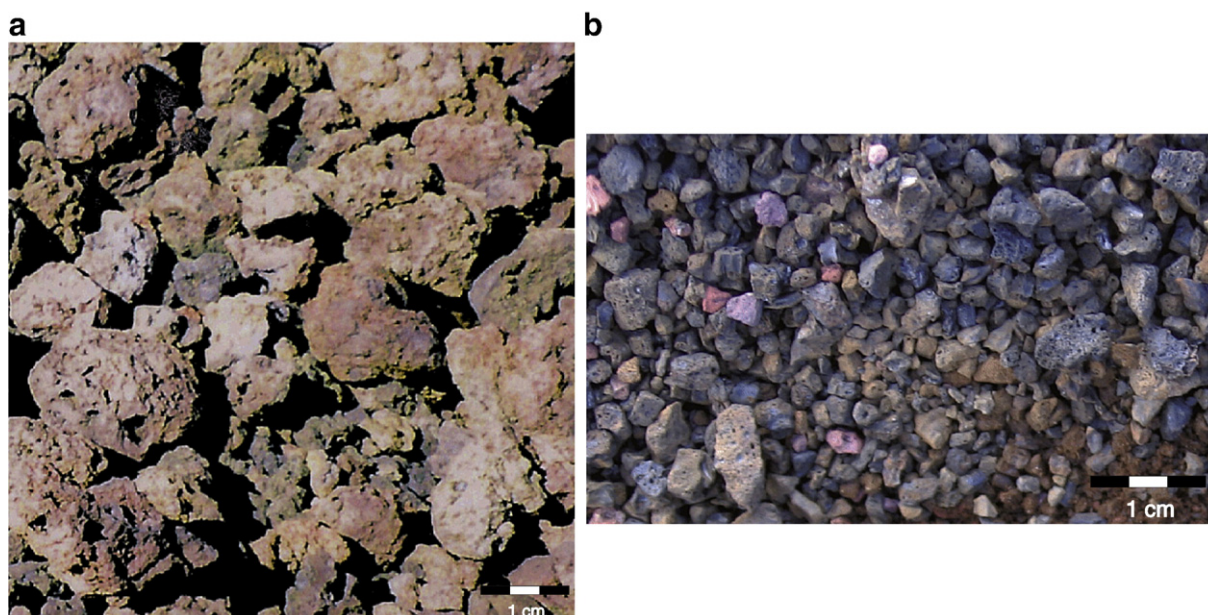


Fig. 3. a) View of blocks and fine lapillis found on the bottom of the SE crater (sites B and D on Fig. 2), b) View of blocks and fine lapillis found on the top of Formica Leo (sites A and C on Fig. 2).

acquired from the caldera rim, as in the 2001 helicopter flyby. The non-Lambertian behavior may still affect the estimated absolute temperatures, but such errors do not affect our application.

Finally, the resolution of the sensor is about $0.08\text{ }^{\circ}\text{C}$ at $30\text{ }^{\circ}\text{C}$. Given the distance of the target, a spatial resolution of $\sim 40\text{ cm}$ is obtained. 30 images have been taken at regular time intervals. Despite the efforts to maintain the camera motionless, winds induced slight offsets. Thus, a geometric correction is required to study the time evolution of the temperature at a given location. We manually selected 10 control points to register and warp each image to the first one, using a RST transformation (rotation, scaling and translation). A maximum misregistration between images of about 40 cm is estimated from the comparison of the position of some objects identified on each image (rocks, fractures, rim crests). Six of the processed images are displayed in Fig. 5. During the night, the floors of both craters of Formica Leo (B and D sites, as indicated on the Fig. 2) are cold while the rim crests are warm. The lapillis at the feet of the flanks of the cone (E site, see Fig. 2) are also cold. The surrounding massive basalts are warmer than the cone with greatest temperatures found inside fractures. As expected, during the day, the hottest regions correspond to the areas illuminated with nearly vertical incidence angles, while cold ones are in the shadow.

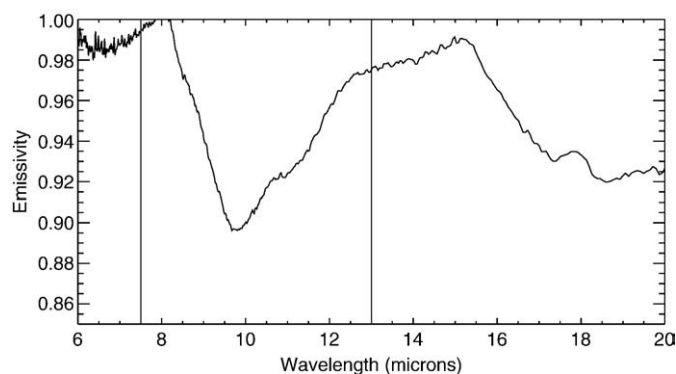


Fig. 4. Emissivity spectrum of basalt from the Arizona State University spectral library (sample 659, basalt substrate – clean). Vertical bars indicate the wavelength band of the thermal camera used in this study. The average emissivity in this 7.5–13 mm band is 0.95.

3. Comparison of observed and calculated diurnal surface temperatures assuming a flat surface

In Appendix A, we review the basic 1-D equations allowing for the diurnal temperature profile $T(z, t)$ through a volcanic vegetation-free soil (z and t designate the depth and time, respectively). The equation is solved with finite difference scheme that is second order in time and space for a soil layer of thickness $H_{\text{lay}} = 0.35\text{ m}$, with a spatial resolution of $3.5 \cdot 10^{-3}\text{ m}$ and time resolution of 1 min. The parameters of the model and their assumed values are summarized in Table 1. Different spots outside and within Formica Leo are studied.

3.1. Diurnal surface temperatures outside Formica Leo

Observed and calculated temperatures at different locations outside Formica Leo are compared (Fig. 6). To avoid difficulties arising from possible residual misregistration, the observed temperatures are averaged on surfaces of about 0.64 m^2 (4 pixels). Within these areas, the standard deviation of surface temperatures between 7 p.m. and 5 a.m. never exceeded $0.1\text{ }^{\circ}\text{C}$. During the day, fine lapillis warm up more rapidly than coarse lapillis, and a difference of $\leq 4\text{ }^{\circ}\text{C}$ is recorded at noon (Fig. 6). Also, coarse lapillis warm more rapidly than massive basalts. Observed profiles match calculated ones provided the following conductivity k for each type of soil is chosen: $0.5\text{ W m}^{-1}\text{ K}^{-1}$ for fine lapillis (5 mm), and $1.5\text{ W m}^{-1}\text{ K}^{-1}$ for an intermediate surface composed of both lapillis and massive basalts and $2.5\text{--}3\text{ W m}^{-1}\text{ K}^{-1}$ for massive basalts.

In order to get a direct estimate of the conductivity of a granular soil, the diurnal temperature evolution was recorded using 17 thermal probes placed at a distance $D = 15\text{ cm}$ depth inside the soil of the Plaine des Sables plateau (Fig. 7) ($d = 0.5\text{ cm}$ grain size). The cooling down process propagating after sunset reached the depth D after about $t = 10\text{ h}$ (Fig. 7). The thermal diffusivity κ of the lapilli soil is calculated using the solution for instantaneous cooling of infinite half-space (Turcotte and Schubert, 2002):

$$\kappa = \frac{D^2}{4t} = 1.510^{-7}\text{ m}^2 \quad (1)$$

The volumetric heat capacity of the soil h_s is approximatively equal to:

$$h_s = (1-n)\rho_b c_b \quad (2)$$

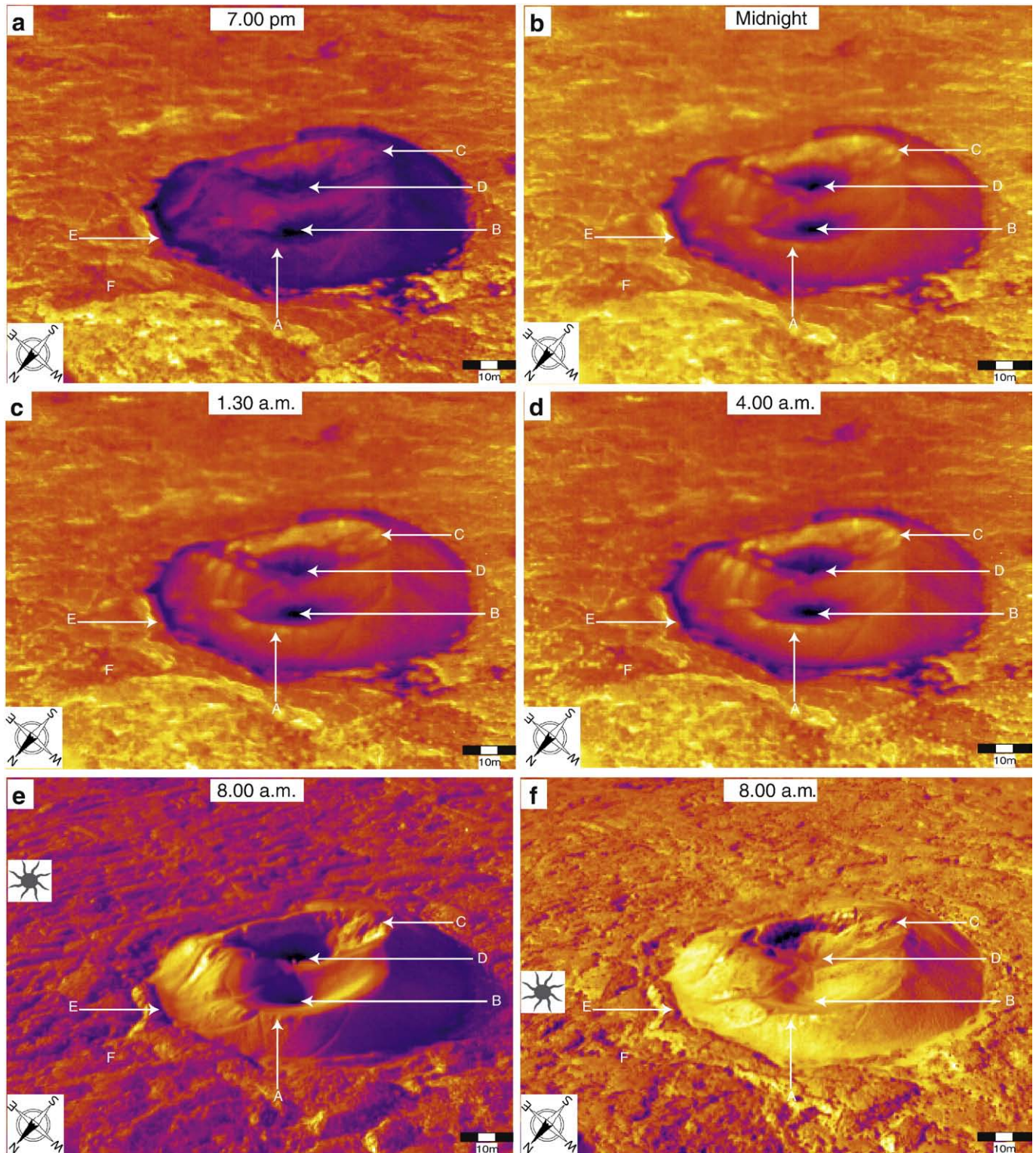


Fig. 5. Infrared images at different time. Bright sites are hot and dark sites are cold, arrows point at the lettered sites defined in Fig. 2b. The sun position at 8h00 a.m. and 12.00 p.m. is indicated on the daytime e and f frames.

where the terms are defined in Table 1. These relationships lead to a thermal conductivity $\kappa = 0.4 \text{ W m}^{-1} \text{ K}^{-1}$, i.e. a value very close to the one deduced from the radiometric data from lapilli (Fig. 6) and of (Lardy and Tabbagh, 1999) similar measurements in basaltic soils.

The soil of Formica Leo has huge variations in grain size 0.5 cm up to 15 cm. From a recent review of thermal conductivity models for granular material (Kurita et al., 2007), it appears that a good first order

approximation for the effective conductivity k of porous rocks and soils follow the *geometric mean model* (Woodside and Messmer, 1961):

$$k = k_a^n k_b^{n-1} \quad (3)$$

(See Table 1 for notation). This conductivity is formally independent of the grain size in this equation. Note that, if we use the values of

Table 1

Physical parameters related to the conductive–radiative model.

Thickness of the soil layer	H_{lay}	0.35 m
Density of the basalt	ρ_b	2700 kg m ⁻³
Basalt specific heat constant	c_b	1000 J kg ⁻¹ K ⁻¹
Basalt thermal conductivity	k_b	2.7 W m ⁻¹ K ⁻¹
Soil porosity	n	0.4
Soil grain size	d	0.5 cm–10 cm
Soil volumetric heat capacity	$h_s = \rho_b c_b$	2.7×10^6 J K ⁻¹ m ⁻³
Solar constant	S_0	1367 W m ⁻²
Direct + diffuse energy fraction at the soil	C	0.5
Latitude of Formica Leo	λ	20° S
Day number of the year (April, 24th)	J	113
Solar declination (April, 24th)	δ	0.2 rad
Emissivity	ε	0.95
Stefan–Boltzman Constant	σ	5.67×10^{-8} W m ⁻² K ⁻⁴
Air thermal conductivity	k_a	2×10^{-2} W m ⁻¹ K ⁻¹
Mean air temperature	T_0	281 K
Amplitude of the air temperature	T_{amp}	7.5 K
Phase shift	t_{ph}	3,600 s
Duration of the diurnal cycle	P_{dc}	86,400 s

k_a and k_b given in Table 1 along with a porosity of 0.4, we obtain a value $k = 0.4$ W m⁻¹ K⁻¹ in agreement with the estimate above.

3.2. Surface temperatures inside Formica Leo

During the night, the center of each crater is cold while the rim is warm (Fig. 5a to d). Infrared temperatures at midnight along profiles Tr1 and Tr2 across SE and NW craters are displayed in Fig. 8a and b, respectively. The locations of each profile are shown in the Fig. 5b. In both cases, a temperature drop of about 4 K from the rim crest toward the crater center is observed. Evolution of the infrared surface temperatures from 7 p.m. to 11 a.m. at A and B, C and D sites (see Fig. 2b for the location of the areas) are shown on Fig. 9a and b. Diurnal evolution of the infrared surface temperatures on the rim of the NW crater (A site) is compared to that of the flat coarse lapilli floor (E) and massive basalt (F) outside the cone in Fig. 9c and d. From 9 p.m. to 2 a.m., the fine lapillis along the rim become progressively warmer than the coarse lapillis at the centers and even hotter than the massive basalts surrounding the cones. These temperature patterns could result from a rim to center thermal conductivity drop. The slopes of the craters and their centers are covered with coarse lapillis (5 cm), and aggregates of vesiculated rocks up to 10–15 cm in size, respectively, with a porosity similar to that of the fine lapillis found at the rim crest. The fraction of the porosity corresponding to the vesicles should not inhibit significantly the effective thermal conductivity of the soil (Kurita et al., 2007). Thus, there is no reason for the rocks found at the craters centers to have a significantly lower thermal conductivity than the fine lapillis. Moreover, the contacts between fine, coarse lapillis and blocks are well-marked on Formica Leo. If the thermal patterns inside the craters corresponded to thermal conductivity variations, strong temperature contrasts between the different lithologies should be observed along Tr1 and Tr2 profiles, which is not the case. The present radiative–conductive modeling valid for flat surfaces should be modified to explore the effects of the local topography.

4. Influence of the cone topography on the diurnal surface temperatures

In the craters, a portion of flank exchanges energy with the sky and with others flanks in the upper hemisphere (2π solid angle). Neglecting absorption and diffusion in the atmosphere, face to face surfaces with the same temperature have a zero net radiative balance. During the night, the surface temperature contrast along the different faces of the cones is small as all flanks of Formica Leo receive the same amount of solar energy during the day. This implies that the thermal

budget between the flanks is negligible. The cooling of the flank is controlled by the radiative exchange with the fraction of the sky seen from that portion of the flank (Whiteman et al., 1989, 2000). This situation decreases the rate of energy loss $E(x)$ along all the slopes of the cones in comparison to that of a flat surface (Fig. 10):

$$E(x) = p(x)\varepsilon\sigma T^4 \quad (4)$$

where p is the fraction of sky seen at the distance x of the rim. We approximate the sky fraction $p(x)$ by $\alpha(x)/\pi$ where $\alpha(x)$ is the angle between each rim evaluated at each point of the flank (Fig. 10). From the rim down to the center of the SE crater, p decreases from 1 to 0.63 (cf. Fig. 10). The 1-D calculation of surface temperatures is done taking into account the variable rate of energy loss along a radial profile of the cone. Atmospheric radiations are also taken into account and are described in Appendix A, assuming a thermal conductivity of 0.4 W m⁻¹ K⁻¹ (Section 1). The calculated temperature at midnight is compared with those measured along Tr1 (Fig. 11). The rim to crater center drop p induces a non linear increase in surface temperature (Eq. (4)), which reaches 20 °C in the crater center. This is opposite to the observations (Fig. 11).

5. Convection model inside Formica Leo: the slope effect

5.1. Additional field observations suggesting air convection

In the previous sections, we have shown that the observed temperatures inside Formica Leo cannot be explained neither by a contrast of thermal conductivity associated with a difference of lithology in the cone nor by the radiative effects associated with topography. Other thermal processes have been searched to explain field observations but negative conclusions have been obtained for the two following alternative hypotheses. i) Water evaporation could extract heat from the center of the cone, cooling it. Humidity measurements show that during the night, air is saturated with water vapor (97–98% relative humidity). Then, we do not see the reason why evaporation could differentially extract heat from some areas of the soil of the cone with a homogeneous saturated atmosphere above it. ii) The presence of nighttime irregular fog at the center of the cone could also affect the thermal image. However, the atmosphere was perfectly clear in several cases for which the temperature contrast is observed. Fog,

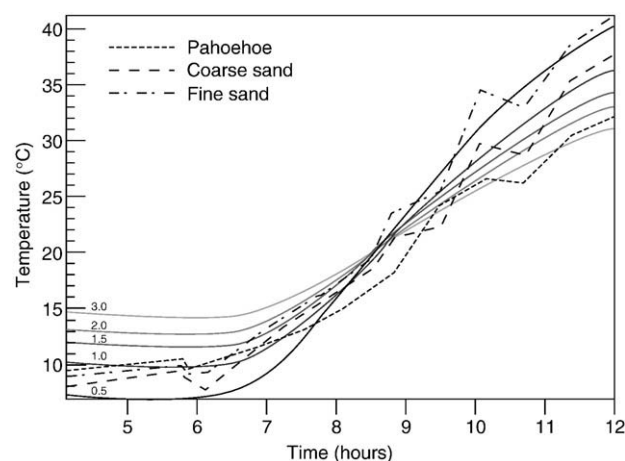


Fig. 6. Observed and calculated surface temperatures from 4 a.m. to noon at three locations on the plateau outside Formica Leo. Dotted lines are infrared temperatures on fine, coarse lapillis and massive basalt soils (E and F sites). The calculated profiles are for the thermal conductivities of the porous basalt layer ranging from 0.5 W m⁻¹ K⁻¹ (black line) to 3 W m⁻¹ K⁻¹ (light-grey line). The lower values of conductivity match the observations for the fine and coarse lapilli soils while the higher ones match the massive basalt.

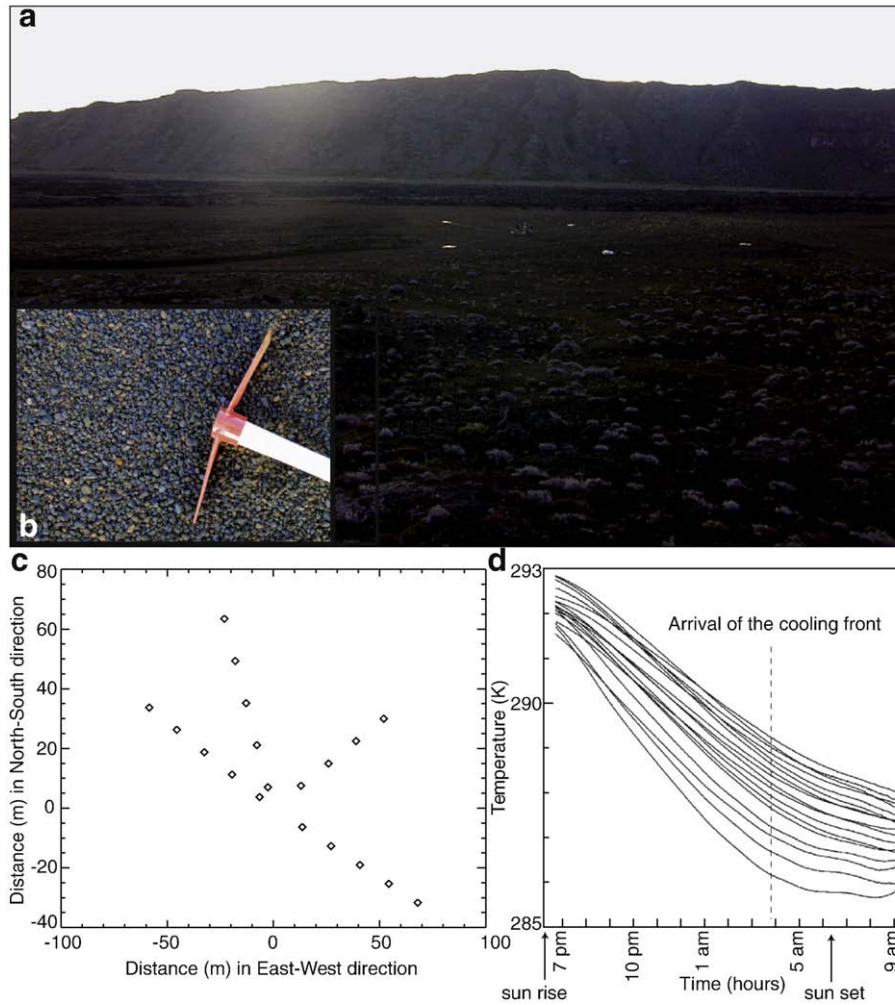


Fig. 7. a) Picture of the thermal probes installed at the Plaine des Sables plateau; b) Plaine des sables typical granular size (grain size $d \approx 5$ mm); c) Field map of the 17 thermal sensors (PT100 probes); d) Time evolution of the temperatures measured by the sensors at depth $D = 15$ cm.

when present, is not responsible for the rim crest to crater center temperature drop.

Having reviewed all thermal processes that could affect the surface temperatures at Formica Leo, we believe that the only way to explain

the observed thermal profiles is air convection. This idea is also suggested by several other field observations. On the morning following our April 25th nighttime infrared measurements, an anemometer (Campbell Scientific anemometer) placed 10 cm above the

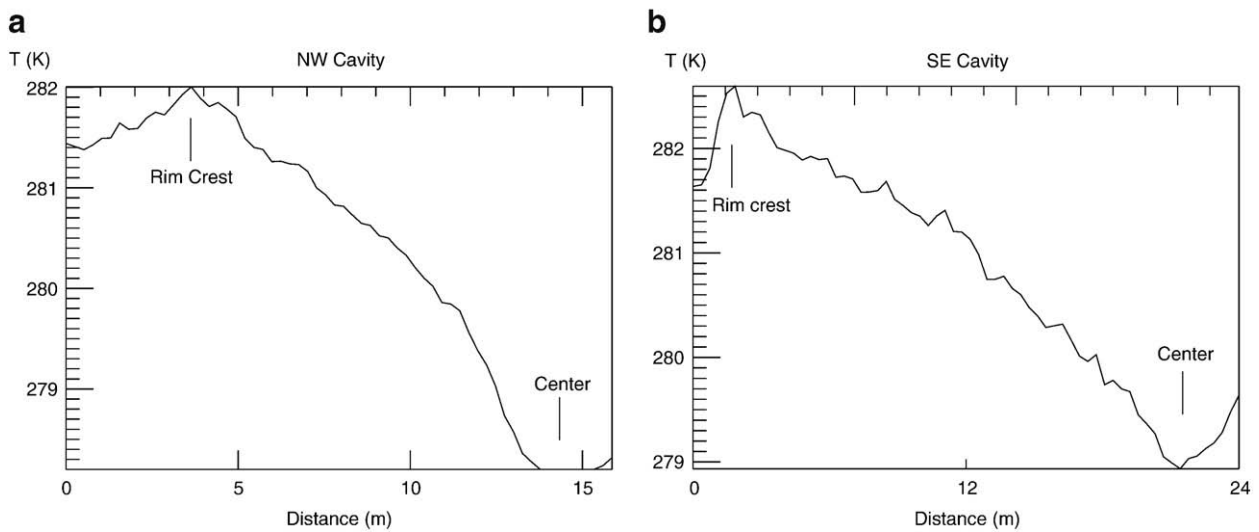


Fig. 8. Infrared surface temperature at midnight along Tr1 and Tr2 transects, respectively (see Fig. 5b for transects locations).

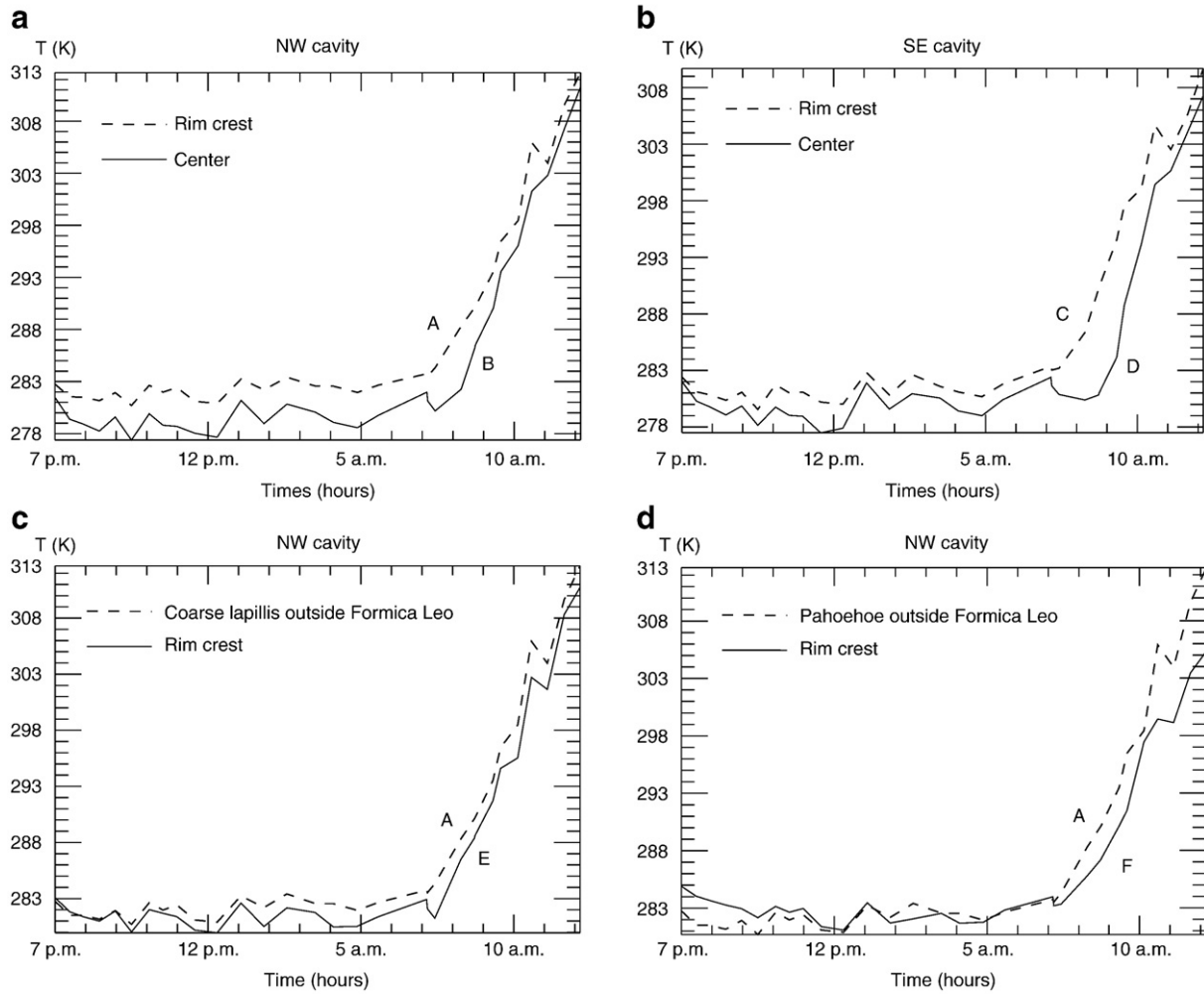


Fig. 9. Time evolution of surface temperatures: (a) dashed and solid curves represent the temperature at the rim and at the center of the NW crater of Formica Leo (A, B sites), respectively; (b) similar temperature profiles on the SE crater (C,D sites); (c) temperatures on the rim of the NW crater (A site) and on the coarse lapillis floor outside the cone (E site); (d) Temperatures on the rim (D site) and on the massive basalt outside the cone (F site).

crater center detected air speed as low as 20 cm s^{-1} . When the propellers were parallel to the surface, they rotated fast, while the motion was much slower when they were placed perpendicularly to the surface. This direct observation indicates the presence of an air flow with a dipping component much stronger than the horizontal one inside the highly permeable soil. It constitutes an important independent observation in favor of air convection within Formica Leo craters. This strong vertical component of the air flow was specific to the crater center and nothing comparable was seen elsewhere, in particular at the rim of the cone. Another direct evidence of air convection was obtained in August 2007. A 30 cm depth temperature profile across the SE crater was measured using 30 thermal probes and a digital thermometer (Fig. 12). This profile displays a rim to crater

center temperature drop of about $6 \text{ }^\circ\text{C}$. Such subsurface temperature variations can be explained only assuming a convective air flow. In the following, a physical model for the air flow inside the cone is presented and the possibility of convection depending mainly on permeability is explored by numerical simulations.

5.2. The equations of air convection

Numerous experimental and numerical studies consider the convection of water in inclined porous layers (Boriès and Combarous, 1972; Wood and Hewett, 1982; Caltagirone and Boriès, 1985; Rosenberg et al., 1993; Chevalier et al., 1998; Baytas and Pop, 1999; Rabinowicz et al., 1999; Zhao et al., 2004; Zhang et al., 2005).

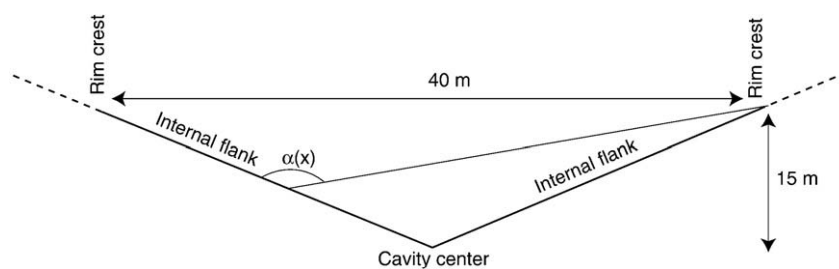


Fig. 10. Sketch of Formica Leo craters and geometric parameters for the calculation of the sky proportion p (see Eq.).

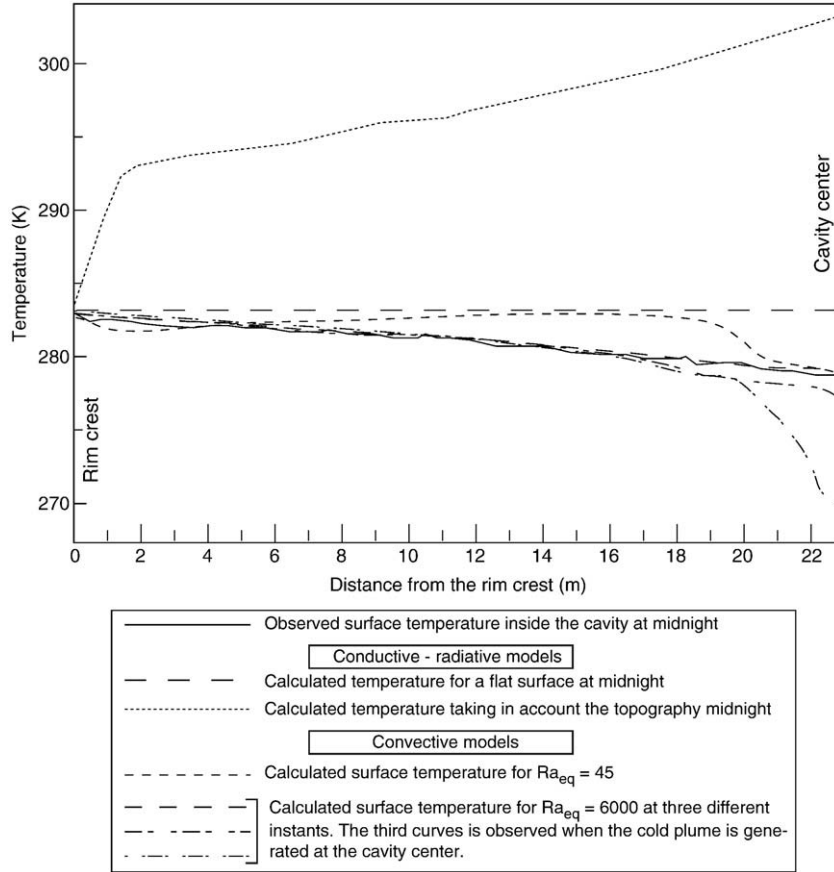


Fig. 11. Comparison of the infrared temperature profile across SE crater of Formica Leo at midnight for the conductive–radiative models with flat and sloped surfaces, and for the convective models.

Numerical and experimental works have been done on convection of air in subarctic soils to study its influence on avalanches of snow (Sturm, 1991; Sturm and Johnson, 1991). Others have done laboratory (Yu et al., 2005) and numerical (Zhang et al., 2005) investigations on rock cooling by air convection in permafrosts for railway/roadway engineering purposes. Rose and Guo (1995) conducted numerical studies of thermal convection of air in sloped soils. No previous work reports on air convection within sloped ventilated volcanic systems whose surface temperature evolves during day and night. Our

objective is to explain surface temperatures across Formica Leo just before the dawn, when the surface temperature is a minimum, and the effect of illumination angles and topography are negligible. We use a 2-dimensional code already developed in our laboratory (Rabinowicz et al., 1999). The mathematical development of the 2-dimensional porous flow convection is based on the following standard equations. The equation of mass conservation is:

$$\vec{\nabla} \cdot \vec{q} = 0 \tag{5}$$

where \vec{q} is the Darcy velocity which represents the product of the air velocity \vec{v} in the porous medium with the porosity n of the rock ($\vec{q} = n \vec{v}$). We write the Darcy's equation:

$$\frac{\partial P}{\partial x} + g\rho_a \sin \phi - u \frac{\mu}{K} = 0 \tag{6}$$

$$\frac{\partial P}{\partial z} + g\rho_a \cos \phi - w \frac{\mu}{K} = 0 \tag{7}$$

where u and w are the Darcy velocities projected along the x and z directions which are parallel and orthogonal to the slope of the porous layer, respectively (z points downward, cf. Fig. 13). The angle of the porous layer with respect to the horizontal direction is ϕ . P is the gas pressure, g is the gravity, ρ_a and μ are the density and the dynamical viscosity of the air, respectively. The heat transfer equation is:

$$(1 - n)\rho_b C_b \frac{\partial T}{\partial t} + n\rho_a C_a \left(u \frac{\partial T}{\partial x} + w \frac{\partial T}{\partial z} \right) = \kappa \vec{\nabla}^2 T \tag{8}$$

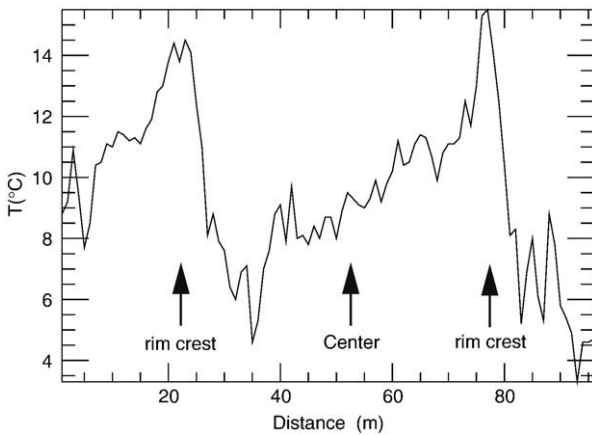


Fig. 12. Temperature profile at the largest crater of Formica Leo and at 0.3 cm depth. The temperature profile was acquired between 3 p.m. and 5 p.m. The large temperature variations can be only explained by the occurrence of convection cells with cold air entering the center of the crater and warm air exiting through the rims.

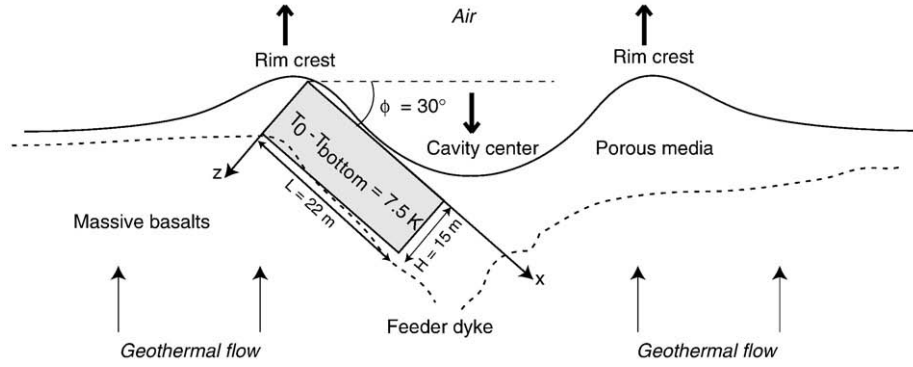


Fig. 13. Representation of the inclined box used to model air convection within Formica Leo.

where C_a is the heat capacity of the fluid. Dividing both sides of the equation by the soil volumic heat capacity $(1 - n) \rho_b C_b$, the equation becomes:

$$\frac{\partial T}{\partial t} + \gamma \left(u \frac{\partial T}{\partial x} + w \frac{\partial T}{\partial z} \right) = \kappa \nabla^2 T \quad (9)$$

where γ is the air-soil volumic heat capacity ratio:

$$\gamma = \frac{\rho_a C_a n}{\rho_b C_b (1 - n)} \quad (10)$$

In the numerical code, γu and γw are related to the stream function by:

$$\gamma u = \frac{\partial \psi}{\partial z} \quad (11)$$

$$\gamma w = - \frac{\partial \psi}{\partial x} \quad (12)$$

These equations apply to an incompressible air flow which is slow enough for the temperature of the air and the solid fraction of the porous media to be the same. The incompressibility is easily verified: the excess pressure during air convection in soils is negligible in comparison to the hydrostatic pressure. Because of the slow rate of the temperature variations with time in the soil (see below) the air and soil are likely in equilibrium all times. We used the following equation of state for the air density:

$$\rho_a = \rho_0 (1 - \alpha(T - T_0)) \quad (13)$$

where ρ_0 and α are respectively the density of the air and the thermal expansion coefficient at the mean temperature T_0 . The non-dimensional temperature (\bar{T}), the stream function ($\bar{\psi}$), the distances (\bar{x} and \bar{z}), velocities (\bar{u} and \bar{w}), and time (τ) are introduced using the following scaling:

$$T - T_0 = \Delta T \bar{T} \quad (14)$$

$$x = H \bar{x} \quad (15)$$

$$z = H \bar{z} \quad (16)$$

$$\psi = \kappa \bar{\psi} \quad (17)$$

$$\gamma u = \frac{\kappa}{H} \bar{u} \quad (18)$$

$$\gamma w = \frac{\kappa}{H} \bar{w} \quad (19)$$

$$t = \frac{H^2}{\kappa} \tau \quad (20)$$

where H is the layer thickness, $\Delta T = T_{\text{bottom}} - T_0 = 7.5 \text{ K}$ and $T_{\text{bottom}} = 288.5 \text{ K}$ is the temperature at the bottom of the soil layer. Assuming that the viscosity μ , the permeability K and the thermal expansion coefficient α are constant, the equations of convection become:

$$\frac{\partial \bar{T}}{\partial \tau} + \left(\bar{u} \frac{\partial \bar{T}}{\partial \bar{x}} + \bar{w} \frac{\partial \bar{T}}{\partial \bar{z}} \right) = \nabla^2 \bar{T} \quad (21)$$

and

$$\nabla^2 \bar{\psi} = - \gamma Ra \left(\frac{\partial \bar{T}}{\partial \bar{x}} \cos \phi - \frac{\partial \bar{T}}{\partial \bar{z}} \sin \phi \right) \quad (22)$$

where Ra is the Rayleigh number:

$$Ra = \frac{\rho_0 g \alpha \Delta T H K}{\mu \kappa} \quad (23)$$

In the case of water porous flow, the volumetric heat capacity of the water $\rho_w c_w$ is approximately that of the basalt. With $\gamma \approx 1$ (Cherkaoui and Wilcock, 1999), the above dimensionless equations are similar than those describing convection of water. However, the air has a volumetric heat capacity which is over 3 orders of magnitude less than that of the rock ($\gamma = 5.0 \times 10^{-4}$). In consequence, the heat transported by the air is large in comparison with conducted heat at the condition that the Darcy velocity of the air is extremely high. This is the reason why air convection is generally not considered in modelling the transport of heat through volcanic structures. However, we show below that air convection can transport significant heat in the soil of Formica Leo craters because of their high permeability and high associated velocities.

Table 2

Notation and values of the physical parameters used for the convective model.

Notation	Value
Height of the box	H 15 m
Length of the box	L 22 m
Slope of the box	ϕ 30°
Heat capacity of the air	C_a 1000 J kg ⁻¹ K ⁻¹
Air density	ρ_a 1 kg m ⁻³
Air thermal expansion	α 3.7 × 10 ⁻³ K ⁻¹
Air Viscosity	μ 1.5 × 10 ⁻³ Pa s
Air-soil volumic heat capacity ratio	γ 5.0 × 10 ⁻⁴
Permeability of the soil	K 3 × 10 ⁻⁸ –10 ⁻⁵ m ²
Thermal conductivity of the soil	k 0.4 W m ⁻¹ K ⁻¹
Porosity of the soil	n 0.4
Top to bottom temperature contrast	ΔT 7.5 K
Phase shift	ζ 0
Pulsation scale	Ω 45,507 s
Darcy velocity scale	v 2.7 × 10 ⁻⁵ m s ⁻¹
Geothermal heat flux (for $k=2.5$)	1250 mW m ⁻²
Equivalent Rayleigh number	Ra_{eq} 20.4–6800

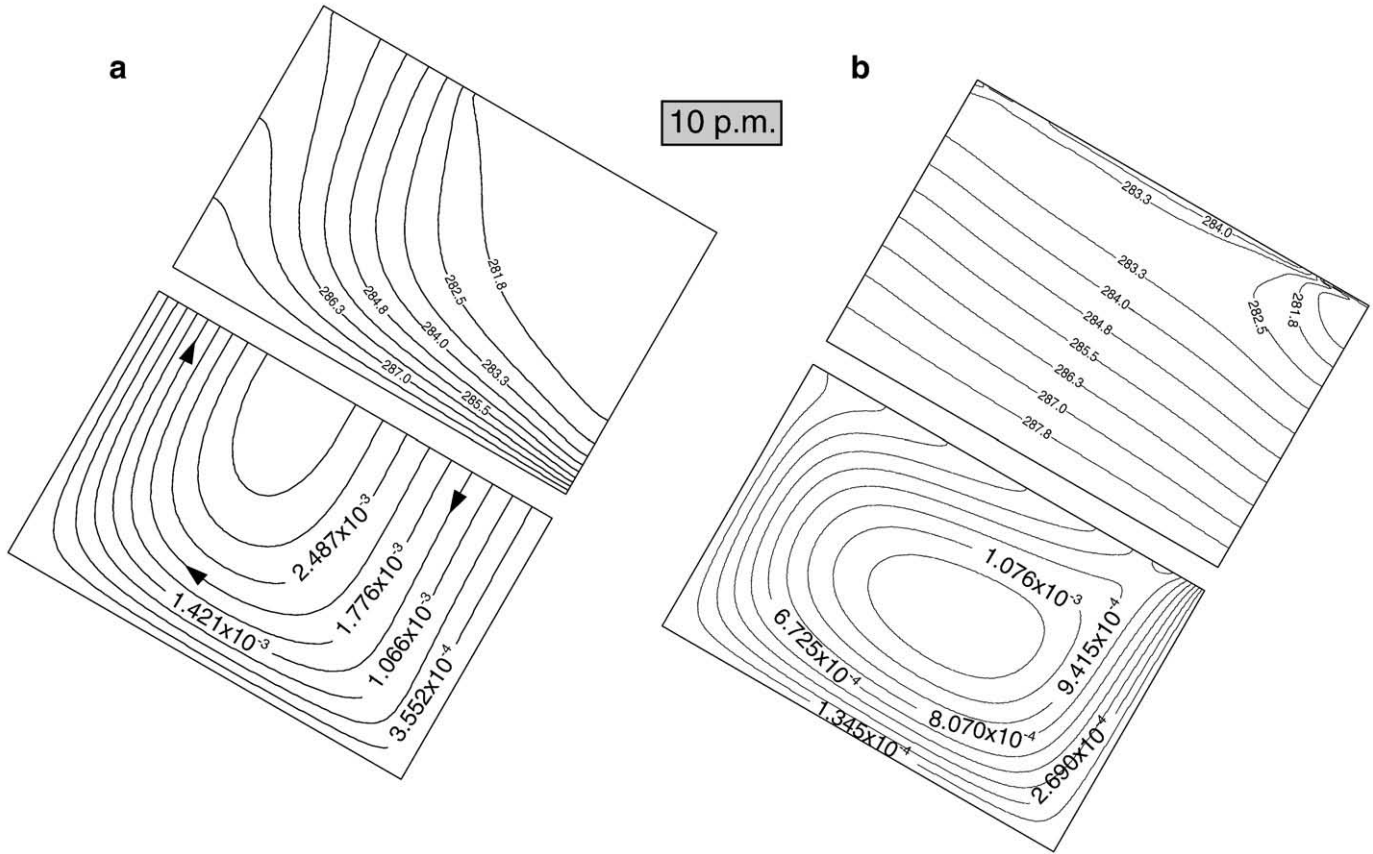


Fig. 14. Comparison of isotherms (in degree K) and stream lines ψ (in $\text{m}^2 \text{s}^{-1}$) for a model with an equivalent Rayleigh number Ra_{eq} of 45 with a (a) constant top temperature and (b) with a fluctuating surface temperature (b); (a) represents the steady solution and (b) is the snapshot at 10 p.m. Since $\psi = 0$ on the border of the cell, the value of the streamline represents the flow rate between the border of the box and this streamline. Note that the flow rate within the convective cell is much lower when the surface temperature fluctuates (b) than when it is constant (a).

5.3. Parameter values and boundary conditions of the model

The vigor of air convection within the porous media is characterized with the equivalent Rayleigh number $Ra_{\text{eq}} = \gamma Ra$. The temperature Eq. (21) is solved with an alternative direction implicit finite difference method (Douglas and Rachford, 1956) tested for various convective problems (Rabinowicz et al., 1993; Ormond et al., 1995; Rabinowicz et al., 1999). The flow equation is solved using a spectral decomposition (Rabinowicz et al., 1999). We simulate the air flow and the temperature of the media within a rectangular sloped box representing the flank of craters (Fig. 13). The porous media has an open top permitting free circulation of the air ($\partial\bar{\psi}/\partial\bar{z} = 0$), its bottom is impervious ($\bar{\psi} = 0$). The sides are adiabatic ($\partial\bar{T}/\partial\bar{x} = 0$) and impervious ($\bar{\psi} = 0$). The air temperature at the surface is given by:

$$\bar{T}(\bar{x}, \bar{z} = 0) = T_0 + \Delta T \sin(\Omega\tau + \zeta) \quad (24)$$

where $T_0 = 281 \text{ K}$, $\Delta T = 7.5 \text{ K}$ and τ is the time. ζ is the phase shift and Ω is the diurnal pulsation scale:

$$\Omega = \frac{2\pi H^2}{P_{\text{dc}} \kappa} \quad (25)$$

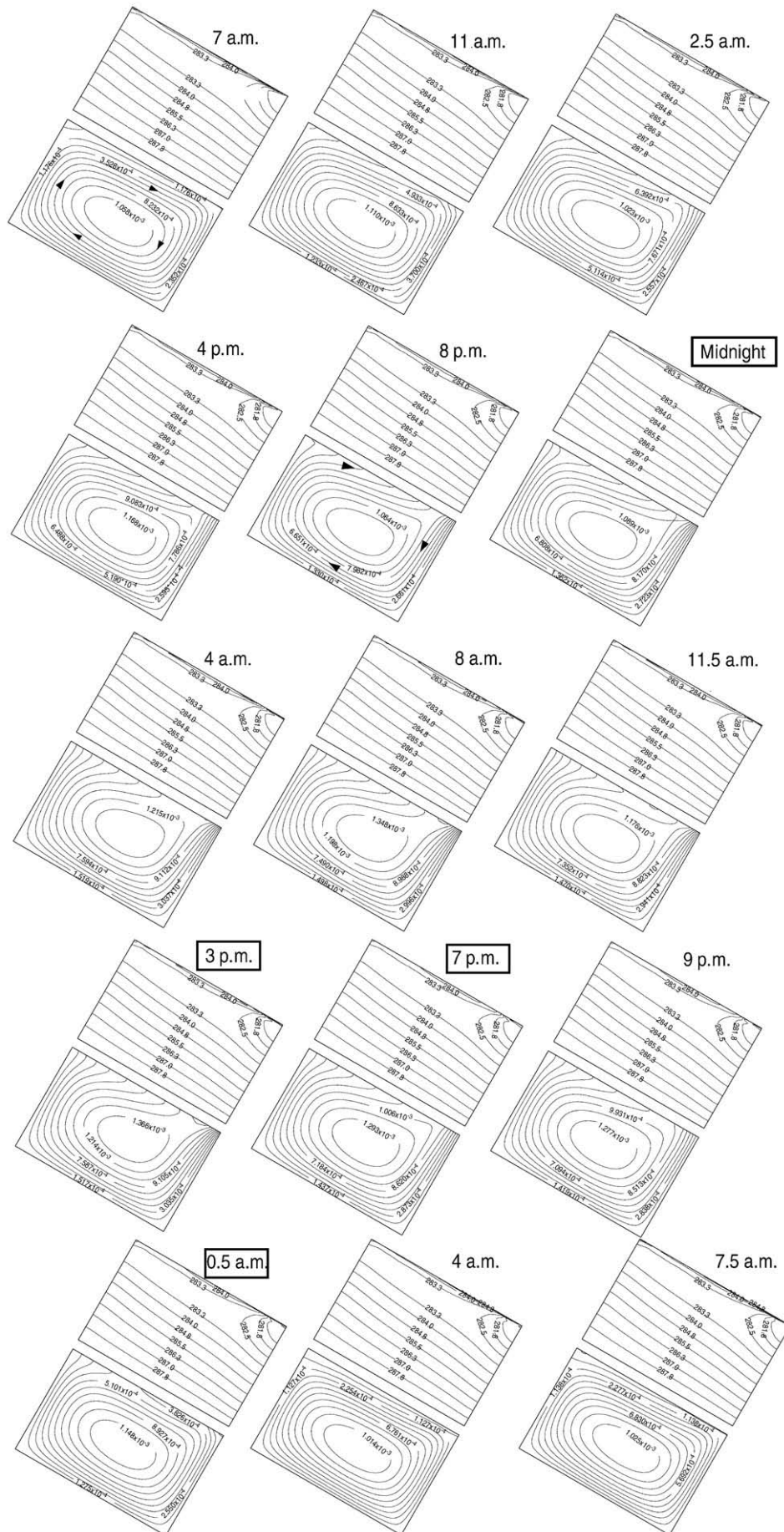
Ω and ζ are set to have a maximum temperature of 288.5 K at 6 p.m. ($\bar{T} = 1$) and a minimum temperature of 273.5 K at 6 a.m.

($\bar{T} = -1$) (Fig. 13, Table 2). As radiative processes at the surface are approximated using a sinusoidal function, the temperature profile within the thermal skin depth is expected to be different from the one given by the convective model. Some uncertainties remain when comparing the results of the model and the observations from the infrared camera which only has access to the surface temperature.

For advection across the upper boundary, the temperature of the entering air is that of the atmosphere, while the temperature of the exiting air is that at the grid point immediately below the surface. The use of this boundary condition is essential for correct modelling of the convection (Cherkaoui and Wilcock, 1999). The numerical experiments are initialized with a 1-D conductive temperature solution with $T_0 = 281 \text{ K}$ at the top of the box and of $T_{\text{bottom}} = 288.5 \text{ K}$ at its bottom.

Table 2 shows the different values of the parameters and physical constants used. We assume that the bottom of the box representing the interface between massive basalts and soil is parallel to the sloped surface (Fig. 13). As a result, the approximative thickness H of the soil throughout Formica Leo is 15 m. Outside the cone, the soil being indurated has a conductivity k of about $2.5 \text{ W m}^{-1} \text{ K}^{-1}$ (Section 1). The assumption predicts the conductive heat flux in the volcano $k\Delta T/H = 1250 \text{ mW m}^{-2}$. This value is reasonable for a volcano with a magmatic chamber lying between about 1 and 2 km depth (Rabinowicz et al., 1998).

Fig. 15. Time evolution of isotherms (in degree K) and stream lines (in $\text{m}^2 \text{s}^{-1}$) during 63 h for the model with an effective Rayleigh number Ra_{eq} of 45 and a fluctuating surface temperature (see Fig. 14b).



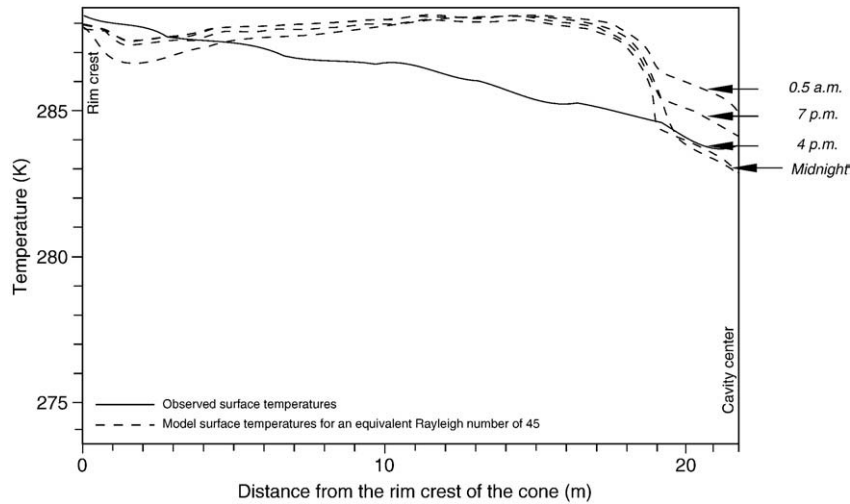


Fig. 16. Surface temperatures of the convective model with an equivalent Rayleigh number $Ra_{eq} = 45$ at different times (dotted lines). For comparison, the observed surface temperature (plain line) at midnight along the SE crater is displayed (Tr1 transect, see Figs. 5b and 11).

The permeability K is estimated from Kozeny–Carman equation (Carman, 1961):

$$K = \frac{n^3 d^2}{(1-n)^2 \cdot 172.8} \quad (26)$$

The soil filling the central parts of the craters is particularly coarse ($d \approx 5$ to 10 cm). A straight application of Kozeny–Carman's permeability law leads to K values ranging from 3.10^{-6} m^2 to 10^{-5} m^2 . However, this law supposes that the space between aggregates is filled with air. It is likely that Formica Leo aggregates are partially filled with Plaine des Sables type of lapilli. The size of the grains composing this soil are relatively small ($d \approx 5$ mm), leading to a permeability K of $3 \times 10^{-8} \text{ m}^2$. Thus, the permeability of the soil can be reasonably bounded by $K = 3 \times 10^{-8} \text{ m}^2$ to 10^{-5} m^2 . Within this range of permeability, the equivalent Rayleigh number Ra_{eq} ranges from 20 to 6800, a value generally above the critical value for convection in a horizontal layer 27.1, (Cherkaoui and Wilcock, 1999). Thus, air convection should occur within Formica Leo. Measured permeability of the Piton de la Fournaise massive basalt yields a value of about 3.10^{-11} m^2 (Fontaine et al., 2002). With this permeability, the equivalent Rayleigh number $Ra_{eq} = \gamma Ra$ of water saturated media is close to critical value for convection. Assuming the permeabilities estimated at Formica Leo (3×10^{-8} – 10^{-5} m^2), the equivalent Rayleigh number ranges from 1000 to 3×10^5 . For the highest permeabilities values (preferred here, see below) we can expect the convective water flow to be highly turbulent with a quasi constant subsurface temperature (Caltagirone and Boriès, 1985). In such case, constant temperatures through Formica Leo would be observed, in contradictions with our IR data. In most volcanoes, highly permeable soils are likely saturated with water and will not be able to sustain the rim to crater center radiometric temperature drop we observe at Formica Leo.

5.4. Air convection with a Rayleigh number of 45 and a constant temperature prescribed at the surface

Fig. 14a displays the asymptotic steady flow obtained when the effective Rayleigh number Ra_{eq} is 45 and the surface temperature is arbitrarily supposed to remain equal to the mean air surface temperature $T_0 = 281 \text{ K}$ during the whole diurnal cycle. A unique cell develops: the air enters the box at the center of the cone and exits it at the rim crest. The exit temperature has a parabolic shape decreasing

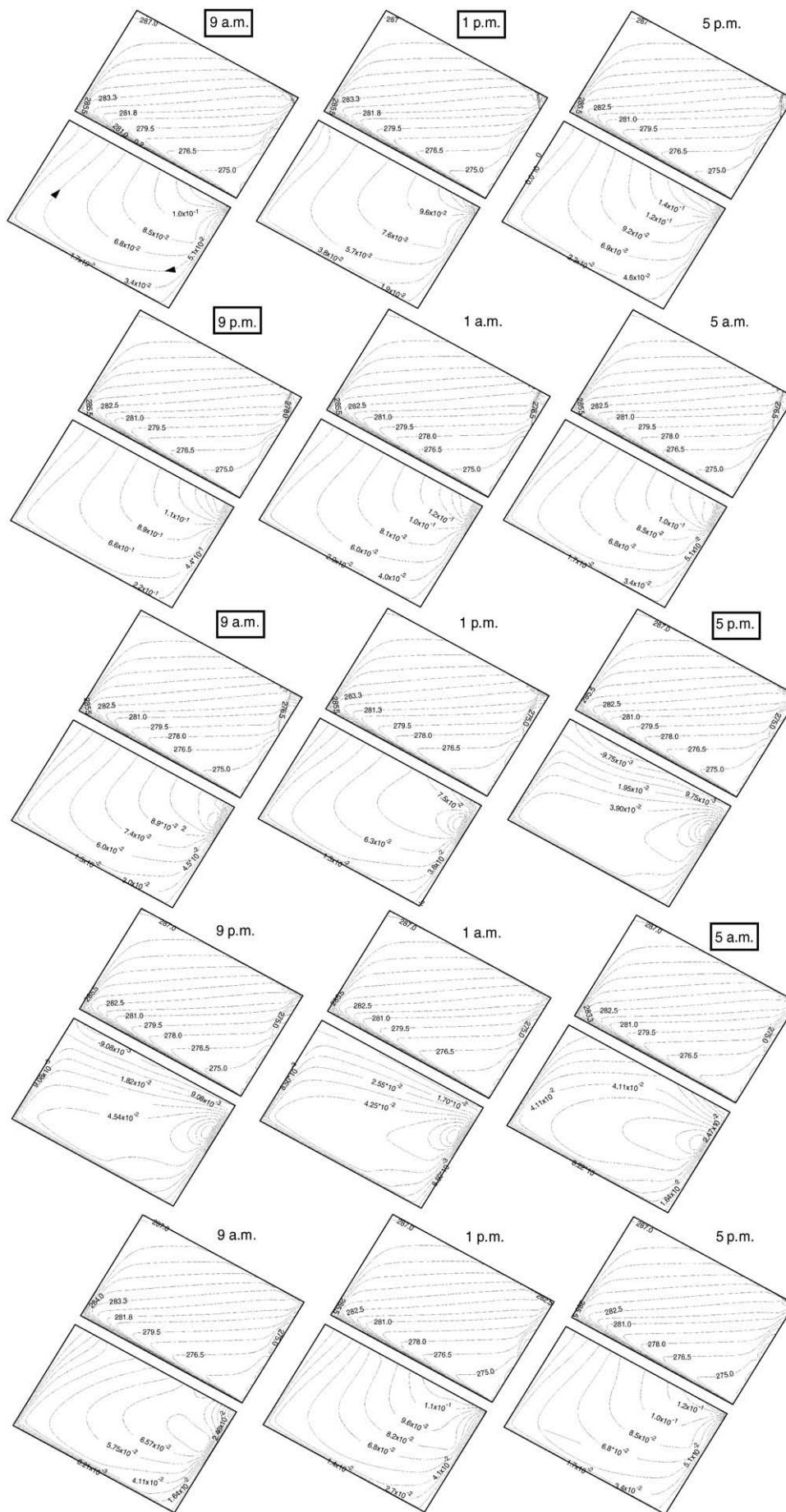
from 286 K at the rim down to 281 K at mid-flanks (Fig. 14). The entrance Darcy velocity at the crater center is about 0.5 mm s^{-1} . Thus, the heat is advected at a velocity ($\gamma u, \gamma w$) equal to about 1 mm h^{-1} because $\gamma = 5 \times 10^{-4}$ (see Eq. (9)). After 1 h, this velocity is small enough for the air temperature to equilibrate with 1 cm grains. The isotherms obtained with an effective Rayleigh number of 20 (not shown here) are strictly parallel to the slope. This confirms that, whatever the Rayleigh number, convection occurs in an inclined layer. However, convection transports sufficient heat in order to deform the isotherms from the conductive solution only when the effective Rayleigh Ra_{eq} is above the critical value for the horizontal case (27.1).

5.5. Air convection with a Rayleigh number of 45 and a surface temperature following the diurnal cycle

Figs. 14b and 15 display the 3 days transient evolution of convection with an equivalent Rayleigh number Ra_{eq} of 45 and a 7.5 K oscillating surface temperature oscillating. The experiment starts with the temperature field obtained from a preliminary run lasting several years, during which the temperature reaches quasi-asymptotic regime, at which the mean heat flux is stabilized. Three striking observations are reported: (1) no steady motion is reached, (2) the fluctuations of the isotherms with time are not compatible with a daily cycle, (3) convection exhibits two different patterns: during some periods, the convective cell is entirely confined within the box; at other periods air enters the box at the crater center and exits it at the rim crest. The cell is confined in the box for ≈ 15 h and opens during about 45 h.

We note the development of a thick thermal convective boundary layer. It develops because of the transient confinement of the air flow. The opening and closing of the convective cell is not compatible with a daily cycle because it depends on the physics of the thermal boundary layer. We note that the convective circulation is much slower and that the lateral gradients of temperature are much less steep than the ones found with a constant surface temperature model (cf. comparison between Fig. 14a and b). Strikingly, the temperature field in the lower half of the box remains steady, while the temperature in the very shallow subsurface below the crater center is alternatively warm and cold. Fig. 16 shows temperature profiles at different times. Then, the crater center displays a temperature difference with that of the rim crest of $\approx 4 \text{ K}$ and 6 K when the box is closed and opened, respectively.

Fig. 17. Isotherms (in K) and stream lines (in $\text{m}^2 \text{ s}^{-1}$) of the convective porous flow over 30 h for a model with an equivalent Rayleigh number Ra_{eq} of 6000 and a fluctuating top temperature. The frames indicate the time of the profiles obtained in Fig. 18.



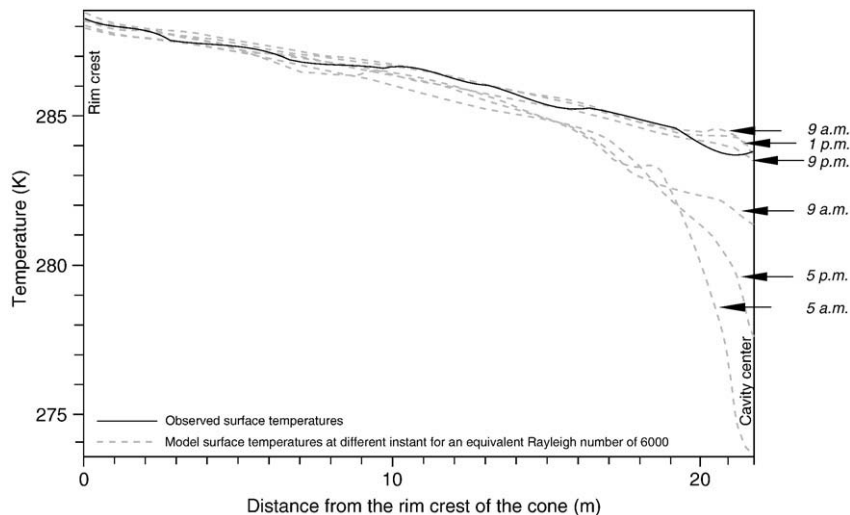


Fig. 18. Surface temperatures of the convective model with an equivalent Rayleigh number $Ra_{eq} = 6000$ at different times (dotted lines). For comparison, the observed surface temperature (plain line) at midnight along the SE crater is displayed (Tr1 transect, see Figs. 5b and 11).

5.5.1. Air convection with a Rayleigh number of 6000 and a surface temperature following the diurnal cycle

Fig. 17 displays a 30 h transient evolution of the convective circulation when Ra_{eq} is 6000. The thermal structure of the flow is very different from that calculated when the Rayleigh is 45 (Fig. 15). In particular, the thermal field is quasi symmetric about a line joining the upper right corner to the lower left corner of the box. It implies that the region along the axis of the crater is particularly cold: its temperature is close to the minimum surface air temperature (273.5 K). The surface temperature in the rim crest region remains roughly constant and close to that of the bottom of the crater ($T_{bottom} = 288.5$ K).

We observe a periodic cold plume developing just below the surface of the crater center. The detachment of each plume occurs about every 30 h. The Darcy velocity of the air below the center reaches about 20 cm s^{-1} . The isotherms are advected at a velocity ($\gamma u, \gamma w$) of about 20 cm s^{-1} . When the detached cold plume reaches approximately the mid-depth of the box, a new one forms at the crater center. At that time, the convective cell is entirely confined inside the cone. The variations of temperature during a daily cycle are small enough that the 20 cm h^{-1} -thermal waves equilibrates with basaltic aggregates of 10 cm (the larger grains at Formica Leo). The calculated surface temperatures at distinct moments, presented in Fig. 17, show a rim to crater center temperature drop up to 13 K. The shape of this profile differs from that of the $Ra_{eq} = 45$ model (Fig. 16).

5.5.2. Fitting calculated surface temperatures at midnight with observed ones

The $Ra_{eq} = 45$ model explains the observed rim crest to crater center temperature drop but not its shape. The temperature profile for the $Ra_{eq} = 6000$ model matches the observed shape, while its amplitude is generally twice as large, except when the cold plume has just detached from the top convective layer (Fig. 18). The shape of the temperature profile is matched for high permeabilities, i.e. in the range 1000–6000. The convection develops progressively and becomes more and more vigorous between $Ra_{eq} = 45$ and $Ra_{eq} = 6000$. This is the reason why we only shown two models at the extremities of permitted Ra_{eq} range. The bottom temperature of the crater T_{bottom} with a soil conductivity of $k = 0.4 \text{ W m}^{-1} \text{ K}^{-1}$ yields a surface conductive heat flux $k\Delta T/H$ of 200 mW m^{-2} . In the model, air convection in the crater enhances the heat transfer by an order of magnitude. Thus, when $Ra_{eq} = 6000$, the heat flux at the surface is $\times 2000 \text{ mW m}^{-2}$, i.e. twice the heat flux estimated in the surrounding regions (Section 3). This disequilibrium cannot be maintained for a long period of time. It is likely that the temperature

at the bottom of the crater T_{bottom} will decrease gradually. If we still assume an effective Rayleigh number of $Ra_{eq} = 6000$, but an equilibrium heat flux of 1000 mW m^{-2} , we can drop by a factor of 2 to $\Delta T = 3.5$ K and increase the permeability by the same factor. This change does not modify γRa , implying that the surface temperature profiles when $\Delta T = 3.5$ K and $K = 2 \times 10^{-5} \text{ m}^2$ would only differ from those of Fig. 18 by the scale of temperature which would be divided by 2. Such a change would yield an excellent fit between computed and observed profiles.

6. Conclusion

Thermal Infrared images obtained during a diurnal cycle of the 250 years-old small inactive scoria cone of Formica Leo (Piton de la Fournaise volcano, Reunion Island) have been studied. Outside the cone, the surface temperature is explained by insolation and soil thermal conductivities. Inside Formica Leo, just before the dawn, the rim crests are warm compared to the crater centers. We demonstrate that air convection within the craters can explain the observed temperature pattern, provided the soil permeability is high ($\sim 10^{-5} \text{ m}^2$, a value consistent with the pluricentimetric scorias composing the cone). Then, the downward interstitial air velocity at the center of the crater is of the order of 50 cm s^{-1} , a value commensurable with the one deduced by the anemometer measurements. The equations describing air convection in the soil are the same than those of water convection, if we multiply the Darcy velocity of air and the Rayleigh number by γ , the ratio of the heat capacity of air to that of the soil (Eq. (10)). With such a permeability, it is important to mention that the Rayleigh number of porous convection for water saturated soil would be extremely elevated (3×10^5). In this case, turbulent flows with very thin boundary layers and small plumes would lead to surface temperatures pattern clearly undetectable at 100 m distance with the IR camera. In the case of air convection, low Rayleigh numbers lead to laminar flows in larger plumes and surface temperature pattern detectable with the IR camera.

The convection of air in Formica Leo is a transient process, as described in our model. Indeed, porous flow within an open-top inclined layer leads to unsteady flow due to the development of hot transient plumes at the bottom boundary layer (Rabinowicz et al., 1999). Here, because of the diurnal temperature fluctuations, the soil surface is alternatively cooler and hotter than the air above the cone. It results that there are moments during which the flow is strictly confined within the cone and phases during which it is opened upward. As a result, a top convective boundary layer develops.

Fluctuations in this boundary leads to the periodic development of cold plumes which sink within each crater center. The strength of the flow dramatically increases during the phase of detachment of this plume. Note that the cyclicity of the plume is completely different from that of the diurnal cycle. The occurrence of these alternating regimes is strongly dependent on permeability. The flow is not confined for periods up to several days at the condition that the permeability is high and actually close to an upper bound of reasonable estimates (10^{-5} m^2). During all these sequences, the lower boundary layer remains steady implying that no transient hot plumes take birth at the vicinity of the massive basalts lower boundary. Our models are bidimensional. It is clear that because of the conic shape of the structure, the axial deeping current will also mark the 3D pattern of convection in Formica Leo. But, a splitting of the upwelling flow along the rim of the cone is likely possible (Caltagirone and Boriès, 1985; Ormond et al., 1995). It is not clearly seen on the IR images (Fig. 5), indicating that the dominant mode of air convection is circular along the rims. Therefore, future studies of the thermal field of Formica Leo based on temperature probes measurement and electromagnetic data will provide complementary information of the tridimensional structure of the flow along the rim.

Our study constitutes the first demonstration that air convection can transport significant amount of heat within PdF volcano. Indeed, the volcanic edifice is composed by many highly permeable materials (e.g., fractures, scorias layers, buried scoria cones, lava tubes, etc...). IR images acquired at Bory Dolomieu crater (in particular, at fractured zones) in 2007 and 2008 also suggest that these regions are affected by air convection. Bory Dolomieu crater, where most eruptions initiated, presents a conic permeable structure with 30° slopes which rims are clearly warmer at night than the center of the crater. We believe that the understanding of the relationships between the ascent of the magma and the convection of air would make in the future a significant contribution for the prediction of volcanic hazards.

Acknowledgements

This study benefited from a grant INSU-CNRS ‘Programme Catastrophes naturelles et tsunamis 2006’ VOLCARISK. The Ph.D. thesis of Raphael Antoine was supported by Region Reunion. We thank Dr. William Wilcock and Dr. Lionel Wilson for constructive reviews that helped improve the clarity of the paper.

Appendix A. Modelling diurnal temperature variations assuming a flat surface: the conductive–radiative model

The transient temperature in the soil, $T(z, t)$ is solution of the equation:

$$\frac{\partial T(z, t)}{\partial t} = \kappa \frac{\partial^2 T(z, t)}{\partial z^2} \quad (.1)$$

where z is the depth, t is the time and κ is the thermal diffusivity of the soil, which is related to the thermal conductivity k , the heat capacity C_p and the mass density ρ of the soil through:

$$\kappa = \frac{k}{\rho h_s} \quad (.2)$$

A zero heat flux condition is set at the lower boundary of the model. For a flat surface, the surface temperature during a diurnal cycle depends on the solar heat flux (I_s), the soil radiative emission (I_e), and the atmospheric radiative flux (I_l). Thus, the boundary condition at the surface is given from the balance of solar, atmospheric and emitted radiations (Watson, 1973):

$$k \frac{\partial T(z=0, t)}{\partial t} = I_s - I_e + I_l \quad (.3)$$

The solar flux I_s absorbed by the surface verifies:

$$I_s = (1 - A)S_0 C \cos(Z) \quad (.4)$$

where A is the surface albedo and S_0 is the solar constant. C is fraction of the incident power arriving at the soil including the direct sun light and the diffuse radiations for a cloudy sky. Z is the zenith angle of the sun which can be estimated from the latitude ϕ of the observation point (Watson, 1973):

$$\cos(Z) = \cos \phi \cos \delta \cos(\theta) + \sin \phi \sin \delta \quad (.5)$$

where δ is the solar declination as a function of the number of day in Jovian year J (Deffie and Beckman, 1980) and is expressed here in radian:

$$\delta = 0.409 \sin\left(\frac{2\pi}{365}J - 1.39\right) \quad (.6)$$

The longitude angle θ expressed also in radian corresponds to the time t in hours past noon:

$$\theta = 2\pi \frac{t}{24} \quad (.7)$$

Then, the thermal emitted flux from the surface I_e is given by:

$$I_e = \epsilon \sigma T^4 \quad (.8)$$

where ϵ is the soil emissivity averaged in the thermal infrared wavelengths and $\sigma = 5.67 \times 10^{-8} \text{ JK}^{-4} \text{ m}^{-2} \text{ s}^{-1}$ is the Stefan–Boltzman constant. The thermal radiations from the atmosphere I_l are approximated following the empirical relation (Brunt, 1932):

$$I_l = \sigma T_a^4 (0.55 + 0.65 \sqrt{e_a}) \quad (.9)$$

where T_a is the air temperature in Celsius degrees and e_a is the saturation pressure of water in the air expressed in bar. $T_a(t)$ is approximated by Jansson (1998):

$$T_a(t) = T_0 + \frac{1}{2} T_{\text{amp}} \cos\left(\frac{2\pi(t - t_{\text{ph}})}{P_{\text{dc}}}\right) \quad (.10)$$

where T_0 is the mean air temperature during the diurnal cycle, and T_{amp} is the contrast of temperature between day and night as measured during the experiment. P_{dc} represents the duration of the diurnal cycle and t_{ph} is the time shift between the maximum of the solar incident radiations and the maximum air temperature. This model results in a minimum air temperature at the sunrise and a maximum air temperature at t_{ph} after the zenith. Finally, e_a verifies the empirical law (Deffie and Beckman, 1980):

$$e_a = 0.6108 \exp\left(\frac{17.27 T_a(t)}{T_a(t) + 237.3}\right) \quad (.11)$$

References

- Baytas, A.C., Pop, I., 1999. Free convection in oblique enclosure filled with a porous medium. *Int. J. Heat Mass Transfer* 42, 1047–1057.
- Bonneville, A., Vasseur, G., Kerr, Y., 1985. Satellite thermal infrared observations of Mt. Etna after the 17th March 1981 eruption. *J. Volcanol. Geotherm. Res.* 24 (3–4), 293–313.
- Boriès, S.A., Combarous, M.A., 1972. Natural convection in a sloping porous layer. *J. Fluid Mech.* 57, 63–79.
- Brivio, P.A., Lo Guidice, E., Zilioli, E., 1989. Thermal infrared Surveys at vulcano Island: An experimental Approach to the thermal monitoring of volcanoes, in *Volcanic Hazard*, edited by Springer–Verlag, pp. 357–371, IAVCEI Proceedings in volcanology, J.H. Latter ed., Berlin, 1989.

- Brunt, D., 1932. Notes on radiation in the atmosphere. *Quart. J. Roy. Meteorol. Soc.* 58, 389–420.
- Caltagirone, J.P., Boriès, S.A., 1985. Solution and stability criteria of natural convective flow in an inclined layer. *J. Fluid Mech.* 155, 267–287.
- Carman, P.C., 1961. L'écoulement des gaz à travers les milieux poreux, Bibliothèque des Sciences et des techniques nucléaires. Press Universitaires de France, Paris. 198 pp.
- Cherkaoui, A.S.M., Wilcock, W.S.D., 1999. Characteristics of high Rayleigh number two-dimensional convection in an open-top porous layer heated from below. *J. Fluid Mech.* 394, 241–260.
- Chevalier, S., Bernard, D., Joly, N., 1998. Natural convection in a porous layer bounded by impervious domains: from numerical approaches to experimental realization. *Int. J. Heat Mass Transfer* 42, 581–597.
- Chongbin, Zhao, Hobbs, B.E., Ord, A., Shenglin, Peng, Mühlhaus, H.B., Liangming, Liu, 2004. Theoretical investigation of convective instability in inclined and fluid-saturated three-dimensional fault zones. *Tectonophysics* 387, 47–64.
- Christensen, P.R., Bandfield, J.L., Hamilton, V.E., Howard, D.A., Lane, M.D., Piatek, J.L., Ruff, S.W., Stefanov, W.L., 2000. A thermal emission spectral library of rock-forming minerals. *J. Geophys. Res.* 105 (E4), 9735–9739.
- Coret, L., Briottet, X., Kerr, Y.H., Chehbouni, A., 2004. Simulation study of view angle effects on thermal infrared measurements over heterogeneous surface. *IEEE Trans. Geosci. Remote Sens.* 42 (n°3), 664–672.
- Deffie, J.A., Beckman, W.A., 1980. *Solar Engineering of Thermal Processes*. John Wiley and sons, New York, pp. 1–109.
- Douglas, J., Rachford, G., 1956. On the numerical solution of heat solution problems in two and three variables. *Trans. Am. Math. Soc.* 82, 421–439.
- Fontaine, F., Rabinowicz, M., Boulègue, J., Jouniaux, L., 2002. Constraints on hydrothermal processes on basaltic edifices: inferences on the conditions leading to hydrovolcanic eruptions at Piton de la Fournaise, Reunion Island, Indian Ocean. *Earth Planet. Sci. Lett.* 200 (1–2), 1–14.
- Jansson, P.-E., 1998. Simulation Model for soil water and heat conduction – Description of soil model, PhD thesis, Swedish University of Agricultural Sciences, Uppsala.
- Kurita, K., et al., 2007. Thermal imaging of volcanic areas and implications for the interpretation of surface temperatures on mars. Seventh International Conference on Mars. Pasadena, California, USA. 3113 pp.
- Lardy, M., Tabbagh, A., 1999. Measuring and interpreting heat fluxes from shallow volcanic bodies using vertical temperature profiles: a preliminary test. *Bull. Volcanol.* 60 (6), 441–447.
- Myers, V.J., Heilman, M.D., 1969. Thermal infrared for soil temperature studies. *Photogrammetr. Ing. J.* 35, 1024–1032.
- Ormond, A., Boulgue, J., Genthon, P., 1995. A thermoconvective interpretation of heat flow data in the area of Ocean Drilling Program Leg 116 in a distal part of the Bengal Fan. *J. Geophys. Res.* 100 (B5), 8083–8095.
- Rabinowicz, M., Rouzo, S., Sempere, J.-C., Rosemberg, C., 1993. Three-dimensional mantle flow beneath mid-ocean ridges. *J. Geophys. Res.* 98 (B5), 7851–7869.
- Rabinowicz, M., Boulègue, J., Genthon, P., 1998. Two- and three-dimensionnal modeling of hydrothermal convection in the sedimented Middle Valley segment, Juan de Fuca ridge. *J. Geophys. Res.* 103 (B10), 24045–24065.
- Rabinowicz, M., Sempéré, J.C., Genthon, P., 1999. Thermal convection in a vertical slot: implications for hydrothermal circulation along mid-ocean ridges. *J. Geophys. Res.* 104 (B12), 275–292.
- Rose, A.W., Guo, W., 1995. Thermal convection of soil air on hillsides. *Environ. Geol.* 25 (4), 258–262. doi:10.1007/BF00766755.
- Rosenberg, N.J., Spera, F.J., Haymon, R.M., 1993. The relationship between flow and permeability field in seafloor hydrothermal systems. *Earth Planet. Res. Lett.* 116, 135–153.
- Rowan, L.C., Offield, T.W., Watson, K., Cannon, J.P., Watson, R.D., 1970. Thermal infrared investigations, Arbuckle mountains, Oklahoma. *Geol. Soc. Amer. Bull.* 81, 3549–3562.
- Sabins, F.F., 1969. Thermal infrared imagery and its application to structural mapping in southern California. *Geol. Soc. Amer. Bull.* 80, 397–404.
- Sturm, M., 1991. The role of thermal convection in heat and mass transport in the subarctic snow cover. *USACRREL Report* 91–19, 84 p.
- Sturm, M., Johnson, J.B., 1991. Natural convection in the subarctic snow cover. *J. Geophys. Res.* 96 (11), 657–671.
- Turcotte, D.L., Schubert, G., 2002. *Geodynamics*. Cambridge University Press. 456 pp.
- Watson, K., 1973. Periodic heating of a layer over a semi-infinite solid. *J. Geophys. Res.* 78 (26), 5904–5910.
- Watson, K., 1975. Geologic applications of thermal infrared Images. *Proc. IEEE* 63, 128–137.
- Whiteman, C.D., Allwine, J., Fritschen, L.J., Orgill, M.M., Simpson, J.R., 1989. Deep valley radiation and surface energy budget microclimates, Part I: Radiation. *J. Appl. Meteorol.* 28, 414–426.
- Whiteman, C.D., Zhong, S., Bian, X., Fast, J.C., Doran, J.C., 2000. Boundary layer evolution and regional-scale diurnal circulations over the Mexico Basin and Mexican plateau. *J. Geophys. Res.* 105 (D8), 10081–10102.
- Wood, J.R., Hewett, T.A., 1982. Fluid convection and mass transfer in porous sandstones – a theoretical model. *Geochim. Cosmochim. Acta* 46, 1707–1713.
- Woodside, W., Messmer, J.H., 1961. Thermal conductivity of porous media: I Unconsolidated sand. *J. Appl. Phys.* 32, 1688–1691.
- Yu, W., Lai, Y., Zhang, X., Niu, F., 2005. Experimental study on the ventiduct embankment in permafrost regions of the Qinghai–Tibet railroad. *J. Cold Reg. Eng.* 19 (2), 52–60. doi:10.1061/(ASCE)0887-381X(2005)19:2(52).
- Zhang, M., Zhang, J., Yuanming, L., 2005. Numerical analysis for critical height of railway embankment in permafrost regions of Qinghai–Tibetan plateau. *Cold Reg. Sci. Technol.* 41 (2), 111–120.

5.2 Subsurface Hydrology of the Lake Chad Basin from Convection Modelling and Observations (Survey in Geophysics)

Subsurface Hydrology of the Lake Chad Basin from Convection Modelling and Observations

T. Lopez¹ · R. Antoine² · Y. Kerr¹ · J. Darrozes³ ·
M. Rabinowicz³ · G. Ramillien⁴ · A. Cazenave^{4,5} ·
P. Genthon⁶

Received: 23 March 2015 / Accepted: 20 January 2016
© Springer Science+Business Media Dordrecht 2016

Abstract In the Lake Chad basin, the quaternary phreatic aquifer (named hereafter QPA) presents large piezometric anomalies referred to as domes and depressions whose depths are ~15 and ~60 m, respectively. A previous study (Leblanc et al. in *Geophys Res Lett*, 2003, doi:10.1029/2003GL018094) noticed that brightness temperatures from METEOSAT infrared images of the Lake Chad basin are correlated with the QPA piezometry. Indeed, at the same latitude, domes are ~4–5 K warmer than the depressions. Leblanc et al. (*Geophys Res Lett*, 2003, doi:10.1029/2003GL018094) suggested that such a thermal behaviour results from an evapotranspiration excess above the piezometric depressions, an interpretation implicitly assuming that the QPA is separated from the other aquifers by the clay-rich Pliocene formation. Based on satellite visible images, here we find evidence of giant polygons, an observation that suggests instead a local vertical connectivity between the different aquifers. We developed a numerical water convective model giving an

✉ T. Lopez
teodolina.lopez@cesbio.cnes.fr

¹ Centre d'Etudes Spatiales de la Biosphère, Unité mixte de Recherche Université Toulouse 3, Centre National d'Etudes Spatiales, Centre National de la Recherche Scientifique, Institut de Recherche pour le Développement, 31400 Toulouse, France

² Centre d'Etudes et d'Expertise sur les Risques, l'Environnement, la Mobilité et l'Aménagement, Laboratoire Régional de Rouen, Groupe Sciences de la Terre, CS 90245, 76121 Le Grand Quevilly, France

³ Géosciences Environnement Toulouse, Unité mixte de Recherche Université Toulouse 3, Centre National d'Etudes Spatiales, Centre National de la Recherche Scientifique, Institut de Recherche pour le Développement, 31400 Toulouse, France

⁴ Laboratoire d'Etudes en Géophysique et Océanographie Spatiales, Unité mixte de Recherche Université Toulouse 3, Centre National d'Etudes Spatiales, Centre National de la Recherche Scientifique, Institut de Recherche pour le Développement, 31400 Toulouse, France

⁵ International Space Science Institute (ISSI), Bern, Switzerland

⁶ Laboratoire Hydrosociétés Montpellier, Unité mixte de Recherche Université Montpellier, Institut de Recherche pour le Développement, Centre National de la Recherche Scientifique, 34000 Montpellier, France

alternative explanation for the development of QPA depressions and domes. Beneath the depressions, a cold descending water convective current sucks down the overlying QPA, while, beneath the dome, a warm ascending current produces overpressure. Such a basin-wide circulation is consistent with the water geochemistry. We further propose that the thermal diurnal and evaporation/condensation cycles specific to the water ascending current explain why domes are warmer. We finally discuss the possible influence of the inferred convective circulation on the transient variations of the QPA reported from observations of piezometric levels and GRACE-based water mass change over the region.

Keywords Lake Chad · Piezometric anomalies · Vertical permeability · Infrared data · Convection · GRACE

1 Introduction

Water resource management in the Sahel regions of Africa is of prime importance. In countries such as Mali, Niger, Chad and Sudan to name just a few, water resources essentially come from groundwater reservoirs that are either weakly or even non-renewable (OSS-UNESCO 2001). In order to improve their sustainability over the medium and long term, it is important to understand their dynamics. A direct indicator of phreatic water dynamics is the variation of their piezometric level (i.e. surface level) forming piezometric anomalies. Piezometric anomalies have been reported in the phreatic aquifers of Trarza in Mauritania; Ferlo in Senegal; Gondo, Nara and Azaouad in Mali and Yaere in North Cameroon (e.g., Archambault 1960; Aranyossy and Ndiaye 1993). In the Lake Chad basin, the quaternary phreatic aquifer (named hereafter QPA) presents large piezometric anomalies extending over a few tens of km, forming domes and depressions at the piezometric surface. Their mean depth is ~ 10 and ~ 60 m, respectively (Schneider and Wolff 1992).

Various assumptions have been proposed to explain the origin of the piezometric depressions, e.g., groundwater overexploitation, water drainage into a deeper aquifer, geological subsidence, changes in sea level and evapotranspiration loss (Dieng et al. 1990; Aranyossy and Ndiaye 1993). The latter factor was favoured because it explains observed piezometric depressions, and the associated water deficit generated by evapotranspiration that is not compensated by lateral groundwater flow. Therefore, it became the most accepted explanation. METEOSAT images of the Lake Chad basin reveal that brightness temperatures and piezometric anomalies are correlated (Leblanc et al. 2003). These authors observed that domes are $\sim 4\text{--}5$ K warmer than the depressions during wet years, suggesting that, above piezometric depressions, evapotranspiration is dominant during the temperature diurnal cycle and leads to surface cooling.

In sedimentary basins, it has been shown that, at regional scales, convective groundwater flows are usually governed by surface topography and geothermal gradients of the sediment infill (e.g., Garven 1995). In numerous cases, weakly compacted clay formations deposited in the upper part of basins may prevent interactions between superficial and deep groundwater. However, vertical permeability can be generated in weakly compacted clay formations by the development of large-scale polygonal fault systems (e.g., Cartwright and Dewhurst 1998; Neal et al. 1968).

Building on these different observations, here we suggest that evapotranspiration is coupled to the water convective circulation, explaining both the piezometric anomalies' formation and their correlation with observed surface temperature. We first describe the geological and hydrogeological setting of the Lake Chad basin. We next discuss the permeability field of the basin, taking into account potential compaction of the clay formations at depth (Sect. 3). In Sect. 4, we develop a 2D convective model simulating large-scale flow within the whole sedimentary basin. Finally, we investigate whether the modelled convective flow can explain observed bottom hole temperatures (BHT), hydro-chemical data, and GRACE-based space gravity data of water storage changes.

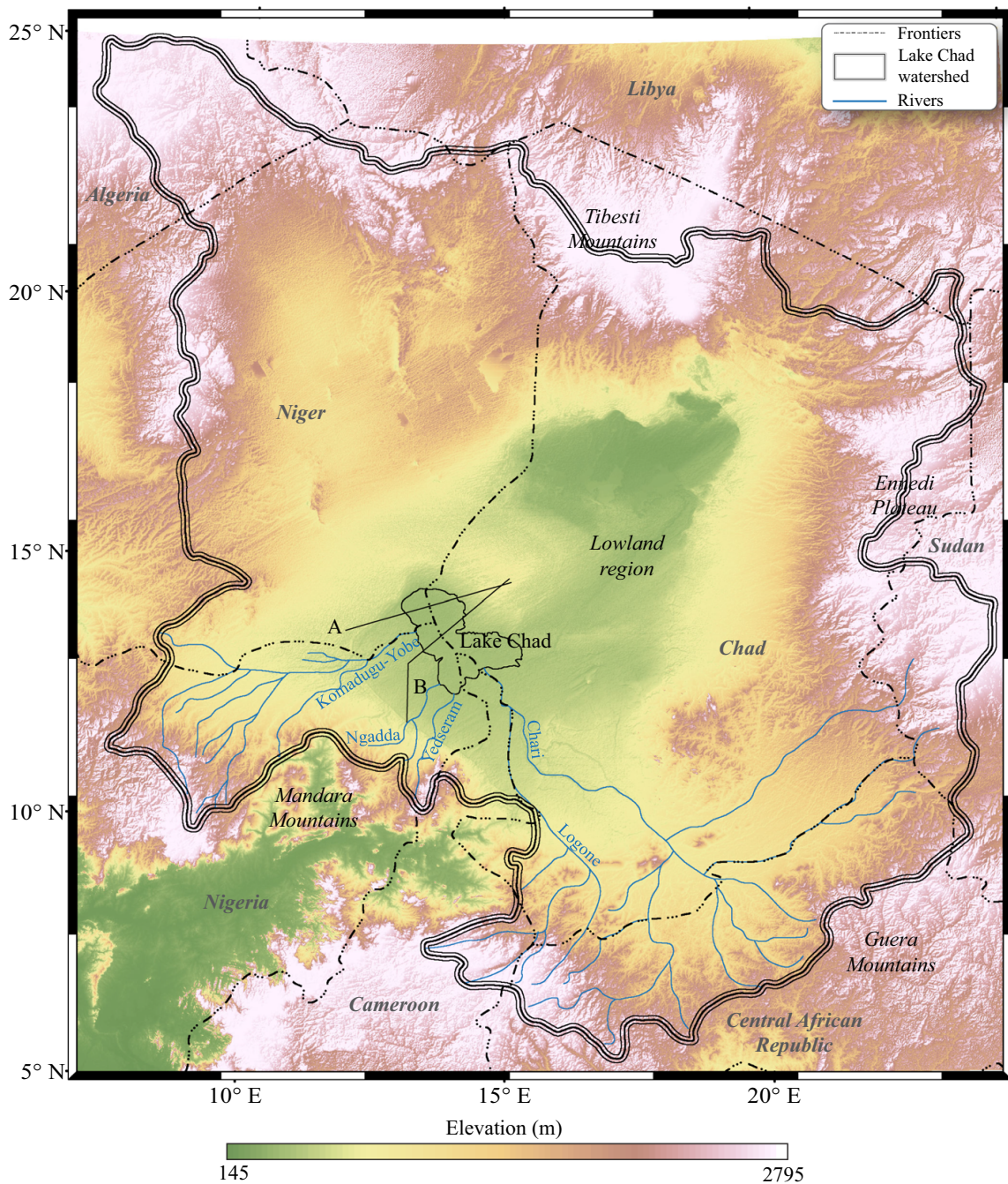


Fig. 1 Shuttle radar topography mission (SRTM) topographic map of the Lake Chad watershed, showing its extension, its tributary rivers, the main mountains and the Lowland region. *Black lines A and B* represent the geological cross sections drawn in Fig. 3

2 Description of the Lake Chad Basin

2.1 Hydrology of Lake Chad

The Lake Chad watershed extends from 5°N–25.6°N to 7°E–27°E, covering 2,500,000 km² over seven countries (Algeria, Cameroon, Central African Republic, Chad, Niger, Nigeria and Sudan; Fig. 1). The central part of the basin is flat, while its surroundings consist of mountain ranges, i.e. Tibesti Mountains, Ennedi Plateau, Guera Mountains and Mandara Mountains (Fig. 1). Without any direct outlet to the sea, it is the largest endorheic watershed of the world. During the Holocene, Lake Chad extended over an area of ~350,000 km² (Schuster et al. 2005; Leblanc et al. 2006) but, since the early 1980s, its size decreased to only ~2500 km² (Cretaux and Birkett 2006; Bader et al. 2011). It is now named “Small Lake Chad” (Bader et al. 2011). The current hydrological active part of the lake is concentrated in its southern part. It is fed by the Chari and Logone perennial rivers as well as the seasonal Yedseram and Ngadda rivers. In the northern part, surface waters are essentially seasonal (e.g., the Komadugu-Yobe) (Fig. 1). The average rainfall above Lake Chad ranges from 200 to 400 mm year⁻¹, and potential evapotranspiration is on the order of 2 m year⁻¹ (e.g., Bader et al. 2011; Descloitres et al. 2013). Discharges from the Chari and Logone rivers represent ~91 % of the fresh water supplies, while seasonal rivers bring only relatively small inputs (Roche 1980). Rainfall represents only ~10 % of the total water supply. Water loss over the lake mainly results from evapotranspiration (between 80 and 90 %) and infiltration through the lake bottom (~10 %) (Roche 1980; Olivry et al. 1996; Bader et al. 2011).

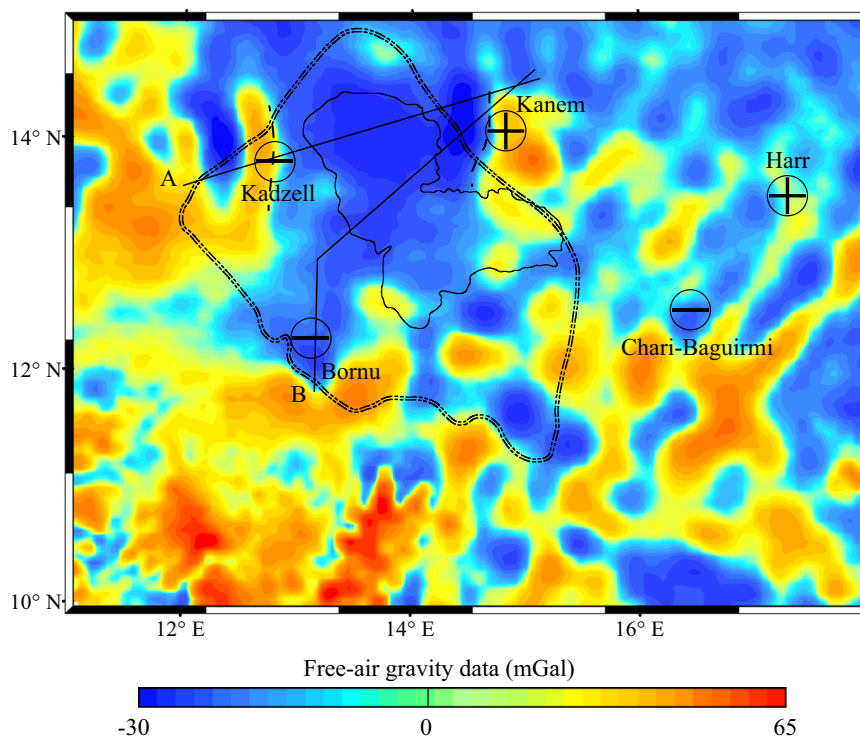


Fig. 2 Free-air gravity map obtained from the world gravity map (WGM) of 2012. *Dashed lines* locate the presence of faults delimiting the basin. *Double dashed lines* represent the artesian limit of the Pliocene aquifer. Piezometric domes and depressions are located by the *plus* and *minus* symbols. *Black lines A and B* represent the geological cross sections drawn in Fig. 3

2.2 Geology of the Chad Basin

The Chad basin is considered as the largest intra-cratonic basin belonging to the east and central African rift system (Genik 1993; Olugbemiro and Ligouis 1999). These rifts were active from the Cretaceous to the early Palaeogene and then reactivated during the early to mid-Tertiary (Genik 1993; Griffin 2006). The free-air gravity map (Fig. 2), based on the Earth Gravitational Model EGM2012 (Balmino et al. 2011), displays gravity anomalies ranging between ~ -30 to ~ 65 mGal. Negative gravity anomalies correspond to thick sediment infill (i.e. sediment density being lower than the basement density), while positive anomalies are linked to the shallow depth basement. A large area of nearly constant gravity (e.g., the Bornu region) can be interpreted as a zone of homogeneous sediment thickness. Gravity dipoles seen in Fig. 2 (dashed lines) correspond to normal faults delimiting the Kadzell and Kanem regions (Avbovbo et al. 1986). Between the two regions, the sediment thickness increases towards the Kanem region while gravity decreases from ~ -2 to ~ -30 mGal. The SW–NE geological cross section through the Kadzell to the Kanem regions (Fig. 3a) indicates that the sediment infill is fan-shaped and oriented eastward.

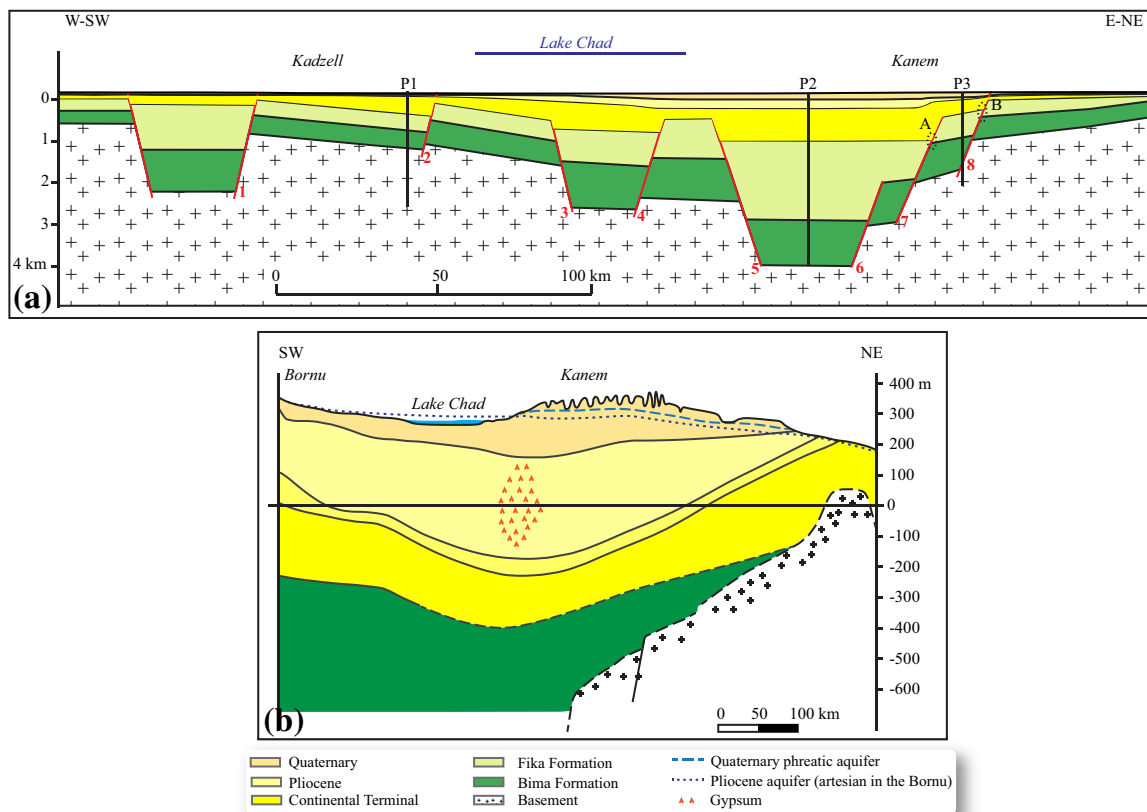


Fig. 3 **a** Geological cross section between Kadzell and Kanem (modified from Pouclet and Durand 1983). The deposits consist of inter-bedded clay formations (Fika formation and Pliocene formation) with sandy deposits as the Quaternary formation, the Continental Terminal formation and the Bima formation. The Early Pliocene formation is integrated in the Pliocene formation. *Red lines* highlight the faults of the basin. The Lake Chad basin is controlled by an extensional tectonic of horsts (2–3 and 4–5) and grabens (1, 3–4, 5–6). *Dashed ellipses* highlight the stratigraphic throws of faults 7 and 8 that impact the Fika formation. *Vertical black lines* highlight the location of temperature profiles P1, P2, P3 displayed in Fig. 10. **b** Geological cross section of the upper part of the sedimentary infill, between Bornu and Kanem (modified from Schneider and Wolff 1992). The Early Pliocene formation has been distinguished from the Pliocene one

As indicated by the gravity map (Fig. 2), sediment thickness ranges from ~ 850 m under Kadzell to ~ 4000 m under Kanem. The stratigraphic sequence starts with the deposition of the Bima formation (Albian to Cenomanian) that consists of inter-bedded continental shales and sandstones. Its thickness is ~ 400 and ~ 1000 m below Kadzell and Kanem, respectively (e.g., Pouclet and Durand 1983; Avbovbo et al. 1986; Olugbemiro and Ligouis 1999). Then a shallow marine deposit (inter-bedded with some limestone), called Fika formation, settles from the Turonian to Santonian. Its thickness can reach up to 2 km in the deepest part of the basin (Pouclet and Durand 1983). It is followed by a sedimentation gap associated with an erosion episode that ends at the end of the Eocene–Oligocene (Pouclet and Durand 1983; Griffin 2006). The sedimentation starts again possibly during the Oligocene until the late Miocene, corresponding to the Bodele series that consist of mixed mudstone and sandstone over a thickness of ~ 100 m (referred to hereafter as the Continental Terminal formation) (Schneider and Wolff 1992). During the Pliocene, deposits dated from the early Pliocene (referred hereafter as the Early Pliocene formation) consist of fluvial sands of 10–40 m thickness (Maduabuchi et al. 2006). These are overlaid by lacustrine clays with a thickness that can reach ~ 300 m (referred to hereafter as the Pliocene formation) (Schneider and Wolff 1992; Griffin 2006; Schroeter and Gear 1973). The stratigraphic sequence ends with the Quaternary formation, essentially composed of aeolian sand and fluvio-deltaic deposits (Griffin 2006). Its thickness varies from ~ 15 m under Kadzell to ~ 100 m under Kanem.

The eastern border of the rift is characterised by a succession of normal faults (7 and 8 on Fig. 3a) shifting the Bima formation base from 2 to 1 km in depth and the Fika formation base from 1 km to ~ 500 m. *Ellipses A and B* in Fig. 3a highlight the throws generated by faults 7 and 8 at the base of the Fika formation. For example, at circle B, the throw associated with the fault 8 is ~ 150 m. A detailed geological cross section of the upper part of the sediment infill from Bornu to Kanem (Schneider and Wolff 1992) is

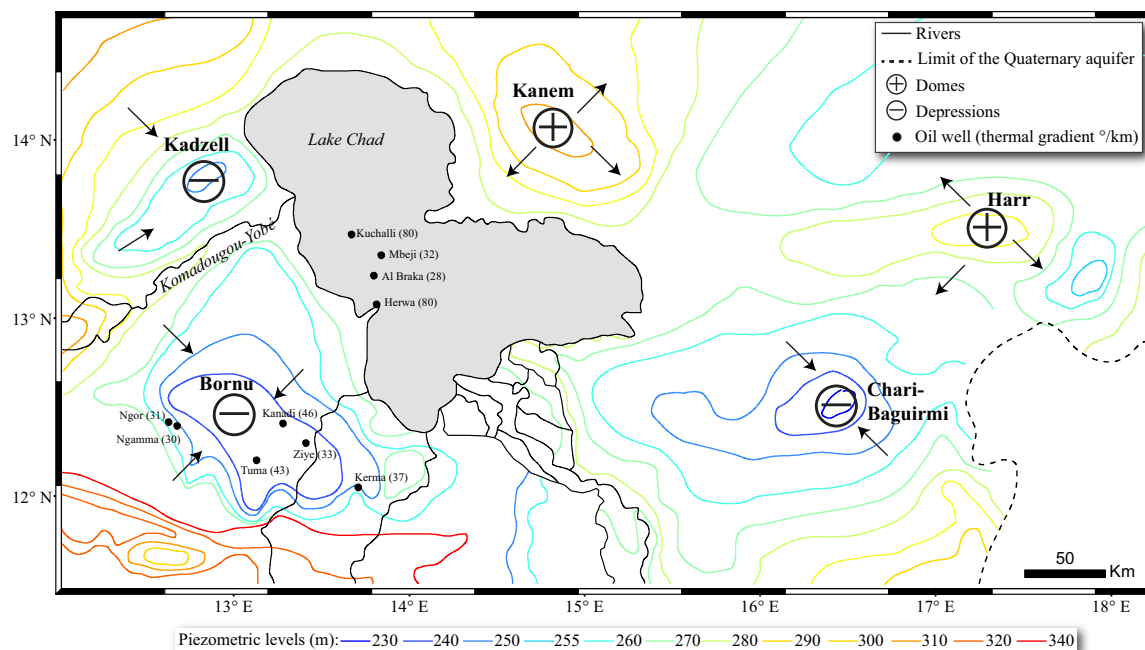


Fig. 4 Piezometric map of the quaternary phreatic aquifer (QPA) around Lake Chad. Piezometric domes and depressions are located by the *plus* and *minus* symbols. Arrows highlight the flow directions in the QPA (modified from Schneider 1969). Black dots represent oil well locations from Nwankwo and Ekine (2010) with their thermal gradients for the first ~ 300 m depth

displayed in Fig. 3b. Below Bornu, the thickness of the Pliocene and Quaternary formations is ~ 230 and ~ 70 m, respectively. Below Kanem, because of basin subsidence (Schneider and Wolff 1992), the maximum thickness of the Pliocene and Quaternary formations is 300 and 140 m, respectively.

2.3 Hydrogeology of the Basin

The basin comprises three main aquifers. Most of the human water use comes from the QPA. This phreatic aquifer has a continuous water table in the Quaternary formation, providing an extensive reservoir covering an area of about 500,000 km² (Eberschweiler 1993; Schroeter and Gear 1973). Hydraulic conductivity measurements indicate that this layer has a hydraulic conductivity from 1 to 100 m day⁻¹ (Schneider and Wolff 1992; Guideal et al. 2011; Descloitres et al. 2013). These values correspond to permeabilities ranging from 10^{-12} to 10^{-10} m². Piezometric anomalies in this aquifer have been reported by Schneider (1969) as well as by Schroeter and Gear (1973). Piezometric domes have been described in the dune field of Kanem and Harr (Fig. 4), east of Lake Chad. The Kanem dome covers approximately 17,000 km², and the highest piezometric level stands at an altitude of 310 m a.s.l. (i.e. at a depth of ~ 10 m below ground). In Harr, the dome area covers about 5500 km² and has an altitude of 290 m. In the western part of the QPA, three deep piezometric depressions affect the water table. The Kadzell depression area is ~ 4400 km², and its deepest piezometric level stands at 250 m (corresponding to a depth of ~ 50 m below ground). The deepest depression develops in Bornu and covers about 16,500 km². The water table falls at 240 m (i.e. at a depth of ~ 60 m below ground). The largest piezometric depression is the Chari-Barguimi, located at the south of the lake. It covers a surface area of 17,500 km², and its water table stands at an altitude of 230 m (i.e. at ~ 40 m below ground). The QPA flows from the domes towards Lake Chad and the depressions (Fig. 4). Moreover, the flow is oriented from the lake towards the depressions (e.g., Greigert 1979; Isiorho et al. 1996; Leduc 1991).

Piezometric contours superimposed on the gravity map reveal that piezometric domes and depressions are located on or nearby normal faults limiting the basin (Fig. 2). The Pliocene aquifer is confined in the Early Pliocene formation. It is of artesian type over the whole basin, except in the central and eastern part of Kanem (Figs. 2, 3b) where the water level stands a few tens of metres below the surface (Schneider and Wolff 1992) and flows from the south towards the northeast. The Continental Terminal aquifer is confined in the Continental Terminal formation. Its thickness ranges from 100 to 200 m (Eberschweiler 1993). Below Kanem, the Pliocene aquifer and the Continental Terminal merge to form a single aquifer with a thickness exceeding 275 m (Schneider and Wolff 1992; Eberschweiler 1993). During oil drilling, a deep aquifer called Continental Hammadian (~ 4 km deep) was discovered in the Bima formation (Schroeter and Gear 1973). However, very little is known so far about this aquifer.

2.4 Potential Permeability Field of the Basin

Fluid migration in clay-rich formations is extremely slow because of their small permeability ($\leq 10^{-15}$ m², e.g., Schwinka and Moertel 1999). In submarine sedimentary deposits, fractures intersecting in plan view to form polygonal patterns have been described in fine-grained sediments (e.g., Cartwright and Dewhurst 1998) and are referred as giant polygonal faults. Besides, in some oceanic basins, a regional slope of $\leq 1^\circ$ may have a major impact on the development of giant polygons (Gay et al. 2004).

In the Lake Chad basin, the Bornu and Kadzell piezometric depressions and the Kanem dome are systematically located near to major slope breaks (Fig. 5). In the Bornu region, we discovered with satellite visible images many lineaments (Fig. 6a, b) that may be reminiscent of the giant polygons described by Gay et al. (2004). The surface topography near the slope breaks is close to 1° , a value sufficient to generate fractures in clay-rich sediment of the Pliocene formation (Gay et al. 2004). An important concentration of trees along these lineaments is observed, suggesting local access of the vegetation to the deep QPA water table. In the Kadzell region, no such giant polygonal structures are observed. However, the presence of meanders or palaeo-meanders (Fig. 6c) along the Komadugu-Yobe River (or other palaeo-rivers) is indicative of coarse deposits, locally providing a good vertical permeability down to the Continental Terminal formation (Descloitres et al. 2013). Finally, we find no surface evidence of giant polygons in Kanem, presumably a result of the thick sandy Quaternary formation. The relatively weak artesianism of the Pliocene aquifer below Kanem may indicate that the ~ 300 m Pliocene formation is fractured. Consequently, we suggest that water exchanges indeed exist between the Quaternary and Continental Terminal aquifers on both sides of the basin.

Except in the central part of the basin, the compaction is weak as the depth of the basin is ~ 1.5 km (Sclater and Christie 1980). Consequently, clay-rich Pliocene and Fika formations (blocks delimited by faults 1–2–3–7–8) may be overpressured (Fig. 3a) (the artesian nature of the Pliocene aquifer can be evidence of the overpressure of the Pliocene formation). At the centre of the graben, delimited by faults 5 and 6, the Fika formation lies between 1 and 3 km depth. At such depth, clays with initial fluid concentration of 60 % per volume lose up to 40 % of their volume by compaction (Sclater and Christie 1980). Such water loss induces a ~ 800 m vertical shortening. With an initial density of 1600 kg m^{-3} for the 60 % water-rich clay, this water loss may increase the clay density up to

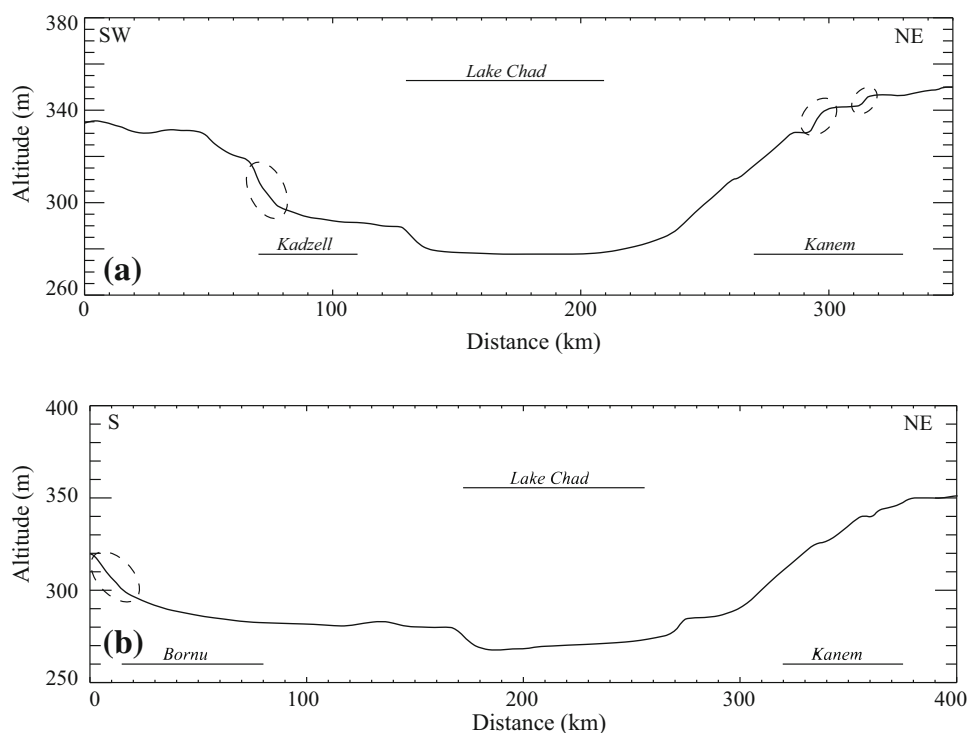


Fig. 5 Advanced spaceborne thermal emission and reflection radiometer (ASTER) topographic profiles **a** from Kadzell to Kanem and **b** from Bornu to Kanem. *Dashed ellipses* surround slope breaks located above or close to the piezometric anomalies; their extensions are represented by the *black lines*

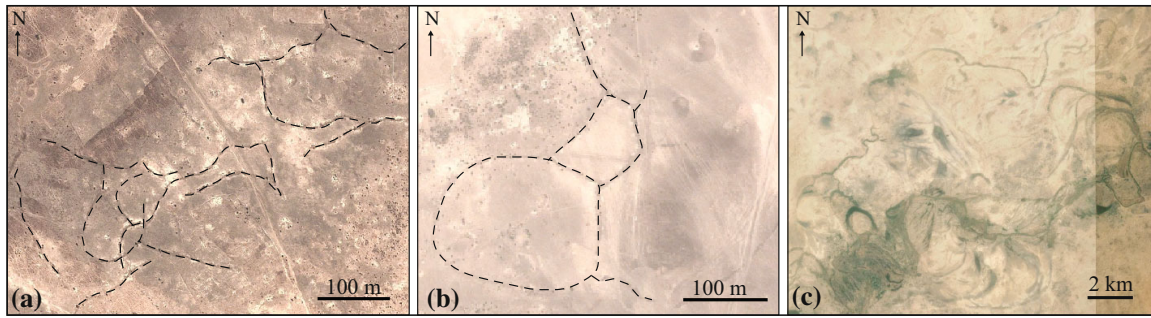


Fig. 6 Google Earth extracts from **a** fractures (image centred at 13.78°E–11.86°N), **b** polygonal fractures (image centred at 13.70°E–12.04°N) highlighted by *black dashed lines* above the Bornu depression) and **c** palaeo-meanders of the Komadugu-Yobe river (image centred at 12.90°E–13.50°N)

2200 kg m⁻³. Considering the thickness of the Fika formation and its 600 kg m⁻³ extra-weight, a 12 MPa differential load may be induced by compaction. This stress level exceeds the yield strength of clays containing 24 % of water (Kopf 2002). Accordingly, compaction may produce clay fracturing in the vicinity of faults 5 and 6, causing an increase in the clay effective permeability (Luo and Vasseur 2002), and thus fluid percolation through the Fika formation and hydraulic connection between all the aquifers. Finally, in the Bima formation blocks, from faults 6–8, good hydrodynamic connectivity possibly exists. At fault 8, the throw of the Fika formation (circle B, Fig. 3a) partly inhibits vertical water circulation.

From the above discussion, we infer the following values of the horizontal permeability K (Fig. 16): 10^{-18} m² for the substratum, with 2×10^{-13} m² for the Bima formation, 10^{-15} m² for the Fika one, 10^{-13} m² for the Continental Terminal, 10^{-15} m² for the Pliocene and 10^{-12} m² for the Quaternary (this latter value is assumed because of computational limitations, although higher values are equally possible). Faults 5 and 6 are considered to be ~ 10 km wide, i.e. a reasonable value for faults in a pluri-hectokilometric sedimentary basin. Their horizontal and vertical permeabilities (K_x and K_z) are assumed to be from 10^{-15} to 10^{-14} m², respectively (Table 1). Finally, because of the vertical connectivity generated by polygonal fractures or normal faults in Kadzell and Kanem, a vertical permeability of 10^{-14} m² is assigned to the Pliocene formation.

3 2D Convective Model

In this section, we present results from a 2D convective model used to simulate the circulation of water in the Lake Chad basin. For this purpose, we build upon the numerical convection model developed by Genthon et al. (1990) for a slightly sloped ($<1^\circ$) terrain. The latter study showed that large convective cells develop, with descending/ascending currents along highly permeable borders spaced a few hundred kilometres apart. Three conditions are required for this circulation to occur: (a) a minimum slope $\leq 1^\circ$, (b) an appreciable horizontal to vertical permeability ratio, and (c) the equivalent vertical Rayleigh number (Ra) lower than $4\pi^2$ (i.e. the threshold for the development of free porous flow convection; Eq. 7 in Appendix 1). Such conditions are fulfilled for the Lake Chad basin where the slope of the sedimentary layer is $\sim 1^\circ$, the interspersed high permeability formations (i.e. Bima, Continental Terminal and Quaternary formations) with low permeability ones (Fika and Pliocene formations) produces a strong effective horizontal

Table 1 Physical parameters used in the 2D convective model

<i>Physical parameters of water</i>	
Density	1000 kg m ⁻³
Thermal conductivity	0.6 W m ⁻¹ K ⁻¹
Heat capacity	4180 J kg ⁻¹ K ⁻¹
<i>Geophysical parameters of the formations</i>	
Quaternary	
Density	2650 kg m ⁻³
Heat capacity	900 J kg ⁻¹ K ⁻¹
Permeability	10 ⁻¹² m ²
Porosity	0.4
Pliocene	
Density	2600 kg m ⁻³
Heat capacity	900 J kg ⁻¹ K ⁻¹
Permeability	10 ⁻¹⁵ m ²
Porosity	0.07
Continental terminal	
Density	2650 kg m ⁻³
Heat capacity	900 J kg ⁻¹ K ⁻¹
Permeability	10 ⁻¹³ m ²
Porosity	0.3
Fika	
Density	2600 kg m ⁻³
Heat capacity	900 J kg ⁻¹ K ⁻¹
Permeability	10 ⁻¹⁵ m ²
Porosity	0.07
Fika faults	
Permeability	$K_x = 10^{-15} \text{ m}^2, K_z = 10^{-14} \text{ m}^2$
Porosity	0.07
Bima	
Density	2650 kg m ⁻³
Heat capacity	900 J kg ⁻¹ K ⁻¹
Permeability	$2 \times 10^{-13} \text{ m}^2$
Porosity	0.4
Substratum	
Density	2600 kg m ⁻³
Heat capacity	950 J kg ⁻¹ K ⁻¹
Permeability	10 ⁻¹⁸ m ²
Porosity	0.02

versus vertical permeability anisotropy, and the effective vertical Ra number is at most equal to 31 (Eq. 7).

We performed numerical simulations in order to assess the possible hydrological regimes occurring within the Lake Chad basin. The model is built in such a way that it reproduces the detailed geological cross section of Fig. 3a. The governing equations (mass conservation, Darcy's law and heat transport), effective parameters (effective thermal conductivity and volumetric heat capacity) and boundary conditions used to describe the

circulation and the temperature distribution within the basin are detailed in Appendices 1 to 4.

We first solve the transient conductive heat equation until reaching the steady state, in order to evaluate the temperature field (Fig. 7a) when the sediment horizons are assumed to be impermeable. The time needed to reach steady state is ~ 2 Ma, which corresponds to the conductive time of a ~ 8 -km-thick horizon. We observe that the 70°C isotherm deepens towards the eastern border of the basin. This trend results from the increase in the thickness of the Fika formation towards the East, which acts as a thermal insulator due to its low thermal conductivity. The temperature drop is particularly strong in the 2-km-thick Fika formation between faults 5 and 6. Consequently, heat is not actively transported by conduction and the temperature rises to 173°C within the underlying Bima formation, while at similar depths outside this domain the temperature is $\sim 150^\circ\text{C}$. The surface conductive heat flow profile displayed by the model is represented in Fig. 8. The heat flow gradually decreases from the west to the centre of the graben located between faults 5 and 6 and then rises again when the thickness of the basin decreases eastward. The Kadzell region exhibits an important heat flow of 100 mW m^{-2} . This value is due to the proximity of the high conductivity substratum ($5.3\text{ W m}^{-1}\text{ K}^{-1}$) that lies at a depth of ~ 1 km. Between faults 5 and 6, heat flow reaches a minimum of $\sim 65\text{ mW m}^{-2}$ and a value of 110 mW m^{-2} on the eastern part of the basin. Finally, the conductive mean heat flow at the surface is $\sim 90\text{ mW m}^{-2}$.

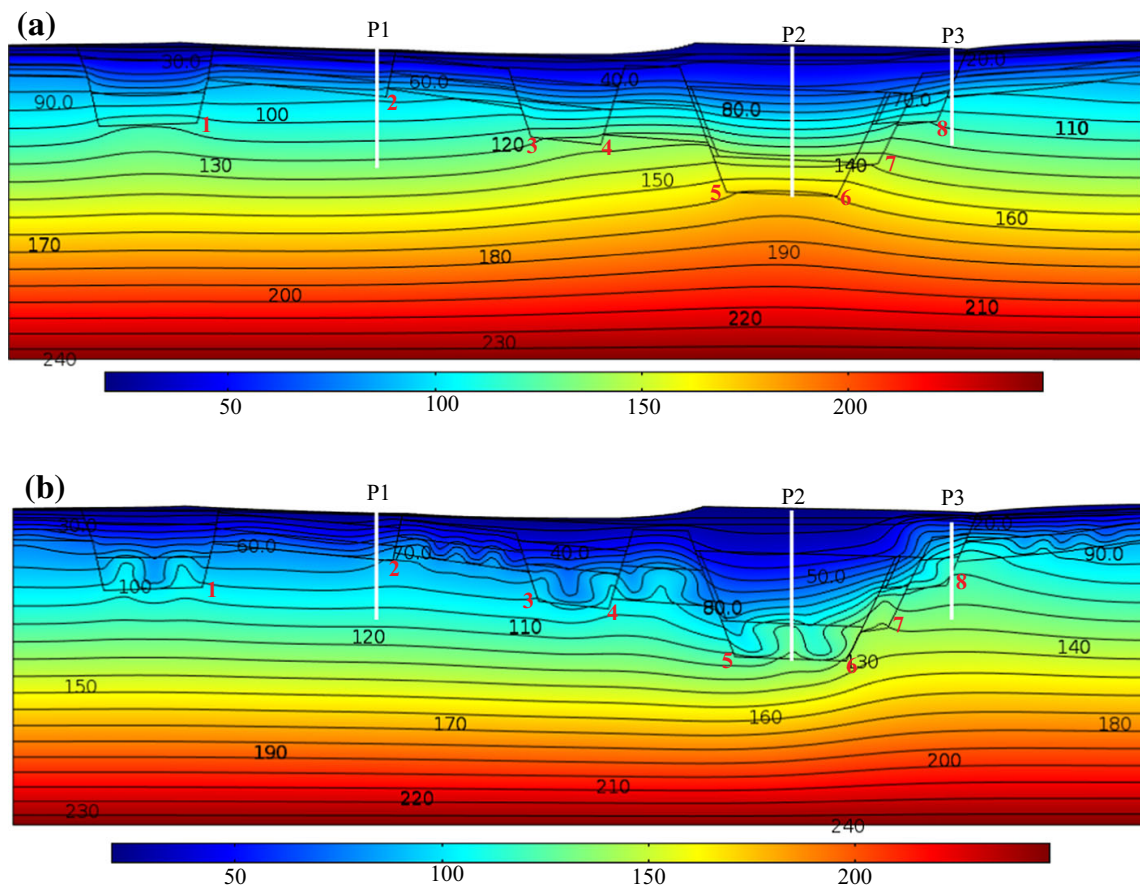


Fig. 7 Temperature maps in $^\circ\text{C}$ of **a** the conductive model and **b** the convective model. The isotherms are displayed each 10°C . Vertical white lines highlight the location of temperature profiles P1, P2, P3 displayed in Fig. 10

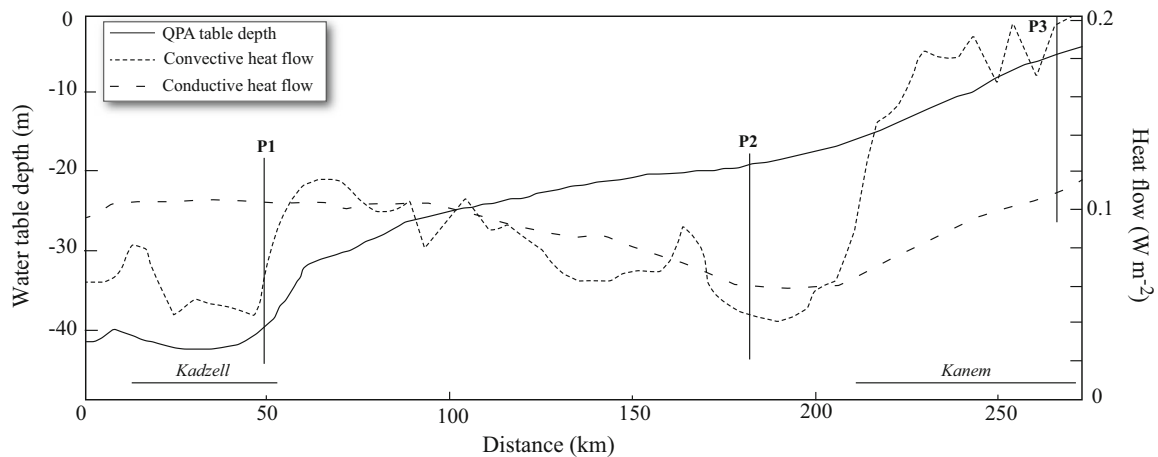


Fig. 8 Dotted lines represent the convective heat flow calculated at the surface, while the dashed lines represent the conductive heat flow. Continuous lines represent the calculated piezometric level between Kadzell and Kanem derived from the pressure variations associated with the convective circulation. Profiles P1, P2, P3 are located by vertical black lines

Figure 7b displays the $\sim 500,000$ years snapshot of the temperature field obtained when the sedimentary horizons are permeable. Due to the large-scale slopes of the isotherms in the initial conductive temperature field, convection is triggered whatever the Rayleigh number; a basin-wide convective cell is generated. We find that a large-scale current descends along the western border of the basin, then flows towards the east in the Bima formation and finally rises up to the surface along faults 6 to 8. A cold current is located just beneath Kadzell and slightly deforms the isotherms crossing the Fika and the Bima formations. The calculated surface convective heat flow in the Kadzell region ranges from 30 to 60 mW m^{-2} (Fig. 8). Between faults 2 and 8, small convective plumes develop in the thermal boundary layer within the Bima formation and are dragged along the basin-wide west–east current: this results from the fact that the vertical Rayleigh number of that layer exceeds $4\pi^2$ (Eq. 7). The convection triggered in the shallow parts of the basin (e.g., between faults 2 and 3) can induce a surface convective heat flow as high as 120 mW m^{-2} (Fig. 8).

It is notable that, due to the permeability contrast between the Bima and Fika formations, small-scale convective cells remain confined within the Bima and do not enter into the quasi-impervious Fika formation. Along the eastern flank of the graben, between faults 6 to 8, a powerful 30-km-wide warm ascending current rises from the bottom of the Bima formation up to the Quaternary formation, i.e. ~ 100 m beneath Kanem. In the core of this current, the temperature drops from 120 to 45 $^{\circ}\text{C}$. Such current provides a high heat flow at the surface. It ranges between 120 and 200 mW m^{-2} (Fig. 8), a heat flow range also observed in other continental rift zones (e.g., Pribnow and Schellschmidt 2000). This high heat flow has two causes: (a) high conductivity of the sand at the surface ($\sim 2.1 \text{ W m}^{-1} \text{ K}^{-1}$) compared to the low conductivity of the clay-rich western part of the basin ($\sim 1.3 \text{ W m}^{-1} \text{ K}^{-1}$) and (b) isotherms rise on the eastern part of the basin. The spatial fluctuation of the heat flow visible in Fig. 8 over the Kanem causes fluctuations of the temperature field associated with the ascending current. Cold descending currents follow faults 5 and 6. These cold currents fall through the Continental Terminal, Fika and Bima formations and locally cause strong temperature drops, and the heat flow is decreased down to 40 mW m^{-2} . Mean surface convective heat flow amounts to 110 mW m^{-2} , a value corresponding to a Nusselt number of 1.2 for basin-wide convective cell. This suggests that although the local conductive heat transfer is significantly perturbed by the

convective circulation (for instance underneath Kanem), the mean heat transfer through the whole basin slightly increases due to convection. Such a phenomenon is well known in sedimentary basin modelling (Quintard and Bernard 1986; see also Appendix 4).

Figure 9a–d displays the vertical and horizontal components of the velocity. Water enters the basin in the Kadzell region with a mean Darcy velocity of 4 mm year^{-1} (Fig. 9a). The fluid begins to circulate in the highly permeable (10^{-12} m^2) Quaternary formation, then falls down into the Pliocene, Continental Terminal and Fika formations halfway between faults 1 and 2, before penetrating into the Bima formation. At the bottom of the Bima formation, the fluid circulates eastward at a mean velocity of 10 cm year^{-1}

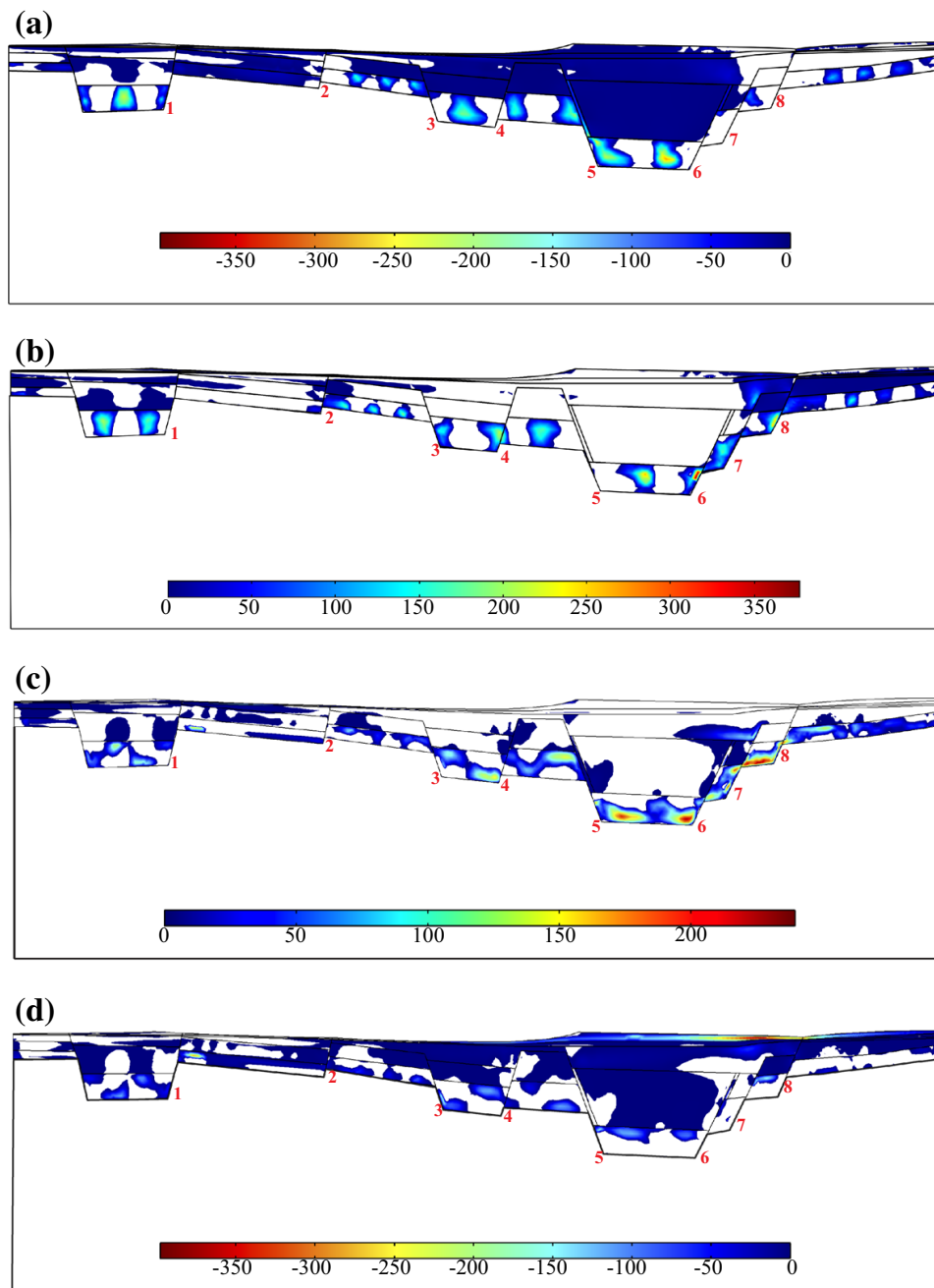


Fig. 9 Vertical and horizontal Darcy velocities of the convective model (in mm year^{-1}). **a, b** Maps of the positive and negative *vertical* velocity fields, respectively, and **c, d** maps of the positive and negative *horizontal* velocity fields, respectively

(Fig. 9c) and follows the lower boundary layer of the basin-wide convective cell. Meanwhile, it is warmed by the basement and, below Kanem, rises up to the surface (Fig. 9d). Between faults 6 and 8 in the Bima formation, from a depth of 4 km up to 700 m, the mean velocity of the ascending water reaches 10 cm year^{-1} . The obstruction due to the presence of the throw at fault 8 in the Fika formation (circle B) decreases the mean velocity to $\sim 4 \text{ cm year}^{-1}$ from 700 m depth up to the surface (Fig. 9c; Appendix 4). Westward of Kanem, between the surface and 1.1 km depth, an important backflow is generated (Fig. 9d). The horizontal velocity within the Quaternary formation reaches a maximum of 39 cm year^{-1} west of fault 8 and then progressively decreases to reach $\sim 7 \text{ cm year}^{-1}$ near fault 2. The backflow develops with a mean horizontal velocity of 3 cm year^{-1} along the $\sim 600\text{-m-thick}$ Continental Terminal aquifer between faults 5 and 6, and to a lesser extent within the Fika formation (0.3 mm year^{-1} velocity). A vertical descending current develops with velocities of 6.5 and 3 cm year^{-1} , within the Continental Terminal formation and faults 5 and 6, respectively, before entering inside the Bima formation (Fig. 9a). This backflow produces complex mixing of water between Kanem and Kadzell. Moreover, it cools the Fika formation and generates an asymmetric temperature field across the graben. Considering the small velocity of the basin-wide convective cell inside the Bima formation (10 cm year^{-1}), the overturn time of the convective flow is a few tens of Ma. This indicates that the increase in the mean geothermal heat flow due to the basin-wide convection generates transient cooling through the 4-km-thick crust and the sediment infill. Consequently, the surface heat flow progressively decreases during a few tens of Ma, then reaching the heat flow recorded at the steady-state conductive regime. It is worth noticing that the convective circulation in the basin is unsteady whatever the evolution time of the system. This results from two factors: high local Ra numbers in the Bima formation and along the faults 6–8 and high temperature at the bottom of the basin that drastically enhances the viscosity and coefficient of thermal expansion (see Appendix 2) (Fontaine et al. 2002).

Figure 10 shows three vertical temperature profiles derived from our model (Fig. 7b), crossing Kadzell (P1), the centre of the graben between faults 5 and 6 (P2) and Kanem (P3). For each profile, the temperatures for the conductive and convective models are shown. The temperature profiles display a linear behaviour for the conductive model. On the contrary, the convective circulation impacts the temperature by the presence of concavities. Indeed, when the profile is concave, the current is descending while, when it is

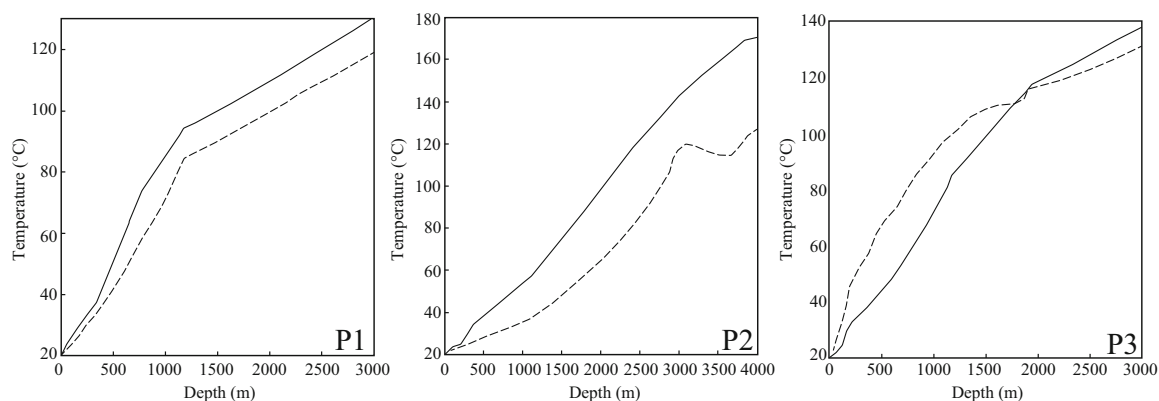


Fig. 10 Comparison of the temperature profiles P1, P2 and P3 obtained from the convective and the conductive models. The *solid lines* represent the conductive temperatures, while the *dashed lines* represent the convective ones

convex, the current is ascending. In P1, the convective profile is located underneath the conductive one, suggesting that the layers constituting the Kadzell become colder during the convective process. The temperature difference between the two profiles reaches 15 °C at the bottom of the Bima formation (1000 m deep). The concavity of the profile down to 1 km depth is due to the cold water descending current. Nevertheless, the weak concavity of the profile is explained by the low velocity ($\sim -4 \text{ mm year}^{-1}$) of the fluid, unable to efficiently cool the sediments. In P2, the convective profile is located beneath the conductive one. The strong concavity of this profile is explained by the presence of the intense cold descending current within fault 5. The profile is concave down to 3 km, where the temperature reaches 100 °C. Then, the profile crosses the axis of a small ascending current within the Bima formation and its temperature remains constant between 3 and 3.6 km depth. It crosses the thermal boundary layer at the bottom of the Bima formation between 3.6 and 4 km. Finally, the convective profile at P3 is typical of a warm ascending current: the convective profile is above the conductive one, and the temperature profile is convex down to 1.5–2 km. At this depth, the temperature reaches $\sim 95 \text{ °C}$. At larger depths, the profile crosses the substratum and reaches $\sim 110 \text{ °C}$ at 3 km.

Garven and Freeze (1984a, b) showed that pluri-kilometric long convective circulations develop in sedimentary basins at velocity of $0.1\text{--}0.2 \text{ m year}^{-1}$. The general pattern of the circulation produced by our model (descending/ascending current from one border to the other border) is consistent with results of Garven and Freeze (1984a, b) and Gvirtzman et al. (1997). However, the conditions required to generate such cells are generally not explained in works dealing with basin-wide convection cells. It seems that two conditions are required: (a) long wavelength horizontal temperature variations in the conductive state and (b) a vertical Ra number less than $4\pi^2$ (otherwise the large-scale convection cells split into smaller cells). The first condition is achieved from the slope and/or thickness variations of the different formations, which have their own thermal conductivity. The second condition is fulfilled in the thickest part of the basin. Assuming an effective vertical permeability across the whole basin of 10^{-14} m^2 for the thick domain separating faults 5 and 6 (values assigned to the faults themselves), the Ra number is equal to 31 (Eq. 7). Alternatively, a model run with a K_v of 10^{-13} m^2 in faults 5 and 6 shows splitting of the basin-wide convective cell into smaller cells. If K_v equals 10^{-15} m^2 , the large convective circulation is too sluggish to have any hydrodynamical and thermal impact at the surface. Our different runs lead us to conclude that the parameters considered in this study (Table 1) are optimal to obtain a wide basin convective circulation with a good fit to the observations.

Figure 11 presents the observed and model-based water table topography along the profile A. The pressure difference generated between ascending and descending currents is $\sim 0.35 \text{ MPa}$. It correctly reproduces the location of the observed piezometric depression and dome. The minimum pressure generated by our model is located beneath the Kadzell region, while the maximum is found below Kanem. This result can be interpreted as follows: the core of the warm current, circulating along the eastern side of the graben, presents a mean temperature excess with its surrounding of about 40 °C. Considering the thermal expansion of water ($\alpha = 3.85 \times 10^{-6} \text{ K}^{-1}$ at 40 °C) and current height of 4 km, we deduce that the buoyancy of the warm current induces a 0.8 MPa excess pressure. Such an excess pressure is essentially used to drive the backflow of the large convective cell in the Quaternary and Pliocene formations and eventually along the Bima formation. Assuming that half of the excess pressure is used to drive the circulation at the top and bottom cell boundaries, we estimate that the excess pressure on the horizontal interface of

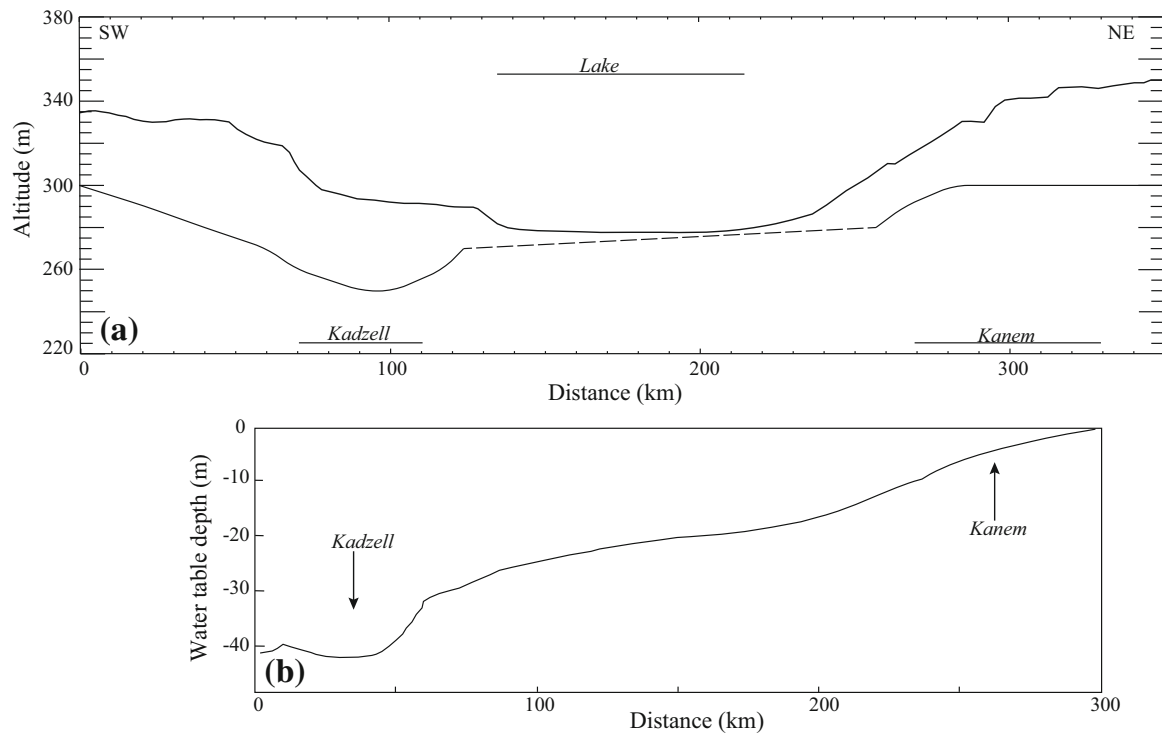


Fig. 11 Comparison between **a** the observed water table of the QPA between Kadzell and Kanem and **b** calculated piezometric level derived from the pressure variations associated with the convective flow within the Lake Chad basin

the current below Kanem, used to drive the backflow, amounts to ~ 0.4 MPa, in agreement with the model results.

Annual rainfall amounts to 200–400 mm over the region (e.g., Bader et al. 2011; Descloitres et al. 2013). It accumulates over the aquifer water table maintained by the large convection cell. Considering the permeability assigned to the different formations, we infer that the rain flows from Kanem to Kadzell at a velocity of 2 cm year^{-1} and 2 mm year^{-1} in the Quaternary and Pliocene formations, respectively. Such velocities are comparable to the backflow of the warm current in these formations. This circulation is designated as the “forced convective flow” by Gvirtzman et al. (1997). Generally, in mountainous areas, the topographic slope is a hundred times larger than the slopes generated by free convection cells. This shows that “forced convection” is the dominant transfer mode of water in mountainous areas. However, this scheme does not work in the Lake Chad basin. This does not mean that the topography at the borders does not impact the basin. The slow eastward circulation of descending cold currents observed between faults 1 and 2 (with subcritical Ra number) probably results from the “forced convection” at the western side of Kadzell. Such forced convection explains why the descending current of the basin-wide convective circulation does not follow fault 1 but is localised at the centre of the Kadzell area along the P1 profile (Appendix 4).

4 Discussion

In the previous section, we have presented results of a water convection model over the Lake Chad basin. This led us to propose a scenario describing how water circulates at depth under the basin. In this section, we examine to what extent the model results fits with

the observations. Different types of observations are considered as thermal data (subsurface and surface temperature data), hydrochemical data, piezometry evolution and water mass changes.

4.1 Relations Between the Deep Convective Circulation and Thermal Data

4.1.1 Subsurface Thermal Data

Bottom hole temperatures profiles (referred hereafter as BHT) have been collected during the drilling of oil wells in the Nigerian sector of the basin (Nwankwo and Ekine 2010). BHT profiles are located in the northern part of Lake Chad as well as at or near the Bornu piezometric depression (Fig. 4). BHT are obtained at thermal disequilibrium and are used for internal calibration of the drills. Therefore, they are significantly affected by mud circulation during and after drilling. The data shown in Fig. 12 are corrected to first order by using American Association of Petroleum Geologists (AAPG) gradient correction factors (Nwankwo and Ekine 2010). The uncertainty of individual temperature measurements ranges from 5 to 15 °C. Each borehole temperature profile was averaged according to depth to determine the local mean temperature gradient. We observe that the mean temperature gradient substantially increases towards the north-eastern part of the basin. We also note that, in most cases, temperature profiles do not vary linearly with depth (Fig. 12). The profiles' shapes appear similar to those obtained in regions where groundwater circulation transports geothermal heat (Kilty and Chapman 1980; Pribnow and Schellschmidt 2000). In the latter studies, surface heat flow was directly linked to the temperature gradient in the first ~300 m of the basin where the profile is linear and crosses the top boundary layer of the convective circulation. The profiles presented by Nwankwo and Ekine (2010) show that in the first ~300 m the measured and corrected thermal gradients are similar. The thermal gradients derived from the BHT vary from 30 to 80 °C km⁻¹ (Fig. 4), a range consistent with model-based surface heat flow values ranging from 45 to 120 mW m⁻² (Fig. 8). Besides, whatever the error range of the BHT data, the top to bottom shapes of the Nwankwo and Ekine (2010) BTH profiles are not compatible with those expected in a medium where heat transport is conductive. Profile concavity, along ascending or descending convective currents, is also observed in our numerical model

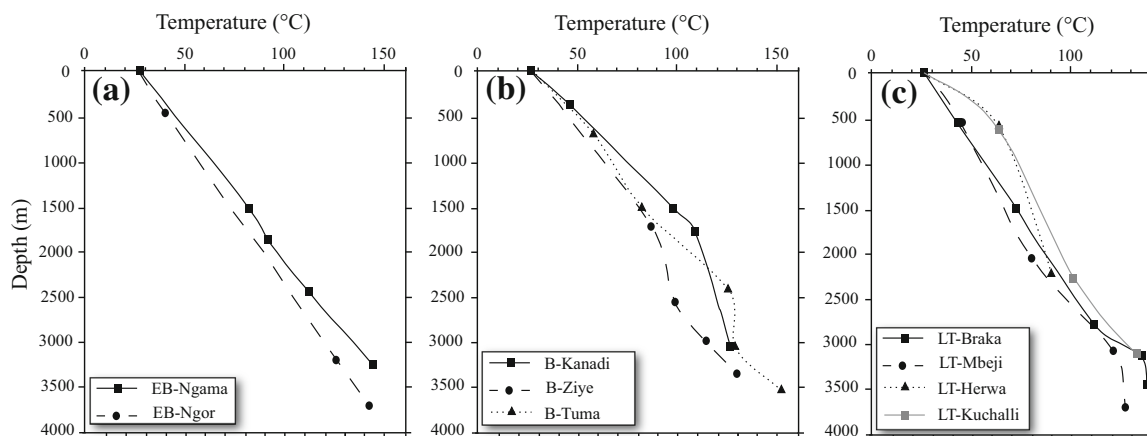


Fig. 12 Thermal profiles obtained during oil drills (modified from Nwankwo and Ekine 2010): **a** slightly outside the Bornu depression, **b** in the Bornu depression and **c** in the ancient bed of Lake Chad (see locations in Fig. 4)

(Fig. 8). For example, between ~ 200 and ~ 1500 m, the convex shape of the LT-Herwa and LT-Kuchalli BHT profiles is similar to that of the P3 profile that crosses the warm ascending current below Kanem (Fig. 8). However, the set of boreholes is not dense enough to constrain the structure of the convective flow in a domain as large as the Lake Chad basin. In the Rhine Graben, for example, the 804 available boreholes allow characterising of the east–west convective cells, but with a very complex 3D distribution of the warm and cold currents (Pribnow and Schellschmidt 2000). By analogy, we can suspect that the real structure of the flow within the Lake Chad basin is also very complex.

4.1.2 Surface Thermal Data

According to our model (domes and depressions associated with warm and cold currents, respectively), we suggest that the brightness temperatures observed by Leblanc et al. (2003) are directly linked to the convective circulation. Leblanc et al. (2003) compared the piezometric map with monthly composite maximal brightness temperatures from the METEOSAT satellite. These data were acquired in August 1999, a period corresponding to the end of the wet season. These authors found that during wet years the piezometric domes are systematically warmer by 4–5 K than the piezometric depressions. A difference of surface heat flow by a factor of two above ascending and descending currents is predicted by our model (see Sect. 3.2). However, a heat flow difference of about ~ 50 – 100 mW m^{-2} cannot maintain a surface temperature difference of 4–5 K (Sabins 1999). Only processes involving the temperature diurnal cycle can explain such a temperature contrast. Leblanc et al. (2003) explained this observation as follows: in the Kanem region, consisting of aeolian sands, rain infiltrates rapidly and deeply into the soil. Consequently, rain water does not contribute to evaporation. Thus, the observed brightness temperature reflects dry surface conditions. In the Kadzell and Bornu regions, the surface consists of a mix of fluvial deposits (sandy clay) and aeolian deposits. In that case, the rain percolates more slowly. Thus, water evaporates, acting as a moderator of the temperature increase during the day (via latent heat).

Maximal surface temperatures obtained from 8-day composite MODIS images allow us to follow temperature seasonal variations over the year. Figure 13 shows daytime and nighttime maximal surface temperatures obtained during the year 2001, a particularly wet year (Bader et al. 2011). Temperatures data cover the Kanem, the Kadzell and the Bornu regions during the dry season (October–June, but we only focus on the January–March time span) and wet season (July–September). Whatever the season, the daytime temperature in Kanem is on average 3–4 K warmer than at Kadzell (Fig. 13a). During the nighttime, for both seasons, a similar behaviour is observed, but the temperature difference decreases to between 1 and 2 K (Fig. 13b). Usually, during the diurnal cycle, the amplitude of the surface temperature variation on dry ground is larger than on wet ground (Byrne et al. 1979; Idso et al. 1975; Sabins 1999). In the wet season, Kadzell should be warmer than Kanem during the night, in contradiction with the observations. If the Kanem soil is dry, the surrounding atmosphere is likely to be wet, because of the presence of numerous ponds which evaporate at ~ 2 m year^{-1} (i.e. ~ 6 mm day^{-1} ; Roche 1980). Besides, such ponds are not the only source of humidity. Because of the high permeability of the Kanem region, the air in the under-saturated zone circulates by convection with Darcy velocities of several cm s^{-1} (Antoine et al. 2009). Such convection maintains a high water concentration in the soil. At night, when the surface temperature is cool enough, warm and humid convective air leaves the system (Antoine et al. 2009), and most of the water vapour contained in the warm convective air condenses. Consequently, it is very likely that, during

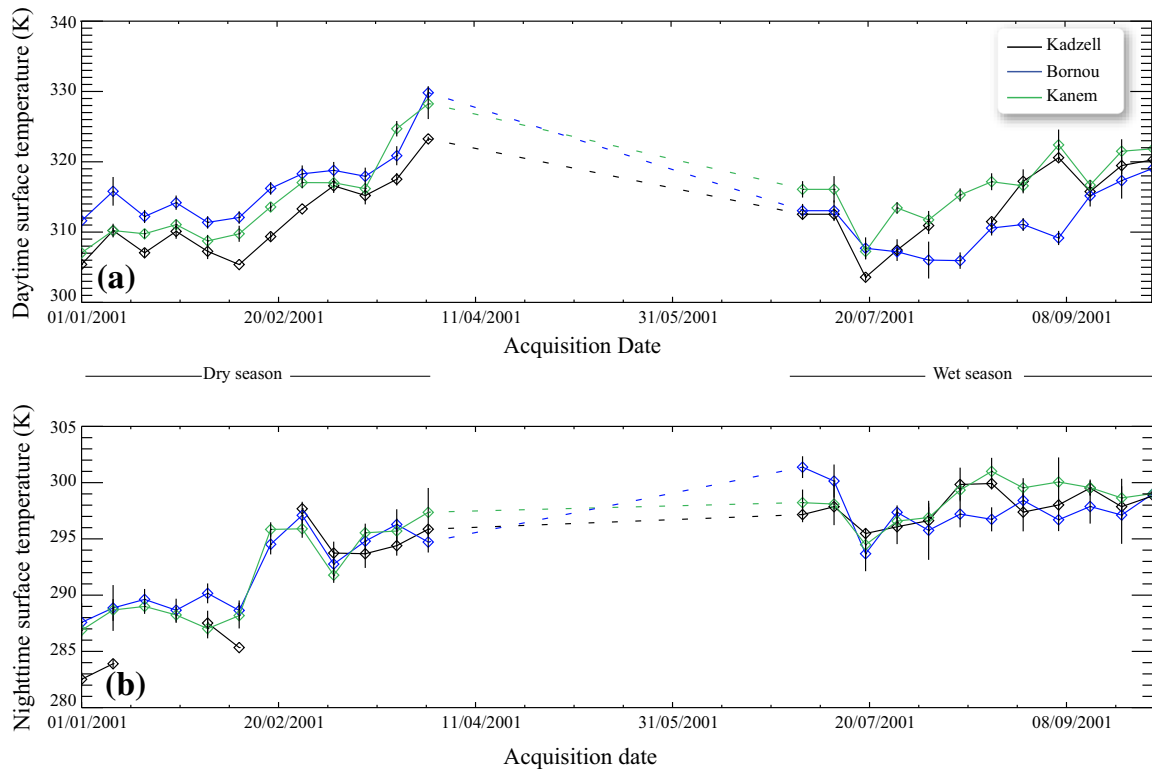


Fig. 13 Satellite TERRA moderate resolution imaging spectroradiometer (MODIS) 8-day composite maximal surface temperature obtained during 2001 **a** by day and **b** at night, for the Kanem, Kadzell and Bornou regions. We have only considered January, February and March as representative for the dry season and July, August and September for the wet season

the night, water condensation of 1–2 mm per day heats the Kanem surface by 1–2 K. Eventually, this water infiltrates into the highly permeable sandy soil, recharges the phreatic aquifer and finally leads to drying of the surface during the day.

During the dry season, the perennial ponds in the Kanem region, linked to the piezometric dome, may be filled by the water coming from the ascending convective current. This may explain why this region remains warm as the evaporation/condensation cycle is still at work. Because of the presence of clays in the Kadzell subsurface, the diurnal temperature cycle is mainly controlled by the in situ evaporation/condensation cycle as considered by Leblanc et al. (2003). This explains why the surface temperature there is colder than in the Kanem region.

During the wet season, the temperature contrast between Bornou and Kanem evolves as in the Kadzell and Kanem regions. During the day, the Kanem region is ~ 5 K warmer than the Bornou region, while at night the temperature difference drops to ~ 2 K (Fig. 13a). However, during the dry season, the situation is reversed: during the day, the Bornou region is warmer than the Kanem region by ~ 3 –4 K, while at night both regions have similar temperatures (Fig. 13b). We suggest that the latter situation results from the impact of the vegetation and the proximity of the Small Lake Chad and Chari-Logone rivers. Indeed, during the dry season, soil humidity in Bornou results from water condensation and evaporation. To explain the temperature diurnal cycle, condensed water should not be available during the daytime. We propose that a significant amount of this water is absorbed by the vegetation (Gaston 1996). In Bornou, the vegetation in the dry season mainly consists of trees spaced ~ 20 m apart, a relatively large tree density that is important for the basin's evapotranspiration/condensation cycle.

4.2 Relation Between Deep Convective Circulation and Hydrogeology

4.2.1 Evolution of the Water Composition

In the Nigerian part of the basin, the Continental Hammadian aquifer contains mainly NaCl waters (Schneider and Wolff 1992). In the Kanem area (Table 2), Schneider and Wolff (1992) have shown that the Continental Terminal aquifer contains mainly NaHCO₃ waters and that the Pliocene aquifer consists mainly of Na₂SO₄ waters. On the contrary, the Quaternary aquifer is described by a geochemical signature of CaHCO₃. Chemical variation of the waters is usually interpreted to be a consequence of separate aquifers. However, our proposed convective scenario considers that all aquifers are connected by vertical drains due to the compaction of clay formations. The total dissolved solid (or TDS) of the QPA is 165 mg L⁻¹, while the mean TDS is 760 mg L⁻¹ for the Pliocene, Continental Terminal and Continental Hammadian aquifers (Schneider and Wolff 1992). Between these three aquifers, the salinity is similar except for some localised pockets of higher salinity. The apparent absence of a notable vertical salinity stratification suggests that the basin-wide convective circulation crosses the entire basin depth. In the case of a vertical salinity stratification, the convective cells are confined to layers with constant salinity and the excess pressure at the phreatic aquifer dramatically reduces the dome height.

In the Kanem region, for the deeper aquifers (i.e. the Continental Hammadian and the Continental Terminal), changes from NaCl to NaHCO₃ waters are interpreted as anion exchanges during the rising of waters through the Fika formation. The enrichment of the Pliocene aquifer in SO₄²⁻ sulphates can be explained by the evaporitic deposit of gypsum/anhydrite during the Early Pliocene. Table 3 presents the detailed chemistry of Pliocene (in italic) and Quaternary aquifers for three regions in Kanem where the water drills were geographically close. The content (in ppm) of ions Mg²⁺, Na⁺, K⁺ and Cl⁻, SO₄²⁻, HCO₃⁻ decreases from one aquifer to the other. On the contrary, the calcium carbonate (Ca²⁺) content increases except for the water wells of Ndelé and Rig Rig. The decrease in the HCO₃⁻ may result from an increase in the Ca²⁺ in solution, causing CaCO₃ precipitation. The decrease in sulphates in solution between these two aquifers may be explained

Table 2 Concentration (in ppm) of the QPA and the Pliocene aquifer (*in italic*) of the main anions and cations (Arad and Kafri 1974; Schneider and Wolff 1992)

	Ca ²⁺	Mg ²⁺	Na ⁺	K ⁺	Na ⁺ + K ⁺	Cl ⁻	SO ₄ ²⁻	HCO ₃ ⁻	CaCO ₃
Mondo	55	6.5	–	–	83.2	15.9	103	116	190
<i>Ngouri</i>	37.1	14.6	209	2.65	–	79.8	271	311	–
Boudouté	45.2	–	–	–	–	11.5	27.2	130	212.5
<i>Keliganga</i>	1	4.25	168	1.37	–	59.9	62.4	308	–
Ndelé	23.9	4.6	–	–	37.5	10.7	49.3	110	67
<i>Rig Rig</i>	37.9	14.9	239	15.2	–	42.5	437	226	–

Wells had been selected by their proximity to the Kanem piezometric dome

Table 3 Equivalent water height obtained by GRACE for the main tiles of the Lake Chad basin

Tiles	Kadzell	Kanem	Bhar-el-Ghazal	Harr	Yobe	Bornu	Chari	Fitri
Trend (mm year ⁻¹)	0.39	0.11	0.89	2.0	1.94	0.48	–0.02	0.50

by the presence of sulphate-reducing bacteria (SRB) in the Pliocene formation (Chapelle 2000) that use sulphate/sulphur as an energy source. This process is known as anaerobic respiration. Indeed, these SRB consume the dissolved sulphate and expel hydrogen sulphide and carbon dioxide (Sylvia 2004). SRB usually flourish in the warm water system, found in the ascending current below Kanem. Moreover, the remaining sulphate precipitates due to its solubility (Serafeimidis and Anagnostou 2015) in the Pliocene Formation, in agreement with the observations of gypsum deposits (Fig. 3b) (Schneider and Wolff 1992).

In the Kazzell and Bornu regions, where the convective current may locally be descending, the chemistry variation can be essentially explained by the exchanges with the clays. Indeed, the phreatic aquifer in the Niger is described as containing sodium and calcium bicarbonate and sulphate waters (Greigert 1979) associated with a relatively low water temperature. The Pliocene aquifer contains only sodium bicarbonate and sulphate waters (Arad and Kafri 1974). A hydrostatic pressure increase leads to the fluidisation of the clay-rich formation (Mainsant et al. 2012) and induces increased exchange surfaces between clay and water. Due to temperature and pressure changes, the Continental Terminal waters present sodium deficit sulphates, suggesting that the sulphate layer has been consumed by SRB. In the case of the Continental Hammadian aquifer, the presence of sodium chloride waters may involve anion exchanges of the clay-rich Fika formation (Carroll 1959).

4.2.2 Comparison Between Convective Velocity and Transient Variations of the Piezometric Level: Inference on Water Mass Changes

Piezometric levels of the QPA in the Kazzell and the Bornu regions have changed between the 1970s and the 2000s (Fig. 14) (Schneider 1969; Schroeter and Gear 1973; Zairi 2008). In the 2000s, the surface area of the Kazzell depression decreased to 3300 km² and the

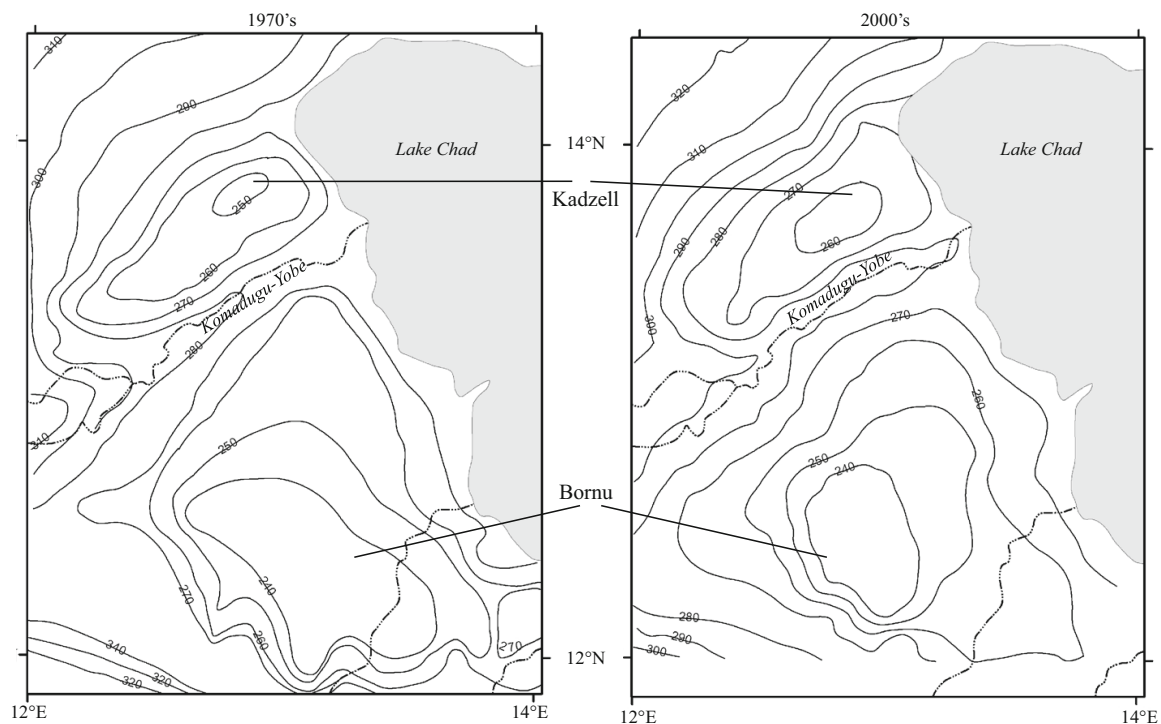


Fig. 14 Piezometric maps of the Kazzell and Bornu depressions in **a** the 1970s (Schneider 1969) and **b** the 2000s (Zairi 2008)

maximum depth of the water table rose by ~ 10 m; i.e. the QPA rose in that region by ~ 30 cm year $^{-1}$. For the Bornu depression, the surface area decreased to 11,500 km 2 while the depth of the depression did not change. Considering the uncertainties in the measurements of the piezometric level during the 1970s, we consider that the 30 cm year $^{-1}$ estimate of the water table rise represents a maximum vertical Darcy velocity of ~ 10 cm year $^{-1}$ (considering a porosity of ~ 35 %). These variations observed over a 30-year time span can be explained by variations of the surface conditions (Leduc and Loireau 1997; Mahe et al. 2003). A rainfall increase can also explain this observation. Unfortunately, no recent data are available for the Kanem and Harr domes to check whether the corresponding water tables have experienced changes since the 1970s or not. The vertical Darcy velocity obtained by our model in the Quaternary formation near Kadzell is 4 mm year $^{-1}$. Thus, the velocity estimate in Kadzell does not match the 30 cm year $^{-1}$ maximal rise velocity of the piezometric level estimated above. The convective circulation has no influence on the piezometric level variations. Besides, the Darcy velocity is proportional to the pressure gradient; the water table rise requires strong modification of the hydraulic head which may be due to an important level variation of Lake Chad.

Launched in March 2002, the gravity recovery and climate experiment (GRACE) mission provides observations of the time-variable gravity field (Bruinsma et al. 2010). We analysed a new GRACE solution computed by Ramillien et al. (2014), providing regional surface water mass time series on a $2^\circ \times 2^\circ$ grid (see also Ramillien et al. 2011, 2012). We derived linear trends over the Lake Chad basin (11° – 17° E and 11° – 20° N) for the period 2003–2012 (Fig. 15). In regions where water accumulation (provided by rainfall, rivers or

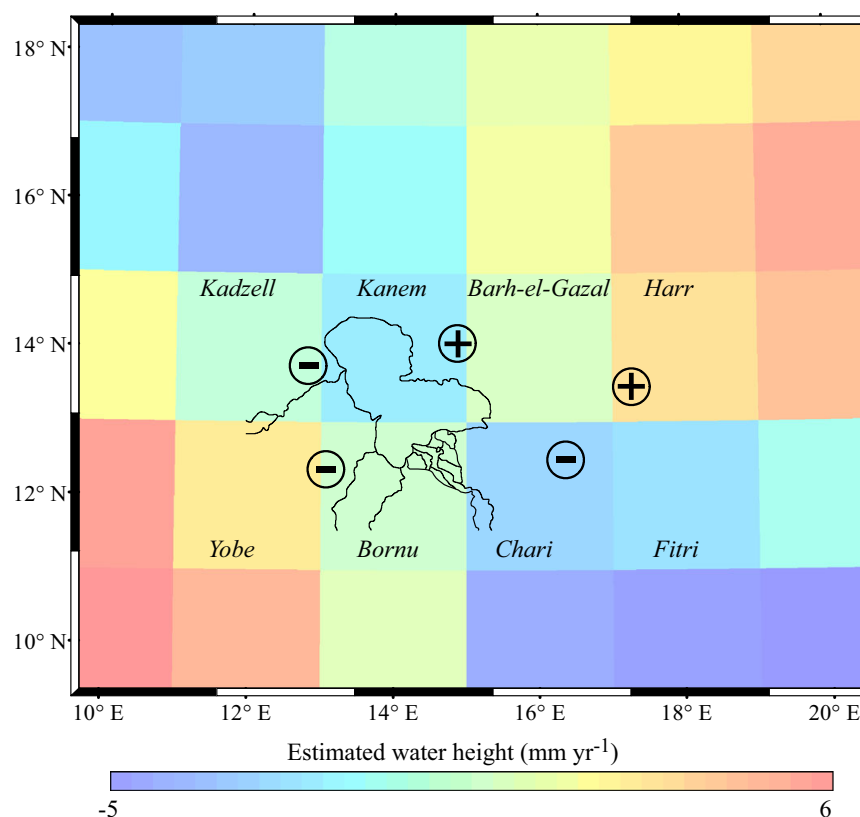


Fig. 15 GRACE-based water surface mass trends in mm year $^{-1}$ from 2003 to 2012 (resolution of each tile is $2^\circ \times 2^\circ$). Tiles around Lake Chad have been named after the covered regions or characteristic features (Kadzell, Kanem, Barh-el-Ghazal, Harr, Yobe, Bornu, Chari and Fitri). The *symbols minus* and *plus* locate the piezometric depressions and domes, respectively

groundwater) is greater than the water deficit (the latter being mainly controlled by the evapotranspiration), the trend is positive while, if water deficit is larger, the trend is negative. The water mass trend is $\sim 1 \text{ mm year}^{-1}$. Our results are summarised in Table 3. The trend observed in the Yobe tile is linked to water supplied by the Mandara Mountains, from both rainfall and/or river discharge. A similar explanation is valid for the Kadzell and Bornu area. The Fitri area is bordered to the south by Guera Mountains that provide water into this region. The Chari and Kanem areas display very small trends. This suggests that the water deficit is compensated by water accumulation over the 2003–2012 time span. The two last areas (Barh-el-Gazal and Harr) display a positive trend close to 2 mm year^{-1} . This water accumulation cannot be explained only by water supply from rainfall ($\sim 200 \text{ mm year}^{-1}$) or rivers (there are no rivers in this area). We conclude that this water accumulation results from the ascending convective currents that develop below the Kanem and Harr domes. These regions are located very close to the zones of the maximum gravity anomalies (Fig. 2), indicating a zone of deep basement.

The GRACE-based observations are in agreement with a situation where thin sediments favour the development of zones of convective recharge, whereas the borders of thick sediments favour zones of convective discharge flows. Another result worth highlighting is the good consistency between the GRACE-based equivalent water height trend (of $\sim 2 \text{ mm year}^{-1}$) and the transient variation of the piezometric levels (corresponding to 6 mm year^{-1} elevation of the QPA for sand with a porosity of $\sim 35 \%$). This is at least one order of magnitude lower than the backflow horizontal velocity of the basin-wide convection circulation. Considering that the convection is in a transient state, the 6 mm year^{-1} variation of the piezometric level in a $2^\circ \times 2^\circ$ mesh may result from the transient modification of the top pressure field induced by the convective circulation.

5 Conclusions

The phreatic aquifers of the Sahelian regions have well-known surface features like depressions (with a mean depth below the surface of $\sim 60 \text{ m}$) and domes (only clearly observed in the Lake Chad basin). These surface features result from evaporation/infiltration differences due to surface pedological variations between depressions and domes (Aranyossy and Ndiaye 1993; Leblanc et al. 2003). This is corroborated by the observed correlation between METEOSAT brightness temperatures and piezometric levels of the QPA in the Lake Chad basin (Leblanc et al. 2003). The results from the present study suggest that a correlation also exists between piezometric levels and sedimentary thickness in the basin. Indeed, a comparison with the free-air gravity anomalies indicates that, where the sediment infill is very thick ($\sim 4 \text{ km}$), the piezometric domes develop. On the contrary, where it is thin, piezometric depressions are observed. This correlation suggests that sedimentary infill characteristics impact the brightness temperature of the surface. In order to explain the piezometric variations and the reported correlations, we propose an alternative hypothesis that combines evapotranspiration with a deep basin-wide convective circulation.

The Lake Chad basin comprises four aquifers. These are (from shallow to larger depth): the QPA, the Pliocene aquifer, the Continental Terminal aquifer and the Continental Hammadian aquifer. Each aquifer is separated by clay layers generally considered as being impervious. This statement is true when the clay layer has an extent commensurate with its thickness. In the study region, the Pliocene formation has an extent of $\sim 300 \text{ km}$ with a

maximum thickness of ~ 300 m. Data from seismic prospecting in oceanic margins reveal that overpressured clay layers develop giant polygonal fractures when they are submitted to horizontal tensile stresses of a few bars. We discovered the existence of such structures in the Bornu region, located close to the eastern border of the basin. By analogy, the horizontal tensile stresses applied to the Pliocene formation result from the slope break of the surface topography. Associated faults probably create a high vertical permeability connecting the phreatic aquifer with the Pliocene one. Between depths of 2 and 3 km, the compacted clay Fika formation has a maximum thickness of ~ 2 km. The development of differential compaction in this layer may explain the formation of fractures, allowing hydrodynamical connexion between the Continental Terminal and Hammadian aquifers.

We developed a 2D numerical convective model along a cross section from the Kadzell depression (western border of the basin) to the Kanem dome (eastern border of the basin). Our model results show that a cold descending current develops below Kadzell and then is channelled in the Bima formation, along the eastern slope of the basin. Meanwhile, it is heated by about 50 °C by the basement geothermal heat. The horizontal Darcy velocity of the fluid in the Bima formation is ~ 10 cm year⁻¹ that corresponds to a mean flow velocity of ~ 1 m year⁻¹. Thus, it takes 1 Myr for the water to flow from the Kadzell depression to the Kanem dome. The characteristic time to heat the ~ 4 -km-thick infill by conduction is $\sim 500,000$ years. These results show that the heat transport in the infill is due equally to conduction and convection. The warm current, which now has a temperature of ~ 100 °C, rises along the permeable blocks delimiting the eastern border of the basin. The excess pressure generated by this warm ascending current at the top of the ~ 4 km sediment infill potentially explains the piezometric level difference between Kadzell and Kanem. Moreover, our model results show that because: (a) thermal conductivity contrast between sediments and basement along the western border of the basin, (b) fracturing induced by the differential compaction, and (c) large sedimentary infill thickness, the eastern border of the basin is a zone of ascending currents.

According to GRACE space gravimetry data and the transient variation of the convective circulation, the perennial existence of water accumulation over the Kanem and Harr piezometric domes (where in both regions there are no water supplies except from rainfall during the wet season) can be explained by water supply from the convective ascending current. Finally, our model suggests that the development of piezometric domes and depressions are linked to the convective circulation and require connected aquifers, a situation which leads to water mixing. Water geochemistry variations between the aquifers are compatible with our convective model taking into account the cation exchange process in clays. Comparison of the thermal profiles obtained by our model and BHT data suggests that the thermal structure of the basin is impacted by the hydrothermal circulation that is possibly linked to a basin-wide convective circulation. The best test to check this hypothesis is to obtain BHT profiles in both the Kadzell and Kanem regions and compare them with the thermal profiles obtained by our model. Unfortunately, such information is lacking.

Heat provided by the warm ascending current below Kanem is not sufficient to explain the 1–2 K brightness temperature difference observed in Kadzell during the night. In order to explain this temperature difference, we need to consider heat provided by water condensation during the night and the possible existence of air convection in the under-saturated zone. In this case, the role of the ascending current is to deliver water to the surface in order to maintain a minimal humidity whatever the season. Finally, the detection of ascending water currents near the surface has been made possible by the combination of a highly permeable formation close to the surface and of warm zones during day and night

in all seasons, detected by space-based thermal imagers. In the future, regions of arid and/or semi-arid conditions showing this combination may indicate the existence of water close to the surface that can be linked to a deep convective circulation.

Acknowledgments This research has benefited from the support by the French Space Agency CNES and TOSCA (Terre, Océan, Surfaces continentales, Atmosphère) support. It has also benefited from the support of Commissariat Général au Développement Durable (CGDD) from the French Ministry of Environment, as part of the CEREMA internal research project HYDROGEO. Thanks are due to the “Bureau Gravimétrie Internationale (BGI)/International Association of Geodesy” for providing the EGM model. We thank G. de Marsily and G. Vasseur for their constructive criticisms, and the Editor in Chief for editorial suggestions, which significantly improved the paper. This paper arises from the ISSI Workshop on Remote Sensing and Water Resources.

Appendix 1: Governing Equations, Parameters and Equations of State

The mass conservation equation for a fluid of variable density within a fluid-saturated porous medium (rock matrix) without an internal fluid source is:

$$\frac{\partial(\varepsilon \cdot \rho_f)}{\partial t} = -\nabla \cdot (\rho_f \cdot \vec{u}) \quad (1)$$

where ε is the porosity, ρ_f the fluid density (kg m^{-3}), t the time and \vec{u} the Darcy velocity vector (m s^{-1}). We write $\vec{u} = (U, V)$, U and V being the fluid velocity component parallel to the x and z directions, respectively. The fluid is incompressible with a constant chemical composition, and its density is temperature dependent.

Darcy’s law is used to describe the fluid velocity field \vec{u} :

$$\vec{u} = -\frac{K}{\mu} \left(\vec{\nabla} p - \rho_f \vec{g} \right), \quad (2)$$

where K is the permeability, μ is the viscosity of the fluid, \vec{g} is the gravity vector and p is the fluid pressure. The fluid density varies linearly with temperature T in $^{\circ}\text{C}$:

$$\rho = \rho_0(1 - \alpha(T - T_0)) \quad (3)$$

where α is the thermal expansion coefficient and ρ_0 is the fluid density at $T_0 = 20$ $^{\circ}\text{C}$, the surface temperature of the model.

Heat transport is achieved by both conduction and advection and is described for an incompressible single-phase fluid by:

$$C_{\text{eq}} \left(\frac{\partial T}{\partial t} \right) = \nabla \cdot \left(\lambda_{\text{eq}} \vec{\nabla} T \right) - C_L \vec{u} \cdot \vec{\nabla} T \quad (4)$$

where C_L is the volumetric heat capacity defined by $C_L = \rho_f C_P$, C_P is the specific heat capacity, C_{eq} and λ_{eq} are the weighted average volumetric heat capacity and equivalent thermal conductivity, respectively, as defined in saturated porous media of porosity ϕ :

$$C_{\text{eq}} = \phi \rho_f C_{P_f} + (1 - \phi) \rho_s C_{P_s} \quad (5)$$

where f and s are subscripts for the fluid and the porous matrix, respectively. We assume that C_L remains approximately constant, a reasonable assumption since the decrease in density with temperature roughly balances the increase in the specific heat capacity with temperature. The equivalent thermal conductivity is written as:

$$\lambda_{\text{eq}} = \lambda_f^\phi \lambda_s^{1-\phi} \quad (6)$$

where λ_f and λ_s are the thermal conductivities of the fluid and the porous matrix, respectively.

The vertical Rayleigh number Ra characterises the vigour of the convection within the stratified porous medium and is defined as follows:

$$Ra = \frac{\alpha \rho g C_L K_z}{\mu \lambda_{\text{eq}}} \gamma h^2 \quad (7)$$

where K_z represents the vertical permeability, g is the acceleration due to gravity, h is the height of the layer and γ is the vertical temperature gradient.

Appendix 2: Parameter values

In our calculations, the parameter describing the temperature dependence, α , follows from the results obtained by Irvine and Duignan (1985). The viscosity of the fluid μ (given in units of Pa s) also varies with temperature, based on the following analytical expression (ASME 1968; Kestin et al. 1978; Rabinowicz et al. 1998a, b):

$$\mu = 0.00002414 \times 10^{\left(\frac{247.8}{T+133}\right)} \quad (8)$$

The pressure dependence of viscosity is not included, because it is small in the range of depth considered here (Norton 1984). Equation (8) shows that the fluid viscosity decreases from 17.5×10^{-5} to 13.5×10^{-5} Pa s in the 2–200 °C temperature interval. Above 200 °C, the viscosity remains approximately constant. In our model, the thermal conductivity λ_{eq} varies with temperature for each type of formation (crystalline rock, sandstone, shale). We used the experimental data provided by Clauser and Huenges (1995) for the thermal conductivities of sandstone, shale and quartz-rich crystalline rock between 0 and 300 °C. Finally, the other parameters such as the porosity ϕ , the heat capacity C of each phase (rock and fluid) and the density of each phase at 20 °C assigned to each geological formation are listed in Table 1.

Appendix 3: Method and Boundary Conditions

The simulations are performed using the Comsol Multiphysics™ finite-element code, which has already been tested and successfully implemented for convective process simulations in various configurations (Holzbecher 2004; Eldursi et al. 2009; Guillou-Frottier et al. 2013). A two-dimensional grid constituted of square elements of size $d = 200$ m was considered. Thus, given the dimensions of the basin, the grid is composed of 40 elements in the z direction and 1500 elements in the x direction. The ratio $0.8d/V_{\text{max}}$, where V_{max} represents the maximal amplitude of the Darcy velocity, determines the optimal time step at which the time evolution of the convective process can be realistically simulated.

The top of the model represents the surface topography of the Lake Chad basin, which is impermeable (the vertical velocity at the interface is zero) and maintained at a constant temperature of 20 °C. The bottom of the model consists of a quartz-rich substratum. It is maintained at a constant temperature of 247 °C and has a permeability low enough to be

considered as impermeable ($\sim 10^{-18} \text{ m}^2$). The flow and temperature along the lateral boundaries of the model are symmetric. All these chosen boundary conditions are the usual ones, except the flow condition along the top interface. Indeed, a real free condition would be mathematically more elegant. The latter condition is needed to adjust the depth of the piezometer (i.e. of the saturated zone) at each iteration, in order to obtain a zero pressure along that interface. That method is particularly costly and difficult to handle, because it does not necessarily ensure the incompressibility of the fluid. Besides, it is not necessarily justified as the depth of variation of the piezometer is small ($\sim 60 \text{ m}$) compared to the depth of the basin. Therefore, the pressure perturbation due to convection and surface topography is small in comparison with the lithostatic pressure variations in the basin. Accordingly, in our model, the coincidence of the surface topography with the piezometer results to be an acceptable first-order approximation (McKenzie et al. 1974). Besides, it is extremely cost-effective as it does not require internal iterations between two time steps of the temperature equation. As the program retrieves the pressure after each time step, we can a posteriori compute the height of the piezometer with first-order precision. Because the topography along the borders of the basin is not flat, local flows are generated and eventually combine with those developed by convection. Actually, they have a notable impact on the circulation recovered in the model over the Kadzell and Kanem area (Sect. 2).

Appendix 4: Evaluation of the Hydrological and Thermal Characteristics of Our Model

The maps of the fluid viscosity of the thermal expansion and of the effective thermal conductivity of the basin of our convective model are displayed in Fig. 16a–d. From these maps, we deduce that, within the Bima horizon, at the location of the P1 profile: $\gamma = 57 \text{ }^\circ\text{C km}^{-1}$, $K = 2 \times 10^{-13} \text{ m}^2$, $h = 400 \text{ m}$, $\alpha = 2.9 \times 10^{-4} \text{ }^\circ\text{C}^{-1}$, $\lambda_{\text{eq}} = 2.3 \text{ W }^\circ\text{C}^{-1} \text{ m}^{-1}$, $\mu = 5 \times 10^{-4} \text{ Pa s}$, and thus, the Rayleigh number is equal to 21 (Eq. 1). Alternatively, around P2: $\gamma = 62 \text{ }^\circ\text{C km}^{-1}$, $h = 900 \text{ m}$, $\alpha = 3.8 \times 10^{-4} \text{ }^\circ\text{C}^{-1}$, and $\mu = 3 \times 10^{-4} \text{ Pa s}$, and the Rayleigh number is equal to 230. Finally, to evaluate the vertical Rayleigh number of the whole basin above faults 5 and 6, we chose the following numbers: $\gamma = 43 \text{ }^\circ\text{C km}^{-1}$, $K = 10^{-14} \text{ m}^2$, $h = 4000 \text{ m}$, $\alpha = 2.6 \times 10^{-4} \text{ }^\circ\text{C}^{-1}$, $k = 2 \text{ W }^\circ\text{C}^{-1} \text{ m}^{-1}$, $\mu = 10^{-3} \text{ Pa s}$, and thus, the Rayleigh number is equal to 31. These numbers indicate that (a) convection likely develops in the Bima horizon outside the block separated by faults 1 and 2, and (b) the basin-wide cell is not split into smaller ones in the graben delimited by faults 5 and 6. Below Kanem, the evaluation of the effective Rayleigh number for the entire depth of the basin is more problematic, due to the permeability variations along the trajectory of the warm current. First, at the eastern border of the basin, the permeability of the contiguous Bima blocks is $2 \times 10^{-13} \text{ m}^2$ in a channel extending from 4 km to $\sim 700 \text{ m}$ depth. In that channel, the vertical Rayleigh number is ~ 380 (i.e. much greater than $4\pi^2$) and the mean vertical velocity is 10 cm year^{-1} .

Actually, in a real 3D geometry, hydrothermal convective currents parallel to the walls of the basin may develop (Rabinowicz et al. 1998a, b). Despite the $\sim 150\text{-m}$ -thick Fika formation (located eastward of fault 8, Fig. 3a), the warm current reaches the QPA through the zone of the Fika formation shift induced by throws of faults 7 and 8 (*ellipses* A and B in Fig. 3a). In the last $\sim 700\text{-m}$ -thick upper sediments, the intensity of the flow remains strong as the mean vertical velocity is $\sim 4 \text{ cm year}^{-1}$. The strength of this warm current

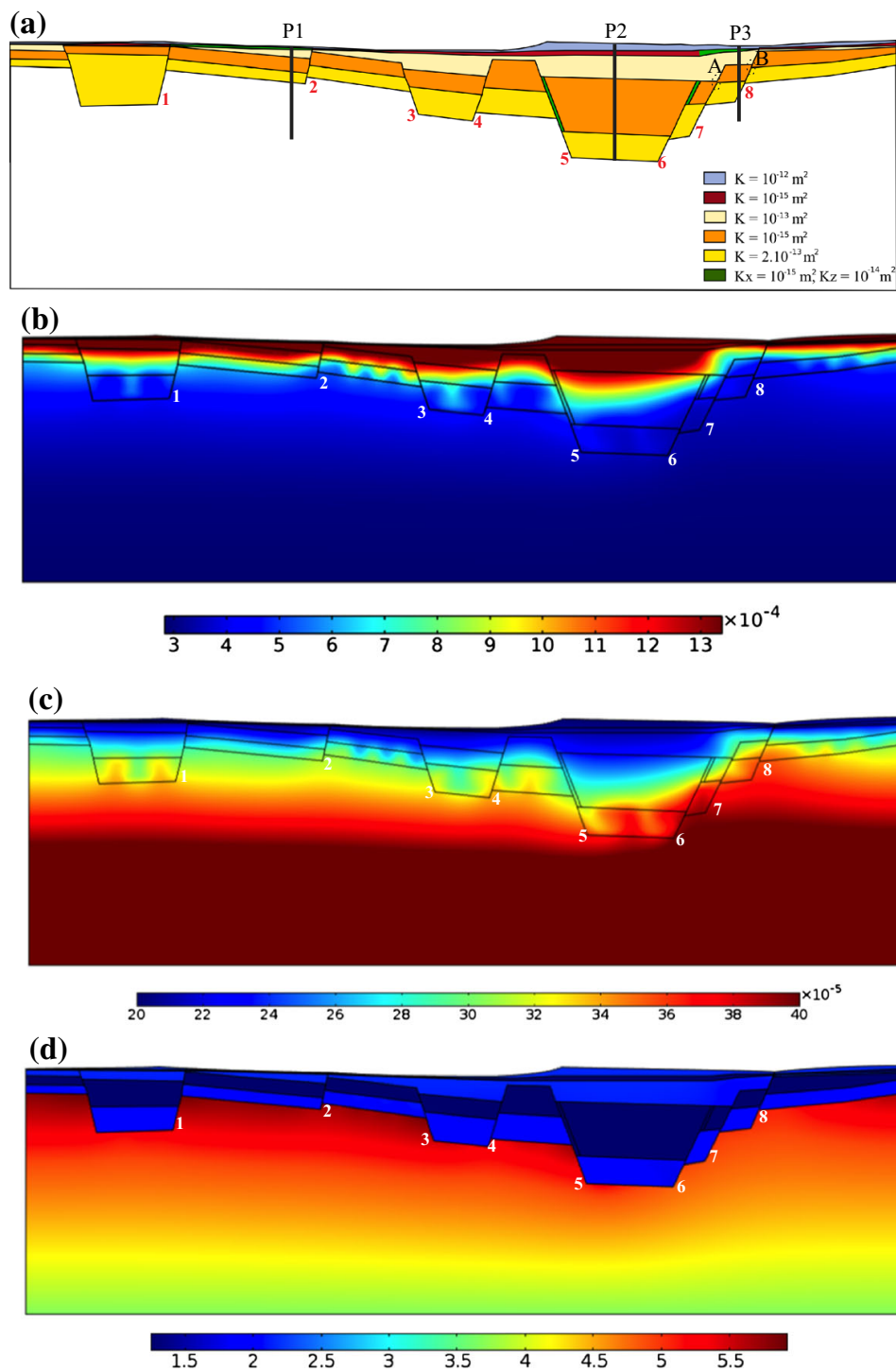


Fig. 16 Maps of the different physical parameters used for the modelling of the convective circulation in the Lake Chad basin: **a** permeability fields assigned to the different formations of the basin. *Dashed ellipses* highlight the stratigraphic throws of faults 7 and 8 that impact the Fika formation and *vertical black lines* highlight the location of temperature profiles P1, P2, P3 displayed in Fig. 10, **b** fluid viscosity field (in Pa s), **c** variations of the thermal expansion coefficient (in K^{-1}) with the temperature and **d** distribution of the effective thermal conductivity (in $\text{W m}^{-1} \text{K}^{-1}$) within the basin

explains the intensity of the backflow of the basin-wide convection, which reaches a horizontal velocity of 39 cm year^{-1} over the Kanem, and down to $\sim 7 \text{ cm year}^{-1}$ at Kadzell. The resulting top pressure drop from Kanem to Kadzell explains the piezometric level topography.

Finally, let us suppose that the ascending and descending convective velocities along the lateral border of the basin-wide cell are constant and have an intensity equal to V . Then, an analytical 1D solution for the steady temperature (Eq. 4) shows that:

$$T(z) = T_{\text{bottom}} + \gamma \frac{(1 - \exp(\pm Pe \frac{z}{h}))}{(1 - \exp(\pm Pe))} \quad (9)$$

and

$$dT(z)/dz = - \pm Pe \gamma \frac{\exp(\pm Pe \frac{z}{h})}{(1 - \exp(\pm Pe))} \quad (10)$$

where Pe represents the Péclet number, which is written as:

$$Pe = \frac{C_L h V}{\lambda_{\text{eq}}} \quad (11)$$

In Eqs. (9) and (10), z represents the height in the column of total thickness h , where the flow is ascending or descending, respectively. Over Kanem, $+V \sim 4 \text{ cm year}^{-1}$, $h \sim 700 \text{ m}$ and $\lambda_{\text{eq}} \sim 2 \text{ W } ^\circ\text{C}^{-1} \text{ m}^{-1}$ and thus $Pe \sim 1.9$. If we assume that $Pe \gg 1$, we see that:

$$dT(z = h)/dz \approx Pe \gamma \approx 1.9 \gamma \quad (12)$$

Alternatively, below Kadzell, where $V \sim -4 \text{ mm year}^{-1}$, $h \sim 1000 \text{ m}$ and $\lambda_{\text{eq}} \sim 2 - \text{W } ^\circ\text{C}^{-1} \text{ m}^{-1}$, $Pe \sim 0.3$. Therefore, assuming that $Pe \ll 1$, we see that:

$$dT(z = h)/dz = \exp(-Pe)\gamma \approx 0.75 \gamma \quad (13)$$

For Kadzell, close to the top of P1 profile, where the axis of the descending current associated with the basin-wide cell is approximatively located, the observed conductive heat flow is $\sim 110 \text{ mW m}^{-2}$ and the convective heat flow is $\sim 70 \text{ mW m}^{-2}$. These values show that the approximation deduced from Eq. (13) is valid. Over the Kanem, close to the top of the P3 profile, the conductive heat flow is $\sim 100 \text{ mW m}^{-2}$ and the convective one is $\sim 200 \text{ mW m}^{-2}$. The approximation given by Eq. (12), which is specifically valid for a fast ascending flow, leads to a good match with this last pair of heat flow values.

In Sect. 2, we emphasise that the mean heat flows at the top of our models are not significantly different when fluids circulate by convection and when the transport of heat at the surface is purely conductive: here 110 mW m^{-2} , instead of 90 mW m^{-2} . Actually, this result can be rationalised as follows. Along the interface of the sediment and the basement, inside the Bima formation, the mean horizontal velocity V of the $L \sim 240 \text{ km}$ basin-wide cell is $\sim 10 \text{ cm year}^{-1}$. Besides, the temperature contrast ΔT between the descending current along P1 and the basement is $\sim 30 \text{ } ^\circ\text{C}$ (Fig. 10). For a boundary layer approximation of the mean heat flow ϕ along a cooling plate (Turcotte and Schubert 2002):

$$\phi = 2\lambda_{\text{eq}}\Delta T \sqrt{\frac{C_L V}{\pi\lambda_{\text{eq}}L}} \approx 13 \text{ mW m}^{-2} \quad (14)$$

This expression correctly accounts for the difference of heat flows between the convective and conductive models.

References

- Antoine R, Baratoux D, Rabinowicz M, Fontaine FJ, Bachèlery P, Staudacher T, Saracco G, Finizola A (2009) Thermal infrared images analysis of a quiescent cone on Piton de La Fournaise volcano: evidence for a convective air flow within an unconsolidated soil. *J Volcanol Geotherm Res*. doi:[10.1016/j.jvolgeores.2008.12.003](https://doi.org/10.1016/j.jvolgeores.2008.12.003)
- Arad A, Kafri U (1974) Geochemistry of groundwaters in the Chad basin. *J Hydrol* 25:105–127
- Archambault J (1960) L'alimentation des nappes en Afrique Occidentale. *Cpt. R. de l'Hydro., Soc. Hydro. France*, 383
- Aranjossy J-F, Ndiaye B (1993) Formation of piezometric depressions in the Sahelian zone: study and modelling. *J Water Sci*. doi:[10.7202/705167ar](https://doi.org/10.7202/705167ar)
- ASME (1968) The 1967 ASME steam tables. *Nav Eng J*. doi:[10.1111/j.1559-3584.1968.tb04564.x](https://doi.org/10.1111/j.1559-3584.1968.tb04564.x)
- Avbovbo AA, Ayoola EO, Osahon GA (1986) Depositional and structural styles in Chad basin of North-eastern Nigeria. *Am Assoc Petrol Geol Bull* 70(12):1787–1798
- Bader J-C, Lemoalle J, Leblanc M (2011) Modèle Hydrologique du Lac Tchad. *Hydrol Sci J*. doi:[10.1080/02626667.2011.560853](https://doi.org/10.1080/02626667.2011.560853)
- Balmino G, Vales N, Bonvalot S, Briais A (2011) Spherical harmonic modeling to ultra-high degree of Bouguer and isostatic anomalies. *J Geod*. doi:[10.1007/s00190-011-0533-4](https://doi.org/10.1007/s00190-011-0533-4)
- Bruinsma S, Lemoine J-M, Biancale R, Valès N (2010) CNES/GRGS 10-day gravity field models (Release 2) and their evaluation. *Adv Space Res*. doi:[10.1016/j.asr.2009.10.012](https://doi.org/10.1016/j.asr.2009.10.012)
- Byrne GF, Begg JE, Fleming PM, Dunin FX (1979) Remotely sensed land cover temperature and soil water status—a brief review. *Remote Sens Environ*. doi:[10.1016/0034-4257\(79\)90029-4](https://doi.org/10.1016/0034-4257(79)90029-4)
- Carroll D (1959) Ion exchange in clays and others minerals. *Bull Geol Soc Am*. doi:[10.1130/0016-7606\(1959\)70\[749:IEICAO\]2.0.CO;2](https://doi.org/10.1130/0016-7606(1959)70[749:IEICAO]2.0.CO;2)
- Cartwright JA, Dewhurst DN (1998) Layer-bound compaction faults in fine-grained sediments. *Bull Geol Soc Am*. doi:[10.1130/0016-7606\(1998\)110<1242:LBCFIF>2.3.CO;2](https://doi.org/10.1130/0016-7606(1998)110<1242:LBCFIF>2.3.CO;2)
- Chapelle FH (2000) The significance of microbial processes in hydrogeology and geochemistry. *Hydrogeol J*. doi:[10.1007/PL00010973](https://doi.org/10.1007/PL00010973)
- Clauser C, Huenges E (1995) Thermal conductivity of rocks and minerals. In: Ahrens TJ (ed) *Rock physics and phase relations: a handbook of physical constants*. American Geophysical Union, Washington. doi:[10.1029/RF003p0105](https://doi.org/10.1029/RF003p0105)
- Cretaux J-F, Birkett C (2006) Lake studies from satellite radar altimetry. *C R Geosci*. doi:[10.1016/j.crte.2006.08.002](https://doi.org/10.1016/j.crte.2006.08.002)
- Descloitres M, Chalikakis K, Legchenko A, Moussa AM, Genthon P, Favreau G, Le Coz M, Bouchera M, Oï M (2013) Investigation of groundwater resources in the Komadugu Yobe Valley (Lake Chad basin, Niger) using MRS and TDEM methods. *J Afr Earth Sci* 87:71–85
- Dieng B, Ledoux E, de Marsily G (1990) Paleohydrogeology of the Senegal sedimentary basin: a tentative explanation of the piezometric depressions. *J Hydrol* 118:357–371
- Eberschweiler C (1993) Monitoring and management of groundwater resources in the Lake Chad basin: mapping of aquifers water resource management—final report. R35985, CBLT-BRGM, France
- Eldursi K, Branquet Y, Guillou-Frotier L, Marcoux E (2009) Numerical investigation of transient hydrothermal processes around intrusions: heat-transfer and controlled mineralization patterns. *Earth Planet Sci Lett*. doi:[10.1016/j.epsl.2009.09.009](https://doi.org/10.1016/j.epsl.2009.09.009)
- Fontaine FJ, Rabinowicz M, Boulègue J, Jouniaux L (2002) Constraints on hydrothermal processes on basaltic edifices: inferences on the conditions leading to hydrovolcanic eruptions at Piton de la Fournaise, Réunion Island, Indian Ocean. *Earth Planet Sci Lett*. doi:[10.1016/S0012-821X\(02\)00599-X](https://doi.org/10.1016/S0012-821X(02)00599-X)
- Garven G (1995) Continental-scale groundwater flow and geologic processes. *Annu Rev Earth Planet Sci* 23:89–117
- Garven G, Freeze A (1984a) Theoretical analysis of the role of groundwater flow in the genesis of stratabound ore deposits. 1. Mathematical and numerical model. *Am J Sci* 284:1085–1124
- Garven G, Freeze A (1984b) Theoretical analysis of the role of groundwater flow in the genesis of stratabound ore deposits. 2. Quantitative results. *Am J Sci* 284:1125–1174
- Gaston A (1996) The pastoral vegetation of the Lake Chad basin. In: CIRAD (ed) *Livestock Atlas of the Lake Chad basin*. Centre Technique de Cooperation Agricole et Rurale, Wageningen, pp 39–56
- Gay A, Lopez M, Cochonat P, Sermondadaz G (2004) Polygonal faults-furrows system related to early stages of compaction—upper Miocene to recent sediments of the Lower Congo basin. *Basin Res*. doi:[10.1111/j.1365-2117.2003.00224.x](https://doi.org/10.1111/j.1365-2117.2003.00224.x)
- Genik GJ (1993) Regional framework, structural and petroleum aspects of rift basins in Niger, Chad and the Central African Republic (C.A.R.). *Tectonophysics*. doi:[10.1016/0040-1951\(92\)90257-7](https://doi.org/10.1016/0040-1951(92)90257-7)

- Genthon P, Rabinowicz M, Foucher J-P, Sibuet J-C (1990) Hydrothermal circulation in an anisotropic sedimentary basin: application to the Okinawa Back Arc basin. *J Geophys Res.* doi:[10.1029/JB095iB12p19175](https://doi.org/10.1029/JB095iB12p19175)
- Greigert J (1979) Atlas des Eaux Souterraines du Niger—Tome 1, fascicule VII: La Nappe Pliocène et le système phréatique du Manga, BGRM
- Griffin DL (2006) The late Neogene Sahabi rivers of the Sahara and their climatic and environmental implications for the Chad basin. *J Geol Soc.* doi:[10.1144/0016-76492005-049](https://doi.org/10.1144/0016-76492005-049)
- Guidale R, Bala AE, Ikpokonte AE (2011) Preliminary estimates of the hydraulic properties of the Quaternary aquifer in N'Djaména area, Chad republic. *J Appl Sci.* doi:[10.3923/jas.2011](https://doi.org/10.3923/jas.2011)
- Guillou-Frottier L, Carre C, Bourguin B, Bouchot V, Genter A (2013) Structure of hydrothermal convection in the Upper Rhine Graben as inferred from corrected temperature data and basin-scale numerical models. *J Volcanol Geotherm Res.* doi:[10.1016/j.jvolgeores.2013.02.008](https://doi.org/10.1016/j.jvolgeores.2013.02.008)
- Gvirtzman H, Garven G, Gvirtzman G (1997) Thermal anomalies associated with forced and free groundwater convection in the Dead Sea rift valley. *Geol Soc Am Bull.* doi:[10.1130/0016-7606\(1997\)109<1167:TAAWFA>2.3.CO;2](https://doi.org/10.1130/0016-7606(1997)109<1167:TAAWFA>2.3.CO;2)
- Holzbecher E (2004) Free convection in open-top enclosures filled with a porous medium heated from below. *Numer Heat Transf Part A Appl.* doi:[10.1080/10407780490474726](https://doi.org/10.1080/10407780490474726)
- Idso SB, Schmugge TJ, Jackson RD, Reginato RJ (1975) The utility of surface temperature measurements for the remote sensing of surface soil waters status. *J Geophys Res.* doi:[10.1029/JC080i021p03044](https://doi.org/10.1029/JC080i021p03044)
- Irvine TF, Duignan MR (1985) Isobaric thermal expansion coefficients for water over large temperature and pressure ranges. *Int Commun Heat Mass.* doi:[10.1016/0735-1933\(85\)90040-5](https://doi.org/10.1016/0735-1933(85)90040-5)
- Isiorho SA, Matisoff G, When KS (1996) Seepage relationships between Lake Chad and the Chad aquifers. *Ground Water.* doi:[10.1111/j.1745-6584.1996.tb02076.x](https://doi.org/10.1111/j.1745-6584.1996.tb02076.x)
- Kestin J, Sokolov M, Wakeham WA (1978) Viscosity of liquid water in the range -8°C to 150°C . *J Phys Chem.* doi:[10.1063/1.555581](https://doi.org/10.1063/1.555581)
- Kilty K, Chapman DS (1980) Convective heat transfer in selected geologic situations. *Ground Water.* doi:[10.1111/j.1745-6584.1980.tb03413.x](https://doi.org/10.1111/j.1745-6584.1980.tb03413.x)
- Kopf AJ (2002) Significance of mud volcanism. *Rev Geophys.* doi:[10.1029/2000RG000093](https://doi.org/10.1029/2000RG000093)
- Leblanc M, Razack M, Dagorne D, Mofor L, Jones C (2003) Application of Meteosat thermal data to map soil infiltrability in the central part of the Lake Chad basin, Africa. *Geophys Res Lett.* doi:[10.1029/2003GL018094](https://doi.org/10.1029/2003GL018094)
- Leblanc M, Favreau G, Maley J, Nazoumou Y, Leduc C, Stagnitti F, van Oevelen PJ, Delclaux F, Lemoalle J (2006) Reconstruction of Megalake Chad using shuttle radar topographic mission data. *Palaeogeogr Palaeoclimatol.* doi:[10.1016/j.palaeo.2006.01.003](https://doi.org/10.1016/j.palaeo.2006.01.003)
- Leduc C (1991) Les ressources en eau du département de Diffa, Projet PNUD-DCTCDNER/86/001/. Direction Départementale de l'Hydraulique de Diffa, Diffa
- Leduc C, Loireau M (1997) Fluctuations piézométriques et évolution du couvert végétal en zone sahélienne (sud-ouest du Niger). Sustainability of Water Resources under Increasing Uncertainty. In: Proceedings of the Rabat Symposium S1, IAHS, 240
- Luo X, Vasseur G (2002) Natural hydraulic cracking: numerical model and sensitivity study. *Earth Planet Sci Lett.* doi:[10.1016/S0012-821X\(02\)00711-2](https://doi.org/10.1016/S0012-821X(02)00711-2)
- Maduabuchi C, Faye S, Maloszewski P (2006) Isotope evidence of palaeorecharge and palaeoclimate in the deep confined aquifers of the Chad basin, NE Nigeria. *Sci Total Environ* 370:467–479
- Mahe G, Leduc C, Amani A, Patrel J-E, Girard S, Servat E, Dezetter A (2003) Augmentation récente du ruissellement de surface en région soudano-sahélienne et impact sur les ressources en eau. Hydrology of the Mediterranean and Semiarid Regions, Proceedings of an international symposium, IAHS, 278
- Mainsant G, Jongmans D, Chambon G, Larose E, Baillet L (2012) Shear-wave velocity as an indicator for rheological changes in clay materials: lessons from laboratory experiments. *Geophys Res Lett.* doi:[10.1029/2012GL053159](https://doi.org/10.1029/2012GL053159)
- McKenzie DP, Roberts JM, Weiss NO (1974) Convection in the earth's mantle: towards a numerical simulation. *J Fluid Mech.* doi:[10.1017/S0022112074000784](https://doi.org/10.1017/S0022112074000784)
- Neal JT, Langer AM, Kerr PF (1968) Giant desiccation polygons of Great Basin playas. *Bull Geol Soc Am.* doi:[10.1130/0016-7606\(1968\)79\[69:GDPOGB\]2.0.CO;2](https://doi.org/10.1130/0016-7606(1968)79[69:GDPOGB]2.0.CO;2)
- Norton DL (1984) Theory of hydrothermal systems. *Annu Rev Earth Planet Sci* 12:155–177
- Nwankwo CN, Ekine AS (2010) Geothermal gradients in the Chad basin, Nigeria, from bottom hole temperature logs. *Sci Afr* 9(1):37–45
- Olivry JC, Chouret A, Vuillaume G, Lemoalle J, Briquet JP (1996) Hydrologie du lac Tchad. *Monogr Hydrol* 12:266
- Olugbemiro OR, Ligouis B (1999) Thermal maturity and hydrocarbon potential of the Cretaceous (Cenomanian-Santonian) sediments in the Bornu (Chad) basin, NE Nigeria. *Bull Soc Géol France* 170(5):759–772

- OSS-UNESCO (2001) Les ressources en eau des pays de l'Observatoire du Sahara et du Sahel: évaluation, utilisation et gestion. Rapport UNESCO, p 88
- Poucllet A, Durand A (1983) Structures cassantes Cénozoïques d'après les phénomènes volcaniques et néotectoniques au nord-ouest du lac Tcahd (Niger Oriental). *Ann Soc Géol Nord CIII (France)*, pp 143–154
- Pribnow D, Schellschmidt R (2000) Thermal tracking of upper crustal fluid flow in the Rhine Graben. *Geophys Res Lett*. doi:[10.1029/2000GL008494](https://doi.org/10.1029/2000GL008494)
- Quintard M, Bernard D (1986) Free convection in sediments. In: Burrus J (ed) *Thermal modeling in sedimentary basins*. Editions Technip, Paris, pp 271–286
- Rabinowicz M, Boulègue J, Genthon P (1998a) Two- and three-dimensional modeling of hydrothermal convection in the sedimented Middle Valley segment, Juan de Fuca Ridge. *J Geophys Res*. doi:[10.1029/98JB01484](https://doi.org/10.1029/98JB01484)
- Rabinowicz M, Sempéré J-C, Genthon P (1998b) Thermal convection in a vertical permeable slot: Implications for hydrothermal circulation along mid-ocean ridges. *J Geophys Res*. doi:[10.1029/1999JB900259](https://doi.org/10.1029/1999JB900259)
- Ramillien G, Biancale R, Gratton S, Vasseur X, Bourgogne S (2011) GRACE-derived surface mass anomalies by energy integral approach. Application to continental hydrology. *J Geod*. doi:[10.1007/s00190-010-0438-7](https://doi.org/10.1007/s00190-010-0438-7)
- Ramillien G, Seoane L, Frappart F, Biancale R, Gratton S, Vasseur X, Bourgogne S (2012) Constrained regional recovery of continental water mass time-variations from GRACE-based geopotential anomalies over South America. *Surv Geophys*. doi:[10.1007/s10712-012-9177-z](https://doi.org/10.1007/s10712-012-9177-z)
- Ramillien G, Frappart F, Seoane L (2014) Application of the regional water mass variations from GRACE satellite gravimetry to large-scale water management in Africa. *Remote Sens*. doi:[10.3390/rs6087379](https://doi.org/10.3390/rs6087379)
- Roche MA (1980) *Traçage naturel isotopique et salin des eaux du système hydrologique du Lac Tchad*, Paris
- Sabins LF (1999) *Remote sensing: principles and interpretation*. W. H. Freeman, San Francisco
- Schneider JL (1969) *Carte hydrogéologique de la République du Tchad*, B.R.G.M
- Schneider JL, Wolff JP (1992) *Carte Géologique et Hydrogéologique à 1/1 500 000 de la république du Tchad*. Mémoire explicatif, B.R.G.M
- Schroeter P, Gear D (1973) *Etude des ressources en eau du bassin du Lac Tchad en vue d'un programme de développement*. FAO-PNUD-CBLT, Rome
- Schuster M, Roquin C, Durringer P, Brunet M, Cagny M, Fontugne M, Mackaye HT, Vignaud P, Ghienne J-F (2005) Holocene Lake Mega-Chad palaeoshorelines from space. *Quat Sci Rev*. doi:[10.1016/j.quascirev.2005.02.001](https://doi.org/10.1016/j.quascirev.2005.02.001)
- Schwinka V, Moertel H (1999) Physicochemical properties of illite suspensions after cycles of freezing and thawing. *Clays Clay Miner* 47:718–725
- Sclater JG, Christie PAF (1980) Continental stretching: an explanation of the post-mid-Cretaceous subsidence of the central North Sea basin. *J Geophys Res*. doi:[10.1029/JB085iB07p03711](https://doi.org/10.1029/JB085iB07p03711)
- Serafeimidis K, Anagnostou G (2015) The solubilities and thermodynamic equilibrium of anhydrite and gypsum. *Rock Mech Rock Eng*. doi:[10.1007/s00603-014-0557-1](https://doi.org/10.1007/s00603-014-0557-1)
- Sylvia DM (2004) *Principles and applications of soil microbiology*, 2nd edn. Pearson Prentice Hall, New Jersey
- Turcotte DL, Schubert G (2002) *Geodynamics*, 2nd edn. Cambridge University Press, Cambridge
- Zairi R (2008) *Etude géochimique et hydrodynamique de la nappe libre du Bassin du Lac Tchad dans les régions de Diffa (Niger oriental) et du Bornou (nord-est du Nigeria)*. Ph.D. thesis

5.3 Permeability and voids influence on the thermal signal, as inferred by multitemporal UAV-based infrared and visible images (Journal of Hydrology)



Research papers

Permeability and voids influence on the thermal signal, as inferred by multitemporal UAV-based infrared and visible images



Raphael Antoine^{a,*}, Cyrille Fauchard^a, Jean-François Oehler^b, Philippe Joignant^c

^a ENDSUM Research Team, Centre d'Etudes et d'Expertise sur les Risques l'Environnement, l'Aménagement et la Mobilité (CEREMA), 10, chemin de la Poudrière, 76140 Le Grand Quevilly, France

^b Service Hydrographique et océanographique de la Marine (SHOM), CS 92803 29228 BREST CEDEX 2, France

^c Grand Port Maritime du Havre (GPMH), Terre-plein de la Barre, 76600 Le Havre, France

ARTICLE INFO

This manuscript was handled by Corrado Corradini, Editor-in-Chief, with the assistance of Frédéric Huneau, Associate Editor

Keywords:

Remote Sensing
Thermal infrared
Photogrammetry
infiltration
Subsurface cavity
Natural hazards
UAV

ABSTRACT

This work presents for the first time associated thermal anomalies and deformations over subsurface cavities/voids located within two harbour quays in Le Havre Harbour, Normandy, France. An U.A.V. (Unmanned Aerial Vehicle) was used to acquire visible and thermal images over a diurnal cycle (from 7 a.m. to 5 p.m.). The visible images were processed to realize an altimetric model of the platforms by mean of the photogrammetric method, while the thermal infrared (TIR) images were used to study the evolution of their surface temperatures. The obtained 3D model shows the location of five topographic depressions on both quays. The analysis of the evolution of the surface thermal field leads to the detection of cold thermal anomalies that are (1) not correlated to surface properties, and (2) spatially associated to the flanks of the five topographic depressions. Using a 2D conductive-radiative model, we show that these anomalies are not directly due to the thermally insulating effect of an air-filled area. Finally, we conclude that preferential infiltration and subsequent evaporation in the micro-fracturation present within the flanks of the depressions may be responsible for the strong cooling of these zones.

1. Introduction

Subsurface cavities/voids are important safety and economical issues for land-use planning. In this context, the identification/characterization of these objects remains an important challenge for stakeholders as well as for scientists. Recently, in situ measurements techniques made important progress to detect anthropic or natural subsurface cavities (Kaufmann et al., 2011; Vadillo et al., 2012; Kaufmann and Romanov, 2016; Benavente et al., 2017; Kolesnikov and Fedin, 2018; Vargemezis et al., 2019; Rahnema et al., 2020). For instance, Artugyan et al. (2020) combined Ground Penetrating Radar (GPR) and Electrical Resistivity Imagery (ERI) to detect and characterize a karst massif in Romania (rock stratification and orientation, sections of these caves galleries and level of karstification). Martinez-Moreno et al. (2018) located a cave in Mira de Aire-Santo Antonio Range (Portugal) using micro-gravity and ERI 3D-inversions. De Giorgi and Leucci (2014) imaged shallow subsurface structures, including karstic features below a road in the Salento Peninsula (Apulia region – South Italy), carrying out a Seismic Refraction Tomography and GPR survey. Integrated interpretation led to the delineation of hazard zone

rich with karstic features and cavities. Mochales et al. (2008) proposed a methodology based on the sequential application of magnetic, GPR and microgravity techniques to detect underground cavities and dolines. Cardarelli et al. (2009) used the joint interpretation of ERI and seismic refraction tomography to map artificial cavities in the city of Rome. Finally, in situ soil temperature sensors were also deployed to detect subsurface cavities. Interestingly, Mosciki (2006) shown that thermal anomalies associated to underground cavities can reach up to 1 °C from field measurements and numerical modelling. Although in situ measurements are very useful on a local scale, they remain difficult to implement on important surfaces and thus are economically unviable.

Remote sensing have also adressed the problem of subsurface cavities for many years, using aerial or satellite observations (Ruth and Degner, 1963; Peters et al., 1996; Youssef et al., 2012; Lee et al., 2016; Kim et al., 2019; Jeffery et al., 2020). For instance, Youssef et al. (2020) integrated remote sensing (LANDSAT imagery) with ERI to characterize the role of agriculture in the formation of sinkholes in Saudi Arabia. Chang and Hanssen (2014) characterized the deformations associated to the upward migration of underground cavities under the city of

* Corresponding author.

E-mail address: raphael.antoine@cerema.fr (R. Antoine).

URL: <https://www.cerema.fr/fr/innovation-recherche/recherche/equipes/endsum-evaluation-non-destructive-structures-materiaux> (R. Antoine).

<https://doi.org/10.1016/j.jhydrol.2020.124907>

Received 20 December 2019; Received in revised form 25 March 2020; Accepted 27 March 2020

Available online 03 April 2020

0022-1694/ © 2020 Elsevier B.V. All rights reserved.

Heerlen (The Netherlands), using satellite radar interferometry. Edmonds et al. (1987) demonstrated the potentialities of detection of collapse and subsidence features in chalk and other limestone rocks with an airborne multispectral scanner and thermal infrared (TIR) data. This last method allows to map the surface temperatures of a soil using a camera. Several teams in the world have shown the importance of TIR method to map geological structures (Watson, 1975; Sabins, 2007; Nasipuri et al., 2005), hydrothermal systems (Antoine et al., 2009; Gaudin et al., 2013), to characterize water resources in arid zones (Leblanc et al., 2007; Lopez et al., 2016) or to detect underground burning coal (Vasterling and Meyer, 2013). Campbell et al. (1996) used airborne TIR method to locate hydrological features in karst watersheds. Gunn et al. (2008) detected abandoned mineshafts in former mining areas after a TIR survey in Great Britain. To our knowledge, although several studies have assessed the potentiality of the TIR method for the characterization of subsurface cavities (Rinker, 1975; Wynne et al., 2008; Lee et al., 2016), few is known about the origin of the observed thermal anomalies, especially when slight subsidence is observed. As a consequence, the methodology to adopt to detect these objects before a collapse event remains unclear. In 2014, a TIR and visible survey was performed above two parts of the Joannes Couvert platform (Le Havre Harbour), the West and East Quays (hereafter named as WQ and EQ), respectively. These structures were selected because of the continuous formation of subsurface voids. For each area, the observations were acquired with an UAV during a semi-diurnal cycle, allowing the TIR monitoring of the surface temperatures (from sunrise to late afternoon) and the acquisition of visible images. After a presentation of the geotechnical context and the methodology used for this survey, the surface temperatures and the altimetric map obtained by photogrammetry are shown for the WQ and EQ. Cold areas associated to surface deformations are detected on both quays, with a temperature contrast of 2–4 °C compared to the surrounding environment. The effect of the surface properties (thermal inertia, albedo) on the thermal signal are first investigated, as they represent the main factors affecting the surface temperatures of the soil. Then, a simplified 2D conductive-radiative model of heat transfer is developed within one quay, namely the EQ, in order to evaluate the direct thermal influence of a subsurface cavity on the surface temperatures. Finally, the last section is dedicated to the analysis of the role of potential fluid flow on the measured signal across the deformed quays.

2. Geotechnical context

Le Havre harbour is built in the Northern part of the estuary of the Seine river (in Le Havre city, Normandy) and is essentially composed of heterogeneous materials resulting from the World War 2 bombing. The study sites (the West and East quays, hereafter named the WQ and EQ) are located at the center of the harbour and is part of the Joannes Couvert quay (Fig. 1). This kilometer-size platform was part of the famous Transatlantic Cruise Terminal in the 1930s. The building plan of the quays is known and in particular, the backfills are massively composed of the war debris (stones and fines materials). Over the years, the infiltration of salted water (associated to storms and tides) within the structure lead to the withdrawal of the fine particules from the quays and generated the formation of subsurface cavities, as well as local surface subsidences (Fig. 2).

The Fig. 3 shows the structure of the WQ and the EQ, respectively. The WQ is mainly composed of concrete backfill, a concrete slab and backfill between 0 m and 9.50 m. Interestingly, the internal structure of the EQ is very different, and essentially constituted of:

- Limestone masonry in its lower part (under 0 m a.m.s.l.);
- a concrete pile and a coarse concrete wall between 0 m and 9.50 m;
- a backside backfill forming the major part of the quay volume above 0 m.

Both quays are covered with pavement having an approximate thickness of 10 cm (Fig. 1a and b). Various indices can be observed at the surface of the structures:

- Pavement (the main constituent of the quay);
- Metallic materials (such as railways);
- Unconsolidated backfills employed to fill previous subsidences;
- Dark asphalt patches;
- Sparse local vegetation.

3. Field survey and methodology

3.1. Photogrammetric survey

Here, our first objective is to detect surface deformations associated to potential subsurface voids, using altimetric data. To do so, a photogrammetric survey of the EQ and WQ was performed on October 2014. We used a drone equipped with a SONY NEX-5R digital camera (vertically positioned) and acquiring images (4912*3264 px). The focal length of the camera is 16 mm (35 mm equivalent: 24 mm) and the sensor size is 23,4 x 15,6 mm. The survey was realized along a pre-defined flight plan, with a longitudinal acquisition at a height above ground of 20 m (Fig. 4). This lead to a surface image footprint of 30*20 m and a resolution of about 5 mm. The UAV flew at a speed of $\approx 1 \text{ m} \cdot \text{s}^{-1}$, with longitudinal and transversal overlaps of the images of 80%. Finally, a total of 194 and 165 images was acquired for the EQ and the WQ, respectively.

The altimetric maps of the quays were calculated using the photogrammetric approach. The 3D reconstruction of a scene is realized from photographs taken at arbitrary angles (Quinn, 1948). For this purpose, the open-source Apero-MicMac code developed by the French National Geographical Institute (IGN) was used (Deseilligny and Cléry, 2011). The processing of the data follows three steps:

- Detection of keypoints and matching between images using the SIFT algorithm (Lowe, 2004) (Tapioca module);
- Calibration of the camera's internal parameters and determination of the 3D positions and orientations of the viewpoints (Snavely et al., 2008). This step also allows the user to georeference manually the model using Ground Control Points (GCPs). At this stage, a 3D undensified point cloud is produced (TAPAS module);
- Dense matching: densification of the point cloud calculated during the TAPAS processing (Furukawa and Ponce, 2010) (MALT module).

The Tapioca processing leads to the detection of an average value of 10000 keypoints per image and for each quay. After this step, the model was georeferenced thanks to Ground Control Points (GCPs) within the Tapas module. For this purpose, we used 29 and 31 GCPs (visible targets from the uav) on the EQ and WQ, respectively (figure). These points were georeferenced using a D-RTK GNSS receptor and were homogeneously placed on the quays. The quality of the measurements was quantified by comparing these data with those obtained using the leveling network of Le Havre Harbour. The comparison was realized on 19 and 15 points for the WQ and EQ, respectively. As a result, for the WQ, the mean error is $0.008 \text{ m} \pm 0.007 \text{ m}$ in the X direction, $0.018 \text{ m} \pm 0.012 \text{ m}$ in the Y direction and $0.043 \text{ m} \pm 0.018 \text{ m}$ in the Z direction. For the EQ, the mean error is $0.007 \text{ m} \pm 0.007 \text{ m}$ in the X direction, $0.021 \text{ m} \pm 0.007 \text{ m}$ in the Y direction and $0.027 \text{ m} \pm 0.017 \text{ m}$ in the Z direction. Finally, during the Tapas processing, the residual error for the 3D positioning and orientation of the Tapas module is 0.8 pixel for both quays (this value has to be lower than 1 pixel).

3.2. TIR survey

The TIR method allows to map the surface temperatures of a surface

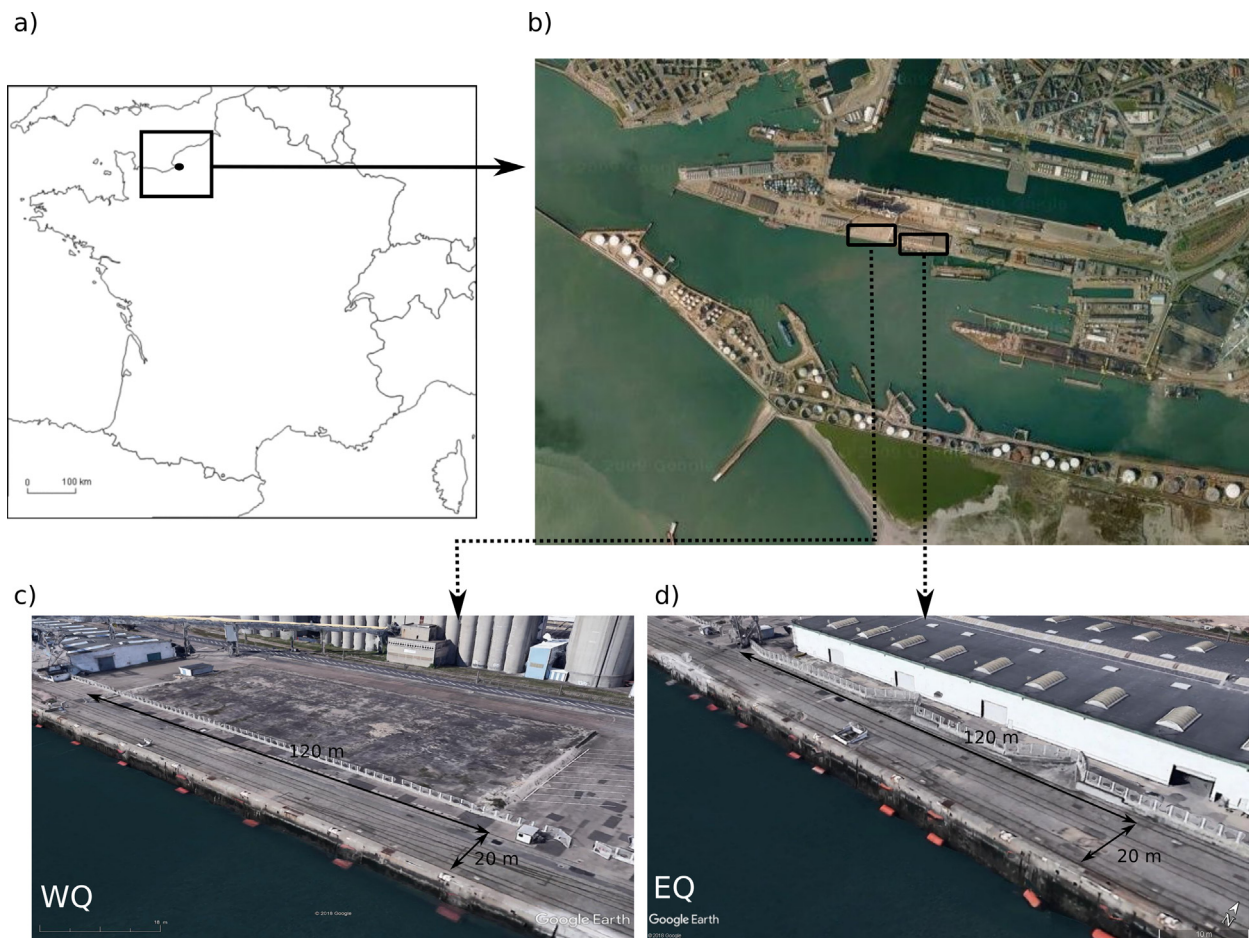


Fig. 1. Location of the studied site in Normandy, France.

using a thermal camera. For a given soil, when no flow occurs, many thermophysical and geometrical properties may control the diurnal cycle thermal signal: the thermal inertia I ($J \cdot m^{-2} \cdot K^{-1} \cdot s^{-1/2}$) is the principal parameter controlling the amplitude and the shape of these thermal oscillations (Watson, 1975; Mellon et al., 2000; Putzig and Mellon, 2007) and albedo (or reflectivity) controls the average temperature (Fig. 5). Eventually, when steep topography is present (for instance, with crest and valleys), the surface temperatures may also be influenced by the geometry of the surfaces, due to their orientation regarding the incident solar radiation (Whiteman et al., 1989; Khesin and Eppelbaum, 1994; Eppelbaum et al., 2014). In the case of the WQ and EQ, the absence of steep slopes prevents from the generation of important thermal gradients associated to topography.

Thermal inertia represents the ability of the material to conduct and store the incident solar radiation at depth during the day, and re-emit this energy during the night. It depends on the porosity and the pore size. For instance, rocks or compacted soils typically have high values of thermal inertia, while loosely packed soils with fine grains exhibit lower values of thermal inertia. Thus, when observed with a thermal camera, compacted soils are warmer than loosely packed materials during daytime, while the opposite situation is observed during nighttime. This characteristic has been used for years with success for geological mapping (Sabins and Floyd, 1969; Watson, 1973; Watson, 1975; Majumdar, 2003; Nasipuri et al., 2005), using satellite and airborne thermal imagery. Thermal inertia is defined as a combination of the thermal conductivity k ($W \cdot m^{-1} \cdot K^{-1}$), the density ρ ($W \cdot m^{-3}$) and the heat



Fig. 2. Photo of typical collapse and deformation observed these last years on the Joannes Couvert quay.

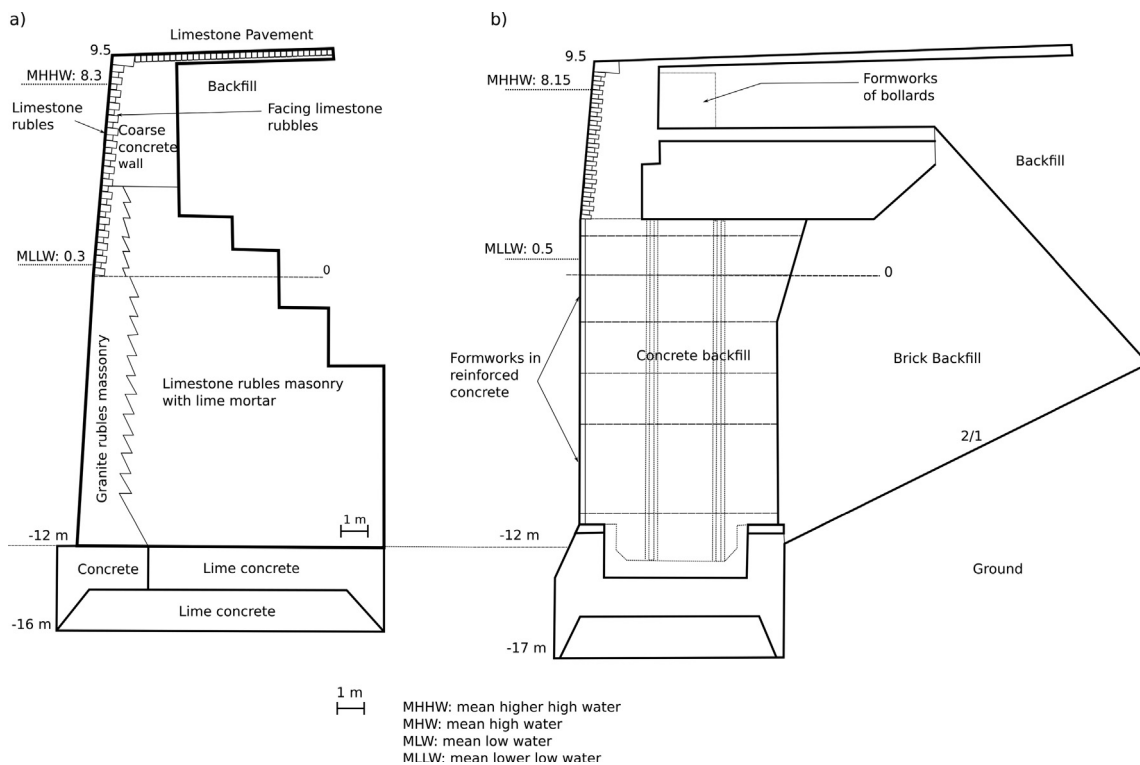


Fig. 3. Sketch of internal structure of the quays (a) EQ and (b) WQ.

capacity c_p ($W.kg^{-1}.K^{-1}$):

$$I = \sqrt{k\rho c_p}$$

As the volumetric heat capacity (ρc_p) has a low variability for soils and rocks [Mermoud, 2006], the principal factor controlling the thermal inertia I is thus the thermal conductivity k .

(1)

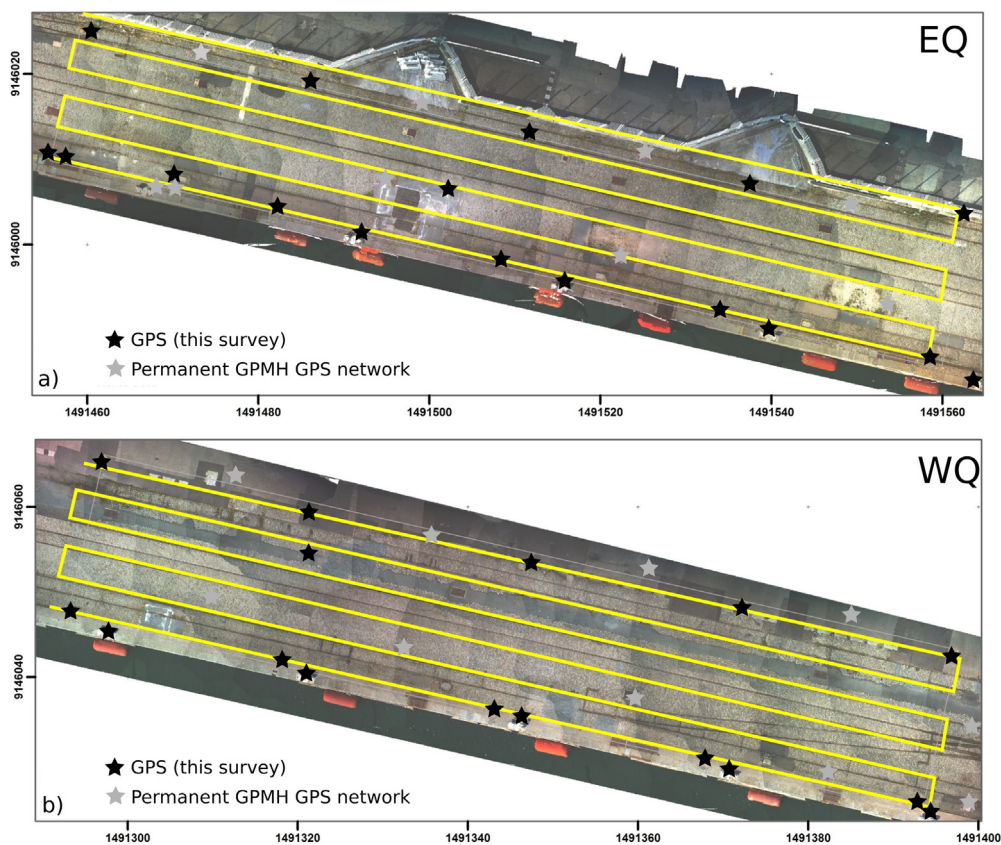


Fig. 4. Sketch of the flight plan used during the survey, superimposed with an aerial view of the quays: (a) EQ and (b) WQ.

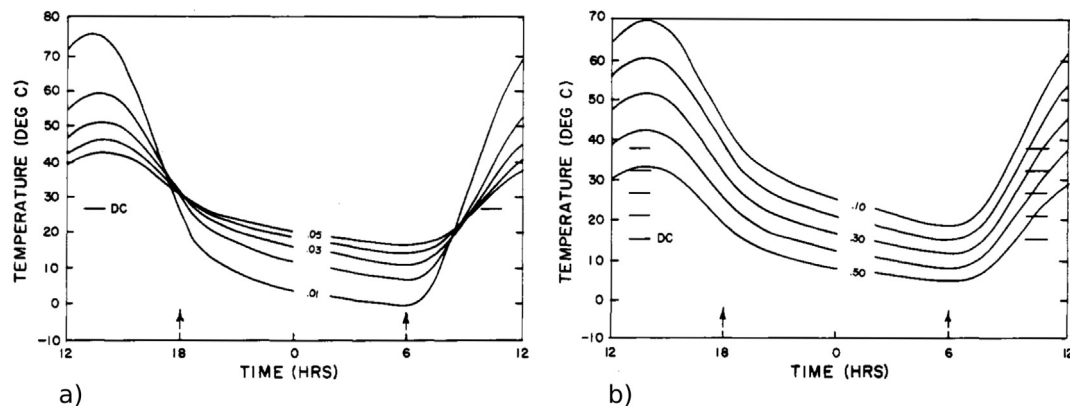


Fig. 5. Influence of the thermal inertia and albedo on the surface temperatures (after Watson, 1975).

In the presence of a flow, the influence of surface properties (thermal inertia and albedo) on the temperature is reduced, due to the mass movement of the fluid bringing or extracting heat from the soil. The efficiency of the heat transfer depends on the nature of the fluid and the soil (in fact their volumetric heat capacity ratio and their thermal conductivity) and also on the Darcy velocity of the fluid, controlled by the permeability of the soil (Antoine et al., 2009). Thus, we define a thermal anomaly as a thermal behavior which cannot be explained by surface properties such as thermal inertia or albedo. This methodology has already been successfully used in some of our works for hydrogeological applications from field works and satellite data (Antoine et al., 2009; Antoine et al., 2017; Lopez et al., 2016).

A thermal infrared campaign was realized at the same moment than the photogrammetric one (i.e. in October 28th 2014). An Optris PI400 Lightweight thermal camera was used on-board the UAV to measure the surface temperature of the soil from 7h15 am to 16h30 pm (sunrise around 7h30 during the survey). This led to the acquisition a time series of 9 images for each quay. During the survey, the weather was clear (thus allowing the flight of the drone), with a small amount of rain and moderate precipitation was observed from October 20th to 24th on the Harbour. During this month, the atmospheric temperature varied from 10° to 17° and the monthly mean temperature remained quasi-stable.

The PI400 thermal camera uses an uncooled microbolometer technology to measure radiations in the range [7–14 μm] and its thermal sensitivity is 0.08°. The size of the sensor is 382*288 pixels sensor, with a Field of View (FOV) value of 29° x 22°. Thus, at a height of 150 m, the camera is able to acquire a thermal scene of a whole quay, with a pixel size of 40 cm.

The surface temperatures measured by the camera are corrected from the effects of the relative humidity of the air, the atmospheric temperature and the distance of the target using the relationships provided by Optris. Most of the building materials have emissivity parameter ranging from 0.90 to 0.96 [Thermoworks, 2018]. Thus, a mean emissivity of 0.93 was used to correct the surface temperature from the effect of emissivity. The thermal images were then orthorectified using the ARCGIS software and georeferenced with the soil targets, as well as remarkable objects on the thermal images (rails, quay borders, etc...).

4. Altimetry of the quays

The Fig. 6 displays the altimetric maps obtained after the photogrammetric processing, as well as longitudinal and transverse profiles of the EQ and WQ, respectively (P1 and P2, Fig. 6b and d). Each map is overlaid with a simplified internal structural characteristics of the quay. Both quays exhibit an increase of the altitude towards land, from 9.32 m to 9.90 m in the case of the EQ and from 9.41 to 10 m for the WQ. The EQ longitudinal profile shows the presence of four altimetric anomalies at the front of the quay (e.g. depressions named AAE1 to

AAE4). These depressions have a nearly similar morphology with the same depth-over-horizontal distance ratio. The largest subsidence reaches up to 15 cm (AAE3) over a distance of 30 m. The deepest one is AAE1, with a vertical amplitude of 10 cm over a distance of 2 m in the transverse direction (i.e. a slope of (i.e. a slope of 3°)). Interestingly, the subsidences occur at the boundary between the backfill and the front concrete wall (Fig. 3). For the WQ, two topographic depressions are observed at the back of the WQ (AAW1 and AAW2), with an amplitude reaching 10 cm over a distance of ≈ 2 m (i.e. a slope of 3°). Here, the subsidence occurs at the boundary between the quay and the land. Note that the depressions are not symmetric, with the presence of a steep slope (the Southern one) and a softer one (Northern slope). This morphology may reflect the heterogeneous conditions within the quays (from a lithological, structural and geomechanical point of view).

5. Observation of surface temperatures

In this section, temperature maps of the WQ and EQ are presented. As mentioned in Section 3.2, a time series of 9 images was acquired for each quay. For the sake of clarity, we only show four snapshots acquired at 7h45, 10h40, 13 h and 16h30 (Fig. 7):

- The first temperature map presented here was obtained at 7h45. It reveals temperatures with a minimum of 5.4 °C and a maximum of 11.5 °C for the quays (Fig. 7a and b). At that time, the most distinguishable objects on the WQ and EQ are the railways (yellow to red colored lineaments on the image), with a temperature around 7 °C
- At 10h40, more than 2 h after sunrise, the soil is warming up (Fig. 7c and d). The surface temperature is observed in the range [7.5 °C–14.5 °C]. Asphalt patches appear in red on the WQ and EQ (warmer objects), with temperatures between 10 °C and 14 °C: indeed their very low albedo permits the absorption of an important amount of solar radiation during the morning and their quick warming. Surprisingly, elongated cold areas appear on both quays (TAW1, TAW2 and TAE1), with a direction parallel to the structure and with a temperature around 9 °C. It is of note that this signal is not distinguishable in the early morning (7h45).
- During the afternoon (13 h and 16h30, Fig. 7e to h), this cold zone become more and more noticeable on the WQ with a temperature of about 14 °C, i.e. with a maximum temperature contrast reaching 2–3 °C, compared with the surrounding environment. The same phenomenon is observed on the EQ: three cold areas (TAE1 to TAE3) are perceptible at the front of the structure at 13 h, with some of them parallel to the direction of the quay (TAE1 and TAE2). They reach a similar temperature contrast than the WQ with their surrounding environment, i.e. about 2–3 °C. In the following sections, we assess the influence of thermal inertia and albedo on the generation of the surface temperatures of the WQ and EQ and intent to explain the origin of the TAE1-TAE3 and TAW1-TAW2 cold zones. It

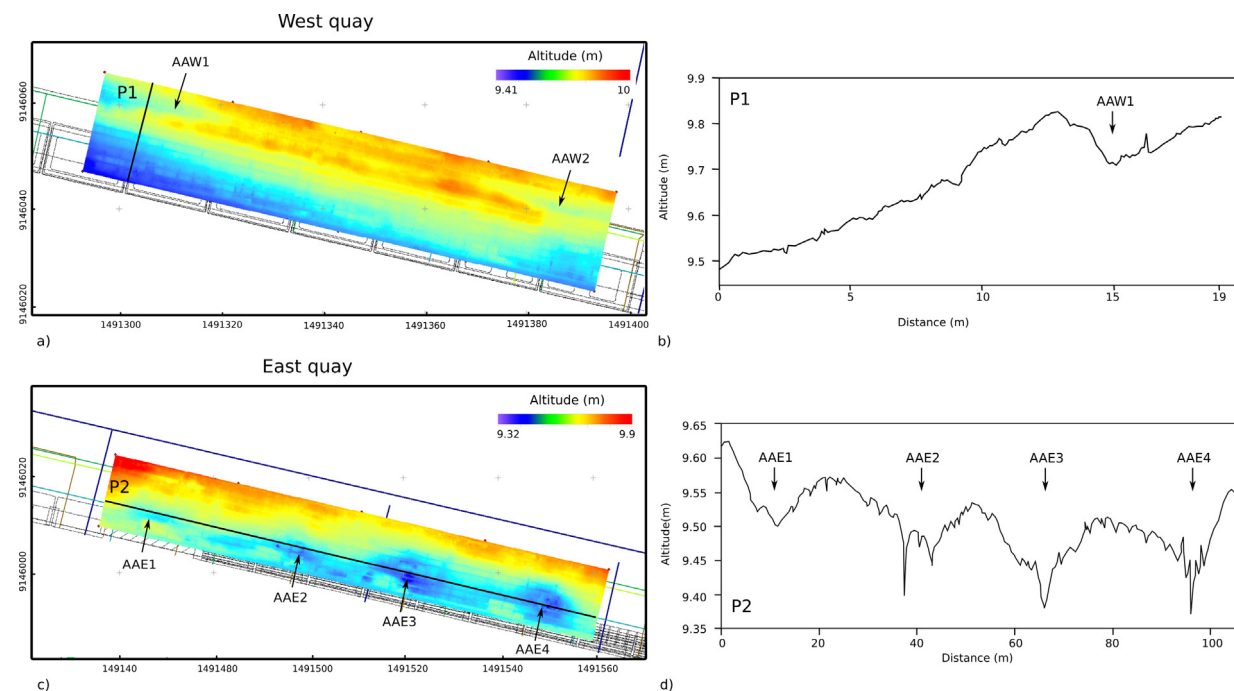


Fig. 6. Altimetric maps and measured topographic profiles of (a), (b) WQ (P1 profile) and (c), (d) EQ (P2 profile), respectively.

is of note that the size of these thermal anomalies is at least 2 m in the transverse direction, i.e. easily analysable given the resolution of our temperature images (0.4 m).

5.1. Temperatures explained by surface properties

Fig. 8 displays the altimetry data (Fig. 8a and d), the thermal images

acquired at 13 h (Fig. 8b and a) classification of all indices present on the WQ and EQ (Fig. 8c and f). These images are superimposed with a simplified structural map of the quays. As expected, at the first order, the essential part of the thermal patterns observed in Section 5 can be explained by the presence of different materials on the quays (i.e. asphalt, backfill, metal, concrete or vegetation) (Fig. 8c and f).

The Fig. 9 displays several examples of temperatures controlled by

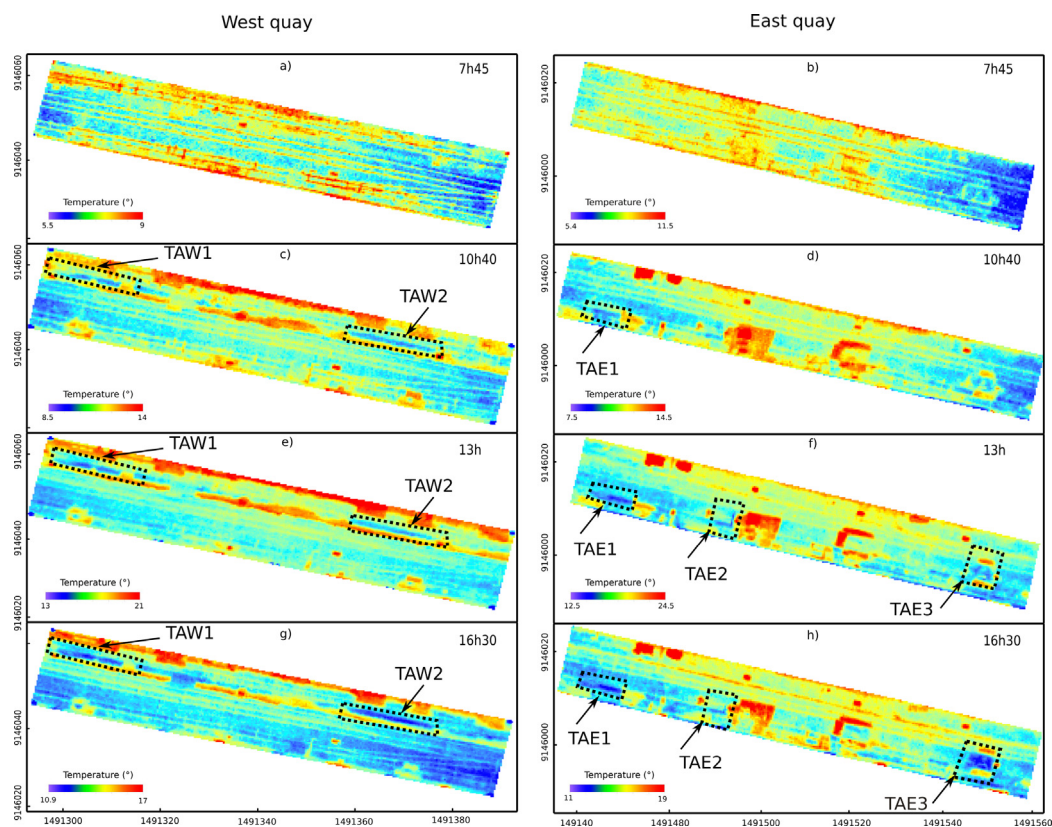


Fig. 7. Temperature maps obtained on the WQ and EQ, respectively, during a semi-diurnal cycle.

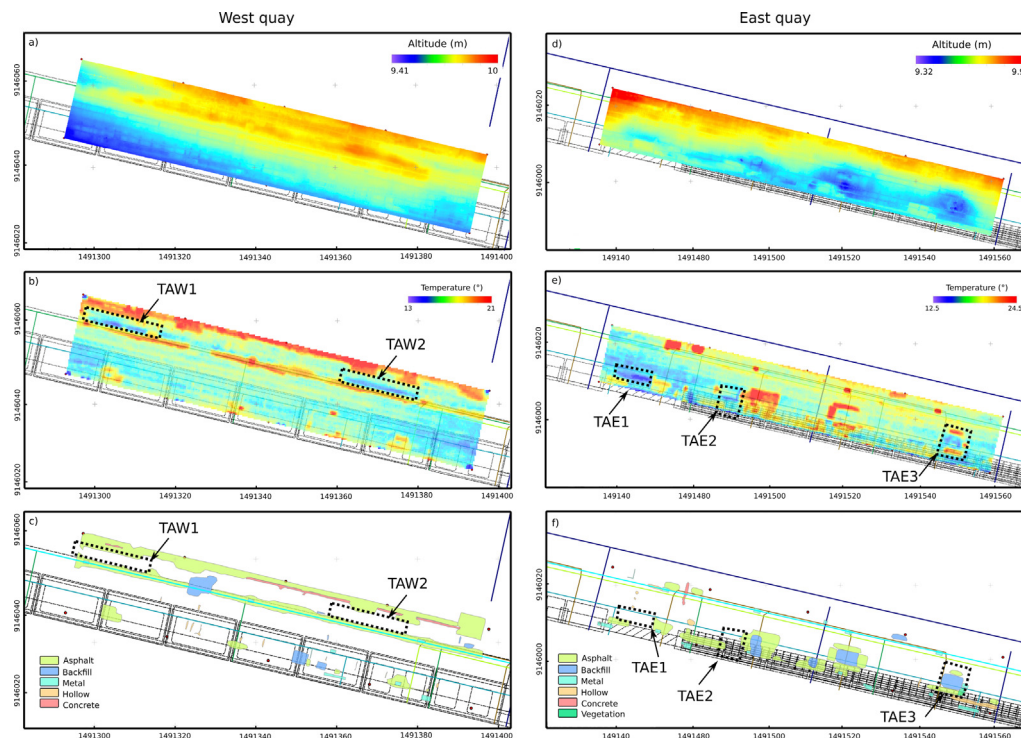


Fig. 8. Comparison between (a), (d) the altimetric map, (b), (e) the surface temperatures and (c), (f) the surface indices obtained from visual inspection of the WQ and EQ, respectively. The images are superimposed with a simplified structural map of the quays.

surface properties. The influence of thermal inertia may be seen in Fig. 9a (as shown theoretically in Fig. 5a): due to their high thermal inertia compared to the pavement, the railways appears warmer before sunrise and cooler during daytime (with a contrast up to 1.5 °C). Such observation is consistent with several previous results obtained using a TIR camera (Watson, 1975; Sabins, 2007; Mellon et al., 2000; Antoine et al., 2009). On the other hand, dark colored material like asphalt having a low albedo ($A = 0.07$) may appear warmer than the pavement ($A = 0.23$) during the whole measurement time (Fig. 9b, as presented theoretically in Fig. 5b) (Watson, 1975; Sabins, 2007).

Finally, vegetation also have a distinct thermal behavior, as illustrated in Fig. 9c. Plants appear slightly cooler than the pavement during daytime (from noon), while being warmer during nighttime. In that case, as described by Sabins (2007) and Whitehead et al., 1986, transpiration lowers the leaf temperature and makes vegetation appearing cooler than soils during daytime. During the night, the insulating effect of air within the leaves and the important water content allow to retain heat, resulting in warm nighttime signature. Finally, it is worth noting the conflicting effect of transpiration with thermal inertia in the vegetation surface temperature. Indeed, plants have a lower thermal inertia than soils due to (1) lower densities and thermal conductivities of foliage compared to mineral constituents (Gates, 1980 and Hillel, 1982), and (2) lower heat capacities for foliage compared to both mineral constituents and organic matter in soil (Hillel, 1982).

5.2. Temperatures not explained by surface properties

When closely analyzing the Fig. 8c and f, TAE1, TAE2, TAW1 and TAW2 are all located on the same pavement. Thus, thermal inertia variations can not be invoked to explain the important temperature contrasts of 2–3 °C on the same material. Fig. 9d and e display an example of temperature evolution for TAW1 and TAE1. These signals have a similar evolution, being several degrees cooler than the pavement during nighttime and daytime, which is not consistent with a variation controlled by thermal conductivity.

The thermal behavior of TAE3 is interesting (Fig. 9f): first, it is

characterized by a cold anomaly like the others, but the material is different (i.e. backfill, Fig. 8e and f). Second, TAE3 is cooler than the surrounding pavement during daytime. Nevertheless, unconsolidated/loosely packed materials are known to have a lower thermal inertia than solid rocks like pavements (due to a lower thermal conductivity and density, Mellon et al., 2000; Putzig and Mellon, 2007). As a consequence, they may appear warmer than solid rocks during the day, which is the opposite of our observation. This last finding definitely rules out the role of thermal inertia on the signal variation.

The Fig. 10 presents a zoom on the surface at the locations of TAW1, TAW2, TAE1 and TAE2. It is clear that no particular contrast in color is observed on the pavement able to explain the thermal spatial variations. Moreover, as the pavement is made with the same limestone material, it is doubtful that emissivity variations may explain such thermal contrasts for both quays.

Our data suggest a good correlation between the thermal anomalies and the topographic depressions present on both quays, except for AAE3, where no significant thermal contrast is observed within the backfill (even though the material thermally evolves in the same way than TAE3). The Fig. 11 presents an example of comparison between a transverse topographic profile and a thermal profile for the WQ (T1, Fig. 11a and b) the EQ (T2, Fig. 11c and d). Interestingly, the minimum of temperature appears to be spatially related with the flank of the deformations for both cases. This finding may not be justified by a thermal effect associated to the topography of these depressions for several reasons: (1) because of the weak amplitude of the subsidences, preventing for the occurrence of shadows (Section 4) and (2) because of the E-W orientation of the quays, which may receive the same amount of energy on their whole surfaces during daytime. This last idea is difficult to reconcile with the presence of E-W elongated thermal anomalies on the quays.

Finally, together, these observations are correlated with the structure of the quays, as mentioned in Section 4 and illustrated in Figs. 3 and 11: boundary between the internal concrete wall and the backfill for the EQ and boundary between the quay and the land for the WQ, inducing elongated thermal anomalies. Such limits may represent

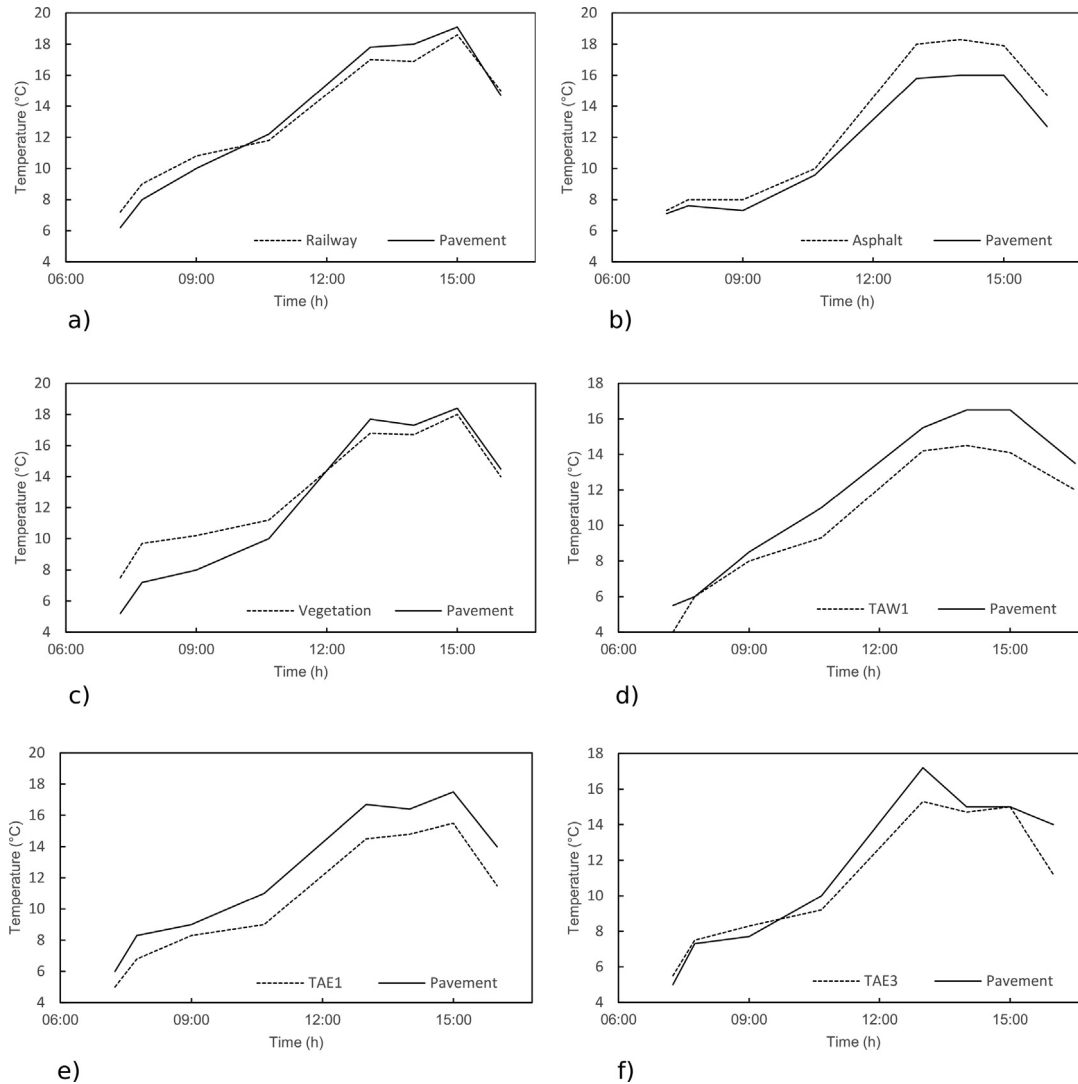


Fig. 9. Comparison of temperature evolutions for different materials on the WQ and EQ, illustrating the predominant influence of several parameters/processes on the surface temperature (a) thermal inertia (see Fig. 5(a), (b)) albedo (see Fig. 5(b) and (c)) impact of the vegetation. Figures (d), (e) and (f) show the temperature evolution of TAW1, TAE1 and TAE3 with their surrounding environment, respectively.

fragile areas for the generation of subsurface voids. In the next sections, we investigate the influence of subsurface process on the thermal signal.

6. Thermal influence of an insulating subsurface cavity within the quays: 2D conductive-radiative numerical modelling

The previous section shows that the observed TAW1, TAW2, TAE1 and TAE2 thermal anomalies (1) may not be explained neither by a contrast of thermal inertia associated to a different material, nor by albedo contrasts and (2) are correlated with topographic depressions associated to potential subsurface cavities or decompressed areas. As a consequence, a subsurface process must be associated to this anomalous signal. In order to show the influence of a thermally insulating body within the quay, a 2D conductive-radiative numerical simulation of the EQ is realized. Our objective is to assess the first-order surface temperature signal induced by a simplified air-filled area at depth.

6.1. Equations and surface energy budget

In the following, we review the basic 2-D equations describing the diurnal temperature profile $T(x,z,t)$ through the quay (x designates the

horizontal distance (m), z represents the depth (m) and t the time (s), respectively). We solve the transient conductive heat equation with the finite elements scheme (second order in time and space) for a soil layer of thickness $d = 9.5$ m, with a spatial resolution of 1 cm and time step of 5 min. The astronomical, geographical and optical parameters of the model, their assumed values and their units are summarized in Table 1. This model is based on the equations published in Antoine et al. (2009), and extended in 2D in this study, using the COMSOL Multiphysics numerical suite (Heat Transfer module). The simulation were done for a transverse section of the quay to save computer time. This assumption may be valid from a physical point of view, as the length over width ratio of the quay is important. The simulations, performed for the EQ, take into account the geometry of the structure and a scheme of the numerical model is given in Fig. 12. The quay exhibits a complex geo-technical configuration (including backfill, limestone rubles, granite rubles, limestone pavement, coarse concrete wall) (Fig. 3). In order to simplify the modelling, four categories of dry materials were considered: limestone (C1, C2, C5 in Fig. 12), concrete (C3), granite (C4) and backfill (C6). The values of the physical parameters used for these materials (thermal conductivity, density, heat constant) are given in Table 2.

The transient temperature in the soil, $T(x, z, t)$ is solution of the

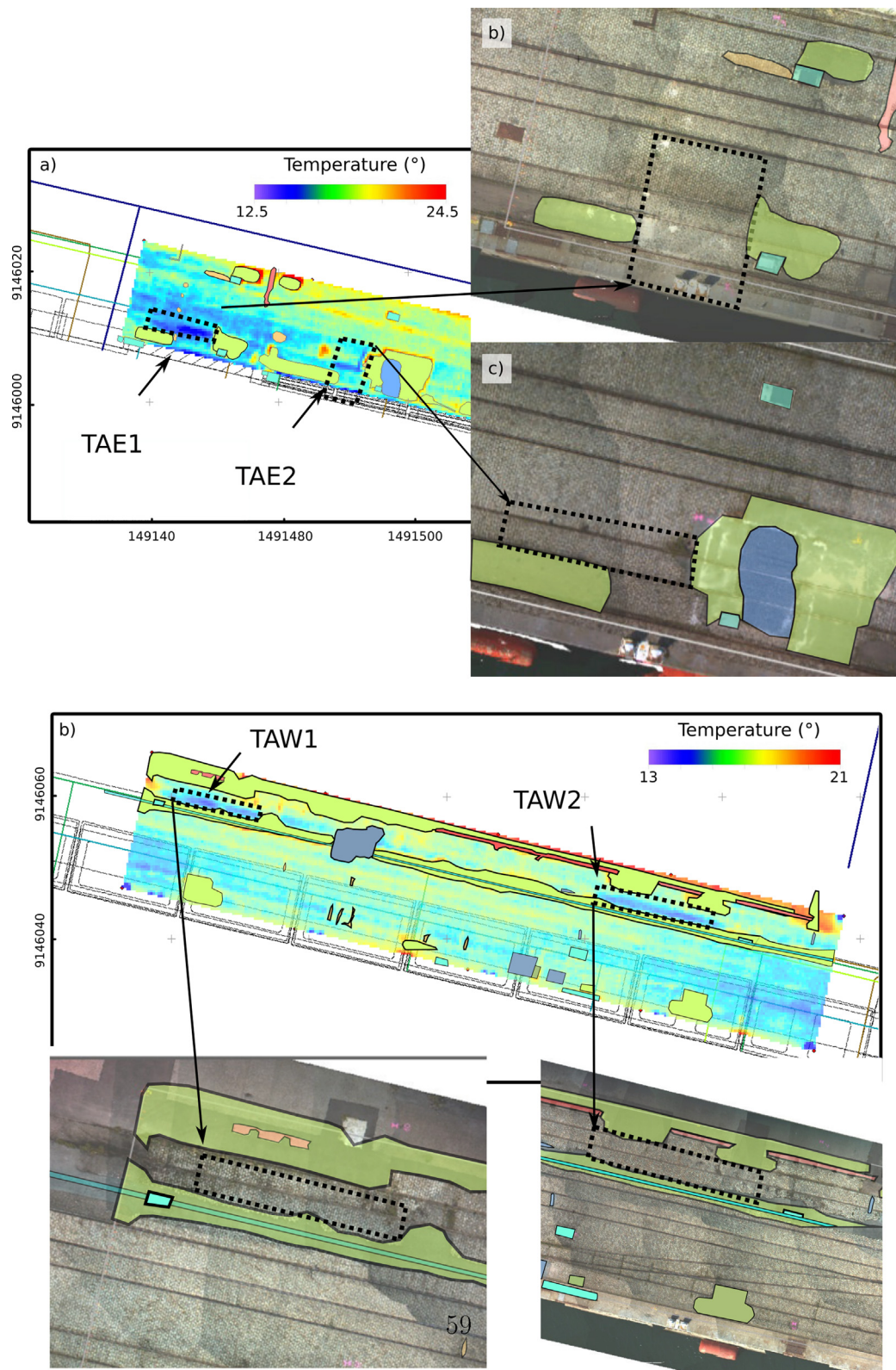


Fig. 10. Example of non-correlation between temperature anomalies and albedo.

equation:

$$\frac{\partial T(x, z, t)}{\partial t} = \kappa \left(\frac{\partial^2 T(x, t)}{\partial x^2} + \frac{\partial^2 T(z, t)}{\partial z^2} \right) \quad (2)$$

where x is the horizontal distance (m), z is the depth (m), t is the time (s) and κ is the thermal diffusivity of the soil, which is related to the

thermal conductivity k , the heat capacity C_p and the mass density ρ of the soil through:

$$\kappa = \frac{k}{\rho C_p} \quad (3)$$

A zero heat flux condition is set at the lower boundary of the model.

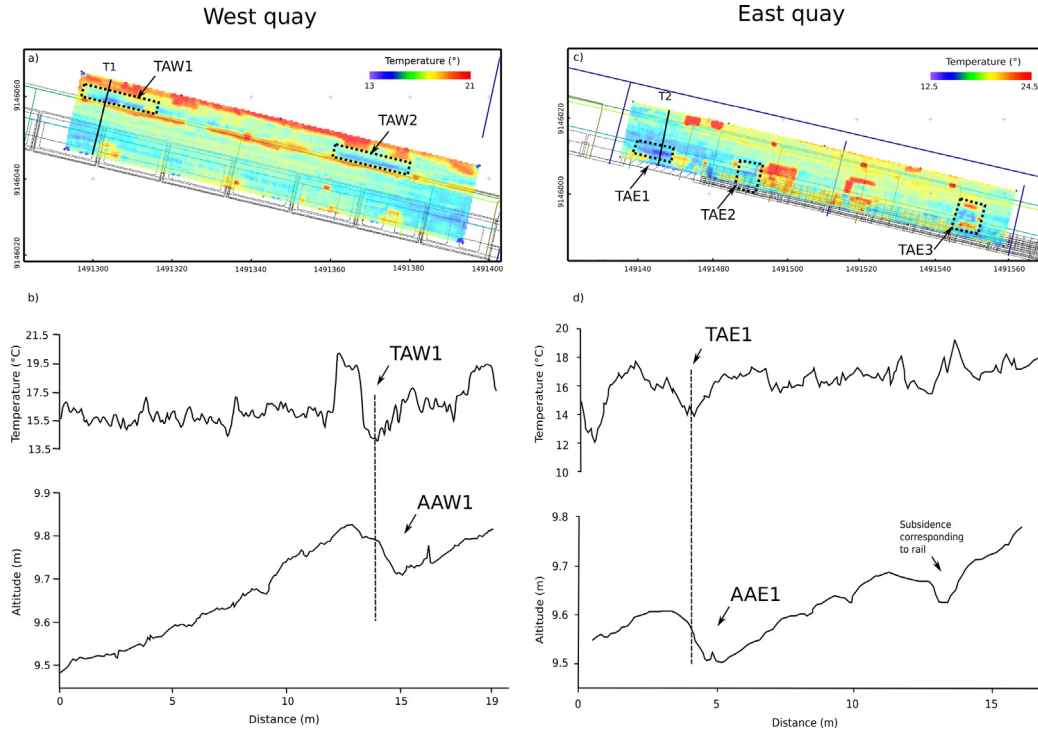


Fig. 11. Comparison between the thermal anomaly and the topographic profile for TAW1 (WQ) and TAE1 (EQ).

Table 1

Physical parameters and units related to the conductive-radiative model.

Solar constant	S_0	1367 W m^{-2}
Direct + diffuse energy fraction at the soil	C	0.5
Latitude of Le Havre Harbour	λ	20°S
Day number of the year (October, 28th)	J	113
Solar declination	δ	0.2 rad
Emissivity	ϵ	0.93
Stefan-Boltzman Constant	σ	$5.67 \times 10^{-8} \text{ W m}^{-2} \text{ K}^{-4}$
Air thermal conductivity	k_a	$2 \times 10^{-2} \text{ W m}^{-1} \text{ K}^{-1}$
Mean air temperature	T_0	12°C
Amplitude of the air temperature	T_{amp}	7.5°C
Phase shift	t_{ph}	3600 s
Duration of the diurnal cycle	P_{dc}	86400 s

For a flat surface, the surface temperature during a diurnal cycle depends on the solar heat flux (I_s), the soil radiative emission (I_e), and the atmospheric radiative flux (I_l). Thus, the boundary condition at the surface is given from the balance of solar, atmospheric and emitted radiations (Watson, 1973):

Table 2

Physical parameters and units related to the materials used in the numerical model (from EngineeringToolbox, 2003 and Javadi et al., 2018). Concerning the thermal conductivities, the values in bracket are the ones taken for the modelling.

Density of the limestone (C1, C2 and C5)	ρ_b	2500 kg m^{-3}
Limestone heat constant	c_b	$830 \text{ J kg}^{-1} \text{ K}^{-1}$
Limestone thermal conductivity	k_b	$1.26 - 1.33 (1.3) \text{ W m}^{-1} \text{ K}^{-1}$
Density of the concrete (C3)	ρ_b	2300 kg m^{-3}
Concrete heat constant	c_b	$1100 \text{ J kg}^{-1} \text{ K}^{-1}$
Concrete thermal conductivity	k_b	$1 - 1.8 (1.5) \text{ W m}^{-1} \text{ K}^{-1}$
Density of the granite (C4)	ρ_b	2600 kg m^{-3}
Granite heat constant	c_b	$770 \text{ J kg}^{-1} \text{ K}^{-1}$
Granite thermal conductivity	k_b	$1.7 - 4 (3) \text{ W m}^{-1} \text{ K}^{-1}$
Density of the backfill (C6)	ρ_b	1500 kg m^{-3}
Backfill heat constant	c_b	$1000 \text{ J kg}^{-1} \text{ K}^{-1}$
Backfill thermal conductivity	k_b	$0.8 - 2.4 (1.5) \text{ W m}^{-1} \text{ K}^{-1}$

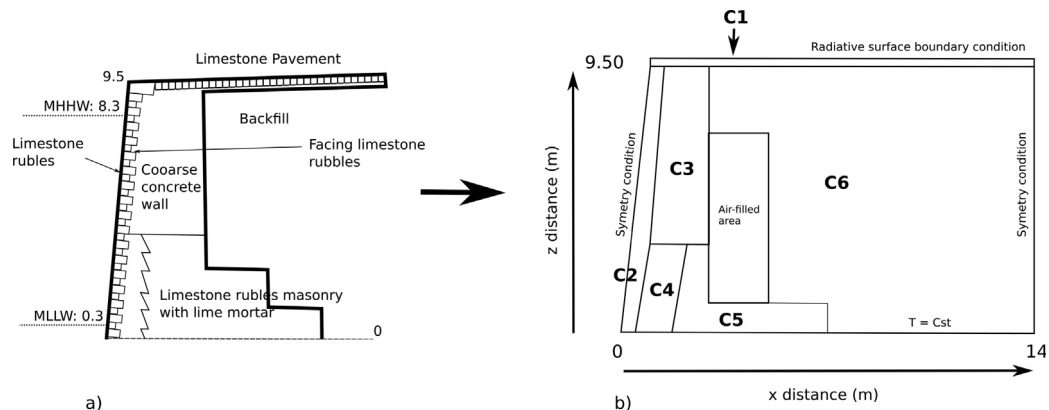


Fig. 12. (a) Section of the EQ used for the conception of the numerical model and (b) Scheme of the thermal model.

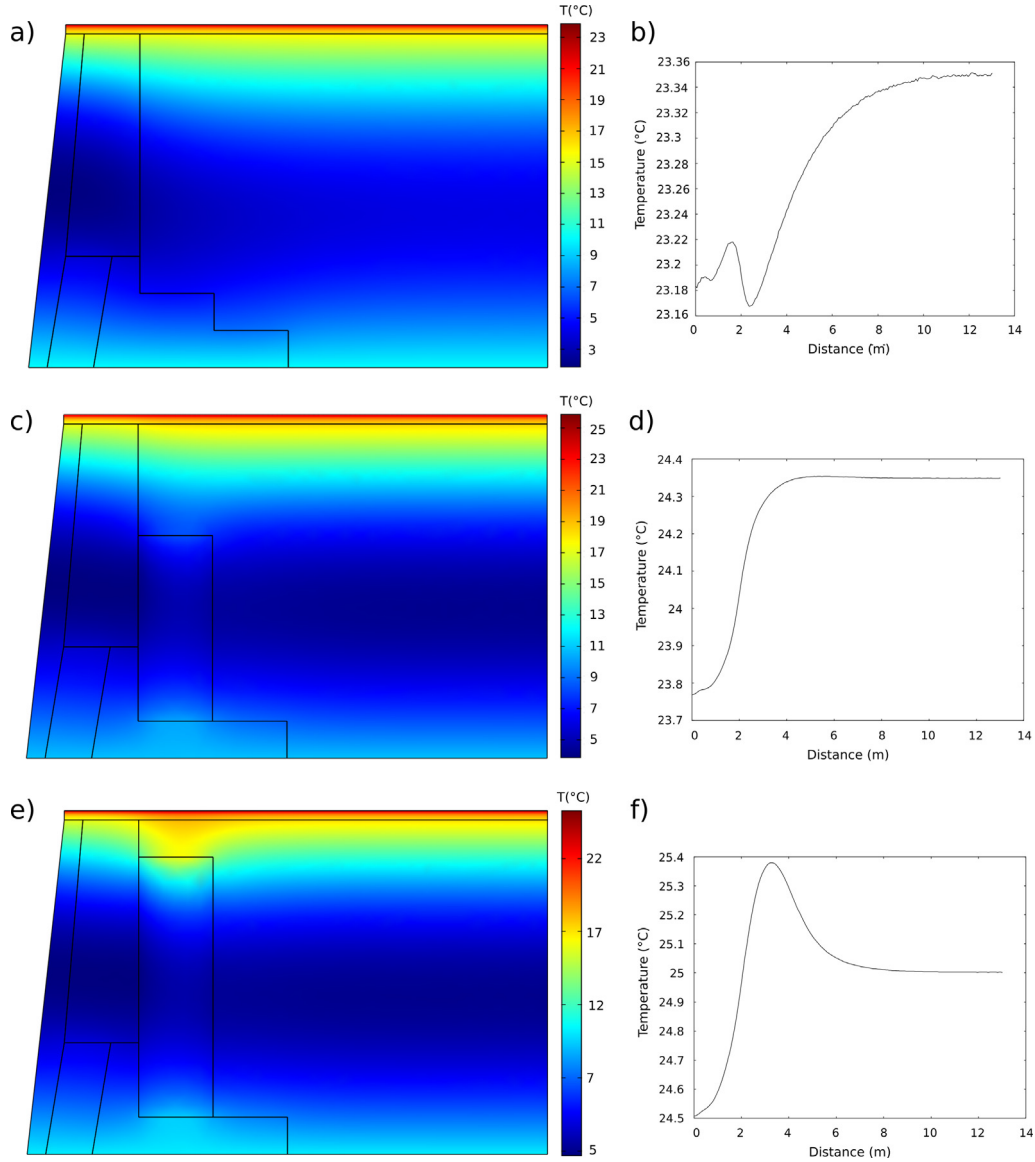


Fig. 13. Numerical modelling of the thermal behavior of the EQ (a) and (b) 2D thermal pattern and surface temperature without cavity; (c) and (d) 2D thermal pattern and surface temperature for a cavity a 3 m depth; (d) and (e) 2D thermal pattern and surface temperature for a cavity a 1 m depth.

$$k \frac{\partial T(z=0, t)}{\partial t} = I_s - I_e + I_l \quad (4)$$

The solar flux I_s absorbed by the surface verifies:

$$I_s = (1 - A)S_0 C \cos(Z) \quad (5)$$

where A is the surface albedo and S_0 is the solar constant. C is fraction of the incident power arriving at the soil including the direct sun light and the diffuse radiations for a cloudy sky. Z is the zenith angle of the sun which can be estimated from the latitude ϕ of the observation point (Watson, 1973):

$$\cos(Z) = \cos\phi \cos\delta \cos(\theta) + \sin\phi \sin\delta \quad (6)$$

where δ is the solar declination as a function of the number of day in Jovian year J (Duffie and Beckman, 1980) and is expressed here in radians:

$$\delta = 0.409 \sin\left(\frac{2\pi}{365}J - 1.39\right) \quad (7)$$

The longitude angle θ expressed also in radians corresponds to the time t in hours past noon:

$$\theta = 2\pi \frac{t}{24} \quad (8)$$

Then, the thermally emitted flux from the surface I_e is given by:

$$I_e = \epsilon \sigma T^4 \quad (9)$$

where ϵ is the soil emissivity averaged in the thermal infrared wavelengths and $\sigma = 5.67 \times 10^{-8} \text{ JK}^{-4}\text{m}^{-2}\text{s}^{-1}$ is the Stefan-Boltzman constant. The thermal radiations from the atmosphere I_l are approximated following the empirical relation (Brunt, 1932):

$$I_l = \sigma T_a^4 (0.55 + 0.65 \sqrt{e_a}) \quad (10)$$

where T_a is the air temperature in Celsius degrees and e_a is the saturation pressure of water in the air expressed in bar. $T_a(t)$ is approximated by Jansson [1998]:

$$T_a(t) = T_0 + \frac{1}{2} T_{amp} \cos\left(\frac{2\pi(t - t_{ph})}{P_{dc}}\right) \quad (11)$$

where T_0 is the mean air temperature during the diurnal cycle, and T_{amp} is the contrast of temperature between day and night as measured during the experiment. P_{dc} represents the duration of the diurnal cycle

and t_{ph} is the time shift between the maximum of the solar incident radiations and the maximum air temperature. This model results in a minimum air temperature at the sunrise and a maximum air temperature at t_{ph} after the zenith. Finally, e_a verifies the empirical law [Deffie and Beckman, 1980]:

$$e_a = 0.6108 \exp\left(\frac{17.27 * T_a(t)}{T_a(t) + 237.3}\right) \quad (12)$$

The lower boundary of the modelling box is considered to be the Mean Lower Low Water level (MLLW) (see Fig. 3), where the ocean level is the lowest. Thus, in this case, the presence of unsaturated areas within the quay are the most probable (with high thermal conductivity contrasts between the soil and air). At this level, the temperature of the lower boundary of the structure is considered as constant (10 °C) at a first approximation. To simulate the presence of a cavity within the medium, we introduce a simplified vertical air-filled zone at the back of the concrete material (Fig. 3). The implementation of this zone at such location may be understandable from a geotechnical point of view, since the backfill is the most probable material subject to cavities, voids or decompressed areas, due to the withdrawal of fine grained materials, when water enters the structure. It is also consistent with the thermal observations, as the TAE1 and TAE2 anomalies are found at the boundary between the concrete and the backfill and are elongated along this boundary (Figs. 3 and 7b). Finally, this air-filled case represents a good candidate for the simulation of important spatial variations of temperature within the medium, because the important contrast of thermal conductivity between air and rock.

6.2. Numerical results

In this section, we present several simulations for the EQ and for 3 different cases as the depth of the potential voids is not known: (1) absence of cavity within the quay; (2) presence of a cavity at 3 m-depth; (3) presence of a cavity at 1 m-depth. For each case, we present the 2D thermal field within the EQ (Fig. 13 a, c and e), as well as a temperature profile at the surface (Fig. 13 b, d and f) calculated at 13 h (for more thermal contrasts). The Fig. 13a presents the 2D temperature behavior of the EQ in the absence of cavity. As the result is presented at 13 h, the surface is the hottest part of the medium. The heat diffuses within the quay from the surface up to a depth of ≈ 2 m. The isotherms are very slightly deformed at the front of the quay, due to the thermal conductivity contrast between the concrete (present at the front of the quay) and the backfill (Fig. 3). As the thermal conductivity is higher in the concrete material at depth, a slight decrease of the surface temperature is generated in this part of the quay (Fig. 16a and b). Such temperature difference between the concrete and the backfill (here, less than 0.5 °C) is obviously impossible to subtract from the diurnal cycle. Finally, the heterogeneous temperature field within the quay is illustrated by the vertical profile given in Fig. 14a, where temperature variation up to 15 °C can be encountered, due to the thermal conductivity contrasts within the structure.

The second case represents the thermal behavior of the quay when a cavity is present at 3-m depth. As said in the previous section, it consists of a vertical zone having the thermal conductivity of the air, located within the backfill just at the back of the concrete. The general thermal pattern is similar to the first case, but the isotherms are deformed within and above the cavity, as it acts as a thermal insulator within the medium (Fig. 13c). At the surface, the temperature decreases from the back to the front of the quay, with a maximum temperature contrast of 0.5 °C (Fig. 13d), but the temperature variation above the cavity is not significant. Nevertheless, it is interesting to note that in comparison with the model without cavity, the surface horizontal thermal gradient is more important in this case (increase of temperature with a shorter wavelength). This spatial variation may be due to the deformation of the isotherms associated with the insulating body at depth. However, such increase in temperature and variation in the shape of the

temperature profile are likely difficult to observe with a thermal camera, considering the amplitude of the diurnal cycle. The vertical temperature profile shown in Fig. 14b is slightly shifted towards higher temperatures above the cavity. Although the general shape of the signal remains controlled by the thermal conductivities of the structure within the quay, the temperature profile is clearly modified when penetrating within the air-filled area. Such change is due to the high contrast between the air and the materials of the EQ.

The last case displays the thermal behavior of the structure with a cavity located at 1-m depth (Fig. 13e and f), i.e. very close to the surface. Here, the subsurface isotherms are strongly deformed, due to the presence of the cavity (Fig. 13e). At the surface, the temperature profile follows the general thermal trend of the previous case (lowest temperatures at the front of the quay with a similar short wavelength), but the maximum of temperature is found just above the cavity. The maximum temperature contrast is 0.9 °C with the front of the quay and less than 0.4 °C with the back of the structure. This result is consistent with the observations of Eppelbaum (2007), who found a warm zone (temperature anomaly of 0.3 °C) just above a 1 m-depth underground cavity, using 40 cm-depth temperature sensors (Fig. 15). Our modelling tends to show that a cavity close to subsurface may produce a thermal signal by its own, due to the 2 order-magnitude difference between the thermal conductivities of the air and of the soil. Indeed, the lowest is the depth, the highest is the amplitude of the thermal anomaly. It is of note that the thermal effect of such insulating zone for this given structure remains limited (less than 1 °C) up to a depth of 1 m and probably not enough to be currently detected. In that case, the vertical temperature profile given in Fig. 14c is drastically modified by the air-filled area. Interestingly, in the first meter below the surface, the shape of the signal is very different from the 3 m-depth case, as the thermal perturbation induced by the cavity interacts with the daily surface heat waves propagating through the pavement and the backfill. Then, below one meter, the air-filled area generate a thermal anomaly but with a whole shape still controlled by the thermal behavior of the EQ.

These three simulations show that an air-filled cavity may directly influence the temperature pattern at the surface of the soil. At depth, the isotherms are deformed at the vicinities of the air-filled cavity, due to the high contrast of thermal conductivities between air and rock. This situation may induce a variation of the surface temperature pattern in two ways (1) an increase of the thermal gradient (here by one order of magnitude: 0.02 °C m⁻¹ without cavity to 0.2 °C m⁻¹ for a location at 3 m depth) and (2) the generation of a maximum of temperature reaching 0.4 to 0.9 °C above the cavity at 1 m depth at mid-day. Despite the high thermal sensitivity of the current thermal cameras (≈ 0.01 °C m⁻¹), such a signal clearly remains a challenge to discriminate from the variations associated to the diurnal cycle. In addition, our models were performed using the highest contrast between thermal conductivities (air and rock), inducing the maximum temperature contrast at the surface. In the case of high tides potentially generating water-filled voids (with temperature contrasts between the rock and the liquid), the situation may be more complex as (1) the thermal signal may be accordingly attenuated, because of the reduced drop of thermal conductivity for water (0.02 W m⁻¹ K⁻¹ for air and 0.6 W m⁻¹ K⁻¹ for water) and (2) the absence of thermal equilibrium between the water and rock may generate additional thermal gradients. Following Turcotte and Schubert (2002), a time l^2/κ is required for temperature changes to propagate a distance l and for a thermal diffusivity κ . Thus, taking a value κ in the range [10⁻⁷ m² s⁻¹–10⁻⁶ m² s⁻¹] for an unconsolidated material like backfill, and a value l of 3 m, the time needed for the temperature changes arriving at the surface is in the range [3 months - 3 years]. For a value l of 1 m, this time is reduced in the range [10 days - 3 months]. Such values shows that a thermal signal associated to water within the water may be mostly masked by seasonal temperature variations. Finally, the results show that the generation of a warm area above the cavity is inconsistent with our observations on the WQ and the EQ. In the next section, an alternative physical phenomenon is

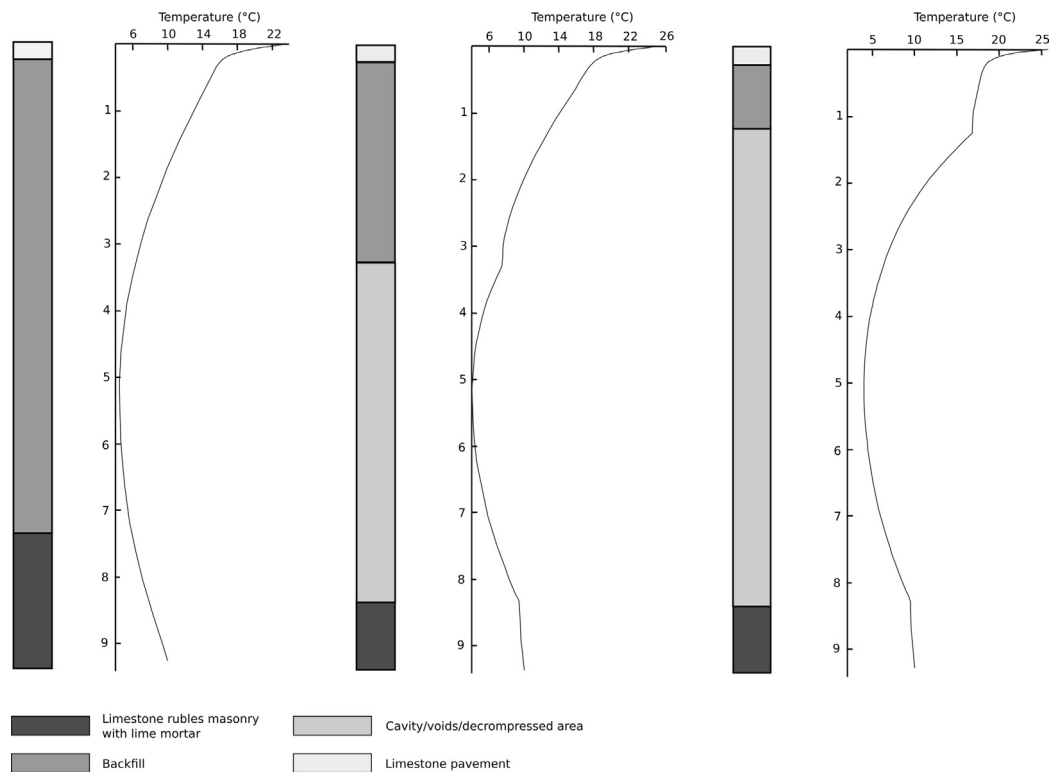


Fig. 14. Geological section and corresponding vertical temperature profile for the EQ (a) without cavity, (b) for a cavity at 3 m-depth and (c) for a cavity at 1 m-depth.

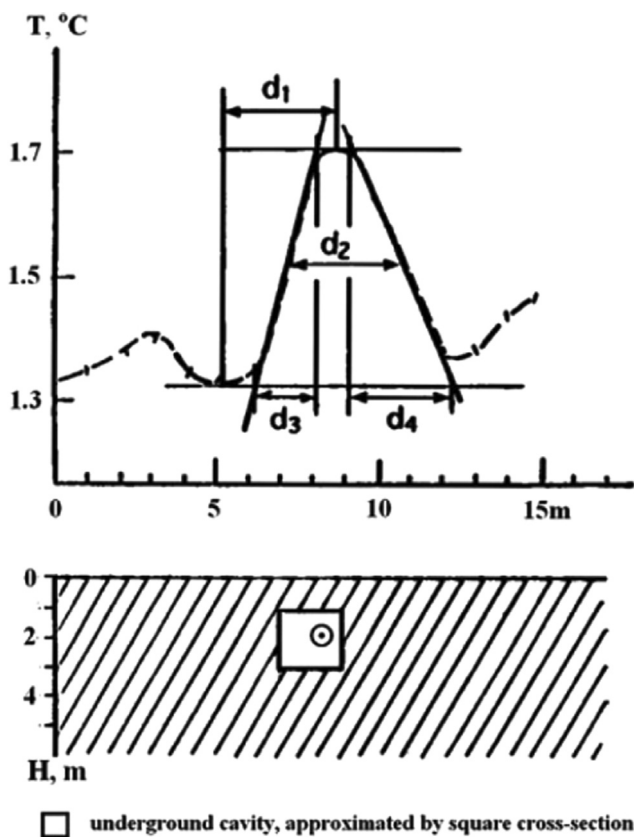


Fig. 15. Observed temperature over an underground cavity and geological section taken from Mosciki (2006). The different labels refer to the characteristic distances explained in the author's paper (Eppelbaum, 2007).

suggested to explain the cold areas associated to the deformations of the quays.

7. On the thermal influence of potential fluid flows within the WQ and EQ

In the previous sections, we have shown that most of the thermal signal of the EQ and WQ may be explained by surface indices (surface properties). However, cool areas persist during daytime that can not be explained (1) by contrasts associated to thermal inertia, albedo or topography and (2) nor by the direct thermal effect of a subsurface cavity located at shallow depth. However, surprisingly, these observations are correlated with deformations, as well as the structure of the quays.

Other processes associated to the presence of a fluid have been searched to explain these temperature drops. For instance, water standing at the surface is cooler during the day and warmer during the night (Sabins, 2007). Nevertheless, the presence of a slope at the location of the thermal anomaly prevents for any stay of water, ruling out this hypothesis. Possible drainage of the fluids within the quays implies the generation of a preferential vertical permeability field. In the case of the WQ and EQ, thermal anomalies are located on the flanks of local subsidences (Fig. 11). From a mechanical point of view, it is known that the slopes of such depressions are subject to extensive stresses, while the center (topographic low) may be rather under compressive forces (Fig. 16) (Berenger et al., 2014; Al-Halbouni et al., 2018; Al-Halbouni et al., 2019; Yin et al., 2019). Consequently, these extensive stresses tend to generate a preferential vertical permeability within the joints of the pavement (through micro-fracturation), while the compressive forces may close the fractures at the center of the topographic depressions. These micro-fractures may not appear everywhere around the deformation, as the medium constituting the quays is highly heterogeneous, with the presence of backfill and concrete.

We propose an alternative cooling mechanism induced by water infiltration through micro-fractures (in the pavement for TAE1, TAE2, TAW1 and TAW2 and within the backfill for TAE3) to explain our

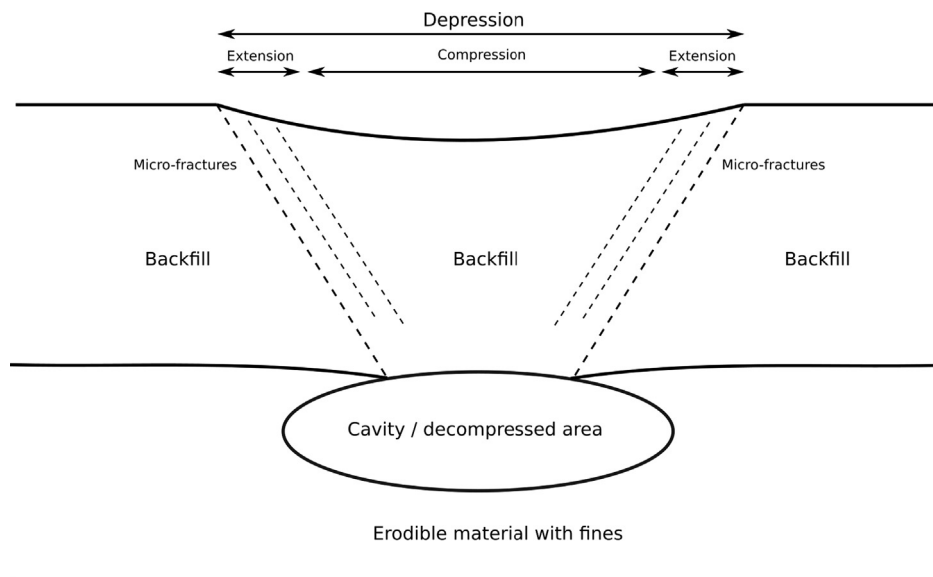


Fig. 16. Conceptual model of the mechanical behavior for an homogeneous soil, when surface deformations associated to a subsurface cavity/void are present.

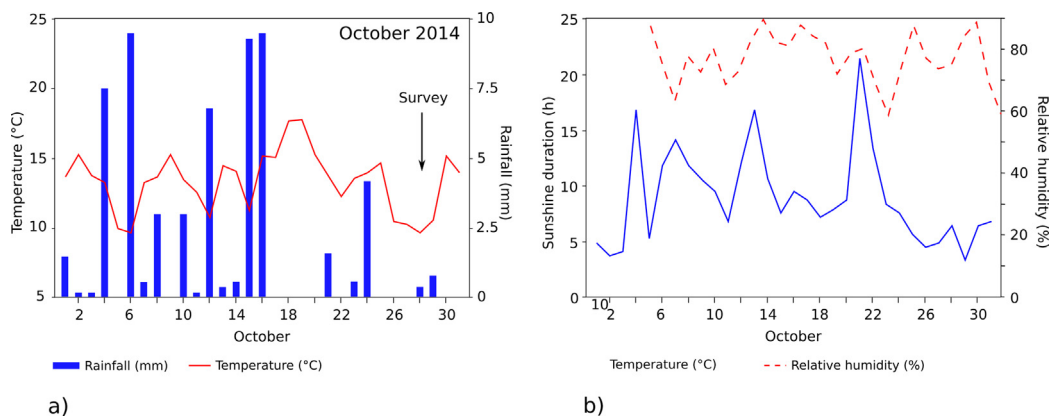


Fig. 17. Meteorological data from the Octeville Station, located at 5 km from Le Havre Harbour (a) rainfall and mean air temperature and (b) sunshine duration and relative humidity.

observations. Indeed, the analysis of meteorological data at stations close to Le Havre Harbour (Cap de la Heve and Octeville) indicates that the October month was particularly rainy, with intermittent to continuous rainfall (Fig. 17). Important rainfall occurred until October 16 h (up to 24 mm), while moderate precipitation was recorded from October 20th to October 24th for Le Havre city (from 1.6 to 4 mm/h). During the following days, the weather was strongly disturbed with a high humidity content on the atmosphere (around 80% of relative humidity) and an important decrease of the hourly solar radiation (from 15 h of sunshine on October 22th to 7 h on October 28th) and small rain on October 28th.

Many works report changes in soil temperature caused by percolating water, following rainfall or irrigation (Callendar, 1895; Franklin, 1921; Shul'gin et al., 1958). Wierenga et al. (1979) experimentally and numerically characterized the thermal effect of infiltration on the shallow subsurface. He measured the temperatures of a soil irrigated with cool (4 °C) and warm (21 °C) water, at different depths (surface to 20 cm). The author shown that irrigation, whatever the temperature of the water, results in lowering the soil temperature below those of non irrigated soil during several days due to Darcy flow, as displayed in Fig. 18. Eventually, the thermal anomaly can persist a longer time below 20 cm depth, due to thermal diffusion. Wierenga et al. (1979) explained this observation by heat transfer between occurring by water movement. The cooling of the soil during water infiltration is also

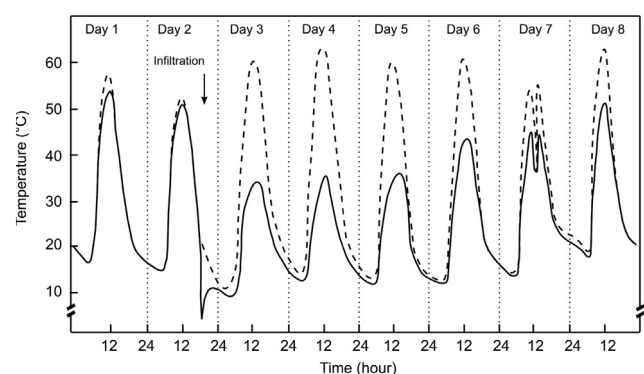


Fig. 18. Diurnal variation in soil temperature at the surface of the soil in irrigated (plain line) and nonirrigated (dashed line) soil (after Wierenga et al., 1979).

described in the numerical results of Lopez et al., 2016, for water flow within a sedimentary basin.

In the case of Le Havre harbour, we propose that the autumn rain in Normandy penetrates the soil of the quays through micro-fractures located on the flanks of the deformations. This infiltration may induce a cooling of the medium by several degrees Celcius (Wierenga et al., 1979), due to the highest Darcy velocity of the water within the

fissures, compared to the rest of the quay. During infiltration, the Darcy velocity is controlled by the effective permeability K of the medium (m^2), defined as $K = d^3/12f$ where d is the fissure aperture (m) and f is the spacing between fissures (m). For an aperture of 0.1 mm and a spacing $f = 1$ m, $K = 10^{-13} m^2$, while this value drops to $10^{-10} m^2$ when $d = 1$ mm, i.e. a range comparable to the permeability of the sand. Heat transfer between rock and water is enhanced due to the downward movement of the fluid and its important volumetric thermal capacity $\rho_w c_{p,w}$. As illustrated in Fig. 18, this cooling may last several hours after the occurrence of infiltration before equilibrium. Eventually, during/after the infiltration process, the evaporation of the water remained stuck on the walls of the fissures by surface tension may also participate to the persistence of the cooling of the medium (Geiger, 1965; Van Bavel and Hillel, 1976), depending on the incoming solar radiation, the atmospheric water content and temperature, the presence of wind and the amount of water available within the soil.

It is currently difficult for us to discriminate the relative influence of infiltration and evaporation on the surface temperatures. Besides, the following elements may be highlighted. The detection of cold anomalies located on the deformations was confirmed for both quays by a second campaign realized in March 2015 19, just after rainy days. This is remarkable, considering that the survey was performed during another season (and thus different radiative, meteorological and soil temperature conditions). The 2015 survey emphasizes several points: (1) the detection of thermal anomalies is repeatable using our methodology, (2) their morphology is comparable to 2014 and (3) important thermal contrasts are observed, similar to 2014, i.e. $\approx 3^\circ C$. In that case, it is proposed that evaporation may influence the surface temperatures to a lesser extent than infiltration, considering the observed difference in the daily average solar radiation in October ($138 W/m^2$) and March ($219 W/m^2$) in Le Havre city (see the irradiation Geographical Information System for Europe for details:). As the evaporation rate directly depends on the incoming solar radiation, a different evaporation rate may be induced at the surface and thus different temperature contrasts, which is not what we observe.

Obviously, further investigations may lead with no doubt to a better evaluation of the role of these two components (infiltration and evaporation) on the thermal field. Numerical modelling may be improved in several ways: (1) implementation of fluid flow in unsaturated media physics, taking into account radiative surface boundary condition, (2) integration of meteorologic, radiative and optical (albedo) field data as input for the modelling. For instance, albedo maps may be obtained using pyranometers on-board drones (Levy et al., 2018) and considerably improve the description of the radiative surface boundary condition and (3) implementation of radiative processes for sloped surfaces to characterize the link between topography and surface temperatures. Finally, analogical experiments may be realized on several soils types in a climatic chamber in order to characterize the link between infiltration, evaporation and thermal infrared observations. In

this frame, the combination of remote sensing and geophysical data (measuring electric or dielectric parameters) may be useful to quantify the relationships between water flow, evaporation rates and soil temperatures.

8. Conclusions

Visible and thermal infrared observations obtained with a light UAV are presented on two port quays. Photographies are used to calculate altimetric maps of the structures by means of the photogrammetric method, while thermal images serve to monitor semi-diurnal temperature variations of the surface. The analysis of the altimetric data reveals several deformations at the surface of the WQ and the EQ and associated to potential subsurface cavities/decompressed areas at depth. The study of thermal maps show that the major part of surface temperatures observed on the WQ and the EQ may be explained by thermal inertia and albedo. Nevertheless, five cold areas (TAW1, TAW2 and TAE1 to TAE3) are revealed on the quays, not explained by these parameters. These anomalies appear in the morning and persist during the all day, with a temperature contrast with the surrounding environment ranging from 2 to 4 °C. Alongside this observation, a clear correlation is found between thermal anomalies, deformations identified on the altimetric data and the structure of the quays. More precisely, the minimum of temperature of the cold regions are located on the flanks of the deformations.

The origin of this correlation is then investigated. A simplified 2D model is developed to quantify the direct surface thermal influence of a subsurface cavity, when present at two different depths (3 m and 1 m below the surface). These simulations show that (1) the gradient of the surface temperature may vary when a subsurface cavity/decompressed area is present at depth; (2) a hot thermal anomaly is induced at the surface by a cavity/decompressed area at depth during the day, which is inconsistent with our observations and (3) the amplitude of the anomaly (less than 1 °C) may be too low to be detected by TIR cameras, given the amplitude of the diurnal cycle. In this study, we only made 2D simulations to assess the first order characteristics of the thermal pattern, but 3D thermal patterns may clearly be present within the medium, due to the complexity of the structures of the quays. Such consideration must be taken into account in future works. We explain the cold anomalies and their correlation with the deformations by the cooling induced by infiltration and subsequent evaporation of water through micro-fractures, permitting the persistence of the anomaly several hours after rainfalls. As a consequence, we argue that the high permeability of the medium induced by stresses within the medium when a cavity/decompressed soil is present may control the surface temperatures observed on both WQ and EQ. To our knowledge, this study is the first establishing a link between thermal anomalies and surface deformations associated to subsurface cavities/decompressed areas. Such result is made possible given the new capabilities of U.A.Vs,

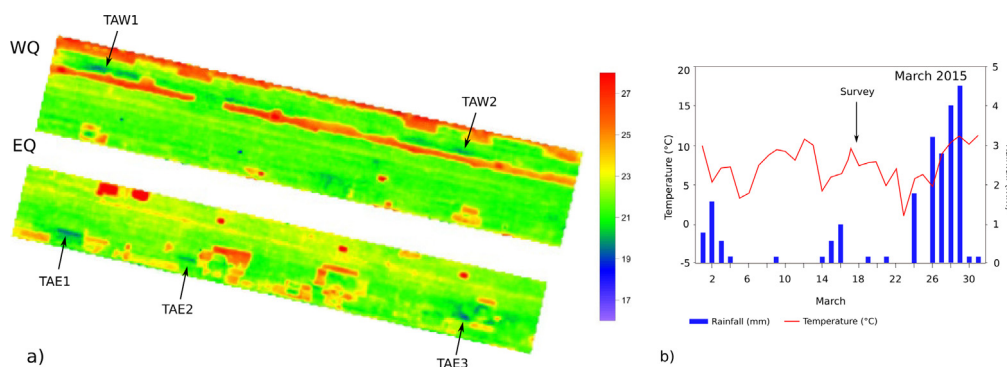


Fig. 19. (a) Thermal images acquired at 16 h on March 19th 2015, showing the same cold anomalies (AAE1 to AAE3, AAW1 and AAW2) present at the same location on the WQ and EQ and (b) Precipitations and temperature during March 2015. Note the occurrence of rainfalls just before the survey.

able to monitor port quays and more broadly civil engineering structures at high resolution, low cost and in a very flexible way. Finally, these methods may also be very useful for the detection of subsurface voids in clayey soils, where classical geophysical tools (like Ground Penetrating Radar) remain inefficient.

Author contribution

Antoine R. designed the UAV-based experiment, made the data analysis and performed the 2D numerical modelling. Fauchard C. made the data analysis with Antoine R. and participated to the corrections of the manuscript. The UAV experiment and data processing were performed by Oelher J-F. Mr. Joignant is the project manager for the GPMH.

Declaration of Competing Interest

The authors declare that they have no known competing financial interests or personal relationships that could have appeared to influence the work reported in this paper.

Acknowledgement

This research project benefited from the support of the Grand Port Maritime du Havre and from the French Ministry for the Ecological and Inclusive Transition. We wish to thank both anonymous reviewers for their very useful and constructive comments.

References

- Al-Halbouni, D., Holohan, E., Taheri, A., et al., 2018. Geomechanical modelling of sinkhole development using distinct elements: model verification for a single void space and application to the dead sea area. *Solid Earth* 9, 1341–1373.
- Al-Halbouni, D., Holohan, E.P., Taheri, A., Watson, R.A., Polom, U., Schöpfer, M.P., Emam, S., Dahm, T., 2019. Distinct element geomechanical modelling of the formation of sinkhole clusters within large-scale karstic depressions. *Solid Earth* 10, 1219–1241.
- Antoine, R., Baratoux, D., Rabinowicz, M., Fontaine, F., Bachlery, P., Staudacher, T., Saracco, G., Finizola, A., 2009. Thermal infrared image analysis of a quiescent cone on piton de la fournaise volcano: Evidence of convective air flow within an unconsolidated soil. *J. Volcanol. Geoth. Res.* 183, 228–244 <https://doi.org/10.1016/j.jvolgeores.2008.12.003>. URL: <http://www.sciencedirect.com/science/article/pii/S0377027308006525>.
- Antoine, R., Finizola, A., Lopez, T., Baratoux, D., Rabinowicz, M., Delcher, E., Fontaine, F.R., Fontaine, F.J., Saracco, G., Bachlery, P., et al., 2017. Electric potential anomaly induced by humid air convection within piton de la fournaise volcano, la réunion island. *Geothermics* 65, 81–98.
- Artugyan, L., Ardelean, A.C., Urdea, P., 2020. Gpr and ert investigations of karst structures at the buhui-cuptoare cave system, anina karst region (banat mountains, romania). In: In: Biswas, A., Sharma, S.P. (Eds.), *Advances in Modeling and Interpretation in Near Surface Geophysics* Springer International Publishing, Cham, pp. 19–38. https://doi.org/10.1007/978-3-030-28909-6_2.
- Benavente, J., Vadiello, I., Li nán, C., Martínez-Moreno, F.J., Galindo-Zaldívar, J., Carrasco, F., 2017. Identification of vadose karst voids and ventilation patterns coupling hydrochemical and geophysical methods (maro spring, near nerja, southern Spain). In: In: Renard, P., Bertrand, C. (Eds.), *EuroKarst 2016*, Neuchâtel Springer International Publishing, Cham, pp. 327–334.
- Berenger, N., Flahaut, R., Mathon, D., Kreziak, C., Marty, F., 2014. Le diagnostic de stabilité des carrières souterraines abandonnées. guide méthodologique.
- Brunt, D., 1932. Notes on radiation in the atmosphere. i. *Q. J. R. Meteorological Soc.* 58, 389–420. <https://doi.org/10.1002/qj.49705824704>.
- Callendar, H., 1895. Preliminary results of observations of soil temperatures with electrical resistance thermometers made at the mcdonald physics building, mcgill university, montreal. *Trans., R. Soc. Canada, Second Series* 1, 63–84.
- Campbell, C.W., El Latif, A., Foster, J.W., 1996. Application of thermography to karst hydrology. *J. Cave Karst Studies* 58, 163–167.
- Cardarelli, E., Cercato, M., Cerreto, A., Di Filippo, G., 2009. Electrical resistivity and seismic refraction tomography to detect buried cavities. *Geophys. Prospecting* 58, 685–695. <https://doi.org/10.1111/j.1365-2478.2009.00854.x>.
- Chang, L., Hanssen, R.F., 2014. Detection of cavity migration and sinkhole risk using radar interferometric time series. *Remote Sens. Environ.* 147, 56–64 <https://doi.org/10.1016/j.rse.2014.03.002>. URL: <http://www.sciencedirect.com/science/article/pii/S0034425714000674>.
- De Giorgi, L., Leucci, G., 2014. Detection of hazardous cavities below a road using combined geophysical methods. *Survey Geophys.* 35, 1003–1021.
- Deseilligny, M.P., Cléry, I., 2011. Apero, an open source bundle adjustment software for automatic calibration and orientation of set of images. In: *Proceedings of the ISPRS Symposium, 3DARCH11*. volume 269277.
- Duffie, J.A., Beckman, W.A., 1980. Solar radiation. *Solar Engineering of Thermal Processes*, pp. 3–17.
- Edmonds, C., Kennie, T., Rosenbaum, M., 1987. The application of airborne remote sensing to the detection of solution features in limestone. *Geol. Soc., London, Eng. Geol. Special Publ.* 4, 125–131.
- EngineeringToolbox, 2003. Thermal conductivity of selected materials and gases. [available online]. URL: https://www.engineeringtoolbox.com/thermal-conductivity-d_429.html.
- Eppelbaum, L., Kutasov, I., Pilchin, A., 2014. *Applied Geothermics*. Springer, Berlin Heidelberg.
- Franklin, T.B., 1921. Viii. the effect of weather changes on soil temperatures. *Proc. R. Soc. Edinburgh* 40, 56–79.
- Furukawa, Y., Ponce, J., 2010. Accurate, dense, and robust multiview stereopsis. *IEEE Trans. Pattern Anal. Mach. Intell.* 32, 1362–1376. <https://doi.org/10.1109/TPAMI.2009.161>.
- Gates, D.M., 1980. Evaporation and transpiration. In: *Biophysical Ecology* Springer, pp. 307–344.
- Gaudin, D., Beauducel, F., Allemand, P., Delacourt, C., Finizola, A., 2013. Heat flux measurement from thermal infrared imagery in low-flux fumarolic zones: example of the ty fault (la soufrière de guadeloupe). *J. Volcanol. Geoth. Res.* 267, 47–56.
- Geiger, R., 1965. *The Climate Near the Ground*, Rev. ed. Harvard University Press, Cambridge.
- Gunn, D.A., Marsh, S.H., Gibson, A., Ager, G.J., McManus, K.B., Caunt, S., Culshaw, M.G., 2008. Remote thermal ir surveying to detect abandoned mineshafts in former mining areas. *Q. J. Eng. Geol. Hydrogeol.* 41, 357–370.
- Hillel, D., 1982. *Introduction to Soil Physics* New York. Technical Report. Academic Press.
- Javadi, H., Mousavi Ajarostaghi, S.S., Rosen, M.A., Pourfallah, M., 2018. A comprehensive review of backfill materials and their effects on ground heat exchanger performance. *Sustainability* 10. <https://doi.org/10.3390/su10124486>.
- Jeffery, Z.E., Penn, S., Giles, D.P., Hastewell, L., 2020. Identification, investigation and classification of surface depressions and chalk dissolution features using integrated lidar and geophysical methods. *Q. J. Eng. Geol. Hydrogeol.* <https://doi.org/10.1144/qjegh2019-098>.
- Kaufmann, G., Romanov, D., 2016. Structure and evolution of collapse sinkholes: combined interpretation from physico-chemical modelling and geophysical field work. *J. Hydrol.* 540, 688–698 <https://doi.org/10.1016/j.jhydrol.2016.06.050>. URL: <http://www.sciencedirect.com/science/article/pii/S0022169416304127>.
- Kaufmann, G., Romanov, D., Nielbock, R., 2011. Cave detection using multiple geophysical methods: Unicorn cave, harz mountains, germany. *Geophysics* 76, B71–B77. <https://doi.org/10.1190/1.3560245>.
- Khesin, B.E., Eppelbaum, L.V., 1994. Near-surface thermal prospecting: review of processing and interpretation. *Geophysics* 59, 744–752. <https://doi.org/10.1190/1.1443632>.
- Kim, J.-W., Lu, Z., Kaufmann, J., 2019. Evolution of sinkholes over wink, texas, observed by high-resolution optical and sar imagery. *Remote Sens. Environ.* 222, 119–132 <https://doi.org/10.1016/j.rse.2018.12.028>. URL: <http://www.sciencedirect.com/science/article/pii/S003442571830587X>.
- Kolesnikov, Y., Fedin, K., 2018. Detecting underground cavities using microtremor data: physical modelling and field experiment. *Geophys. Prospect.* 66, 342–353. <https://doi.org/10.1111/1365-2478.12540>.
- Leblanc, M., Favreau, G., Tweed, S., Leduc, C., Razack, M., Mofor, L., 2007. Remote sensing for groundwater modelling in large semiarid areas: Lake chad basin, africa. *Hydrogeol. J.* 15, 97–100.
- Lee, E.J., Shin, S.Y., Ko, B.C., Chang, C., 2016. Early sinkhole detection using a drone-based thermal camera and image processing. *Infrared Phys. Technol.* 78, 223–232 <https://doi.org/10.1016/j.infrared.2016.08.009>. URL: <http://www.sciencedirect.com/science/article/pii/S1350449516303966>.
- Levy, C.R., Burakowski, E., Richardson, A.D., 2018. Novel measurements of fine-scale albedo: using a commercial quadcopter to measure radiation fluxes. *Remote Sensing* 10. <https://doi.org/10.3390/rs10081303>.
- Lopez, T., Antoine, R., Kerr, Y., Darrozes, J., Rabinowicz, M., Ramillien, G., Cazenave, A., Genthon, P., 2016. Subsurface hydrology of the lake chad basin from convection modelling and observations. In: In: Cazenave, A., Champollion, N., Benveniste, J., Chen, J. (Eds.), *Remote Sensing and Water Resources* Springer International Publishing, Cham, pp. 281–312. https://doi.org/10.1007/978-3-319-32449-4_12.
- Lowe, D.G., 2004. Distinctive image features from scale-invariant keypoints. *Int. J. Comput. Vision* 60, 91–110. <https://doi.org/10.1023/B:VISI.0000029664.99615.94>.
- Majumdar, T.J., 2003. Regional thermal inertia mapping over the indian subcontinent using insat-1d vhr data and its possible geological applications. *Int. J. Remote Sensing* 24, 2207–2220. <https://doi.org/10.1080/0143116021061724>.
- Martnez-Moreno, F., Monteiro Santos, F., Galindo-Zaldívar, J., González-Castillo, L., Pedraza, A., Bernardo, I., Gonçalves, S., Alves Ribeiro, J., 2018. Characterization of a cave by means of microgravity and electrical resistivity 3d-inversions: Z de braga cave (mira de aire, portugal). *First Break* 36, 29–34. <https://doi.org/10.3997/1365-2397.2018004>.
- Mellon, M.T., Jakosky, B.M., Kieffer, H.H., Christensen, P.R., 2000. High-resolution thermal inertia mapping from the mars global surveyor thermal emission spectrometer. *Icarus* 148, 437–455. <https://doi.org/10.1006/icar.2000.6503>. URL: <http://www.sciencedirect.com/science/article/pii/S00191035000965035>.
- Mochales, T., Casas, A.M., Pueyo, E.L., Pueyo, O., Román, M.T., Pocoví, A., Soriano, M.A., Ansón, D., 2008. Detection of underground cavities by combining gravity, magnetic and ground penetrating radar surveys: a case study from the zaragoza area, ne Spain. *Environ. Geol.* 53, 1067–1077. <https://doi.org/10.1007/s00254-007-0733-7>.

- Mosciki, W.J., 2006. Temperature anomalies over underground cavities. *Geophysical Prospecting* 35, 393–423. <https://doi.org/10.1111/j.1365-2478.1987.tb00825.x>.
- Nasipuri, P., Mitra, D., Majumdar, T., 2005. Generation of thermal inertia image over a part of Gujarat: A new tool for geological mapping. *Int. J. Appl. Earth Obs. Geoinf.* 7, 129–139. <https://doi.org/10.1016/j.jag.2005.02.002>. URL: <http://www.sciencedirect.com/science/article/pii/S0303243405000358>.
- Peters, D.C., Livo, K.E., Hauff, P.L., 1996. Remote sensing for analysis of mine subsidence and mine wastes. *Environ. Geosci.* 3, 11–27.
- Putzig, N.E., Mellon, M.T., 2007. Apparent thermal inertia and the surface heterogeneity of Mars. *Icarus* 191, 68–94. <https://doi.org/10.1016/j.icarus.2007.05.013>. URL: <http://www.sciencedirect.com/science/article/pii/S001910350700231X>.
- Quinn, A., 1948. *Elements of Photogrammetry*. Syracuse University Press. URL: <https://books.google.fr/books?id=tC07AAAAAMAAJ>.
- Rahnema, H., Ehsaninezhad, L., Dashti, F., Talebi, G., 2020. Detection of subterranean cavities and anomalies using multichannel analysis of surface wave. *Geomechanics and Geoengineering* 1–14. <https://doi.org/10.1080/17486025.2020.1728394>.
- Rinker, J., 1975. Airborne infrared thermal detection of caves and crevasses. *Photogrammetric Eng. Remote Sensing* 44.
- Ruth, B.E., Degner, J.D., 1963. Characteristics of sinkhole development and implications for potential cavity collapse. *Measurements* 11.
- Sabins, F.F., 2007. *Remote sensing: principles and interpretation*. (3rd ed.). Long Grove, Ill.: Waveland Press. Reissued 2007 by Waveland Press, Inc.–T.p. verso.
- Sabins, J., Floyd, F., 1969. Thermal Infrared Imagery and Its Application to Structural Mapping in Southern California. *GSA Bulletin* 80, 397–404. [https://doi.org/10.1130/0016-7606\(1969\)80\[397:TIHIAI\]2.0.CO;2](https://doi.org/10.1130/0016-7606(1969)80[397:TIHIAI]2.0.CO;2). arXiv:<https://pubs.geoscienceworld.org/gsabulletin/article-pdf/80/3/397/3432489/i0016-7606-80-3-397.pdf>.
- Shul'gin, I., Kleshnin, A., Verbolova, N., 1958. A photoelectric method for determining the optical properties of plant leaves. *Soviet plant physiology, (English translation). Fiziol. Rastanii* 5, 973.
- Snively, N., Seitz, S.M., Szeliski, R., 2008. Modeling the world from internet photo collections. *Int. J. Comput. Vision* 80, 189–210. <https://doi.org/10.1007/s11263-007-0107-3>.
- Turcotte, D.L., Schubert, G., 2002. 2nd ed. *Geodynamics* Cambridge University Press. <https://doi.org/10.1017/CBO9780511807442>.
- Eppelbaum, L.V., 2007. Revealing of subterranean karst using modern analysis of potential and quasi-potential fields. URL:<https://www.earthdoc.org/content/papers/10.3997/2214-4609-pdb.179.0797-810>. doi: 10.3997/2214-4609-pdb.179.0797-810.
- Vadillo, I., Benavente, J., Neukum, C., Grtznar, C., Carrasco, F., Azzam, R., Lin, C., Reicherter, K., 2012. Surface geophysics and borehole inspection as an aid to characterizing karst voids and vadose ventilation patterns (nerja research site, s. Spain). *J. Appl. Geophys.* 82, 153–162. <https://doi.org/10.1016/j.jappgeo.2012.03.006>. URL: <http://www.sciencedirect.com/science/article/pii/S0926985112000547>.
- Van Bavel, C., Hillel, D., 1976. Calculating potential and actual evaporation from a bare soil surface by simulation of concurrent flow of water and heat. *Agric. Meteorol.* 17, 453–476.
- Vargemezis, G., Tsourlos, P., Fikos, I., Diamanti, N., Angelis, D., Amanatidou, E., 2019. Void detection and consolidation filling verification by ert, gpr and seismic refraction methods, 2019, 1–5. URL: <https://www.earthdoc.org/content/papers/10.3997/2214-4609.201902525>. doi: 10.3997/2214-4609.201902525.
- Vasterling, M., Meyer, U., 2013. Kuenzer c., dech s. (eds) *thermal infrared remote sensing. remote sensing and digital image processing. chapter Challenges and Opportunities for UAV-Borne Thermal Imaging*. (pp. 69–92). Springer, Dordrecht. doi:https://doi.org/10.1007/978-94-007-6639-6_4.
- Watson, K., 1973. Periodic heating of a layer over a semi-infinite solid. *J. Geophys. Res.* (1896–1977) 78, 5904–5910. <https://doi.org/10.1029/JB078i026p05904>.
- Watson, K., 1975. Geologic applications of thermal infrared images. *Proc. IEEE* 63, 128–137. <https://doi.org/10.1109/PROC.1975.9712>.
- Whitehead, V.S., Johnson, W.R., Boatright, J.A., 1986. Vegetation assessment using a combination of visible, near-ir, and thermal-ir avhrr data. *IEEE Trans. Geosci. Remote Sensing*, 107–112.
- Whiteman, C.D., Allwine, K.J., Fritschen, L.J., Orgill, M.M., Simpson, J.R., 1989. Deep valley radiation and surface energy budget microclimates. part i: radiation. *J. Appl. Meteorol.* 28, 414–426.
- Wierenga, P.J., Hagan, R.M., Nielsen, D.R., 1979. Soil temperature profiles during infiltration and redistribution of cool and warm irrigation water. *Water Resour. Res.* 6, 230–238.
- Wynne, J.J., Titus, T.N., Diaz, G.C., 2008. On developing thermal cave detection techniques for earth, the moon and mars. *Earth Planet. Sci. Lett.* 272, 240–250.
- Yin, D., Chen, S., Li, B., Guo, W., 2019. Bed separation backfill to reduce surface cracking due to mining under thick and hard conglomerate: a case study. *R. Soc. Open Sci.* 6, 190880 <https://doi.org/10.1098/rsos.190880>.
- Youssef, A.M., El-Kaliouby, H.M., Zabramawi, Y.A., 2012. Integration of remote sensing and electrical resistivity methods in sinkhole investigation in Saudi Arabia. *J. Appl. Geophys.* 87, 28–39. <https://doi.org/10.1016/j.jappgeo.2012.09.001>. URL: <http://www.sciencedirect.com/science/article/pii/S0926985112001577>.
- Youssef, A.M., Zabramawi, Y.A., Gutierrez, F., Bahamil, A.M., Otaibi, Z.A., Zahrani, A.J., 2020. Sinkholes induced by uncontrolled groundwater withdrawal for agriculture in arid Saudi Arabia. integration of remote-sensing and geophysical (ert) techniques. *J. Arid Environ.* 177, 104132. <https://doi.org/10.1016/j.jaridenv.2020.104132>. URL: <http://www.sciencedirect.com/science/article/pii/S0140196320300458>.

5.4 3D assessment of an underground mine pillar by combination of photogrammetric and geoelectric methods (Geophysics)

3D assessment of an underground mine pillar by combination of photogrammetric and geoelectric methods

Yannick Fargier¹, Raphaël Antoine², Ludovic Dore¹, Sérgio Palma Lopes³, and Cyrille Fauchard²

ABSTRACT

The monitoring of underground cavities plays a key role in risk management policies. Mine and underground quarry stakeholders require relevant methodologies and practices to define and assess hazards associated with these structures. To monitor these structures, geophysical methods may offer an interesting compromise among operating cost, invasiveness, and risk assessment reliability. The use of conventional 3D-electric resistivity imaging (ERI) software validated on relatively flat media is not sufficient to efficiently assess complex 3D geometries such as underground mine pillars. We have developed a new approach to evaluate pillar condition by means of a sequential use of two techniques. First, the

photogrammetric method yields a detailed 3D model of the pillar geometry from a set of pictures. Second, 3D-ERI is performed based on this suitable geometry. The methodology is tested on a synthetic model to evaluate the effect of various geometry resolutions on the inversion. We also evaluated the combination of the effect of measurement and geometry error. We performed a quasi 3D-ERI survey (three parallel electrode lines) on a real limestone mine pillar to determine the benefits and limitations of the combined procedure. First results revealed the capacity of the photogrammetric methods to obtain a high-precision geometry and its key role during the inversion process. Second results of the real case study revealed that a highly accurate geometry is required to detect accurately conductive anomalies in a complex 3D context.

INTRODUCTION

Degradation of underground quarries can lead to collapses, which can directly impact buildings and civil engineering structures on the surface and, even worse, dangerously threaten people's safety (Bell et al., 1992; Al Heib et al., 2014). In this context, the monitoring of abandoned quarries is of major importance.

Stability assessment methods of underground chalk mines are mainly based either on structural numerical modeling or on geometric criteria (i.e., tributary area method) (Brady and Brown, 2013). Both are combined with rock physical properties measured in the vicinity of the area studied. Nevertheless, these methods are based on the assumption that the internal properties of pillars are quite homogeneous (Ferrero et al., 2010), and consequently, they are likely to underestimate the associated risk of collapse.

A complementary approach consists of using geophysical methods to overcome this limitation. To this end, Dérobert and Abraham (2000) use seismic and ground-penetrating radar methods to assess

pillar conditions in a gypsum quarry. Results showed that both methods were able to detect internal cracks in the medium.

Electric resistivity imaging (ERI) is a widely used method exhibiting two main benefits when applied to mine pillar assessment. The first is to provide qualitative detection and monitoring of anomalies within the pillar (e.g., cracks or heterogeneous zones [Jones et al., 2014; Li et al., 2015]). The second is to provide a quantitative description of the electric resistivity distribution within the pillar. ERI is considered to be a relevant tool to assess the internal distribution of water content in geologic (Brunet et al., 2010) or civil engineering (Rings et al., 2008) contexts. This quantitative description can be interpreted with empirical laws to link the variation in chalk mechanical properties with water content distribution (Gombert et al., 2013).

However, conventional 2D and 3D imaging techniques are mainly applied to flat surface surveys (Dahlin, 1996) or to surfaces with moderate topography (Fox et al., 1980; Günther et al., 2006; Erdoğan et al., 2008; Demirci et al., 2012; Fargier et al., 2014). Interesting

Manuscript received by the Editor 26 May 2016; revised manuscript received 23 January 2017; published online 9 May 2017.

¹Cerema, Direction Territoriale Normandie Centre, Blois, France. E-mail: yannick.fargier@cerema.fr; ludovic.dore@cerema.fr.

²Cerema, Direction Territoriale Normandie Centre, Rouen, France. E-mail: raphael.antoine@cerema.fr; cyrille.fauchard@cerema.fr.

³LUNAM Université, IFSTTAR, Department GERS, Nantes, France. E-mail: sergio.palma.lopes@ifsttar.fr.

© 2017 Society of Exploration Geophysicists. All rights reserved.

results can be obtained using a 3D forward model (using a complex geometry) and performing a 2D inversion (Lesparre et al., 2014). A 3D acquisition survey (multiple electrode lines) on a complex 3D medium (which is the case of a pillar) requires a full account of the geometry in the 3D inversion process (Marescot et al., 2008). Indeed, studies show that it is of prime importance to use a model closest to reality, including the lowest electrode position error (Oldenborger et al., 2005) and relevant insulating boundary conditions (Audebert et al., 2014).

Laser and photogrammetric techniques can be used to obtain a very accurate description of the external geometry of a complex medium (Chandler et al., 2005; Abellán et al., 2014). The latter often provides a cost-effective solution for building a digital terrain model (DTM) (Bretar et al., 2013). Recently, techniques based on close-range stereophotogrammetry have proven effective in generating accurate 3D models of civil engineering structures for a better interpretation of geophysical measurements (Fauchard et al., 2013). However, this method has never been fully sequentially exploited with the 3D-ERI method to improve the inversion process.

The purpose of this work is to show that photogrammetry and ERI tools can be combined to efficiently assess a complex 3D structure. First, this paper presents the general methodology with the basic principles of photogrammetry and ERI. Second, some numerical tests are performed to highlight the key role of the resolution of the 3D surface geometry on the inversion result. Finally, the methodology is applied to image electric resistivity distribution within a real underground pillar in a chalk mine.

MATERIALS AND METHODS

Methodology

Major ERI software optimized for the assessment of flat or moderately flat media is unsuitable for assessing mine pillars with complex geometry. We propose to sequentially combine a photogrammetric method and a flexible 3D inversion approach (for generating the model) to address this issue. Figure 1 presents a simplified diagram

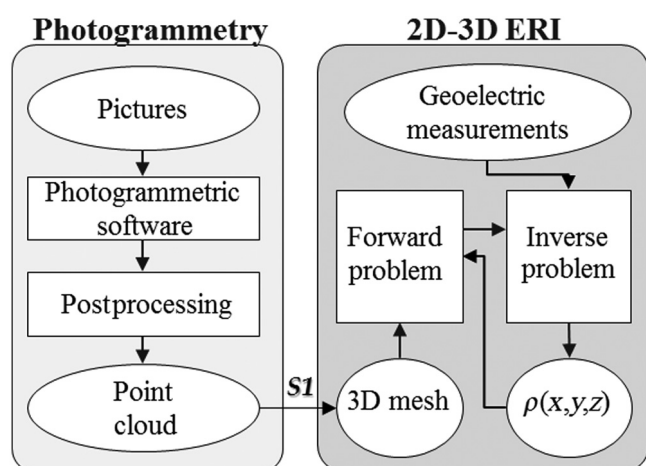


Figure 1. Methodology sequentially coupling ERI and the photogrammetric method to assess a medium with complex geometry. The rectangular elements represent software and methods. The ellipsoidal elements represent input and output data, $\rho(x, y, z)$ is the electric resistivity distribution, and S1 is a denoising postprocessing stage of the raw output point cloud.

of the assessment methodology coupling photogrammetric and ERI techniques. The main idea is that photogrammetry can supply an accurate geometry used as an input model for the ERI inversion process. For this study, the cost-effectiveness of photogrammetry and its flexibility led us to use this method, rather than the laser scanning technique.

Photogrammetry basic principles

Photogrammetry allows the reconstruction of high-resolution 3D point cloud models from images acquired from different locations (Chandler et al., 2005). This technique exploits the difference in the observation of one object viewed from two viewpoints, also known as the parallax principle. The mimic of this perspective shift with a set of photographs is the basic acquisition protocol used for 3D reconstruction. The rapid evolution of digital cameras and computing power has dramatically expanded the variety of potential applications for this method, while simultaneously decreasing the costs of acquisition, processing, and analysis. Photogrammetry is widely used in engineering geology applications for (1) reconstructing high-resolution 3D objects and (2) monitoring the evolution of surfaces. In the framework of this research study, the authors use the APERO/MICMAC photogrammetric software suite developed by the Institut National de l'Information Géographique et Forestière since 2007 (Pierrot-Deseilligny and Clery, 2011). MicMac software follows a classic process consisting of three successive main steps to obtain a point cloud:

- 1) The first step is to compute tie points between images using the scale invariant feature transform (SIFT) algorithm (Vedaldi and Fulkerson, 2010). The picture data set is then organized following the number of tie points between photos.
- 2) The second step of the process computes the orientations of camera for every shot and gives an initial solution minimizing a cost function. The latter is composed of a correlation cost function and a smoothness cost function (Pierrot-Deseilligny and Clery, 2011). A master image is selected that arbitrarily gives the orientation and origin of the coordinates. Next, images are selected computing the relative orientation from the tie points. At this stage, ground control points (GCP) can be used to calibrate the 3D model and to obtain an absolute orientation. A self-calibration method is used during the bundle adjustment to take the lens distortion into account.
- 3) The last step produces a dense 3D point cloud using a multiscale method (Pierrot-Deseilligny and Clery, 2011). The process uses the previous orientations of cameras and starts with a rough approximation of the 3D scene and low-resolution images. Then, the resolution of 3D scene is iteratively improved by a dense matching of the images at higher resolution. The dense matching is based on a pixel-based or window-based normalized crosscorrelation of images.

More details concerning the mathematical principle, the acquisition process, and the applications of the technique can be found in the literature (Pierrot-Deseilligny and Clery, 2012; Bretar et al., 2013).

Geoelectric imaging principles

The ERI method makes it possible to image the electric resistivity distribution within a medium by measuring voltage drops on its surface or boreholes with electrodes (Dahlin, 1996).

The geoelectric inversion code used in this paper is developed with the MATLAB and Comsol Multiphysics software (Multiphysics, 2008). The former is used to solve the inverse problem and manage the latter, which solves the forward problem. The latter is a finite-element method that solves the Poisson's equation (equation 1) for each electrode as a source electrode (s) with a weak formulation approach (Günther et al., 2006):

$$\nabla \cdot (\sigma \nabla V) = -I(\delta(r - r_s)), \quad (1)$$

where V is the electric potential (V) calculated at each node of the finite-element mesh and σ is the electric conductivities at each nodes of the mesh (S/m). The right-hand part of the equation represents the source term, with I being the current intensity (A) injected in the electrode located at r_s (m). Finally, Neumann and Dirichlet boundary conditions are applied to take into account insulating boundaries and ground conditions, respectively.

The inversion procedure is based on a Gauss-Newton algorithm with an Occam-type regularization (deGroot-Hedlin and Constable, 1990). This procedure is used iteratively to find a better model m^{k+1} by updating a model m^k at a previous iteration k (Sasaki, 1994):

$$m^{k+1} = m^k + \tau \Delta m, \quad (2)$$

where τ is a scalar used to ensure the convergence of the algorithm and to limit the overshooting issue. It is computed with the three-point parabola method (Günther et al., 2006). To compute the updating parameter vector Δm , we solve the normal inversion equation (equation 3) (Sasaki, 1994) with a QR decomposition solver:

$$\begin{bmatrix} \mathbf{W}_d \mathbf{S} \\ \sqrt{\lambda} \mathbf{L} \end{bmatrix} \Delta \mathbf{m} = \begin{bmatrix} \mathbf{W}_d \Delta \mathbf{r} \\ 0 \end{bmatrix}, \quad (3)$$

where \mathbf{W}_d is the data-weighting matrix and $\Delta \mathbf{r}$ is the data misfit between the measured and computed data. We use an adjoint-state method to compute the sensitivity matrix (Park and Van, 1991). Regularization of the inverse problem is ensured by a conventional model smoothing matrix \mathbf{L} corresponding to a second derivative of the model (deGroot-Hedlin and Constable, 1990; Sasaki, 1994). The damping factor λ is given an initial value of one, and it is then divided by two before each subsequent iteration (Loke and Barker, 1996).

To improve the interpretation of a numerical study, a similarity index S_i , between the inversion result and the true model is proposed (equation 4). The aim of this criterion is to give an error associated with a reconstruction of a known synthetic medium. An index equal to zero means a perfect reconstruction and one means an average reconstruction error of 100%:

$$S_i = \sqrt{\frac{1}{V_i} \int \left(\frac{\rho_{\text{inv}} - \rho_{\text{true}}}{\rho_{\text{true}}} \right)^2 dV_i}, \quad (4)$$

where V_i is the examined volume of interest, ρ_{inv} is the inverted resistivity distribution, and ρ_{true} is the real resistivity distribution in the volume.

CASE STUDY

Site test description

A real quarry pillar is examined in the following sections (synthetic and real case studies) to test the methodology. La Glacière is an ancient underground limestone quarry located in France near Vendôme (Figure 2a). The quarry covers approximately 6000 m² and was exploited from the seventeenth century until the twentieth century (Figure 2b). Because the quarry stopped being exploited, damage has occurred, such as cracking and local collapsing of the roof and pillars. Some of these cracks are linked with the local geologic faults oriented northwest–southeast. The limestone is a Cretaceous chalk (Senonian) containing flints and fossils (Figure 2a, in green). This chalk is covered by a clayey/sandy formation. Its thickness ranges between 2.5 and 13.5 m. The total thickness of the sedimentary horizon of land above the pillar is 20 m. In the examined area, regular pillars were built. The perimeter of the examined pillar is approximately 25 m, and its mean height is 3 m. It is located approximately 50 m away from the quarry entrance. One of the cracks linked with the geologic fault can be seen around the pillar.

Regarding a possible thermal effect on resistivity (Hayley et al., 2010), preliminary thermal infrared imaging camera observations showed that the temperature is clearly homogeneous over the whole pillar surface. Given its location in the quarry, the temperature within the pillar is considered to be homogeneous.

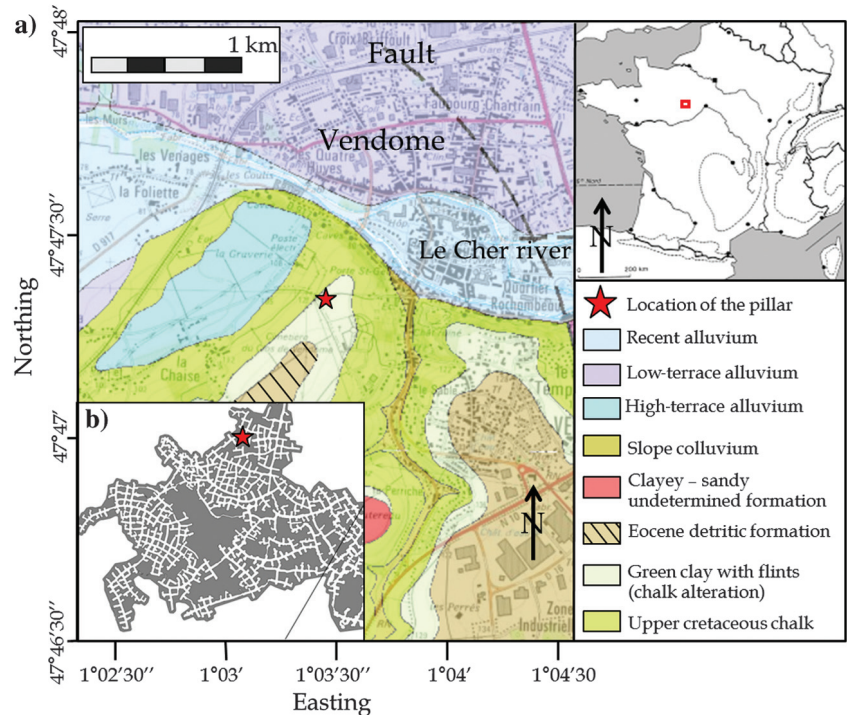


Figure 2. (a) Geologic map of the Vendôme area and (b) map of the quarry. The red star indicates the location of the pillar. Coordinate system: WGS84.

Photogrammetric survey

To produce the photogrammetric surface model, a set of approximately 100 pictures obtained at different angles and distances was taken on the quarry pillar (see Figure 3). For this survey, we followed a linear acquisition path to get the entire data set with an average overlap of 80% between two successive photographs (Pierrot-Deseiligny and Clery, 2012) (see Figure 3). During the acquisition (approximately 1 h), great attention was paid to the four corners of the pillar: More images were acquired for an optimal link between each side of the pillar.

The camera used is a Panasonic GF1 (the focal length is 28 mm, and the sensor size is 18×13.5 mm), creating 12 megapixel pictures. Due to a lack of luminosity in underground context, we used six spots (500 W each) to homogenize the light on the pillar. The difficulty to homogenize the illumination of the pillar appears to be a major cause of noise in the colored point cloud (Figure 3).

We used a set of 192 GCPs corresponding to the location of the electrodes. The GCPs coordinates (x, y, z) were obtained with a laser apparatus first to calibrate the photogrammetric model and second to compare the photogrammetric and laser DTM. Considering the accuracy of this method, the positioning errors are assumed to be negligible. These GCPs are included after the bundle adjustment by giving the pixel location (x, y) of each GCP on 72 photographs out of the complete set of pictures. After the MICMAC computation, the final point cloud is exported to carry out a comparison between

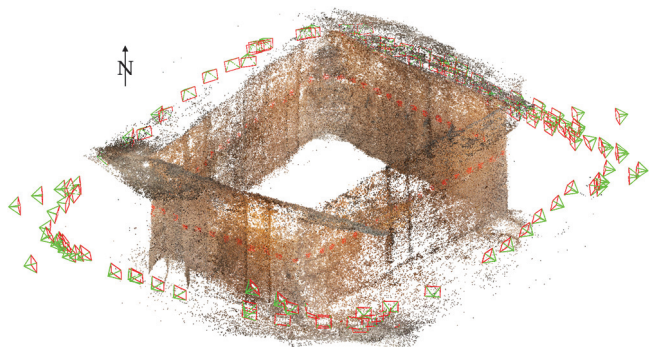


Figure 3. The 3D view of the resulting colored point cloud. The red and green tetrahedrons represent the locations and orientations of the camera.

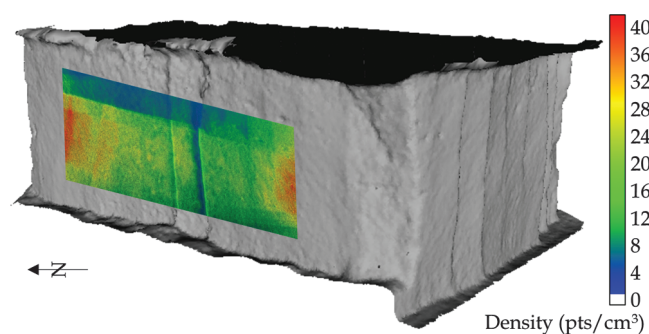


Figure 4. Photogrammetric model obtained after removing outliers and applying the denoising procedure. The superimposed figure in color shows the point density of an area of the photogrammetric model.

laser and photogrammetric results. The study shows a root-mean-square (rms) error of the photogrammetric point cloud less than 2 cm (± 0.4 cm) in all three directions.

Figure 4 shows the result of the photogrammetric computation after removing outliers and applying a denoising procedure. The former procedure consisted of manually removing points that fall outside of the region of interest. The denoising procedure is a statistical outlier removal (SOR) filter computing the mean distance of each point to its neighbors and rejecting points that are farther than this average distance plus a standard deviation (Point Cloud Library [PCL]). We use six neighbors for the mean distance estimation and a standard deviation of one. The average point density on each face of the pillar is 23 points/cm². It can be noted that the lower volume point density near the cutting faces of the pillar is due to blind spots. The resulting photogrammetric model contains approximately 10 million points.

Geoelectric survey

We performed an ERI survey on the pillar. It consists of three electrode belts around the pillar located approximately 1.0, 1.5, and 2.0 m high (entitled H1, H2, and H3, respectively; Figure 5b). Each belt is composed of 64 electrodes with a 37 cm interelectrode spacing. The total perimeter is approximately 24 m.

For each electrode belt, a specific Wenner-Schlumberger protocol (for circular tomography [Lesparre et al., 2014]) was performed with the ABEM Terrameter LS producing three sets of 1224 quadrupole measurements ($a = 1 - 8$ and $n = 1 - 4$). Protocol does not contain crossline measurements (between belts, [Cho and Yeom, 2007]). All of the measurements present an excellent quality factor (mean = 0.08%, Std = 0.09), and no reciprocal measurements were carried out. The electrodes are 8 cm length stainless steel screws embedded to a depth of 4 cm in the chalk. This technical solution represents the best trade-off in terms of cost and contact resistance (the measured average contact resistance is 750 Ω). Three electrodes presented a lower contact resistance (approximately 50 Ω).

Model construction

To be successfully inverted, the model (geometry and meshing) needs to fit the actual medium and physics (electric current diffusion) as accurately as possible. However, the required level of accuracy decreases proportionally to the distance from the electrodes. Consequently, it is necessary to integrate great precision in the electrode locations (Oldenborger et al., 2005) and surface topography nearby. Conversely, a lower accuracy is needed for the remainder of the model. We construct a model composed of three parts (Figure 5a–5c). First, a 20 m high layer of land above the quarry is generated to let the current circulate above the “room” and the pillar. Second, the pillar is surrounded by air (Figure 5b). Third, a hemisphere of earth material (radius: 500 m) is generated below the pillar to let the current circulate below the room within an “infinite” medium (Marescot et al., 2008). As a consequence, the only part of the true geometry that is neglected consists of the other pillars. Given their distance to the electrodes, we assume that they have no significant influence on the data.

Concerning the generation of the pillar, the output model of the photogrammetric survey was used. However, even after a denoising postprocessing stage (CloudCompare, Figure 4), the model was too dense and noisy to be directly used for our applications: 3D

geoelectric modeling. Consequently, to overcome the above limitation and supply a suitable model, we chose to construct it by extrusion and interpolation of horizontal slices extracted at several heights of the previously presented photogrammetric model. More precisely, some extrusion and surface interpolation operations (loft NURBS: nonuniform rational basis splines) between the slices were performed to generate the complete 3D geometry model (Figure 5b). Extrusions of slices were made near the location of electrodes (E_1 , E_2 , and E_3), whereas lofts were made in between the above-mentioned zones (L_1 and L_2) (Figure 5b). Each loft is computed with eight guided curves and four intermediate layers to avoid self-intersections. The choice to use horizontal slices comes from the need to obtain a greater horizontal accuracy of the surface geometry. Indeed, fewer surface geometry variations are expected in the vertical axis and the acquisition (no interbelt measurement) induces a maximum sensitivity between electrodes of the same belt, not between them.

After this simplification, the boundaries of the model are extended to fit the Dirichlet criteria (Figure 5a and 5c). The mesh model is shown in Figure 5a, in which the pillar is centered and surrounded by one hemisphere (beside) and a plate simulating the land above. Insulation conditions are imposed at the boundaries between the lower hemisphere and the land, at the surface of the pillar and at the top of the model (air/media boundaries, Figure 5c).

Numerical test

The aim of this section is to present a numerical study showing how inversion results depend on the resolution of the 3D geometric surface model. A first model, considered as the “true model” and based on slices in full resolution (approximately 40 points between each electrode), is created according to the aforementioned methodology (see Figure 6a). Then, six distinct models of various resolutions are created (M1–M6).

A decreasing resolution is applied from the first (M1) to the sixth model (M6). For M1, 40 points (1 cm spacing) are used between each pair of electrodes to construct the various slices of the model (the same number of points as compared with the true model). This number is decreased to 10 points for M2 (4 cm spacing), five points for M3 (7 cm spacing), two points for M4 (13 cm spacing), one point for M5 (20 cm spacing), and zero point for M6 (40 cm spacing) slightly modifying the contour of the geometry (Figure 6b for M1, M3, and M6). Consequently, for M6, the contours are only based on the “true” electrode positions (see Figure 6a). The enlargement (Figure 6b) shows the contour interpolation for M1, M3, and M6. Figure 6c–6e presents for models M1, M3, and M6 a 2D slice of the 3D forward mesh, and an enlargement of this mesh and the 3D inversion cells, respectively. The two enlargements are proposed in a particular area of interest showing the impact of a lower geometry resolution (near the most angular working face, Figure 6b and 6d). For each model (M1–M6), the inversion cells are composed of four elements (Figure 6e) between each pair of electrodes (explaining a quite constant number of inversion cells and forward meshes). The difference between these models comes from the capacity of the inversion cells fitting the various accuracies of the surface geometry.

Three cylindrical anomalies (vertically oriented) are positioned in the true model of the pillar. The resistivity of the anomalies and the surrounding pillar body are 150 and 250 Ωm , respectively (Figure 7). Anomaly A1 is located near an angular working face of the pillar, whereas A3 is close to a flat side of the pillar. To study the

effect of surface geometry errors on inversion results far from the contour, a larger anomaly A2 is generated in the center of the model. A Wenner-Schlumberger protocol is then simulated for each electrode belt to collect the “measured” data detailed in the subsection “Geoelectric survey.”

Figure 8 summarizes the inversion results of each model at the seventh iteration of inversion. These results are presented from slices extracted at three heights corresponding to the electrode belts

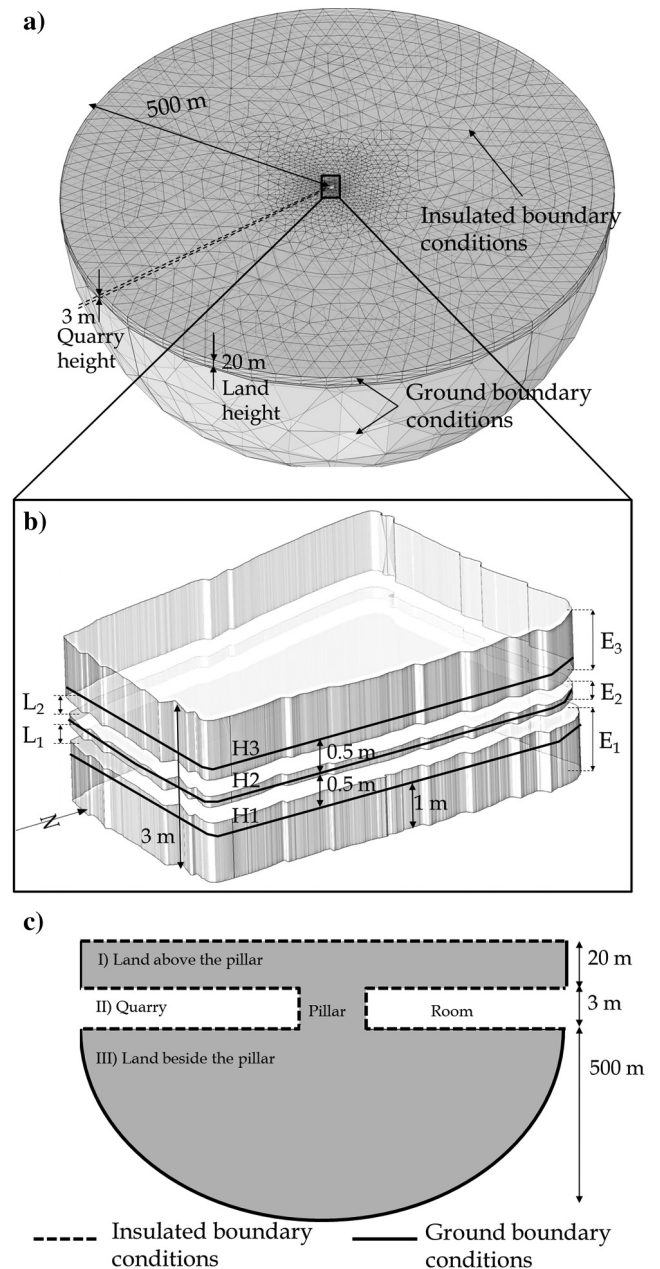


Figure 5. Description of the model with (a) mesh of the global model, (b) the central part of the model simulating the pillar, and (c) a simplified scheme section of the model; E_1 , E_2 , and E_3 represent extrusion zones correlated with the electrode belts; L_1 and L_2 show the loft zones in between the extrusion zones. The solid lines in b show the locations of the three electrode belts noted H_1 , H_2 , and H_3 .

positions (H1, H2, and H3). For M1, the three anomalies are clearly visible at the right location in the model for the three slices even if the model resolution decreases as distance from electrode increases (Rucker, 2012). The resistivity of A1 and A3 slightly differs from the true value, whereas the A2 resistivity value is close to 150 Ωm . However, because of the ℓ_2 -norm used, the inversion does not preserve the sharp interfaces between the anomalies and the pillar. Some small artifacts appear in the result in the vicinity of strong

working faces (near anomaly A1) and near anomaly A3. Because of the inherent loss of sensitivity in the center of the pillar, the detection capability of A3, as suggested by Tejero-Andrade et al. (2015), should be lower. In this study, we assume that the favorable context of our synthetic model facilitates the detection of A3. As proposed by Tejero-Andrade et al. (2015), optimized acquisition arrays could have been used to limit the loss of sensitivity and more accurately detect the central anomaly.

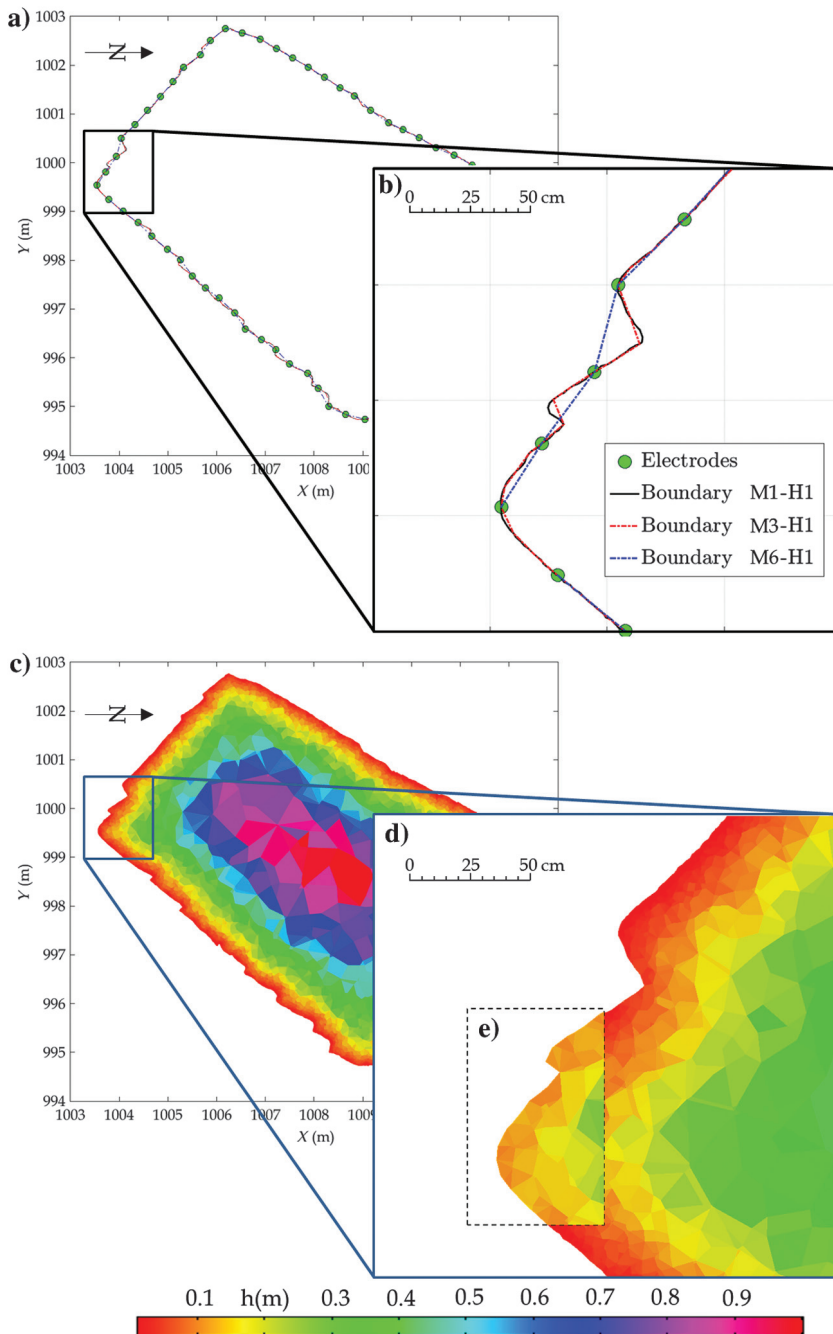


Figure 6. Sketch showing (a) various contours at height H1 used for the models M1, M3, and M6 and (b) an enlargement near a particular zone of M1 at height H1. The green points represent the locations of the electrodes. (c) A slice of the 3D forward mesh at H1, (d) enlargement of a zone of complex geometry, and (e) a slice of the 3D inversion cells. The color scale represents the average height h of the meshes.

The model M2–M5 results are very similar to the previous model showing a high-quality reconstruction of the true model. The main visible difference between M1 and M2–M5 is the new artifacts in H1, H2, and H3 at various locations. The number of artifacts increases from M2 to M5. However, these artifacts do not limit detection of the three anomalies.

The result of M6 is different and presents various artifacts on the slices boundaries. The detection of the anomaly A1 is not possible, whereas the locations of anomalies A2 and A3 remain clear. Table 1 summarizes the input data of each study and information on the inversion results. The rms error increases from M1 to M6 showing the benefits of a more accurate surface geometry.

To enrich the comparison of the six cases investigated, the similarity index S_i between the inversion result and the true model is used (equation 4). This index is computed for four different volumes: S_{A1} , S_{A2} , S_{A3} , and S_P corresponding to anomalies A1, A2, A3, and the embedding pillar body P, respectively. Each index is computed on volumes whose height is bounded by the height of the pillar (3 m). All the similarity index values show a reconstruction error lower than 35% and show a decreasing quality from M1 to M6. This is particularly true for S_{A1} and S_P , indicating that a poor geometry description greatly affects the inversion results near the contour and in the vicinity of strong surface variations.

Concerning anomaly A2, the S_{A2} results tend to show that the degradation of the geometry does not affect the inversion result far from the contour (at the heart of the pillar body). One unexpected result shows that the anomaly is better reconstructed in M5 compared with M3. This result may be due to a better model parameter discretization at the center of the pillar for M3. This difference of discretization can be explained by fewer model parameters near the electrodes for a quite constant number of model parameters in the six models.

The study of the similarity index of anomaly A3 shows little variation between the three models. However, an unexpected greater value is calculated for M1 than for M2. For all the unexpected results, this could be a side effect of the previously mentioned issue, or numerical issues,

or more simply an over-interpretation of small variations in this criterion.

Figure 9 shows the 3D inversion results (slice at H1) for three different noise levels (1%, 5%, and 10%) and three surface geometry accuracies (M1, M3, and M6). We add a white Gaussian noise to “measured apparent resistivities” with a variance of one. The signal-to-noise ratio is adjusted to obtain the desired rms error (1%, 5%, or 10%). Results show that the anomaly A2 can be detected in all the results except Figure 9e and 9i; A1 is only detectable in the results of Figure 9a and A3 in the results of Figure 9a, 9b, and 9d. Results show that surface geometry accuracy could be compared with noise added to the measurements with small electrodes spacing. The second interpretation is that a higher noise level tends to smooth the reconstruction of A2, thus limiting its detectability. This study shows that a noise level superior to 5% and a few intermediate points inferior to five limits the resolution of the inversion result and its interpretability.

Real case study

This section focuses on the data measured on the real underground mine pillar performed in June 2015 and presented in the section “Site test description.” The most complete model (M1) of the previous section is used because it supplies the best choice in terms of results and computing cost. In this study, M6 is also used with the same data set to help identify artifacts due to a poor surface geometry description.

Figure 10 shows for M6 (left column) and M1 (right column) three slices representing the electric resistivity distribution extracted from the 3D inverse model at heights H1, H2, and H3. The slices are extracted at iteration 4 to limit the over-fitting phenomenon and

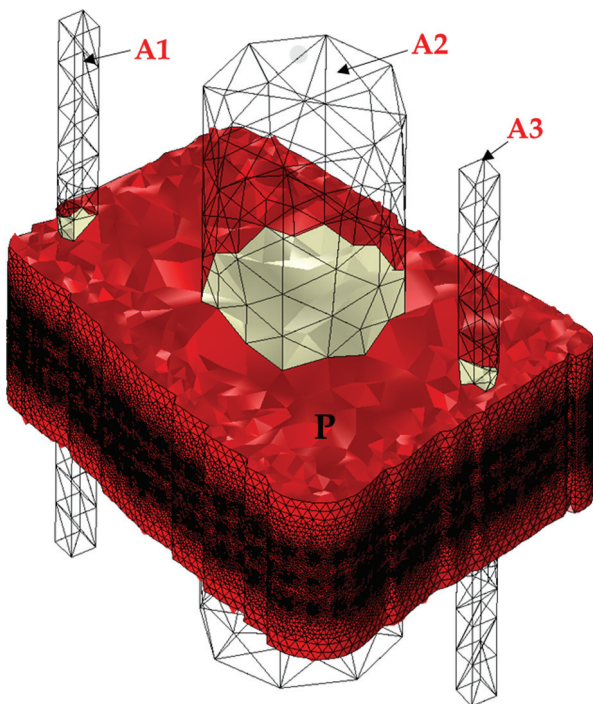


Figure 7. 3D view of the center part (the pillar) of the true model mesh with anomalies A1, A2, and A3. The beige and red colors refer to resistivity of 150 and 250 Ωm, respectively.

present an rms error of 6.78% and 5.25% for M6 and M1, respectively. In the following, M6 inversion results will only be discussed to help the interpretation of the M1 inversion results. For the latter, the distribution is quite homogeneous with a mean resistivity of 250 Ωm, but it presents a few areas where the resistivity ranges from 150 to 350 Ωm. Overall, the three slices not only present a similarity due to a small distance between the belts but also some variations (resistive and conductive) in some particular zones of interest. Some highly resistive zones are persistent on two slices (Ar₁, Ar₃, and Ar₄) but will be considered as artifacts due to the presence of an over-structuration phenomenon (a resistive zone neighboring a conductive zone) or due to strong surface geometry variations in the vicinity. Other highly resistive zones are considered as artifacts due to (1) their nonpersistence on other slices, (2) the presence of an

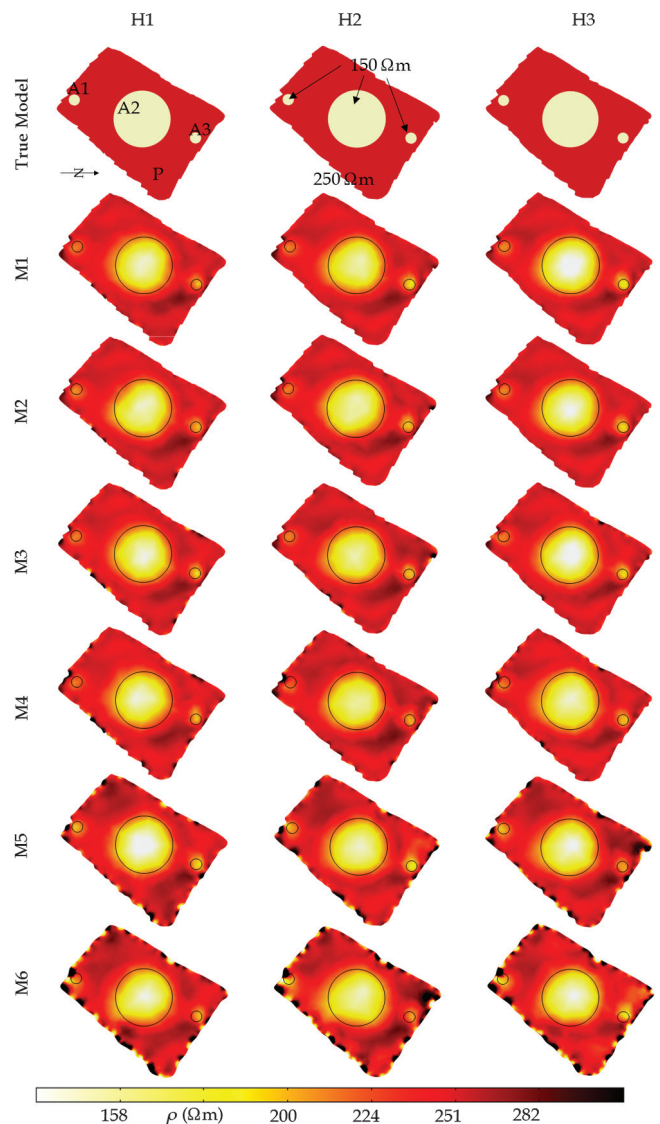


Figure 8. The synthetic study results, each column corresponding to a slice of a 3D model at height H1, H2, and H3. The first line shows the true model used for the synthetic study. Rows two to seven show the inversion results corresponding to cases M1–M6, respectively. The locations of the anomalies (A1, A2, and A3) are superimposed on the inversion results (circles).

over-structuration phenomenon, and (3) strong variations in the surface section geometry nearby (Ar_2 , Ar_5 , Ar_6 , Ar_7 , Ar_{11} , and Ar_{12}). Two conductive zones are considered as artifacts (Ar_9 and Ar_{10} , see H2) due to a small persistence on the other slices and the presence of important surface geometry variations nearby.

A fast zoning is presented on each slice to delineate conductive or resistive zones. Four clusters are defined: (1) a conductive “C,” (2) a moderately conductive “MC,” (3) a moderately resistive “MR,” and (4) a resistive cluster “R.” This zoning shows that the medium is quite homogeneous beyond 50 cm inside the pillar.

Each slice shows persistent resistive and conductive zones that are essential for the risk assessment interpretation. Indeed, Gombert et al. (2013) show that increasing the water content decreases the strength resistance of chalk. Figure 11 summarizes the main results

of this study with the photogrammetric model and the 3D inversion result (extracted slices). This representation provides better understanding of the pillar and its electric properties. It also leads to an improved interpretation of the available data for a better assessment of the structure. The observed resistivity variations are consistent with the results of Lafrance et al. (2016) on two pillars of different lithotypes. In their study, some laboratory tests on core samplings are done from the wall to the center of the pillars. Among all results, the connected porosity varies between 25% and 50%. Following Archie’s law, this porosity variation can induce a resistivity variation of 1:5 (for a saturated soil medium and a cementation exponent of two). This result is consistent with the global resistivity variation inside the pillar (150–400 Ωm). In Figure 11b, we propose a simplified interpretation of the inversion results. Two phenomena seem to be at the origin of the resistivity variations.

First, the geologic variability of the chalk during the sedimentation with an irregular distribution of macroflints and fossils. Second, a vertical drainage through the pillar takes place as proposed by Lafrance et al. (2016). Lafrance et al. (2016) suggest that an increase in connected porosity is therefore a direct effect of dissolution. The drainage plays a key role in the erosion and dissolution process via chemical weathering for the latter. The drainage in the pillar is amplified by two factors: first, the “room and pillar” organization of the quarry increasing water circulation inside the pillar and, second, the presence of cracks due to a collinear fault family. This phenomenon that is visible on the pillar (Figure 11c) can increase microcracks of the chalk and so the porosity. This conclusion is consistent with the results of Lafrance et al. (2016) who propose that the amount “of cracks and pores should be greater at the pillar walls than in the middle of the pillar.”

DISCUSSION

On the one hand, the 3D media of complex geometry such as underground mine pillars cannot be assessed by conventional geoelectric imaging tools. On the other hand, the photogrammetric technique is increasingly used to provide an accurate cost-effective 3D surface description. This paper shows that the sequential combination of photogrammetric and ERI methods proves particularly relevant for the assessment of media of complex 3D geometry. The second finding is that the accuracy of the geometry (or DTM) is correlated with the inversion reliability.

This research follows the works of Sasaki (1994) and more recently the papers of Demirci et al. (2012) and Erdoğan et al., 2008 introducing the problem of topography in the inversion process. The latter present five different solutions based on finite-difference or finite-element modeling and with a half or full representation of the air volume. In contrast with their paper, we choose to explicitly mesh a 3D complex volume without applying any mesh deformation procedure. This difference adds a step to the inversion process but overcomes the error associated with mesh deformation.

This paper also contrasts with the conventional technique used to obtain the surface model. We present the first attempt to explicitly take into account an output photogrammetric model as an ERI input model geometry. For this particular point in our approach, the

Table 1. Information about both entries of the six models and inversion results.

	M1	M2	M3	M4	M5	M6
Number of intermediate points	~40	10	5	2	1	0
Distance interpoints (cm)	1	4	7	13	20	40
Number of inversion parameters	22,788	23,817	22,873	22,646	22,663	22,438
The rms error at iteration 7 (%)	0.009	0.013	0.036	0.073	0.136	0.412
S_{A1}	0.188	0.212	0.224	0.235	0.260	0.354
S_{A2}	0.12	0.122	0.134	0.134	0.132	0.162
S_{A3}	0.124	0.133	0.126	0.137	0.148	0.162
S_P	0.089	0.096	0.105	0.125	0.210	0.324

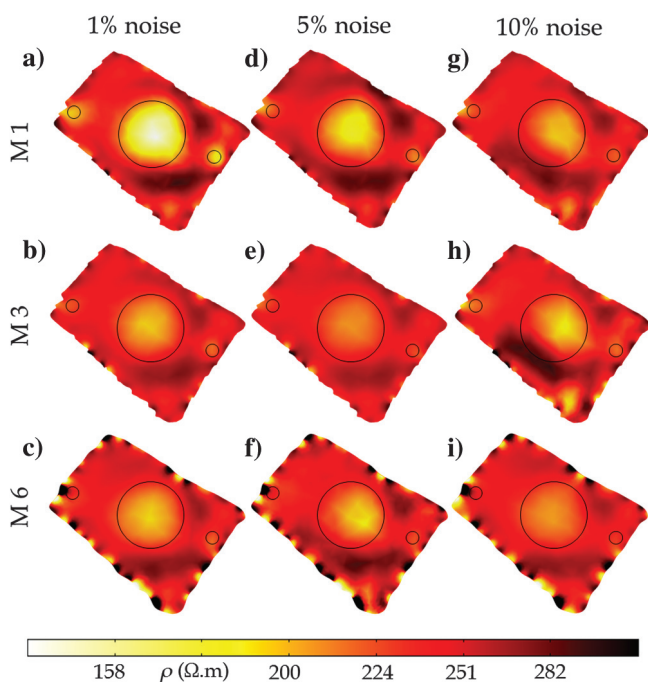


Figure 9. The combined effect of noise (levels: 1%, 5%, and 10%) and surface geometry accuracy (models: M1, M3, M6) on inversion results. The sections are extracted at height H1 of the 3D inversion model at iteration 7.

choice of the photogrammetric method instead of laser technology leads to a cost-effective survey solution. As explained by Bretar et al. (2013), the result of the photogrammetric stage is a surface point cloud exhibiting a resolution better than 2 cm. Results show that it also offers a greater flexibility to obtain an optimized surface reconstruction near areas of interest (cutting face, electrodes). However, the application to an underground mine requires the scene to be lightened.

This paper in one particular aspect goes further than the research presented by Erdoğan et al. (2008), which takes into account only the electrode locations to create the model. We demonstrate here the need to use topography information between electrodes and in their vicinity. Consequently, this result ensures consistency with Maurer and Friedel (2006), who show that it is necessary to integrate information on the medium even in regions away from the electrodes. Moreover, it brings clues as to the resolution needed in between electrodes. For complex models, five elevation points in between each electrode seem to be a minimum trade-off between the inversion quality and the cost of the photogrammetric survey. Conversely, it shows that just a perfect knowledge of the location of the electrodes

(without other geometric information) is not sufficient to achieve a relevant inversion result.

This procedure was applied to a real quarry pillar with a resolution on the model geometry never taken into account before. Due to numerical issues, the complete geometry was not taken into account, leaving questions about the presence of residual artifacts in the inversion result. Due to the construction of the geometry with horizontal slices, the questioning more particularly concerns

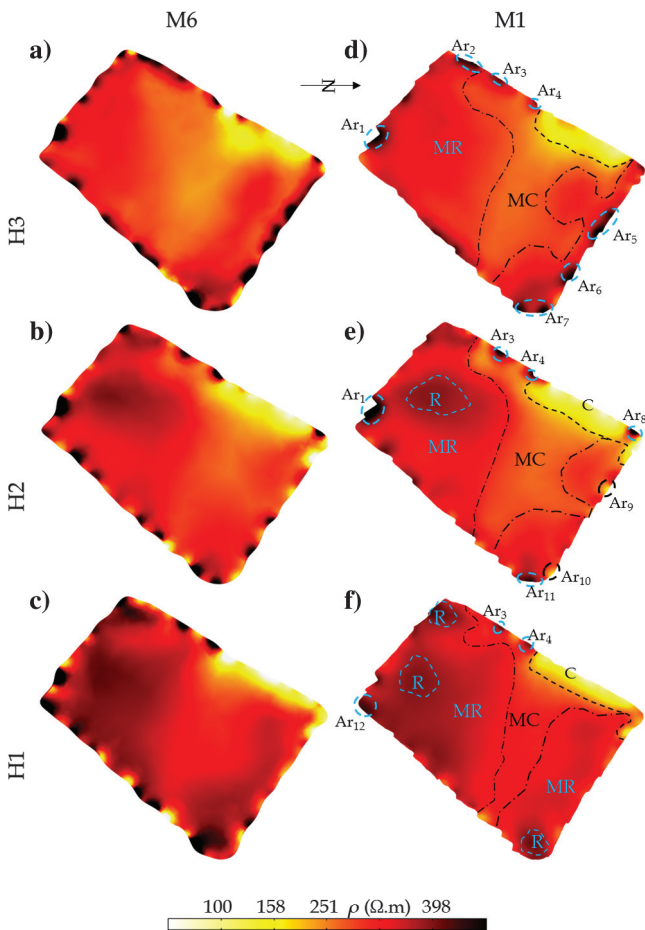


Figure 10. The block figure presenting pillar results of (a-c) model M6 and (d-f) model M1. Each column corresponds to a slice of a 3D model (iteration 5) at heights H1, H2, and H3. The location of the artifacts (Ari) and zoning are superimposed on the inversion results (R, resistive; MR, moderately resistive; MC, moderately conductive; and C, conductive).

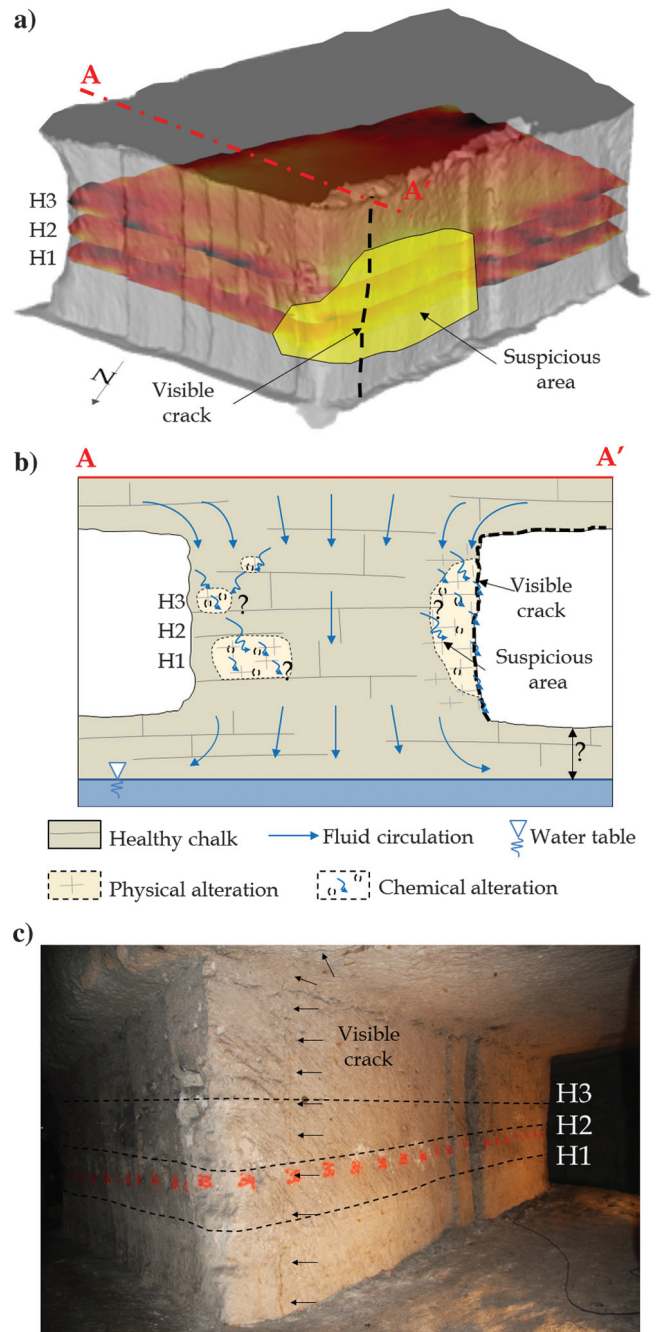


Figure 11. The synthesis of the results with (a) a 3D view of the result of the photogrammetric and ERI surveys, (b) a geologic interpretation of the results, and (c) a picture of the pillar. Some additional information is superimposed such as the location of a visible crack on the surface and the extension of the “suspicious area.”

an incomplete vertical resolution. The extrusion and loft operations greatly limit vertical variations that can occur in the vicinity of electrodes. This result confirms the conclusions of Sjö Dahl et al. (2006) showing that the lateral resistivity variations have an important effect on the measurement itself. This incomplete surface reconstruction appears as one of the main causes of artifact generation in the inversion process. As demonstrated by the synthetic study, the noise on measurement can also generate artifacts and limits the detectability of anomalies inside the pillar. However, main artifacts appear near great surface topography variations.

Results in this paper imply that for the common practice of performing a DTM, one has to take particular care during a geophysical survey. For the example of volcano surveys (Finizola et al., 2002; Brothelande et al., 2014, 2015), or engineering applications (hydraulic structures [Fargier et al., 2014]), the desired ERI resolution is often weaker than the DTM variations between two adjacent electrodes. In this case, our experience shows that the use of a very accurate surface description must become of major importance when the variation between interelectrode spacing and surface electrode spacing (at the same scale) is greater than 30%.

CONCLUSION

A methodology of sequentially combining photogrammetry and ERI is presented and applied to an underground mine pillar to fully process a considerable amount of data. The photogrammetric technique provides a low-cost, high-resolution surface model, set as input geometry data for the ERI inversion. A new ERI inversion code based on MATLAB and Comsol Multiphysics software was developed to fully invert the 3D model. This paper presents the first attempt to fully integrate an output photogrammetric model as an input model for ERI. The paper focuses on one particularly difficult issue of the methodology that consists in adapting the output photogrammetric model to the inversion code. An empirical procedure based on postprocessing stages is proposed to supply a surface model suitable for the 3D ERI. This step is followed by a numerical test showing the negative effect of an incomplete resolution of the photogrammetric model used as an input model for ERI. Some recommendations can be derived from results concerning a minimum acceptable resolution of the photogrammetric model. The methodology is applied to a real case study of an underground mine pillar of chalk. Despite the complex geometry of the examined pillar, our methodology provides reliable 3D inversion results. However, some artifacts partly due to an incomplete vertical resolution of the input model geometry remain present but can be identified by superimposing the ERI reconstruction and the photogrammetric result. In the near future, we hope first to improve this particular point in order to better take vertical variations between electrode belts into account. Further research will then focus on an experimental procedure to link electric resistivity spatial evolution, water content, and unconfined compressive strength to supply a safety criterion for the pillar.

ACKNOWLEDGMENTS

The authors wish to thank the city council of Vendôme for access to the site as well as the research projects PRECAS and APHO-GEOPHY for funding. We are grateful to E. Pairault, Y. Boussafir, and J. Lacogne for field data collection and interpretation.

REFERENCES

- Abellán, A., T. Oppikofer, M. Jaboyedoff, N. J. Rosser, M. Lim, and M. J. Lato, 2014, Terrestrial laser scanning of rock slope instabilities: Earth Surface Processes and Landforms, **39**, 80–97, doi: [10.1002/esp.v39.1](https://doi.org/10.1002/esp.v39.1).
- Al Heib, M., C. Duval, F. Theoleyre, J.-M. Watelet, and P. Gombert, 2014, Analysis of the historical collapse of an abandoned underground chalk mine in 1961 in Clamart (Paris, France): Bulletin of Engineering Geology and the Environment, **74**, 1001–1018, doi: [10.1007/s10064-014-0677-6](https://doi.org/10.1007/s10064-014-0677-6).
- Audebert, M., R. Clément, J. Grossin-Debattista, T. Gunther, N. Touze-Foltz, and S. Moreau, 2014, Influence of the geomembrane on time-lapse ERT measurement for leachate injection monitoring: Waste Management, **34**, 780–790, doi: [10.1016/j.wasman.2014.01.011](https://doi.org/10.1016/j.wasman.2014.01.011).
- Bell, F. G., M. G. Culshaw, B. S. P. Moorlock, and J. C. Cripps, 1992, Sub-sidence and ground movements in chalk: Bulletin of the International Association of Engineering Geology, **45**, 75–82, doi: [10.1007/BF02594906](https://doi.org/10.1007/BF02594906).
- Brady, B. H. G., and E. T. Brown, 2013, Rock mechanics for underground mining: Springer Science & Business Media.
- Bretar, F., M. Arab-Sedze, J. Champion, M. Pierrot-Deseilligny, E. Heggy, and S. Jacquemoud, 2013, An advanced photogrammetric method to measure surface roughness: Application to volcanic terrains in the Piton de la Fournaise, Reunion Island: Remote Sensing of Environment, **135**, 1–11, doi: [10.1016/j.rse.2013.03.026](https://doi.org/10.1016/j.rse.2013.03.026).
- Brothelande, E., A. Finizola, A. Peltier, E. Delcher, J.-C. Komorowski, F. Di Gangi, G. Borgogno, M. Passarella, C. Trovato, and Y. Legendre, 2014, Fluid circulation pattern inside La Soufrière volcano (Guadeloupe) inferred from combined electrical resistivity tomography, self-potential, soil temperature and diffuse degassing measurements: Journal of Volcanology and Geothermal Research, **288**, 105–122, doi: [10.1016/j.jvolgeores.2014.10.007](https://doi.org/10.1016/j.jvolgeores.2014.10.007).
- Brothelande, E., J.-F. Lénat, A. Normier, C. Bacri, A. Peltier, R. Paris, K. Kelfoun, O. Merle, A. Finizola, and E. Garaebiti, 2015, Insights into the evolution of the Yenkahe resurgent dome (Siwi caldera, Tanna Island, Vanuatu) inferred from aerial high-resolution photogrammetry: Journal of Volcanology and Geothermal Research, **299**, 78, doi: [10.1016/j.jvolgeores.2015.04.006](https://doi.org/10.1016/j.jvolgeores.2015.04.006).
- Brunet, P., R. Clément, and C. Bouvier, 2010, Monitoring soil water content and deficit using electrical resistivity tomography (ERT): A case study in the Cevennes area, France: Journal of Hydrology, **380**, 146–153, doi: [10.1016/j.jhydrol.2009.10.032](https://doi.org/10.1016/j.jhydrol.2009.10.032).
- Chandler, J. H., J. G. Fryer, and A. Jack, 2005, Metric capabilities of low-cost digital cameras for close range surface measurement: The Photogrammetric Record, **20**, 12–26, doi: [10.1111/j.1477-9730.2005.00302.x](https://doi.org/10.1111/j.1477-9730.2005.00302.x).
- Cho, I. K., and J. Y. Yeom, 2007, Crossline resistivity tomography for the delineation of anomalous seepage pathways in an embankment dam: Geophysics, **72**, no. 2, G31–G38, doi: [10.1190/1.2435200](https://doi.org/10.1190/1.2435200).
- Dahlin, T., 1996, 2D resistivity surveying for environmental and engineering applications: First Break, **14**, 275–283, doi: [10.3997/1365-2397.1996014](https://doi.org/10.3997/1365-2397.1996014).
- deGroot-Hedlin, C., and S. Constable, 1990, Occam's inversion to generate smooth, two-dimensional models from magnetotelluric data: Geophysics, **55**, 1613–1624, doi: [10.1190/1.1442813](https://doi.org/10.1190/1.1442813).
- Demirci, I., E. Erdoğan, and M. E. Candansayar, 2012, Two-dimensional inversion of direct current resistivity data incorporating topography by using finite difference techniques with triangle cells: Investigation of Kera fault zone in western Crete: Geophysics, **77**, no. 1, E67–E75, doi: [10.1190/geo2011-0130.1](https://doi.org/10.1190/geo2011-0130.1).
- Dé Robert, X., and O. Abraham, 2000, GPR and seismic imaging in a gypsum quarry: Journal of Applied Geophysics, **45**, 157–169, doi: [10.1016/S0926-9851\(00\)00025-2](https://doi.org/10.1016/S0926-9851(00)00025-2).
- Erdoğan, E., I. Demirci, and M. E. Candansayar, 2008, Incorporating topography into 2D resistivity modeling using finite-element and finite-difference approaches: Geophysics, **73**, no. 3, F135–F142, doi: [10.1190/1.2905835](https://doi.org/10.1190/1.2905835).
- Fargier, Y., S. Palma Lopes, C. Fauchard, D. François, and P. Côte, 2014, DC-Electrical resistivity imaging for embankment dike investigation: A 3D extended normalisation approach: Journal of Applied Geophysics, **103**, 245–256, doi: [10.1016/j.jappgeo.2014.02.007](https://doi.org/10.1016/j.jappgeo.2014.02.007).
- Fauchard, C., R. Antoine, F. Bretar, J. Lacogne, Y. Fargier, C. Maisonnave, V. Guilbert, P. Marjerie, P.-F. Thérain, J.-P. Dupont, and M. Pierrot-Deseilligny, 2013, Assessment of an ancient bridge combining geophysical and advanced photogrammetric methods: Application to the Pont De Coq, France: Journal of Applied Geophysics, **98**, 100–112, doi: [10.1016/j.jappgeo.2013.08.009](https://doi.org/10.1016/j.jappgeo.2013.08.009).
- Ferrero, A. M., A. Segalini, and G. P. Giani, 2010, Stability analysis of historic underground quarries: Computers and Geotechnics, **37**, 476–486, doi: [10.1016/j.compgeo.2010.01.007](https://doi.org/10.1016/j.compgeo.2010.01.007).
- Finizola, A., F. Sortino, J.-F. Lénat, and M. Valenza, 2002, Fluid circulation at Stromboli volcano (Aeolian Islands, Italy) from self-potential and CO₂ surveys: Journal of Volcanology and Geothermal Research, **116**, 1–18, doi: [10.1016/S0377-0273\(01\)00327-4](https://doi.org/10.1016/S0377-0273(01)00327-4).
- Fox, R. C., G. W. Hohmann, T. J. Killpack, and L. Rijo, 1980, Topographic effects in resistivity and induced-polarization surveys: Geophysics, **45**, 75–93, doi: [10.1190/1.1441041](https://doi.org/10.1190/1.1441041).

- Gombert, P., C. Auvray, and M. A. Heib, 2013, In-situ and laboratory tests to evaluate the impact of water table fluctuations on stability of underground chalk mines: *Procedia Earth and Planetary Science*, **7**, 304–308, doi: [10.1016/j.proeps.2013.03.138](https://doi.org/10.1016/j.proeps.2013.03.138).
- Günther, T., C. Rücker, and K. Spitzer, 2006, Three-dimensional modelling and inversion of DC resistivity data incorporating topography — Part 2: Inversion: *Geophysical Journal International*, **166**, 506–517, doi: [10.1111/j.1365-246X.2006.03010.x](https://doi.org/10.1111/j.1365-246X.2006.03010.x).
- Hayley, K., L. Bentley, and A. Pidlisecky, 2010, Compensating for temperature variations in time-lapse electrical resistivity difference imaging: *Geophysics*, **75**, no. 4, WA51–WA59, doi: [10.1190/1.3478208](https://doi.org/10.1190/1.3478208).
- Jones, G., P. Sentenac, and M. Zielinski, 2014, Desiccation cracking detection using 2-D and 3-D electrical resistivity tomography: Validation on a flood embankment: *Journal of Applied Geophysics*, **106**, 196–211, doi: [10.1016/j.jappgeo.2014.04.018](https://doi.org/10.1016/j.jappgeo.2014.04.018).
- Lafrance, N., C. Auvray, M. Souley, and V. Labiouse, 2016, Impact of weathering on macro-mechanical properties of chalk: Local pillar-scale study of two underground quarries in the Paris Basin: *Engineering Geology*, **213**, 107–119, doi: [10.1016/j.enggeo.2016.08.014](https://doi.org/10.1016/j.enggeo.2016.08.014).
- Lesparre, N., B. Grychtol, D. Gibert, J.-C. Komorowski, and A. Adler, 2014, Cross-section electrical resistance tomography of La Soufrière de Guadeloupe lava dome: *Geophysical Journal International*, **197**, 1516–1526, doi: [10.1093/gji/ggu104](https://doi.org/10.1093/gji/ggu104).
- Li, S., B. Liu, L. Nie, Z. Liu, M. Tian, S. Wang, M. Su, and Q. Guo, 2015, Detecting and monitoring of water inrush in tunnels and coal mines using direct current resistivity method: A review: *Journal of Rock Mechanics and Geotechnical Engineering*, **7**, 469–478, doi: [10.1016/j.jrmge.2015.06.004](https://doi.org/10.1016/j.jrmge.2015.06.004).
- Loke, M. H., and R. D. Barker, 1996, Rapid least-squares inversion of apparent resistivity pseudosections by a quasi-Newton method: *Geophysical Prospecting*, **44**, 131–152, doi: [10.1111/j.1365-2478.1996.tb00142.x](https://doi.org/10.1111/j.1365-2478.1996.tb00142.x).
- Marescot, L., S. Palma Lopes, S. Rigobert, and A. G. Green, 2008, Non-linear inversion of geoelectric data acquired across 3D objects using a finite-element approach: *Geophysics*, **73**, no. 3, F121–F133, doi: [10.1190/1.2903836](https://doi.org/10.1190/1.2903836).
- Maurer, H., and S. Friedel, 2006, Outer-space sensitivities in geoelectrical tomography: *Geophysics*, **71**, no. 3, G93–G96, doi: [10.1190/1.2194891](https://doi.org/10.1190/1.2194891).
- Multiphysics C, 2008, AC/DC module: User's guide: Comsol.
- Oldenborger, G. A., P. S. Routh, and M. D. Knoll, 2005, Sensitivity of electrical resistivity tomography data to electrode position errors: *Geophysical Journal International*, **163**, 1–9, doi: [10.1111/j.1365-246X.2005.02714.x](https://doi.org/10.1111/j.1365-246X.2005.02714.x).
- Park, S. K., and G. P. Van, 1991, Inversion of pole-pole data for 3-D resistivity structure beneath arrays of electrodes: *Geophysics*, **56**, 951–960, doi: [10.1190/1.1443128](https://doi.org/10.1190/1.1443128).
- Pierrot-Deseilligny, M., and I. Clery, 2011, APERO: An open source bundle adjustment software for automatic calibration and orientation of set of images: *International Archives of Photogrammetry, Remote Sensing and Spatial Information Sciences*, **38**, 5W16.
- Pierrot-Deseilligny, M., and I. Clery, 2012, Some possible protocols of acquisition for optimal use of the “APER0” open source software in automatic orientation and calibration: EuroCOW Workshop.
- Rings, J., A. Scheuermann, K. Preko, and C. Hauck, 2008, Soil water content monitoring on a dike model using electrical resistivity tomography: *Near Surface Geophysics*, **6**, 123–132, doi: [10.3997/1873-0604.2007038](https://doi.org/10.3997/1873-0604.2007038).
- Rucker, D. F., 2012, Enhanced resolution for long electrode ERT: *Geophysical Journal International*, **191**, 101–111, doi: [10.1111/j.1365-246X.2012.05643.x](https://doi.org/10.1111/j.1365-246X.2012.05643.x).
- Sasaki, Y., 1994, 3-D resistivity inversion using the finite-element method: *Geophysics*, **59**, 1839–1848, doi: [10.1190/1.1443571](https://doi.org/10.1190/1.1443571).
- Sjödahl, P., T. Dahlin, and B. Zhou, 2006, 2.5D resistivity modeling of embankment dams to assess influence from geometry and material properties: *Geophysics*, **71**, no. 3, G107–G114, doi: [10.1190/1.2198217](https://doi.org/10.1190/1.2198217).
- Tejero-Andrade, A., G. Cifuentes, R. E. Chavez, A. E. Lopes-Gonzales, and C. Delgado-Solorzano, 2015, L- and CORNER-arrays for 3D electric resistivity tomography: An alternative for geophysical surveys in urban zones: *Near Surface Geophysics*, **13**, 355–367, doi: [10.3997/1873-0604.2015015](https://doi.org/10.3997/1873-0604.2015015).
- Vedaldi, A., and B. Fulkerson, 2010, VLFeat: An open and portable library of computer vision algorithms: *Proceedings of the 18th ACM International Conference on Multimedia*, ACM, 1469–1472, doi: [10.1145/1873951.1874249](https://doi.org/10.1145/1873951.1874249).

5.5 Geoscientists in the Sky : Unmanned Aerial Vehicles Responding to Geohazards (Survey in Geophysics)

Geoscientists in the Sky: Unmanned Aerial Vehicles Responding to Geohazards

**R. Antoine, T. Lopez, M. Tanguy,
C. Lissak, L. Gailler, P. Labazuy &
C. Fauchard**

Surveys in Geophysics

An International Review Journal
Covering the Entire Field of Earth and
Space Sciences

ISSN 0169-3298

Surv Geophys
DOI 10.1007/s10712-020-09611-7



Your article is protected by copyright and all rights are held exclusively by Springer Nature B.V.. This e-offprint is for personal use only and shall not be self-archived in electronic repositories. If you wish to self-archive your article, please use the accepted manuscript version for posting on your own website. You may further deposit the accepted manuscript version in any repository, provided it is only made publicly available 12 months after official publication or later and provided acknowledgement is given to the original source of publication and a link is inserted to the published article on Springer's website. The link must be accompanied by the following text: "The final publication is available at link.springer.com".



Geoscientists in the Sky: Unmanned Aerial Vehicles Responding to Geohazards

R. Antoine¹ · T. Lopez^{2,3} · M. Tanguy⁴ · C. Lissak⁵ · L. Gailler⁶ · P. Labazuy⁶ · C. Fauchard¹

Received: 10 March 2020 / Accepted: 6 August 2020
© Springer Nature B.V. 2020

Abstract

This article presents a review of the use of unmanned aerial vehicles (UAVs) in the context of geohazards. The pluri-disciplinary role of UAVs is outlined in numerous studies associated with mass earth movements, volcanology, flooding events and earthquakes. Scientific advances and innovations of several research teams around the world are presented from pre-events investigations to crisis management. More particularly, we emphasize the actual status of technology, methodologies and different applications that have emerged with the use of UAVs for each domain. It is shown that the deployment of UAVs in the geohazards context has experienced a tremendous increase during the last 10 years, with the development of more and more miniaturized, flexible and reliable systems. The use of such technology (UAV platform, instrumentation, methodologies) is different for each domain, depending on the spatial extent and the time scale of the observed phenomenon, but also on the practical constraints associated with the civil aviation agencies regulations (outside or within urban areas, before or during a crisis...). This paper also highlights the use of recent methodologies associated with semi-automatic/automatic segmentation or deep learning for the processing of important amounts of data provided by UAVs. Finally, although still sparse, the joint use of UAVs and satellite data is progressing and remains a challenge for future studies in the context of geohazards.

Keywords UAV · Geohazards · Mass earth movements · Volcanology · Flooding events · Earthquakes

✉ R. Antoine
raphael.antoine@cerema.fr

¹ Cerema, ENDSUM Team, 10 chemin de la Poudrière, 76121 Le Grand-Quevilly, France

² Géosciences Environnement Toulouse (GET), Institut de Recherche Technologique (IRT) Saint-Exupéry, 14 avenue Edouard Belin, 31400 Toulouse, France

³ International Space Science Institute (ISSI), Hallerstrasse 6, 3012 Bern, Switzerland

⁴ GEOEND, Université Gustave Eiffel, Route de Bouaye - CS 5004, 44344 Bouguenais Cedex, France

⁵ UNICAEN, CNRS, LETG, Normandie Université, 14000 Caen, France

⁶ CNRS, IRD, OPGC, Laboratoire Magmas et Volcans, Université Clermont Auvergne, 63000 Clermont-Ferrand, France

1 Introduction

Robots flying through the sky are no longer a matter of science fiction. Unmanned aerial vehicles (UAVs), or drones, are usually considered as toys, mass surveillance tools or military systems. Besides, this technology is being increasingly implemented into many innovative projects worldwide, for sustainable development goals (Kitonsa and Kruglikov 2018), medical deliveries (Scott and Scott 2019), humanitarian purposes (Sandvik and Lohne 2014) or disaster mitigation (Erdelj et al. 2017). According to the United Nations, for the period 1998–2017, disasters associated with natural hazards killed 1.3 million people and affected 4.4 billion people (Wallemacq et al. 2018), along with economic losses of \$2.9 trillion. In recent years, information provided by manned aircraft and satellites has demonstrated their efficiency during disasters over various temporal and spatial resolutions (from tens of m to km), due to constant up-to-date data availability and efficient GIS (geographical information system) solutions (Voigt et al. 2016). In this frame, UAVs provide an important opportunity to support disaster reliefs and make low-cost observations at the local scale, complementing aircraft and satellites when their deployment remains expensive (for instance, for kilometric size areas). Moreover, in the context of climate change, with extreme weather events increasing in frequency and amplitude, the use of UAVs may be of major interest to improve pre-disaster studies, crisis management and recovery. For example, the August 2017 extreme flood in Sierra Leone, in which the United Nations used drones to complement satellite data over landslides and flooded areas demonstrated how UAVs may assist emergency agencies (<http://www.fao.org/sierra-leone/news/detail-events/en/c/1032705/>). Indeed, for hazard studies, it is essential to investigate areas that are difficult to access. But, it is also necessary to easily change scales of analysis, from local to regional scales. UAV technology can be useful for the mitigation of natural hazards in several ways:

- A huge variety of civil drones as fixed-wing aircraft, multi-copters, rugged UAVs or waterproof systems may be provided for different scales studies and situations,
- Drones can collect multiple types of high-resolution data (from remote sensing to geophysical imagery) to improve early detection and crisis management,
- They can provide access to the web in damaged zones by extension of Wi-Fi,
- These systems can fly over damaged infrastructures, carrying low-weight supplies,
- They can collect massive amounts of data in a limited time (for instance, 15–20 min).

This article provides a review of the literature by examining the role of UAVs in geohazard responses and emphasizing the actual status of the technology. The recent developments from early detection to crisis management, using remote sensing, geochemical or geophysical data of several teams are presented in four different sections. The first section is dedicated to mass earth movements, the second to volcanology, the third to floods, and the last section focuses on earthquakes. The complementarity between data provided by UAVs and satellite imagery is discussed in the last part of this article.

2 UAVs Description

Numerous articles highlight the use of UAVs for detailed morphostructural studies (Gonçalves and Henriques 2015; Cawood et al. 2017; Chesley et al. 2017; Cook 2017), hazard researches (Gomez and Purdie 2016; Giordan et al. 2018) and landslide studies

(Mokhtar et al. 2014; Balek and Blahůt 2017; Casagli et al. 2017; Yu et al. 2017), as support of other remote sensing techniques and field monitoring. Indeed, UAVs provide low-cost aerial surveys, operational flexibility and a better spatial and temporal resolution (Agüera-Vega et al. 2017a). Moreover, the miniaturization of different sensors is underway (Fig. 1), as for the example of magnetic sensors for the measurement of the total magnetic field or of its three components. On-board radars are also in full development. Reflections from around mobile gravimetric sensors dedicated to density measurements are in progress (Limo-G system) (de Saint Jean 2008), with promising prospects for implementation on drones via microelectromechanical system (MEMS) technology (Middlemiss et al. 2016). Thanks to this development, many UAVs platforms as hexacopter (Hastaoğlu et al. 2019), quadcopter (Niethammer et al. 2012; Cook 2017; Peternel et al. 2017) and octocopter (e.g., Turner et al. 2015; Lindner et al. 2016) have been developed for science and civil applications (e.g., DJI Phantom and Mavic quadcopters are very famous). They can acquire a large number of high-spatial-resolution images, defined by their pixel size (0.03–0.08 m/pixel in Niethammer et al. (2012); 0.02 m/pixel in Rossi et al. (2018)) or ground sampling distance (GSD). GSD, generally expressed in cm/pixel, represents the distance between the centres of two consecutive pixels in the image on the ground that can be expressed with the simplified following function:

$$GSD = H * P / f$$

where H is the height of the UAV (m), P is the pixel size of the sensor (micro), and f is the focal length (mm). The bigger the value of the GSD, the lower the spatial resolution of the image and the less visible are details. These images are then used to obtain very quickly (a few minutes per flights), at heights generally lower than 100 m, different digital models as digital surface models (DSM), digital terrain models (DTM, which is a DSM with filtered vegetation), digital elevation models (DEM) with a spatial resolution of 0.02 m/pixel in Rossi et al. (2018) or orthophotographs with a spatial resolution ranging from 0.02 to 0.04 m/pixel (Niethammer et al. 2012; Rossi et al. 2018).
















Surface imaging - Multispectral		Sampling		Geophysics			
Thermal IR	Photogrammetry	Multigaz	Particles	Electromagnetism	Magnetism	Radar	Gravimetry
© FLIR VU PRO	© GOPRO	CO ₂ , SO ₂ , H ₂ S P-T-RH probe	Detection Counting	Helicopter survey (BRGM)	Total Field QTFM	P1Radar	MEMS
							
				La Réunion (© R. Carayol)			
© LMV-OPGC	© CNET - France	© LMV-OPGC			© LMV-OPGC	© OPGC G. Bacques	© Middlemiss et al. (2012)

Fig. 1 Some examples of miniaturized sensors for drone applications, operational or in development in the field of imaging, sampling and geophysics

3 Methodology

One of the major interests of UAVs lies in the fact that several sensors can be simultaneously operated with RGB (red, green, blue), multi-spectral, or thermal sensors (Berni et al. 2009; Zarco-Tejada et al. 2012; Casana et al. 2014; Rossi et al. 2018; Antoine et al. 2019) and LiDAR. However, topographic surveys are possible through the simple use of a set of RGB aerial images with photogrammetric algorithms. Consequently, UAVs developed for fundamental or applied scientific research are traditionally used as a complementary tool to other ground investigations. For example, in morphometric studies, slope kinematics quantification or landslide detection, results from drone imagery interpretation must be calibrated by ground surveys. Concerning data acquisition, several protocols are possible with various parameters: number of photos, flight height, overlap between images, number of ground control points (GCPs). The choice mainly depends on the size of the study area (Chesley et al. 2017) and the expected resolution of the final 3D point cloud. Data acquisition protocols are variable in the bibliography (see Appendices 1 to 4). For 3D model construction, various Structure from Motion (SfM) software packages are now available for creating 3D models from photographs (Cook 2017). Among them, free solutions such as Visual SfM (Wu 2011, 2013) or MicMac (Rupnik et al. 2017) provide accurate solutions for data processing, but a commercial bundle such as Agisoft Metashape (2016) is the most frequently used software for image correlation and generation of 3D point clouds (Turner et al. 2015; Lindner et al. 2016; Balek and Blahůt 2017; Cook 2017). Detailed descriptions of the Metashape workflow (formerly called Photoscan) may be found in Turner et al. (2015).

Nevertheless, the geometric accuracy of 3D models and derived DEMs/DSMs also depends on the acquisition of GCPs by dGPS (Walter et al. 2009; Turner et al. 2015; Thiebes et al. 2016) or theodolite (Peternel et al. 2017). These GCPs are essential for georeferencing the images (Lucieer et al. 2014), and their homogenous distribution on both sides of the study area will influence the accuracy of the obtained point cloud (Agüera-Vega et al. 2017a). With these GCPs, photographs acquired by the drone will be georeferenced and processed in order to obtain a 3D point cloud of the area overflown, but some solutions of direct georeferencing without GCPs exist (Turner et al. 2014; Gabrlík 2015; Mian et al. 2015). Indeed, the SfM and multi-view-stereo (MVS) photogrammetric techniques for airborne or ground images processing are the most widely used photogrammetry techniques in topography studies, to generate high-resolution DEMs and orthophotographs (Turner et al. 2015). This technique allows for a fairly flexible and inexpensive 3D reconstruction of photos acquired by UAV (Westoby et al. 2012; Valkaniotis et al. 2018). The aim is to model a real object or landscape in 3D from a multitude of 2D images, using various algorithms that can detect and identify similar elements between two pictures (i.e. "scale-invariant feature transform") (Lowe 1999, 2004). As a result, a photogrammetric 3D point cloud created from drone photographs can be interpolated into DEMs/DSMs. These datasets are essential for landslide studies (Casagli et al. 2017). The SfM technique is based on multi-view stereopsis (MSV) techniques that provide 3D structure from overlapping photography (at least a 60% overlap in both horizontal and vertical directions) acquired from multiple angles and heights. SfM/MSV techniques are particularly useful and provide dense 3D point cloud and high-resolution digital terrain models with high-spatial resolution (with centimetric to sub-decimetric accuracy) with a possible high temporal resolution. Mesh models (DSMs) generated by triangulation of the dense point clouds can be

created using various algorithms, such as inverse distance weighted (IDW) ones (Comert et al. 2019).

4 Mass Earth Movements

4.1 What Do We Consider as Landslides and How Can We Study Them?

Mass earth movements frequently occur in many disasters involving people and the damage or the destruction of many infrastructures. Every year, mass earth movements (whether landslides, debris flows, mudflows...) trigger in urban or rural areas in various geographical contexts (coastal, mountain). These phenomena can be extremely rapid or slow, in various geological contexts, in saturated or unsaturated materials, in steep channels or without confinement in established channels. Triggering factors are numerous, as they can be associated with external forcing (e.g., meteorological event), or internal forcing (e.g., earthquake) or combination of both (Tang et al. 2019). Nevertheless, the predominant factor is hydro-climatic forcing. In that case, instabilities can be triggered either by accumulated rainfall inducing the progressive saturation of the soil and the rise of the water tables, or by high intensity rainfall events such as thunderstorms and/or tropical storms. Therefore, in a context of global change where precipitation (rates and nature) may change, several studies have focused attention on effects of global warming on heavy rainfall frequency or tropical cyclones intensity (Edenhofer et al. 2014). Consequently, we wonder about the impact of these changes on the occurrence of hydro-gravitational phenomena (frequency, intensity, location). Several types of mass movement exist (Hungar et al. 2014) and their complexity involves a large number of approaches and methods. In order to reduce damages caused by landslides, it is therefore essential to have a precise knowledge of the hazard, especially by mapping its extension and intensity to identify vulnerable areas where elements at risk exist (Graff et al. 2019). In this context, and for operational intervention for risk management, UAVs are essential for many applications. Widely used for hazard inventory mapping and identification of unstable areas (Comert et al. 2019), as ground investigation can be time-consuming, UAVs make possible a fast intervention in post-hazard events. Thanks to high-resolution digital cameras (RGB, but also other sensors such as multi-spectral systems), we can easily obtain high detailed 3D point clouds, DEMs/DSMs and orthomosaics, orthophotographs to easily get a lot of information of the studied areas.

In landslide studies, UAVs facilitate rapid identifications of instabilities after major events with accurate data over areas of several km². The use of UAVs is consequently very effective during crisis situations, when quick identification of affected areas (e.g., road blockages linked to sediment flows for rescue operations) is necessary but can be tedious for very large areas (several hundred km²). In this case, very high-resolution (VHR) satellite imagery will be favoured. Indeed, various satellite systems (e.g., Pleiades system) provide last-minute requests for images acquisition. These data are essential for precision mapping and intervention for public safety (Voigt et al. 2016; Lang et al. 2018). However, according to the geographical context (e.g., slope orientation, tropical area), the acquisition of high spatial, temporal and spectral resolution imagery just after a crisis can be useless. For instance, in tropical/subtropical areas, instabilities mainly occur during rainy (and thus cloudy) season (Saito et al. 2014), when optical imagery is difficult to implement. To overcome this problem, interferometric synthetic aperture radar (InSAR), airborne light detection and ranging (LiDAR) or airborne laser scanning (ALS) can be good alternatives for

risk assessment and landslide monitoring (Delacourt et al. 2007; Jaboyedoff et al. 2012; Scaioni et al. 2014). Indeed, InSAR offers frequent and free solutions for landslide assessment (e.g., Sentinel-1) (Barra et al. 2016) with image acquisition during day and night and all weather conditions. However, this technique is not applicable everywhere because it depends on the landslide kinematics (inappropriate for slow moving landslide), and its orientation (Casagli et al. 2017). The other solution is ALS, a highly adaptable technique providing high-resolution 3D point clouds (Delacourt et al. 2007; Jaboyedoff et al. 2012), which is a great advantage for landslide detection (Mezaal et al. 2018). One of the major drawbacks of LiDAR technology is the cost of data acquisition, especially with manned aircraft. Drones are now equipped with LiDAR sensors, and also multi- and hyperspectral sensors (Morsdorf et al. 2017), but their operational use is still not straightforward (Piégay et al. 2020). In this context, UAVs equipped with optical sensors provide valuable information for hazard identification and disaster assessment with a high potential to replace expensive or time-consuming tasks. This is why the use of UAVs, among landslide monitoring techniques, is spreading widely (Giordan et al. 2020).

With a Google Scholar search for keywords “UAV, landslide,” over 6000 items published since 2015 were returned. For our review, a body of 28 articles have been selected from articles found by a search by keywords in Google Scholar, and Science Direct database (i.e. “UAV, drone, photogrammetry, mass movement, landslide, remote sensing”). In the present cases, implementation of UAVs for landslide survey deals with three main scientific issues: (1) hazard mapping, (2) morphological analysis and (3) landslide physical evolution (Appendix 2).

4.1.1 Landslide Hazard Mapping and Morphological Analysis

Hazard mapping is possible at a medium or large scale, in order to carry out inventories of mass earth movements just after a specific event triggering (Valkaniotis et al. 2018; Comert et al. 2019; Tang et al. 2019), or to locate historical landslides of a region. In both cases, landslide identification can be conducted by manual analysis of orthoimages and 3D models (point clouds, 3D meshes, DEMs) from UAVs. Thus, a simple 3D visualization of a coloured point clouds can help to identify morphological features associated with landslides. Numerous studies are also based on topographic, landscape change detection performed on DEMs (Van Den Eeckhaut et al. 2012; Aditian et al. 2018; Bunn et al. 2019) and/or 3D point clouds acquired at different times. The landscape change detection is usually performed automatically using algorithms developed to compare 3D point clouds. Among them, Cloud-to-Mesh distance (C2M)/Cloud-to-Cloud distance (C2C) tools (Girardeau-Montaut et al. 2005) and M3C2 algorithm (Lague et al. 2013), implemented in the CloudCompare software (CloudCompare v.2.5.4 and newer), are the most used for 3D point cloud analysis (Valkaniotis et al. 2018). Indeed, by comparison of multi-temporal datasets (before and post-failure 3D point cloud or DEM), it is then possible to quantify the amount of removed sediments (Valkaniotis et al. 2018). Landslide inventory maps are essential for risk assessment to avoid the exposure of goods and people to hazard. Inventory maps provide quantitative and qualitative information on landslide hazard such as boundaries, main and secondary scarps, shape, size and depth. Inventories are traditionally based on manual interpretation of aerial images/orthophotographs interpretation and DEM derivatives (Görüm 2019). Several derivatives [e.g., local dominance, positive openness, negative openness, terrain ruggedness index (TRI), local relief model (Fig. 2)] can be exploited from DEM dataset, to extract information

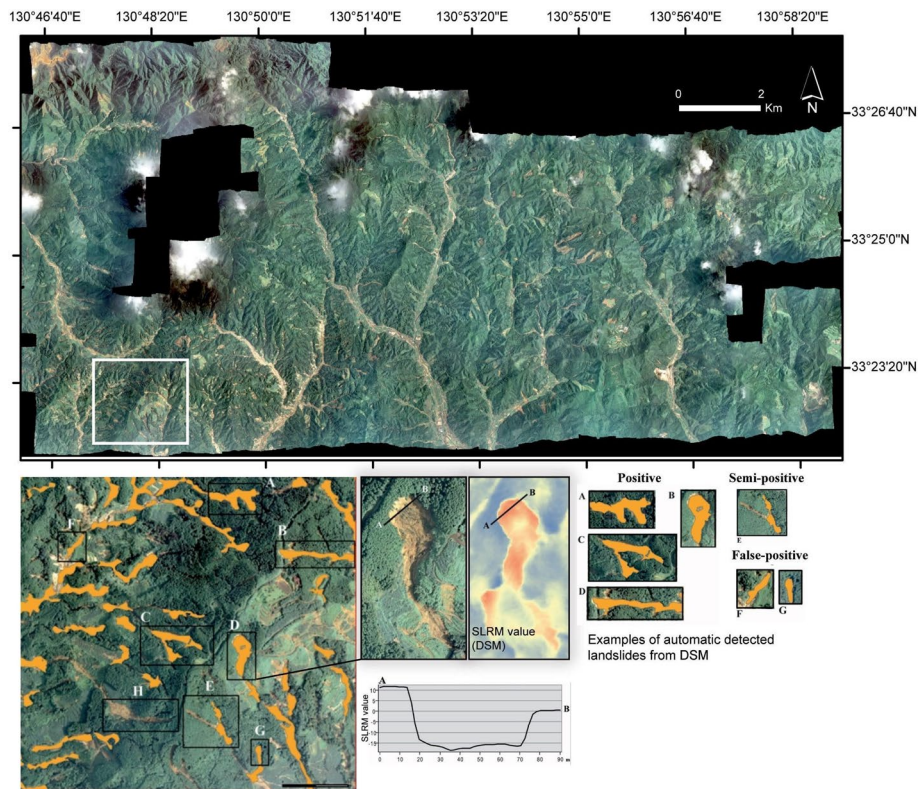


Fig. 2 UAV-based map inventory of multiple shallow landslides triggered in July 2017, Kyushu Island, Japan (photogrammetry process C. Gomez, Kobe University 2017) (Reproduced with the permission of the authors C.Lissak, V. Siccard 2020, Caen University) (Lissak et al. 2019)

on terrain morphologies from topographic anomalies. However, manual interpretation and analysis have been progressively replaced by the automation of landslide recognition with pixel-based image analysis (PBIA) of orthophotographs, or by object-based image analysis (OBIA) of orthophotographs or DEMs and DEM derivatives (Stumpf and Kerle 2011; Lahousse et al. 2011; Rau et al. 2012; Van Den Eeckhaut et al. 2012; Moosavi et al. 2014; Comert et al. 2019). OBIA is based on multi-data combination with metrics analysis with spectral (e.g., Green-Red Vegetation Index-RGVI for RGB images), geometric, contextual, and textural information of image objects defined, DEM derivatives (e.g., slopes, curvature) (Fig. 2) and seems to be a robust method for landslide recognition or microtopography assessment (Rau et al. 2012; Stumpf et al. 2013). At a local scale (1:2000–1:10,000), UAV datasets (orthophotographs, DEMs) associated with field observations (e.g., geotechnical, geophysical, (geo)morphological, geological, hydro(geo)logical surveys), provide high-resolution data to detect and characterize landslides. For example, high-resolution imagery from UAVs makes it easier to locate and provide details of cracks and fissure structures (Walter et al. 2009; Stumpf et al. 2013) by photo interpretation, image and/or 3D point clouds analysis (Akçay 2015), and gain knowledge of slope morphology associated with landslide activity. Such methods may be especially useful for large area analysis, where several hundreds of landslides must be mapped. Comert et al. (2019) show the OBIA can recognize the number and the area of

the landslide with accuracy rate of ca. 83%. Despite good results for landslide detection by OBIA approach, PBIA approach is still the predominant method (Casagli et al. 2017; Bunn et al. 2019). In this context, the employment of multi-spectral images can be useful to automatically detect landslides, especially with the use of spectral vegetation indices such as NDVI values (Lin et al. 2004; Yang et al. 2013) to distinguish the vegetation from the soil (Berni et al. 2009). Whereas collecting RGB-images by UAV is simple and cost effective, integrating other remote sensing sensors on UAVs, such as thermal cameras (Guilbert et al. 2020) or micro-hyperspectral imagers, may be a good solution, but more expensive.

4.1.2 Quantification of Slope Deformation and Volumetric Changes Over Time

Remote sensing approaches are frequently applied for landslide assessment and monitoring (Petley et al. 2002; Delacourt et al. 2007; Jaboyedoff et al. 2012; Tofani et al. 2013; Casagli et al. 2017). To quantify landslide kinematics, airborne observations with UAV and SfM techniques give the possibility to investigate landslides in high temporal resolution with repeated flight campaigns from several days or months (Lindner et al. 2016) to several years (Turner et al. 2015).

To quantify displacement rates and acquire information in magnitude and direction of displacement vectors, a visual interpretation of the morphological changes with time can be useful with observation of specific objects such as, for example, the locations of blocks (Walter et al. 2009) and/or tree locations (Fernandez Galarreta et al. 2015; Peternel et al. 2017). However, for an exhaustive mapping of surface displacements and the characterization of the landslide evolution, several other techniques are possible:

1. image correlation of multi-temporal orthophotographs (Torrero et al. 2015; Hastaoğlu et al. 2019),
2. comparison of 3D point clouds (Stumpf et al. 2015) based on automatic process of Cloud-to-cloud differences (Cook 2017; Eker et al. 2018) and using an open-source algorithms such as the M3C2 algorithm,
3. by comparison of DEM (DEM of Difference, DoD) (Fernandez Galarreta et al. 2015; Lindner et al. 2016; Thiebes et al. 2016; Rossi et al. 2018).

The multi-temporal model analysis can be based on DEMs created from UAVs photogrammetric surveys (Fig. 3) (Lucieer et al. 2014; Turner et al. 2014; Lindner et al. 2016; Rothmund et al. 2017; Tanteri et al. 2017; Eker et al. 2018; Rossi et al. 2018) but also compared with models created by airborne or terrestrial LiDAR surveys (Rossi et al. 2016; Thiebes et al. 2016). The interpretation of data obtained from drones must be calibrated with ground surveys and monitoring campaigns because, according to image or 3D point cloud resolution, statistical differences are possible. Various studies combine airborne techniques for landslide kinematics and field monitoring with terrestrial laser scanner (TLS), terrestrial SfM photogrammetry combined with permanent GNSS (Thiebes et al. 2016), theodolite surveys (Peternel et al. 2017) and inclinometers (Rossi et al. 2016).

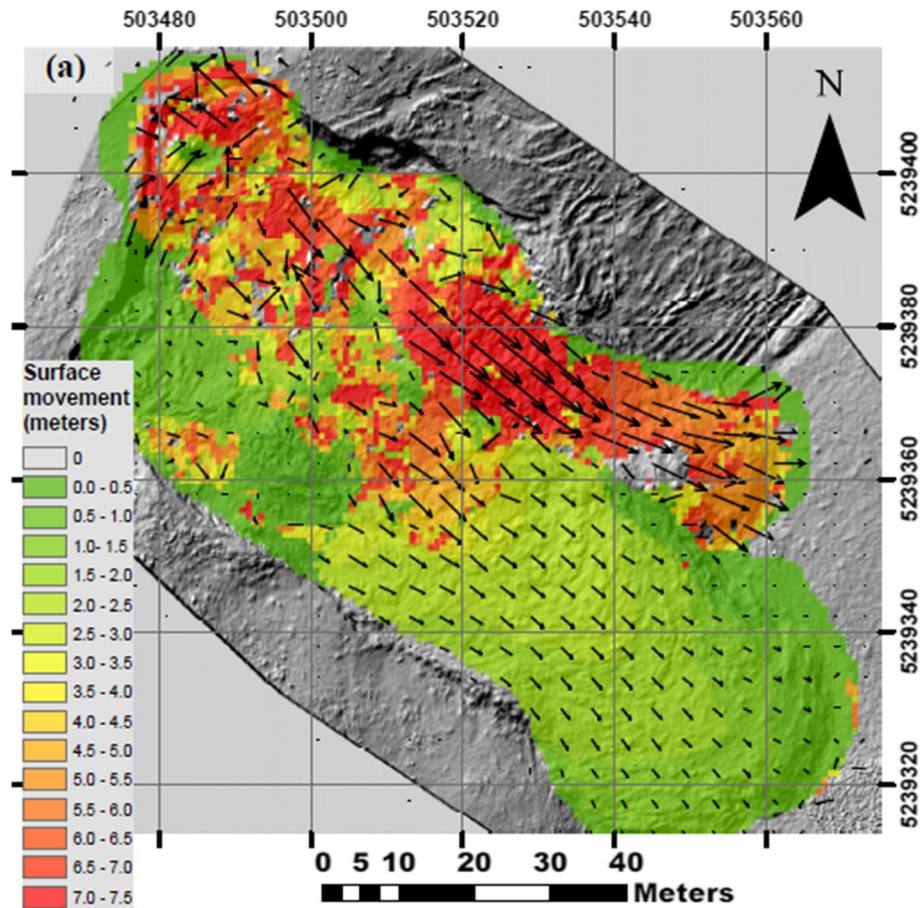


Fig. 3 Surface deformation map generated using the software COSI-corr and two different DSMs of the same area representing the surfaces at different times (from Turner et al. 2015)

5 UAVs for Volcanology

5.1 Why Use UAV Measurements to Reinforce the Monitoring of Volcanoes?

Because volcanic phenomena integrate various spatiotemporal scales, multi-disciplinary and complementary approaches are necessary. Volcanic field observations and analyses are essential, including photos, videos of eruptive phenomena, physicochemical sampling and geophysical imagery. However, in situ data acquisition remains difficult or even impossible due to complex settings (e.g., topographic barriers and danger due to eruptions). Using UAVs as instrumentation vectors will overcome these limitations by providing a more homogeneous, extensive, safer and faster prospecting. Today, this is an essential advance to improve our understanding of volcanic systems and to efficiently monitor them.

The choice of the UAV is, at the first order, a question of scale: measurements carried out at high altitude will cover regional and deep structures or atmospheric phenomena, whereas measurements close to the ground will focus on local and more shallow systems

or phenomena at even higher resolution. It will also be greatly conditioned by the sensitivity and weight of the sensor(s) that should be mounted, and that depends on the volcanic issues to be addressed (e.g., measurements of surface, internal and atmospheric phenomena) (Gonzalez Toro and Tsourdos 2018). Amongst these problems, it is fundamental to map and characterize active volcanic structures on the surface, such as lava flows (De Beni et al. 2019), intrusions (Dering et al. 2019), volcano-tectonics features and deformation (Bonali et al. 2019). Repeated UAV measurements over time enable quantification of the temporal evolution of these structures (Derrien et al. 2015; Darmawan et al. 2018). Another important issue in volcanoes monitoring is to quantify heat flux associated with volcanic activity at the surface and in near-real-time through mapping the spatial distribution of thermal expressions (Walter et al. 2020). More in-depth information on fluid transfers and magmatic dynamics is now provided thanks to the development of UAV geophysical measurements such as, for example, magnetism (Catalán et al. 2014) and/or gravity (Middlemiss et al. 2016). Sampling and analysing volcanic products and gas emissions dynamics through UAV physicochemical measurements could also be envisioned with dedicated sensors (Gomez and Kennedy 2018; Rüdiger et al. 2018; Terada et al. 2018; James et al. 2020). The ultimate goal is to perform combined approaches including simultaneous and complementary measurements (e.g., Mori et al. 2016).

We now present a (non-exhaustive) list of vectors and sensors (operational or in development) commonly used or that could be used for volcanology, and some applications and developments.

5.2 UAV and Physicochemical Sensors for Studying Volcanoes

Vectors: The emergence of UAV, together with rapid and continuous technological progress, now offers an intermediate detection scale between regional satellite and local ground observations (Kreye et al. 2006). It opens the doors to high-resolution measurements, at both spatial and temporal scales, to enhance volcanic systems imaging and monitoring (Fig. 1). Different vectors exist, each with specific characteristics and performance (flight altitude, time and payload). As an example, the U.S. Department of Defense has provided a categorization into five groups (Marshall et al. 2015) and various syntheses have been proposed (Fahlstrom and Gleason 2012; Watts et al. 2012; Villa et al. 2016).

Sounding balloons have been designed to make measurements at high altitude in the stratosphere (Everaerts 2008). They are of main interest to study the volcanic products into the atmosphere (gas and particles) for meteorological, socio-economic and aeronautical issues. Fixed-wing drones such as long-range flying systems have basically limited payload but offer the possibility of flying for several hours for homogeneous investigation of large areas (Saggiani et al. 2006). Big rotor wing drones (octopters or hexicopters) have more limited flight times, but larger payload and could be used as multi-method platforms. The lightest quadcopter-type drones (see Villa et al. 2016 for details) have even more limited capacities in terms of flight time and payload, but have the advantage of being very easy and rapid to implement in the field. For given applications, a swarm of UAVs flying on similar or complementary trajectories could also be deployed (Techy et al. 2010). More recently, unmanned underwater vehicles (UUVs) have been developed to operate, among others, in submarine volcanic contexts (Caratori Tontini et al. 2019). UUV can be remotely controlled in real time (remotely operated vehicles, ROVs) or not (autonomous underwater vehicles, AUVs).

Sensors: A large range of applications may be envisioned for volcanoes imaging and monitoring (Fig. 1). For several years, UAV photogrammetry has now been fully operational for imaging volcanic structures and their evolution on the ground surface (e.g., Derrien et al. 2015; Bonali et al. 2019; De Beni et al. 2019). On-board cameras acquire photos from different points of view to derive an orthophotography (e.g., geometry, colour, texture, relief) of a selected volcanic target. One of the most interesting applications is to generate high-resolution DEMs (i.e. multi-centimetric; Harvey et al., 2016 and references therein). UAV LiDAR (light detection and ranging) surveys are also commonly used to construct DTMs at infra-metric resolution (e.g., Jones et al. 2009; Assali et al. 2014; Casini et al. 2016). The miniaturization of infrared (IR) cameras (<500 g) also offers the opportunity to carry out acquire thermal images rapidly (e.g., Wessels et al. 2013; Walter et al. 2020). Temperature information on the scale of an entire eruptive site in areas otherwise inaccessible such as active eruptive centres (Mori et al. 2016), lava flows (Spampinato et al. 2011; Blakett 2017 and references therein) and/or fracturing centres (Schneider et al. 2005) can be acquired.

UAV geophysical measurements and physical parameters characterization are also in development to monitor volcanic activity at greater depth. Magnetic sensors progressively become operational (Funaki et al. 2014); the development of gravity sensors is also in full swing for the last few years Middlemiss et al. 2016).

Regarding UAV sensors for sampling of volcanic products, in situ measurements remain challenging for physical and chemical characterizations of volcanic emissions (plumes of gas and ashes). Based on the in-depth knowledge of atmospheric teams, custom sensors (Hervo et al. 2012; Picard et al. 2019) are now being developed in order to: (1) measure the total concentration of particles and their size spectrum, (2) sample particle aggregates, (3) sample ashes with a collector for quantifying the flux of particles within the plume and their size distribution and (4) quantify major volatile components (H₂O, CO₂, H₂S and SO₂) with a MultiGas system and a [P, T, RH] (pressure, temperature, relative humidity) probe.

5.3 Some Examples of Application

At the scale of volcanic edifices, various phenomena interact at different spatiotemporal scales (e.g., stress variations, deformation, fracturing, fluids transfer, thermal variations). Those phenomena are driving a large variability of physical properties in volcanic reservoirs, shallow structures and emitted products that could be efficiently addressed thanks to UAVs measurements. Some of the most striking examples of applications are presented in the following sections.

5.3.1 Imaging Volcano-Tectonic Structures and Their Temporal Evolution

Deformations linked to volcanic activity are commonly due to magma transfers, precursors of eruptions, and require almost real-time monitoring to better follow and prevent eruptions. UAV photogrammetry has great potential in monitoring such dynamic processes (lava flows monitoring) (Favalli et al. 2018; De Beni et al. 2019). Right now, most of the drones are equipped with high-resolution cameras. The advantage of UAV photogrammetry is to repeat surveys and, therefore, to rapidly emphasize the evolution of structures with successive photogrammetric models (e.g., before and after an eruption). A recent striking

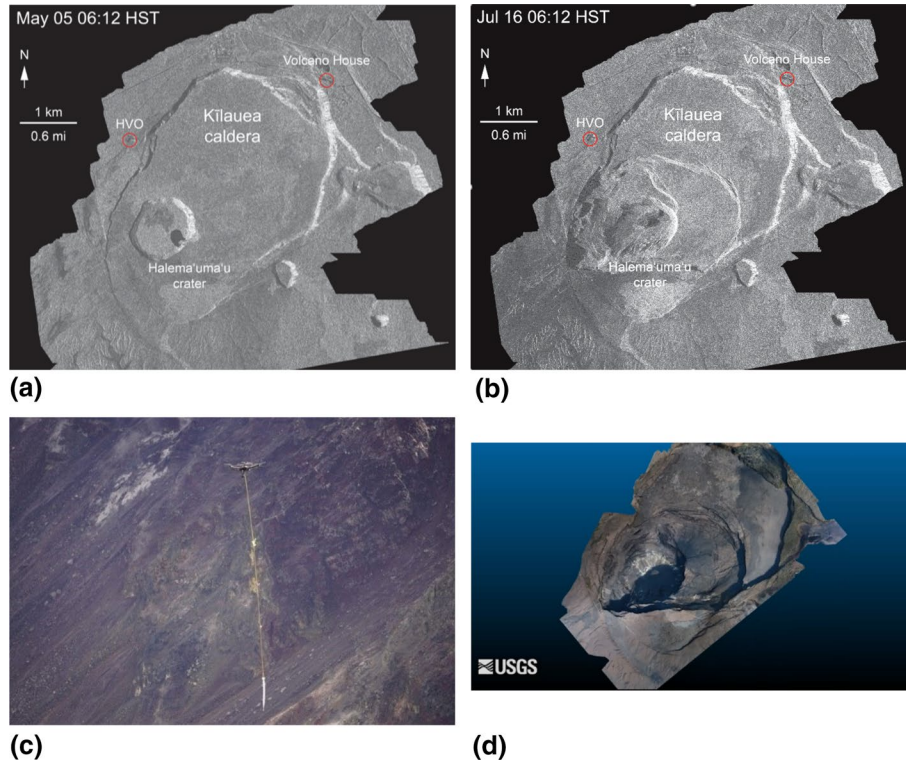


Fig. 4 Changes to the caldera area of Kilauea Volcano on Hawaii Island due to 2018 eruption: **a** May 05 and **b** July 16 (extract from GIF, JAXA). **c** Drone survey for photogrammetry and sampling. **d** 3D model from aerial photographs. Credit: U.S. Geological Survey

example of the potential of UAV photogrammetry was the monitoring of the evolution of Kilauea volcano (Hawaii), all along its main eruptive crisis in 2018 (Fig. 4a and b) (Patrick et al. 2019). Successive flights were carried out with an octocopter (Fig. 4c) by the USGS-Hawaiian Volcano Observatory scientists (https://volcanoes.usgs.gov/volcanoes/kilauea/multimedia_chronology.html), to build a 3D model and to follow the evolution of the volcano-tectonic structures at Kilauea's summit (Fig. 4d) (Patrick et al. 2019). It also enables to follow the water pond level evolution that appeared one year after the collapse event in the deepest portion of the crater.

5.3.2 Quantifying Heat Flux, Thermal Anomalies and Mass Transfers in Near Real Time

a. Infrared imagery

Mapping thermal anomalies, fluid movements, and quantifying the associated heat fluxes is commonly performed through IR thermal imaging at large scale by satellites (Bato et al. 2016), by helicopters or in situ by hand-held ground IR cameras (Harris et al. 2005; Antoine et al. 2017) and more recently on UAVs (e.g., Mori et al. 2016; Thiele et al. 2017). Following variations in the distribution and intensity of thermal anomalies thanks to the repetition of IR measurements enables to quickly and evenly image active areas: volcanic vents (e.g., Harris and Stevenson 1997), domes (e.g.,

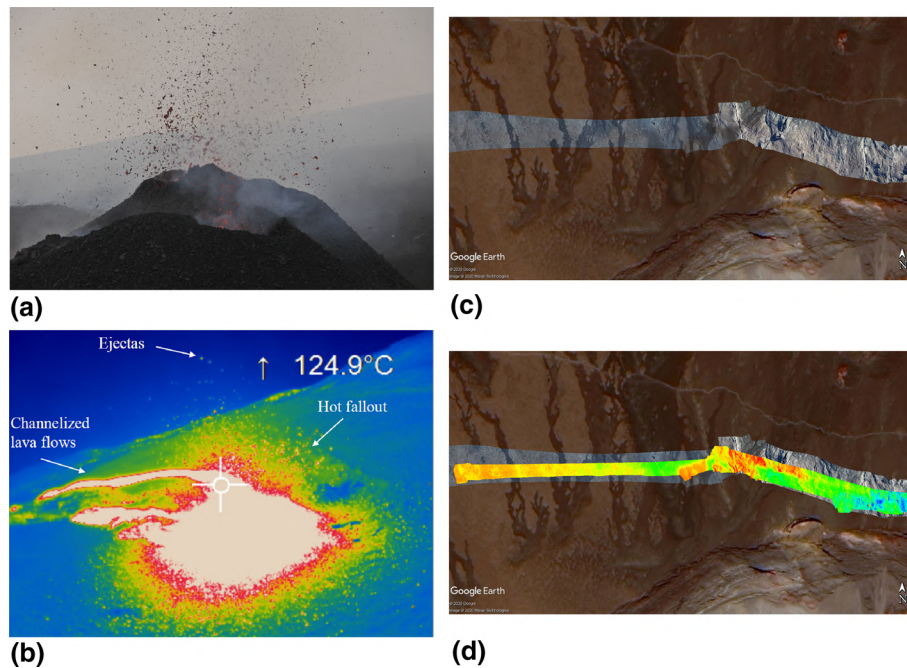


Fig. 5 **a** Eruption of Etna in July 2014 on the northeast crater (©R. Paris, LMV) and associated with **b** IR thermal imaging by drone (OPTRIS PI 450, ©Technivue and P. Labazuy, LMV-OPGC). **c** Kilometric high-resolution visible orthoimage (1.3 cm/px @ 50 m height) of the Northern Part of Dolomieu crater superimposed with Google Earth data (©R. Antoine, CEREMA/ENDSUM, SlideVOLC ANR project) and **d** IR thermal orthoimage (FLIR Vue Pro, 9.4 cm/px @ 50 m height), superimposed with the drone and Google Earth Data (©R. Antoine, CEREMA/ENDSUM, SlideVOLC ANR project)

Pallister et al. 2013), lava flows (e.g., Calvari et al. 2003; James et al. 2006) or even fumarolic zones (e.g., Harris and Baloga 2009). The thermal state of an overall eruptive site and ejectas (Turner et al. 2015) as well as the channelization of a lava flow (Patrick et al. 2017) could be accurately imaged. As an example, the IR airborne survey carried out using an octocopter during the 2014 eruption at Mount Etna has provided a high-resolution map of the active vent and associated products, otherwise invisible in surface (Fig. 5a, b) (Labazuy 2015). 3D temperature maps are now developed for IR thermal data, using the principle of photogrammetry and producing a so-called thermogravimetric model (Fig. 5c,d) (Peltier et al. 2018). This survey was done in 2018 at a kilometre scale on Piton de la Fournaise, using a DJI Phantom 4, highlighting the main thermal characteristics of the Northern part of the Dolomieu crater. Such a thermal photogrammetric approach could also be used to monitor dome eruptions (Thiele et al. 2017).

b. UAV magnetic measurements

Beyond visible and infrared measurements, UAVs are also dedicated to conduct geophysical measurements for more in-depth studies. Magnetic field measurements are particularly relevant in volcanology to map structural contacts between formations of different ages or nature. They are also a powerful tool for imaging deep thermal anomalies and intrusive systems because there is a strong influence of temperature on the

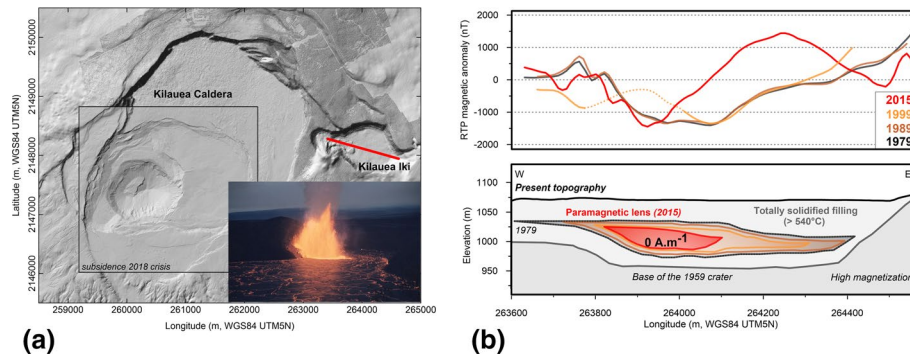


Fig. 6 Monitoring of the cooling of the Kilauea Iki lava lake (Hawaii, 1959) using reiteration of magnetic measurements along the profile located on the left. ©Photo: USGS-HVO; Composite terrain: USGS-HVO, opentopo.org

measurements of the magnetic field and associated local magnetic anomalies. Since magma and basaltic rocks above the Curie temperature (~ 580 °C) are paramagnetic (i.e. null magnetization), a loss of magnetization of volcanic formations will occur in response to heat transfers or hydrothermal alteration (Gailler et al. 2016). The advantage is to detect and follow heat transfers at depth through time, thanks to measurements reiteration. Such an approach was applied at the scale of the lava lake of Kilauea Iki (Hawaii), where the evolution of magnetic anomalies has enabled reconstructing the evolution of the still thermally active magmatic lens from 1959 to 2015 (Fig. 6) (Gailler and Kauahikaua 2017). Thanks to the miniaturization of magnetic sensors, it is now possible to conduct such magnetic surveys using UAVs in order to detect efficiently any temporal changes in magnetic signals due to volcanic activity (Catalán et al. 2014).

c. Future developments: UAV gravity measurements

UAV gravity measurements are even more challenging due to a strong effect of in-flight acceleration on such measurements. They are, however, in full development with the MEMS technology (Middlemiss et al. 2016). These measurements will complete magnetic measurements, help to better characterize magmatic systems (Magee et al. 2018) and evaluate mass transfers in depth at the scale of intrusions, conduits and reservoirs (Blaikie et al. 2014).

5.3.3 Physicochemical Measurements for Analysing Volcanic Gases

Another main natural hazard of volcanoes explosive activity concerns ash plumes and related products (gases, primary aerosols), within and in the vicinity of volcanic plumes, fumarolic zones or eruptive vents. Among them, knowledge of the composition and concentration of particles and gases from volcanic plumes is essential for understanding the processes related to their evolution in the atmosphere and associated climatic issues. Their importance was highlighted during the eruption of the Icelandic volcano Eyjafjallajökull (April–May 2010), in particular for the management of the aeronautical crisis in real time by the VAACs (Volcanic Ash Advisory Centers) (Labazuy et al. 2012; Millington et al. 2012). Such measurements are performed mainly by means of satellite or ground remote sensing in the infrared domain and may now be envisioned thanks to UAVs in situ

measurements (see Gonzalez Toro and Tsovdos 2018 and references therein). Here, one of the major scientific goals is to quantify the composition and dynamics of volcanic plumes (particle concentration flux and mass, velocity field) (Pieri et al. 2002) to monitor the gas emission rate inside plumes (Rüdiger et al. 2018) and the interactions between all of these key parameters.

All these complementary techniques will considerably improve our knowledge of volcanic dynamics (deformation, fracturing, landslides, magmatic and hydrothermal transfers) to better prevent eruptive precursors, associated hazards and their management, in real time.

6 Flood Monitoring and Management

Satellite remote sensing has been extensively used over the last 30 years for detecting, monitoring or modelling flood events (Smith 1997; Klemas 2015; Domeneghetti et al. 2019). However, the temporal and spatial resolutions of data acquired by space-borne sensors are not always adapted to fast evolving events and to fine-scale analysis (Schumann and Domeneghetti 2016; Ridolfi and Manciola 2018). Satellite data may also be affected by cloud cover, often dense and persistent during flooding. Manned aircraft can overcome these constraints. Flying below clouds, they do not have revisit limitations, and produce higher accuracy and resolution data (Feng et al. 2015). Nonetheless, their important cost, the time needed to plan and validate a flight, as well as flight restrictions, have limited their implementation for flood related studies.

Conversely, UAVs have gained increased interest over the last few years (Appendix 3). Cheaper to operate and more flexible than manned aircraft, they can be deployed for rapid monitoring and mapping of flooded areas, along with routine studies (Feng et al. 2015; Popescu et al. 2017). In addition, their ability to operate at low altitude ensures the acquisition of accurate data and meets the requirements of pre- and post-crisis flood monitoring and management. This section presents examples of the use of UAVs for flood management support.

6.1 Flood Observations and Flood Extent Mapping

One of the first examples of UAV deployment in response to a flooding disaster occurred during Hurricane Katrina in 2005. Small multi-copters and fixed-wing UAVs, equipped with RGB video cameras, were deployed immediately in the aftermath of the hurricane (Murphy et al. 2016). The video feeds were used to locate people and to determine potential threats of the Pearl River. Since then, drones equipped with RGB or IR thermal sensors have been frequently used worldwide for flood observation and to help to rescue people during or right after the peak of flooding (Fernandes et al. 2018). The main interest of digital cameras on drones during the emergency lies in the supply of real-time video scenes transmitted to ground operators or crisis management services. Visual assessment of the flood extent, debris and damage is indeed often enough for experts to make the first decisions and to deploy first emergency responses (Murphy et al. 2016).

Accurate mapping of inundated areas is also particularly important to prioritize and better organize the response actions on the impacted areas. Surprisingly, to our knowledge, no operational tool, allowing for real-time or near-real time flood extent mapping using UAVs,

and tested under real conditions, is available at this time. Nonetheless, results from the few studies that have specifically addressed this topic are rather promising. For instance, Popescu et al. (2017) have reached an accuracy of 99% in detecting flooded areas using an innovative segmentation approach in a set of 50 images acquired over a small rural flooded area in Romania, using a RGB digital camera mounted on a fixed-wing UAV. More recently, Gebrehiwot et al. (2019) has presented results obtained using a deep learning classification approach, based on convolutional neural networks (CNN). The approach has been tested on three sets of data (two sets of 30 images and one set of 70 images), acquired over three different urban flooded areas in the USA, using RGB cameras mounted on fixed-wing and multi-copter UAVs. It achieved about 97.5% accuracy in extracting flooded areas. Feng et al. (2015) have also used a RGB sensor to monitor serious waterlogging in a complex urban environment, in Yuyao (China). A large set of 400 images was processed using a hybrid method combining grey-level co-occurrence matrix texture features and random forest classifier. The approach showed good performance in urban flood mapping, with an overall accuracy of 87.3% (Fig. 7). Despite its high accuracy in flood extent mapping, the machine learning approach faces the issue of the time required to pre-process and analyse sets of several tens of very high-resolution images [e.g., up to thirteen hours in Gebrehiwot et al., (2019); nine hours in Feng et al. (2015)]. This is an important barrier to the operational use of such methods for crisis management. If multi-spectral visible sensors are the most frequently used over flooded areas, examples of flood detection using active microwave or infrared sensors, which have already proved useful for flood extent mapping from space or airplanes (Smith 1997; Sanyal and Lu 2004; Klemas 2015) are extremely scarce. Visible sensors being only efficient during the day, there is currently no solution allowing for flood extent mapping using UAVs at night.

Imam et al. (2019) considered an alternative approach, using data collected by UAV-based global navigation satellite systems (GNSS) passive radar sensor to detect water bodies on ground. Their approach has been tested in Northern Italy on water surfaces (rivers, lakes, ponds, etc.) from small to large sizes, using a custom-made GNSS-R sensor and a multi-copter. It proved successful at detecting the boundaries between ground and water with few tens of metres accuracy and at estimating the surface water extension with an extremely high accuracy (about 92%). However, the capacity of this approach to generate

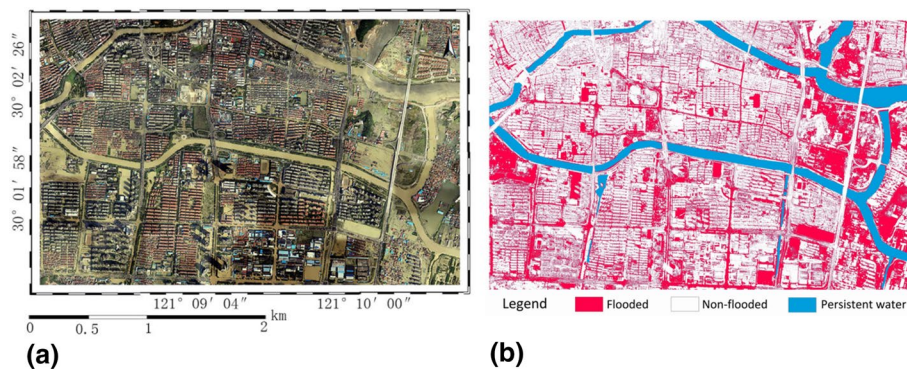


Fig. 7 a, b Orthomosaic and flood extent map (right) using a hybrid method combining grey-level co-occurrence matrix texture features and random forest classifier, applied to an orthomosaic of RGB images (left) acquired after a flood in Yuyao (China). Modified from Feng et al. (2015)

instantaneous maps, and not to provide measurements in the form of surface tracks, which have less value for flood monitoring operations, has not yet been demonstrated.

6.2 Data Acquisition for Numerical Flow Modelling

The potential of UAVs systems to provide accurate data for flood modelling at fine scale and in complex environments has also been investigated (Leitão et al. 2016; Langhammer et al. 2017; Yalcin 2018; Rinaldi et al. 2019). Their results agree on the following points: (1) topographic data derived from UAV-on-board RGB camera are comparable to DEMs generated from traditional aerial LiDAR data in term of accuracy and (2) such topographic results are appropriate for fluvial modelling in both rural and urban landscapes, which opens the way towards the use of low-cost sensors for such applications.

Research on water level estimation using UAVs systems is less documented in the literature (Bandini et al. 2017; Ridolfi and Manciola 2018). Bandini et al. (2017) have tested the capacity of three different payloads (a radar, a sonar and an in-house developed camera-based laser distance sensor) to estimate water levels on a small lake in Denmark. Water level estimations were obtained by subtracting the measured range to water surface from the vertical position retrieved by the on-board GNSS receiver. Interesting performances were obtained using the radar sensor, with measurements accuracies better than 5 cm. The approach proposed by Ridolfi and Manciola (2018) substantially differs. A RGB camera mounted on a multi-copter was used to retrieve water levels on a dam site in Italy. Water edge along the dam is extracted from a mosaic of orthorectified and calibrated images, using a supervised classification procedure accounting for edges and pixels colour, texture and contextual information. Water levels are then estimated by determining the distance between GCPs placed on the dam and the edge of water. Again, experimental results proved appropriate for flood modelling, with accuracies around 5 cm.

Lastly, it is also worth mentioning the interest given by authors to quantitative surface velocity measurements using UAVs and video cameras. The algorithms commonly used for this purpose include the large-scale particle image velocimetry (LSPIV) algorithm (e.g., Tauro et al. 2016), the Particle Tracking Velocimetry (PTV) algorithm (Eltner et al. 2020; Koutalakis et al. 2019), or the Kanade–Lucas–Tomasi (KLT) algorithm (e.g., Perks et al. 2016). The main challenge faced by these studies is the image pre-processing (co-registration and motion correction) extracted from video frames. Despite these difficulties, flow velocity estimations obtained using these algorithms are relevant and generally stay within an acceptable range of error from reference measurements, when available [around 0.15 m s^{-1} in Perks et al. (2016); around 0.25 m s^{-1} in Tauro et al. (2016) and around 0.03 m s^{-1} in Eltner et al. (2020); no reference measurements are available in Koutalakis et al. (2019)].

6.3 Monitoring of Flood Protection Structures

Fluvial and coastal structures such as levees, sea dikes and dams are frequently subjected to high loads, violent flows or debris flow impacts. On structures with pre-existing structural deficiencies, this may result in the development of major disorders and to their failure. Monitoring of such structures, before, during and after severe events enable the implementation of adequate, and often less costly repairs, before major failures occur (King et al.

2017). Several studies have recently examined the use of cameras mounted on drones to perform noninvasive and time efficient monitoring of these structures, at reasonable cost.

For instance, King et al. (2017) used a commercial multi-copter UAV to perform a survey of a 25-km length complex coastal structure at Byron Bay, Australia. A set of 455 images was processed using the SfM algorithm, helped by GCPs georeferencing. The authors reported some difficulties during the photogrammetric processing of the images, due to the presence of waves not handled by the SfM algorithm. Nevertheless, the obtained orthophotograph and DEM (RMSE of 0.068 m) were precise enough to reveal structures not observed from a classical land-based visual inspection. Brauneck et al. (2016) recorded the beginning and the evolution of a levee failure along the Elbe river (Germany), using a UAV-on-board video camera. Sets of images were extracted from five video frames and were processed into 4 DSMs, after masking their dynamic parts (flowing water areas). The main issue faced by the authors was the absence of georeferenced GCPs, which could not be positioned before the flight due to the risks involved in the area. Instead, GCPs were created by extracting the coordinates of static objects present on the images. The obtained DSMs and orthomosaics were combined to characterize the evolution of the breach and of the flow discharge within it, using a numerical 1-D hydrogeological model.

It is of note that the use of LiDAR data for DSMs generation of fluvial or sea protection structures remains less frequent. This may be explained by the important cost of LiDAR sensors compared to RGB cameras. However, optical images fail to identify disorders on a dike covered by vegetation, and accuracy of generated DSM (usually, several centimetres) are not suitable for the characterization of disorders such as dike settlement or initiation of slope sliding (Tournadre et al. 2014). For this last point, Zhou (2019) developed an innovative approach in order to generate a very high precision DSM (1 cm vertical accuracy) of such structures using a combination of oblique and nadir optical images plus embedded GNSS and only one GCP. The inclusion of oblique images helps decrease image deformations. It compensates the effects of focal lengths drifting on nadir images, which leads to more accurate camera pose estimation, and it also decreases the effects of focal lengths variations due to camera temperature changes. A camera readout time calibration method is also integrated to the approach, in order to correct the rolling shutter effect of the camera on the image measurements.

Important efforts have been made very recently for the development of operational systems for dike monitoring using UAVs. The DiDRO project (DIke monitoring by DRones) aims at developing a solution for routine and crisis monitoring of dikes, using UAVs carrying multiple remote sensing, aquatic and geophysical equipment (Antoine et al. 2019). The routine monitoring mode includes a LiDAR, IR thermal, near-infrared and visible sensors, and provides high-resolution data of the surface. These sensors, never combined before on a UAV for this type of survey, allow the detection of many surface indicators of internal and external dike disorders. They can be carried out whatever the UAV (helicopters or multi-copters), using a structure specifically developed for these needs (Fig. 8).

Data are processed to generate 3D information of the dike (multi-spectral points clouds, DSMs, DEMs, orthophotographs, profiles) and will be available for interpretation in a dedicated GIS web platform (Fig. 8d). The crisis monitoring mode uses a fixed-wing UAV equipped with a visible and IR thermal camera with a 360° rotation capacity. It allows day and night in-flight video transmission to the emergency services. This mode can be complemented by aquatic measurements, which consist (1) in surface velocity measurements using floating targets dropped in water by the UAV and (2) in water turbidity estimation

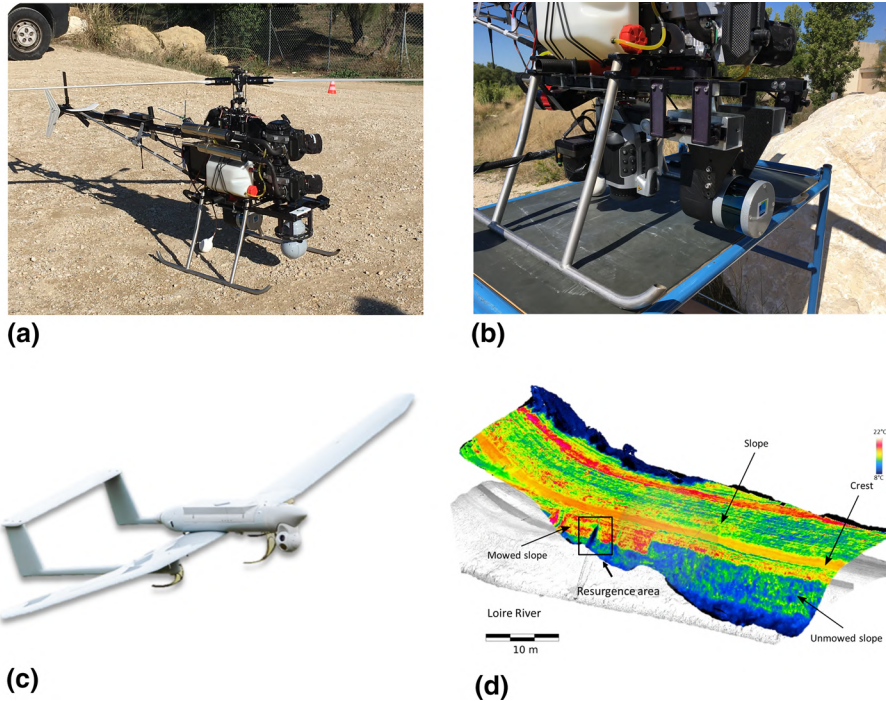


Fig. 8 **a, b** DiDRO unmanned helicopter equipped with LiDAR, HR IR thermal, near-infrared and visible cameras payload developed for routine surveys (Photo: R. Antoine ©Survey Copter/DiDRO consortium), **c** Fixed-wing drone used for crisis management (©SurveyCopter/DiDRO consortium) and **d** 3D thermal point cloud generated from IR thermal data, acquired over a dike along the Loire river (France) and superimposed with meshed DSM. Squared area: cold thermal anomaly associated with an artificial resurgence on the river-side slope of the dike observed in summer (©R. Antoine and Jonathan Lisein/DiDRO consortium)

towed by the UAV. This system is particularly useful for the detection of erosion during a flood.

The SAFEDAM project (Weintrit et al. 2018) shares some similarities with the previously mentioned system. The preventive mode includes a multi-rotor platform, specifically developed for the purposes of the system and equipped with a LiDAR sensor and a digital camera. The data are processed to obtain a DTM and an orthomosaic, both with high accuracies, and are integrated into a dedicated GIS. The embankment condition can then be assessed through visual interpretation of the data, be helped by archived data and by simple processing tools (e.g., differential DTM, change detection, etc.). When deployed during a crisis, the UAV is equipped with a video camera providing emergency services with in-fly video streaming in the optical and in the thermal infrared spectrum. A camera also allows the acquisition of nadir optical images, transmitted to the GIS after landing of the UAV. These images are automatically processed into an orthomosaic, using only the georeferencing information provided by the on-board GNSS platform of the UAV.

7 From Tectonophysics Studies to Post-earthquakes Disaster Management

7.1 Paleoseismology and Neotectonics Pre-disaster Studies

When making an extensive paper research on Web of Science scientific database using «uav earthquakes» keywords, the use of drones in a seismic context is relatively recent and is essentially focused on post-event imagery and LiDAR collection (monitoring, damage evaluation and mapping, communication improvements, etc.). Nevertheless, some developments have been achieved for pre-disasters studies, in order to understand paleoseismicity, map folds, faults and fractures, quantify slip rates on faults or interseismic shallow deformations. As for flood studies, photogrammetry is currently preferred to LiDAR, but relatively recent in the fields of paleoseismology and neotectonics (Johnson et al. 2014; Angster et al. 2016). Visible images are collected at various heights (< 120 m, due to regulation limitations), with diverse cameras and essentially using multi-copters. The characteristics of the flights described in this section are brought together in Appendix 4.

Bemis et al. (2014) made a review paper based on terrain and UAV observations for structural geology and paleo-seismicity. They show that centimetric 3D points clouds and orthophotographs of exposed stratigraphy or deformation features (like sigmoidal veins) may be now easily obtained using multi-copters, as they are very stable (compared to fixed-wing systems) and can fly at very low altitude along complex surfaces (vertical faces,

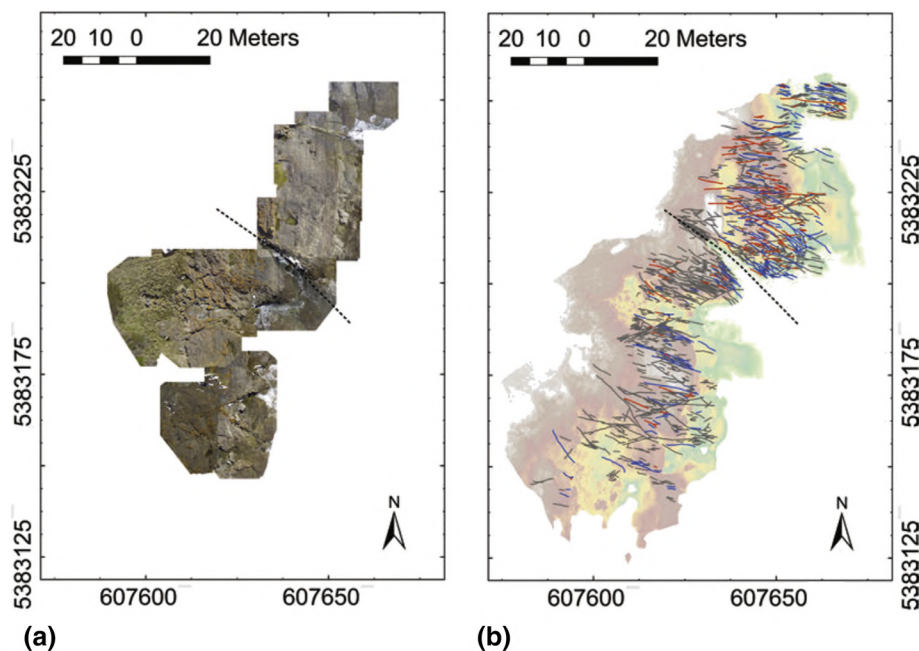


Fig. 9 **a** Orthorectified photomosaic obtained by UAV for a portion of an outcrop at Piccaninny Point. Pixel resolution 1 pixel $\frac{1}{4}$ 10 mm and **b** Structural interpretation of fault and associated damage zone, showing dextral (red), sinistral (blue) and unidentified offset faults (grey) developed around a large fault (black dash), superimposed over the DEM (modified from Bemis et al. 2014)

corners, etc...). The calculated 3D models then serve for 1) sedimentary interpretation, 2) paleo-seismic offsets characterization (Gao et al. 2017) and 3) extraction of crack direction or bedding orientation to assess the geometrical characteristics of folds and faults (Fig. 9) (Vollgger and Cruden 2016; Menegoni et al. 2018). Drones can also be deployed for active tectonics studies: Giletycz et al. (2017) built a DSM of the active Hengchun fault (Southern Taiwan) using a very small DJI Mavic Pro, to analyse the deformation patterns of active fault cracks and its possible mechanisms. Deffontaines et al. (2017) use the same approach combined with field work to update the geological mapping of the active fault located at the Pingting Terraces area. In that case, the use of fixed-wing Skywalker X5-X8 UAVs was appropriated, given the large area to investigate ($\sim 40 \text{ km}^2$, see Appendix 4 for details).

If the works presented in this section produce 3D models for structural or geological mapping, kinematics studies along faults or during a seismic event have also been derived from UAVs results. Following the processing workflow of Johnson et al. (2014), Angster et al. (2016) propose a refined evaluation of the slip rate of the Pyramid Lake 50-km-long Fault Zone in Nevada (USA). The obtained DEMs permit quantification of the displaced geomorphological features (offsets) at seven chosen sites, with a resolution ranging from 5 to 9 cm (Appendix 4) and a RMS from 7 cm to 50 cm. The observed offsets (8 to 21 m) yield slip rates ranging from 0.5 to 1.9 mm yr^{-1} along the fault. If the errors calculated in this paper are significantly less than the observed offset values, it is important to keep in mind that the accuracy of such observations drastically depends on different factors affecting the photogrammetric process: quality of the photos (blurring), overlap percentage, camera calibration, acquisition angle and precision of the georeferencing strategy (target numbers and location, GPS accuracy) (Agüera-Vega et al. 2017a, b; Sanz-Ablanedo et al. 2018)

7.2 Post-earthquake Disaster Observations

7.2.1 Immediate Support During Emergency

Recent earthquakes have seen the use of single or multiple UAV systems for immediate support just after an earthquake, in complement with aircraft and satellites (Michael et al. 2014; Nedjati et al. 2016). As for flooding events, drones are usually used (1) to obtain quick local information about a situation (emergency, offset mapping during mainshocks, damage degree evaluation of facades, etc.) and (2) to complement space-borne data when the weather is too cloudy. UAVs can then be implemented with imagery and LiDAR systems for safety missions (Lee et al. 2016), geological mapping (Jiang et al. 2014) and structures and infrastructure surveying (Yamazaki and Liu 2016). For instance, the Chinese authorities used for the first time drones after the magnitude 7.9 May 2008 Sichuan earthquake to assess damages to buildings and infrastructures, or to optimize the deployment of rescue teams by observing the extent of damaged roads and/or traffic jams (<https://www.wired.com/2017/01/chinas-launching-drones-fight-back-earthquakes/>). Recently, the magnitude 7.5 earthquake Sulawesi earthquake and its subsequent tsunami in September 2018 caused widespread damages in the city of Palu. Under the leadership of the Indonesian emergency services, data acquired by drones were combined with satellite observations to create aerial maps evaluating damages to buildings, roads, bridges and other infrastructures. It was also possible to produce real-time HD imagery analysis and offline near-real-time 3D mapping without ground targets, using recent software platforms (DroneDeploy, Pix4D, Agisoft Metashape, etc...). Indeed, in emergency conditions, a “rough”

georeferencing of the scene only taking into account the GPS metadata available in the photos (with a horizontal accuracy of 1-5 metres) may be sufficient to analyse most of the situations within a GIS software.

7.2.2 Geological Reconnaissance and Building Surveys

Various papers also investigated the utility of UAVs for geologic and geotechnical early reconnaissance after a seismic event, usually difficult to realize during the emergency phase (Gong et al. 2010; Rathje and Franke 2016; Gori et al. 2018; Saroglou et al. 2018) and damage degree evaluation of the buildings that will serve to reconstruction planning (Baiocchi et al. 2013; Sui et al. 2014; Fernandez Galarreta et al. 2015; Li et al. 2015; Yamazaki and Liu 2016; Duarte et al. 2018; Mavroulis et al. 2019). Gori et al. (2018) present field and aerial works achieved just after each of the three mainshock events that occurred in August and October 2016 in Central Italy. In this highly complex situation, geologists and remote sensing scientists worked together to locate and monitor the extent of the rupture zones. The multi-disciplinary approach using both conventional field methods and an original combination of UAV/LiDar sensing capabilities allowed (1) to find

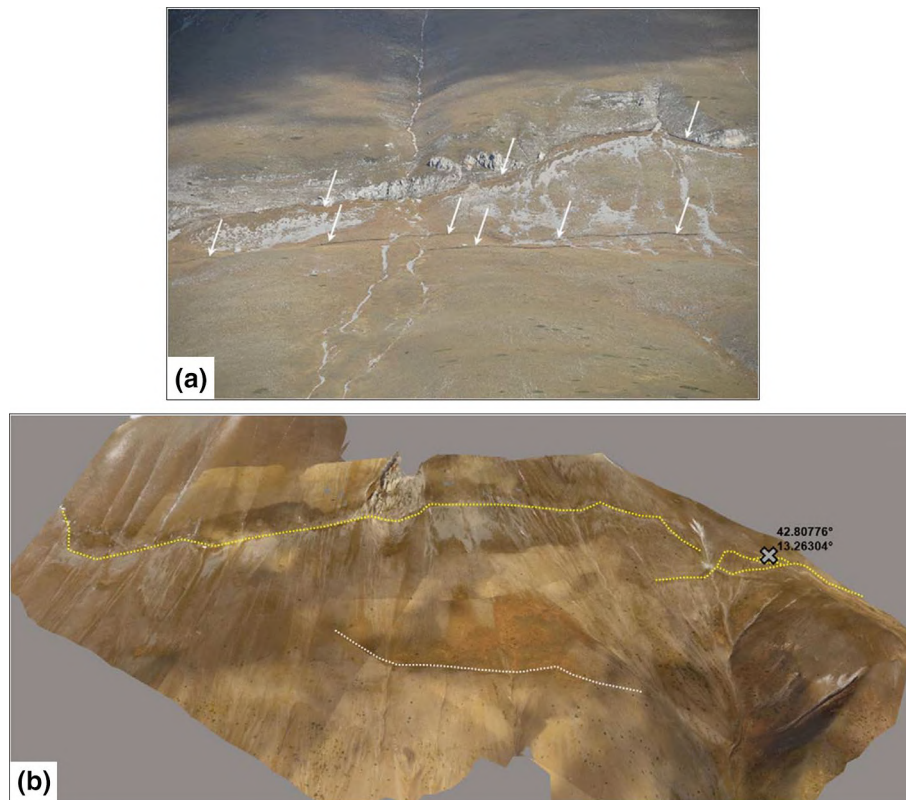


Fig. 10 **a** Surface ruptures caused by the M6.5 30 October event along the Mt. Vettore western slope, indicated by white arrows and **b** UAV-based orthomosaic model of the SW face of the Mt. Vettore Massif, showing fault traces as mapped by UAV. Yellow lines denote primary fault rupture. White line indicates rupture of the mid-slope splay (modified from Gori et al. 2018)

additional rupture zones over large areas and steeply sloping ground, (2) to observe the co-seismic vertical offsets along the fault, ranging from 0–35 cm and 70–200 cm for the 24 and 30 August, respectively (Fig. 10). Saroglou et al. (2018) present an original kinematic study of co-seismic rockfall in Greece, using a DTM, an orthophotograph and numerical modelling of the boulder movements down the slope, that successfully described the rolling and bouncing section of the trajectory. The detection of impact marks from the rock trajectory was first identified on the orthophotograph. Then, an analytical reconstruction of the rockfall is realized, with initial conditions derived from the earthquake characteristics.

Another advantage of UAVs in a post-earthquake scenario is their capacity to map the state of structures and infrastructures degraded during the seismic event, for instance, using classification methods (Xu et al. 2018) or change detection algorithms (Sui et al. 2014). Building damage detection methods traditionally focus on 2D changes detection (Chesnel et al. 2008; Brunner et al. 2010), while 3D data provide information on the height of the scene and enrich the interpretation of the experts. For instance, Fernandez Galarreta et al. (2015) propose a classification tool for the survey of buildings affected by earthquakes. They develop an object-based technique (OBIA, see Sect. 1), to evaluate the damage degree of the structures (following the European Macroseismic Scale of 1998), with photogrammetric 3D point clouds obtained by an UAV. The damaged structures are identified on the 3D point cloud and provide object-based damage indicators that are then used as auxiliary information by building analysts. Nex et al. (2019) propose a solution for autonomous building damage mapping in near real time, using a commercial UAV. The fast on-the-fly processing workflow combines photogrammetric methods with deep learning algorithms to show the location of the damages directly on an orthophotograph. In this case, the algorithms are optimized to fulfil the near-real-time conditions. Finally, when multi-resolution data are available (satellite, aerial and/or terrestrial), an interesting approach consists in merging observations to enrich classification and segmentation (Zhang 2010; Fu et al. 2017; Vetrivel et al. 2018). Duarte et al. (2018) propose deep learning (CNN) for the classification of building damages (rubble piles and debris), using fused multi-resolution imagery coming from sensors mounted on different platforms (satellite and manned/unmanned aircraft). Using thousands of images, they show that the fusing methodology is particularly powerful compared to the traditional classification of building damage, being able to capture both high-resolution degradation patterns (using UAV data) and contextual information (with satellite). The performance of the CNN drastically depends on the number of images, the quality of the fusion module, able to merge and blend the multi-resolution feature maps.

8 Discussion and Conclusions

The preceding sections share some common considerations: (1) the use of massive 3D UAV-based datasets to obtain 3D point clouds or orthophotographs, popularized by the development of user-friendly photogrammetric softwares and georeferencing methods, (2) the production of centimetric resolution photogrammetric products, also possible using low-cost UAV platforms and sensors, (3) the widespread use of small commercial low-cost multi-copters or fixed-wing drones with high safety guarantees, although self-made UAV are also used and (4) a considerable strengthening of the use of RGB data (either with photos or videos), compared to other observations (near-infrared, thermal infrared, hyperspectral, geophysical imagery or chemical sampling). Besides, some differences can be noticed:

new modes of acquisition in geophysical sampling using UAVs are tested for pre-disaster studies in volcanology, while to our knowledge, such observations are difficult to find in another natural hazard domain. This is probably due to two phenomena: (1) depending on the country, it may be easier to obtain flight permissions from the regulation authority to make experiments in an unpopulated volcanic/geothermal area and (2) given the amplitude of volcanic processes, the actual resolution and accuracy of geophysical and sampling by UAV may be sufficient to observe a phenomenon. Post-disaster methodologies have been rather developed during/after huge and frequent events (landslides, earthquakes or floods), in conjunction with authorities, to ease rescue operations or assess damages in buildings and infrastructures. This article also shows that the use of UAVs is different depending on the studied domain, as it involves phenomena with different temporal scales, spatial extents and magnitudes. For the first time, drones give access to very high-resolution spatialized observations and open new research paths. In this context, one of the most important challenges will consist in combining different observation scales to understand geological processes. Combination of UAVs and space-based data has already been done in coastal line evolutions (Nikolakopoulos et al. 2019), ground deformations (Cigna et al. 2017) and on landslide surveys (Voigt et al. 2016) and after the Mw 6.5 Lefkada earthquake (Zekkos et al. 2017). These studies obtained interesting results as (1) a good estimation of the landslide volume and enabled to precisely distinguish different generation of landslides (Zekkos et al. 2017), (2) an excellent georeferencing of coarse satellite images (Nikolakopoulos et al. 2019) and (3) information about very localized deformations (Cigna et al. 2017). However, while different applications of UAVs in preventing and reducing the risks associated with natural hazards as landslides, floods, volcanic eruptions and earthquakes exist, a few studies taking advantages of a multi-resolution data based on multi-platform sensors in post-disasters management have been made (Kakooei and Baleghi 2017; Zekkos et al. 2017; Duarte et al. 2018). The main advantage of both UAVs and space-based sensors in hazards studies is that they can provide images quickly after the disaster. Depending on the sensor (optical or radar), space-based images can be dependent on atmospheric conditions, but the high number of very high-resolution (VHR) satellites constellations increases the chance to acquire cloud-free images, while UAVs are mainly sensible to winds, depending on the type of machine (8-10 m/s for a multi-copter, 12.5 m/s for a fixed-wing aircraft). On the one hand, UAVs partial advantages rely on the multi-function portability, the high spatial and temporal resolution low-cost sensors (Casagli et al. 2017), and the possibility to consider collaboration, coordination and cooperation between UAVs when several of them are available (Pajares 2015). On the other hand, space-borne sensors are not vulnerable to the hazard itself and thus can provide pre-/co-/post-disaster images with a daily temporal resolution that cover wider areas. The drastic development of the monitoring of post-disaster areas provides precise information that may help stakeholders to react adequately. Post-disaster management may have already relied on the International Charter "Space and Major disasters," founded in 2000 by the European, French and Canadian space agencies (ESA, CNES and CSA, respectively) for major disasters (Bally et al. 2018). Once activated by national authorities, it provides and delivers at no cost a unified system of space-borne acquisition data at HR to VHR to those affected by hazards (Bally et al. 2018). One can imagine in the near-future a systematic combined workflow between space-based data that might be provided by the activation of the International Charter and UAVs based on the example provided by the use of UAVs inside the Copernicus Emergency Management Service (EMS).

Acknowledgements This paper arose from the International Workshop on “Natural and man-made hazards monitoring by the Earth Observation missions: current status and scientific gaps” held at the International Space Science Institute (ISSI), Bern, Switzerland, on April 15-18, 2019. The thermal survey of Piton de La Fournaise in 2018 was supported by the SlideVOLC French ANR project. We thank all the authors whose illustrations are presented in this article.

Appendix 1

Author	Scientific issue	Method analyse	UAV platform	UAV Equipment	Camera	Flight parameters	GSD (m)	Software
Balek & Blahut 2017	Landslide kinematics	DEM difference (DoD)	Octocopter	DJI Phantom	Nikon D100 / GoPro	20m height	0.004-0.112 m	Agisoft/Photomodeler
Comert et al. 2019	Landslide detection	OBIA	Fixed wing	Sensafly	Sensafly 20-megapixel S.O.D.A camera	212m height / 1186 photos / 75% overlap (ov.)	DEM 0.50m / Ortho 0.10m	Mapper
Cook 2017	Landslide kinematics	3D point Cloud comparison (PCC)	Quadrocopter	Dji Phantom 2	Canon IXUS	60-120m height / 250 photos 27-38 GCP	Ortho 0.03m	Agisoft
Eker et al. 2018	Landslide kinematics	DoD / PCC	Octocopter	ARF MikroKopter OktoXL	Canon EOS 650 DSLR	39 - 41 m height / 94-396 photos / 70-90% ov. / 8-9 GCP	DEM 0.10m / Ortho 0.10m	Agisoft
Fernandez et al. 2015		DoD	Octocopter	ASCTEC Falcon 8	Sony Nex-5N	90 m height	Ortho 0.03 m	Agisoft
Fernandez et al. 2016	Landslide kinematics	Visual Interpretation + DoD DSM	Octocopter	Falcon 8 Asctec/Aluges FV-8	Sony Nex 5N / Canon G12	100-120m height / 72-364 photos 70-90% ov. / 8-13 GCP	DSM 0.10m / Ortho 0.5m	Agisoft
Hastaoglu et al. 2019	Landslide kinematics	Ortho comparison (pixel)	hexacopter	Dji Matrice 600 Pro	Rosin MX Gimbal and Sony A7R camera	85m height / 1867 photos 60-80% ov.		PIX4D Mapper
Lindner et al. 2016	Landslide kinematics	DoD + Fissure observations	Octocopter	ARF MikroKopter OktoXL	Canon EOS 650D DSLR	90-100 m height / 400-1700 photos / 70-90% ov. / 8-22 GCP	DSM 0.10m	Agisoft
Niethammer et al. 2012	Landslide kinematics / Fissure map	DoD (TLS/UAV)	Quadrocopter			100-250m height / 59 images 199 GCP	Ortho 0.03 - 0.08m	sfm= VSM / image matching algorithm, GOTCHA
Peternel et al. 2017	Landslide kinematics	Visual Ortho comparison (tree, boulder) + DoD	quadrocopter / hexacopter	Microdrone MD4 1000 / Survey Drone 01 hexacopter	Olympus Pen	40 m height / 155 photos / 60 % ov.		
Peterman et al. 2015	Landslide kinematics	Point Cloud comparison	hexacopter		Olympus 2EP	40m height / 66-75 % overlap / 9 GCP		
Rau et al. 2011	Landslide detection	OBIA	Fixed wing		Canon EOS 450D	1400m height	DEM 5m / Ortho 0.20m	
Rossi et al. 2016	Landslide kinematics	PCC - TLS/UAV	Multicopter	Multicopter Saturn		68m height / 58 photos 50-60% ov. / 7 GCP	DEM 0.050m / Ortho 0.02m	Agisoft
Rossi et al. 2018	Landslide detection	DoD	Multicopter	Multicopter Saturn	Sony digital RGB camera with 8-MP	45-106 photos / 5-12 GCP	DEM 0.20m / Ortho 0.02m	
Stumpf et al. 2013	Microtopography, fissure evolution	OBIA	Quadrocopter			104 GCP	Ortho 0.03-0.10m	
Tang et al. 2019	Landslide detection / Kinematics	DoD	Fixed wing	F1000	Sony a5100	100-250m height	DSM 1m	PIX4D Mapper
Thiebes et al. 2016	Landslide kinematics	DoD (TLS/UAV)	Octocopter	SolLeon GmbH	Ricoh GR 16.2 Megapixel camera	70m height / 2033 photos GCP	DSM 0.015m	PIX4D Mapper
Turner et al. 2015	Landslide kinematics	DoD	Octocopter			60-80% ov. / 40m height	Ortho 0.03-0.05m	sfm = Agisoft / image correlation = CDS-Corr (ENVi)
Valkaniotis et al. 2018	Landslide detection	PCC - TLS/UAV	Quadrocopter	DJI Phantom 3	FC300X camera	75 photos / 8 GCP	DSM 0.08m / Ortho 0.08m	Agisoft

Bibliographic overview of case studies for mass movements

Appendix 2

	Fields of investigation	Methods	Goals	References
State of progress	Surface imaging	Photogrammetry	Mapping and monitoring Lava flows emplacement and volume estimation for risk mitigation	<i>Favalli et al. (2018)</i> ; <i>De Beni et al. (2019)</i>
			Changes in topography and volcano-tectonic features of deformation	<i>Derrien et al. (2017)</i> ; <i>Darwawan et al. (2018)</i> ; <i>Bonali et al. (2019)</i> ; <i>Patrick et al. (2019)</i>
			Multiscale analysis	<i>Dering et al. (2019)</i>
			Quantifying volume of volcanic ash-plume and understanding gas emissions dynamics	<i>Gomez and Kennedy (2017)</i>
			Mapping and multi-scale analysis of dyke swarms	<i>Dering et al. (2019)</i>
	Optical and radiometric infrared cameras	Mapping spatial distribution of thermal expressions	<i>Mori et al. (2016)</i> ; <i>Thiele et al. (2017)</i> ; <i>Walter et al. (2018)</i> ; <i>Peltier et al. (2018)</i>	
	Combined approaches	In-situ measurements, thermal imaging, particles sampling	Origin of plume gases : high-temperature magmatic fluid of a deep origin and hydrothermal system	<i>Mori et al. (2016)</i>
	Sampling	In situ measurements of volcanogenic gases and aerosols	Monitoring gas emission rate in volcanic plumes	<i>Hervo et al. (2012)</i> ; <i>Rüdiger et al. (2018)</i> ; <i>Picard et al. (2020)</i> ; <i>Pieri et al. (2020)</i>
			Quantifying composition and behaviour of such plumes from explosive volcanic eruptions	
		Water sampling	Monitoring volcanic unrest and water chemistry	<i>Terada et al. (2018)</i>
Geophysical imaging	Magnetism	Monitoring changes of magnetic anomalies due to volcanic activity (alteration...)	<i>Funaki et al. (2014)</i> ; <i>Catalan et al. (2014)</i>	
	Gravimetry	Monitoring : tracking magma and mass transfers under volcanoes (laboratory development)	<i>Middlemiss et al. (2016)</i> ; <i>Magee et al. (2018)</i>	

Bibliographic overview on developments around sensors mounted on drone and volcanoes case studies.

Appendix 3

Case study	Application	UAV type	Sensor	Resolution	Flight height	Location
Murphy <i>et al.</i> , 2016	Location of people and flood crest monitoring	Multi-copters and fixed wings	Video camera	?	?	Urban areas, Louisiana, USA
Popescu <i>et al.</i> , 2017	Detection and mapping of flooded areas	Fixed-wing	RGB digital camera	?	100 m	Urban area near Bucharest, Hungary
Gebrehiwot <i>et al.</i> , 2019	Detection and mapping of flooded areas	Fixed Wing and Multicopter	RGB digital camera	1.5 to 2.6 cm	?	Urban areas, North Carolina, USA
Feng <i>et al.</i> , 2015	Detection and mapping of flooded areas	Fixed-wing	RGB digital camera	20 cm	350 m	Dense urban area, Yuyao, China
Imam <i>et al.</i> , 2019	Detection and delineation of water surfaces	Multi-copter	GNSS-Reflectometry sensor	Few tens of meters	450 m	Lake, Avigliana area, Italy
Langhammer <i>et al.</i> , 2017	DSM and DTM of a for 2D hydraulic flood modelling	Multi-copter	RGB CMOS digital camera	1.8 cm	88 m	Javofí Brook, Šumava Mountains, Czech Republic
Leitão <i>et al.</i> , 2016	DEM for overland flow modelling in urban areas	Fixed-wing	RGB CMOS digital camera	From 2.5 cm to 10 cm	From 85 m to 310 m	Urban area, Adliswil, Switzerland
Rinaldi <i>et al.</i> , 2019	DSM for 2D hydraulic flood simulation in urban areas	Multi-copter	RGB CMOS digital camera	?	100 m	Urban area, Tandil, Argentina
Yalcin, 2018	High-resolution DSM and land cover map for 2D modelling of flash floods	Multi-copter	RGB CMOS digital camera	4.32 cm	120 m	Dense urban area, Kirsehir city, Turkey
Bandini, 2017	Water level estimations from different sensors	Multi-copter	Radar + Sonar + Camera based laser distance sensor (CLDS)	10 cm (radar), 30 cm to 14 m (sonar), 1 m to 2 m (CLDS)	From 10 m to > 60 m	Small lake in Denmark
Ridolfi <i>et al.</i> , 2018	Water level estimation on a dam site	Multi-copter	RGB camera	2.1 mm	15 m from the dam surface	Ridraooli lake, Italy
Tauro <i>et al.</i> , 2016	Quantitative characterization of surface flow	Multi-copter	RGB video camera	?	?	Rio Cordon, Italy
Koutalakis <i>et al.</i> , 2019	Estimation of water surface velocity	Multi-copter	CMOS digital camera	?	40 m	Aggitis river, Greece
Perks <i>et al.</i> , 2016	Characterization of surface flow	Multi-copter	RGB video camera	6 cm	?	Alyth Burn, Scotland
King <i>et al.</i> , 2017	Monitoring of coastal structures and coastal areas	Multi-copter	Visible digital camera	i. 3 cm ii. 2.9 cm	i. 70 m ii. 60 m	i. Byron Bay, Australia ii. Ajman, United Arab Emirates
Brauneck <i>et al.</i> , 2016	Monitoring of levee breaches for flow discharge estimation	Multi-copter	RGB video camera	?	?	Saale River at Breitenhagen, Germany
Weintrit <i>et al.</i> , 2018	Routine and crisis monitoring of flood protection structures	Multi-copter	RGB digital camera	10 cm	40 m	Vistula River, Annopol, Poland
Antoine <i>et al.</i> , 2019	Routine and crisis monitoring of flood protection structures	Helicopter, Multi-copter and fixed-wing	RGB and infrared cameras, LiDAR sensor	Depending on the sensor	70 m	Several dikes In France

Main characteristics of the studies cited on the bibliographic overview on flood monitoring and management using UAVs. Information not provided by the authors in the reviewed studies is marked by the symbol “?”.

Appendix 4

Case study	Type of UAV (M, FW or H)	Sensor	Pixel size	Distance from the target	Application
Bernie et al., 2014	Oktocopter (Mikrocopter flight controller)	Canon 550D 15 Mp	10 mm	30-40 m	Mapping (faults, sigmoidal veins)
Menegoni et al., 2018	Hexacopter	Sony 6000 ILCE	4-10 mm	31-52 m	Mapping (folds, bedding, fractures)
Gao et al., 2017	Hexacopter Y6 950 CO-AXIAL	Sony NEX 5T	16 mm	60 m	Mapping (terrace risers, seismic offsets)
Saroglou et al., 2018	Quadcopter DJI Phantom 3 Pro	DJI Camera 1/2.3" CMOS, 12,3 MP	49 mm	115 m	Mapping (DSM, DTM and orthophotos)
Giletycz et al., 2017	DJI Mavic Pro		?	?	Mapping (DSM, deformation pattern, crack analysis)
Angster et al., 2016	DJI Phantom 1	Ricoh GR 8.3 MP / f=5.3 mm	30 to 80 mm	< 30 m	
Deffontaines et al., 2016	Skywalker X5 and X8	Sony DSC-QX100 and Sony ILCEQX1	77 mm	?	Mapping (DSM, orthophotos)
Gori et al., 2018	Phantom 4 Pro	DJI Camera 1" CMOS, 20 MP	?	?	Mapping just after earthquake (DSM, seismic offsets)
Fernandez Galarreta et al., 2015	Albot X6 V1	Canon 600D	7 mm	70 m	Damage degree Evaluation(3D points clouds)

Technical overview of the flights described in Sect. 7 “From tectonophysics studies to post-earthquakes disaster management.”

References

- Adition A, Kubota T, Shinohara Y (2018) Comparison of GIS-based landslide susceptibility models using frequency ratio, logistic regression, and artificial neural network in a tertiary region of Ambon, Indonesia. *Geomorphology* 318:101–111. <https://doi.org/10.1016/j.geomorph.2018.06.006>
- AgiSoft Metashape (2016) AgiSoft PhotoScan Professional. Version 1.2.6
- Agüera-Vega F, Carvajal-Ramírez F, Martínez-Carricondo P (2017a) Assessment of photogrammetric mapping accuracy based on variation ground control points number using unmanned aerial vehicle. *Measurement* 98:221–227. <https://doi.org/10.1016/j.measurement.2016.12.002>
- Agüera-Vega F, Carvajal-Ramírez F, Martínez-Carricondo P (2017b) Accuracy of digital surface models and orthophotos derived from unmanned aerial vehicle photogrammetry. *J Surv Eng.* [https://doi.org/10.1061/\(ASCE\)SU.1943-5428.0000206](https://doi.org/10.1061/(ASCE)SU.1943-5428.0000206)
- Akçay O (2015) Landslide fissure inference assessment by ANFIS and logistic regression using UAS-based photogrammetry. *ISPRS Int J Geo-Inf* 4:2131–2158. <https://doi.org/10.3390/ijgi4042131>
- Angster S, Wesnousky S, Huang W et al (2016) Application of UAV photography to refining the slip rate on the Pyramid Lake Fault Zone, Nevada. *Bull Seismol Soc Am* 106:785–798. <https://doi.org/10.1785/0120150144>
- Antoine R, Finizola A, Lopez T et al (2017) Electric potential anomaly induced by humid air convection within Piton de La Fournaise volcano, La Réunion Island. *Geothermics* 65:81–98. <https://doi.org/10.1016/j.geothermics.2016.01.003>
- Antoine R, Tanguy M, Palma Lopes S, Sorin J-L (2019) DIDRO—an innovative multi-sensor UAV system for routine and crisis monitoring of dikes. *AGUFM 2019*:
- Assali P, Grussenmeyer P, Villemin T et al (2014) Surveying and modeling of rock discontinuities by terrestrial laser scanning and photogrammetry: semi-automatic approaches for linear outcrop inspection. *J Struct Geol* 66:102–114. <https://doi.org/10.1016/j.jsg.2014.05.014>
- Baiocchi V, Dominici D, Mormile M (2013) UAV application in post-seismic environment. *Int Arch Photogramm Remote Sens Spat Inf Sci* 1:W2
- Balek J, Blahůt J (2017) A critical evaluation of the use of an inexpensive camera mounted on a recreational unmanned aerial vehicle as a tool for landslide research. *Landslides* 14:1217–1224. <https://doi.org/10.1007/s10346-016-0782-7>

- Bally P, Papadopoulou T, Tinel C, Danzeglocke J, Wannop S, Kuklin A (2018) The 17th annual report: international charter space and major disasters, p 72. <https://disasterscharter.org/documents/10180/188210/Annual-Report-17.pdf>
- Bandini F, Butts M, Jacobsen TV, Bauer-Gottwein P (2017) Water level observations from unmanned aerial vehicles for improving estimates of surface water–groundwater interaction. *Hydrol Processes* 31:4371–4383
- Barra A, Monserrat O, Mazzanti P et al (2016) First insights on the potential of Sentinel-1 for landslides detection. *Geomat Nat Hazards Risk* 7:1874–1883. <https://doi.org/10.1080/19475705.2016.1171258>
- Bato MG, Froger JL, Harris AJL, Villeneuve N (2016) Monitoring an effusive eruption at Piton de la Fournaise using radar and thermal infrared remote sensing data: insights into the October 2010 eruption and its lava flows. *Geol Soc Lond Spec Publ* 426:533–552. <https://doi.org/10.1144/SP426.30>
- Bemis SP, Micklethwaite S, Turner D et al (2014) Ground-based and UAV-based photogrammetry: a multi-scale, high-resolution mapping tool for structural geology and paleoseismology. *J Struct Geol* 69:163–178
- Berni JAJ, Zarco-Tejada PJ, Suárez L et al (2009) Remote sensing of vegetation from UAV platforms using lightweight multispectral and thermal imaging sensors. *Int Arch Photogramm Remote Sens Spat Inf Sci* 38:6
- Blackett M (2017) An overview of infrared remote sensing of volcanic activity. *J Imaging* 3:13. <https://doi.org/10.3390/jimaging3020013>
- Blaikie TN, Ailleres L, Betts PG, Cas RAF (2014) Interpreting subsurface volcanic structures using geologically constrained 3-D gravity inversions: examples of maar-diatremes, Newer Volcanics Province, southeastern Australia. *J Geophys Res Solid Earth* 119:3857–3878. <https://doi.org/10.1002/2013JB010751>
- Bonali FL, Tibaldi A, Marchese F et al (2019) UAV-based surveying in volcano-tectonics: an example from the Iceland rift. *J Struct Geol* 121:46–64. <https://doi.org/10.1016/j.jsg.2019.02.004>
- Brauneck J, Pohl R, Juepner R (2016) Experiences of using UAVs for monitoring levee breaches. *IOP Conf Ser Earth Environ Sci* 46:012046. <https://doi.org/10.1088/1755-1315/46/1/012046>
- Brunner D, Lemoine G, Bruzzone L (2010) Earthquake damage assessment of buildings using VHR optical and SAR imagery. *IEEE Trans Geosci Remote Sens* 48:2403–2420. <https://doi.org/10.1109/TGRS.2009.2038274>
- Bunn M, Leshchinsky B, Olsen M, Booth A (2019) A simplified, object-based framework for efficient landslide inventorying using LIDAR digital elevation model derivatives. *Remote Sens* 11:303. <https://doi.org/10.3390/rs11030303>
- Calvari S, Neri M, Pinkerton H (2003) Effusion rate estimations during the 1999 summit eruption on Mount Etna, and growth of two distinct lava flow fields. *J Volcanol Geotherm Res* 119:107–123. [https://doi.org/10.1016/S0377-0273\(02\)00308-6](https://doi.org/10.1016/S0377-0273(02)00308-6)
- Caratori Tontini F, Tivey MA, Ronde CEJ, Humphris SE (2019) Heat flow and near-seafloor magnetic anomalies highlight hydrothermal circulation at Brothers Volcano Caldera, Southern Kermadec Arc, New Zealand. *Geophys Res Lett* 46:8252–8260. <https://doi.org/10.1029/2019GL083517>
- Casagli N, Frodella W, Morelli S et al (2017) Spaceborne, UAV and ground-based remote sensing techniques for landslide mapping, monitoring and early warning. *Geoenviro Disasters* 4:9. <https://doi.org/10.1186/s40677-017-0073-1>
- Casana J, Kantner J, Wiewel A, Cothren J (2014) Archaeological aerial thermography: a case study at the Chaco-era Blue J community, New Mexico. *J Archaeol Sci* 45:207–219. <https://doi.org/10.1016/j.jas.2014.02.015>
- Casini G, Hunt DW, Monsen E, Bounaim A (2016) Fracture characterization and modeling from virtual outcrops. *AAPG Bull* 100:41–61. <https://doi.org/10.1306/09141514228>
- Catalán M, Martos YM, Galindo-Zaldívar J, Funaki M (2014) Monitoring the evolution of Deception Island volcano from magnetic anomaly data (South Shetland Islands, Antarctica). *Glob Planet Change* 123:199–212. <https://doi.org/10.1016/j.gloplacha.2014.07.018>
- Cawood AJ, Bond CE, Howell JA et al (2017) LiDAR, UAV or compass-clinometer? Accuracy, coverage and the effects on structural models. *J Struct Geol* 98:67–82. <https://doi.org/10.1016/j.jsg.2017.04.004>
- Chesley JT, Leier AL, White S, Torres R (2017) Using unmanned aerial vehicles and structure-from-motion photogrammetry to characterize sedimentary outcrops: an example from the Morrison Formation, Utah, USA. *Sediment Geol* 354:1–8. <https://doi.org/10.1016/j.sedgeo.2017.03.013>
- Chesnel A-L, Binet R, Wald L (2008) Damage assessment on buildings using multisensor multimodal very high resolution images and ancillary data. In: *IGARSS 2008—2008 IEEE international geoscience and remote sensing symposium*. IEEE, Boston, MA, USA, pp 1252–1255

- Cigna F, Banks VJ, Donald AW et al (2017) Mapping ground instability in areas of geotechnical infrastructure using satellite InSAR and Small UAV surveying: a case study in Northern Ireland. *Geosciences* 7:51. <https://doi.org/10.3390/geosciences7030051>
- Comert R, Avdan U, Gorur T, Nefeslioglu HA (2019) Mapping of shallow landslides with object-based image analysis from unmanned aerial vehicle data. *Eng Geol* 260:105264. <https://doi.org/10.1016/j.enggeo.2019.105264>
- Cook KL (2017) An evaluation of the effectiveness of low-cost UAVs and structure from motion for geomorphic change detection. *Geomorphology* 278:195–208. <https://doi.org/10.1016/j.geomorph.2016.11.009>
- Darmawan H, Walter TR, Brotopuspito KS et al (2018) Morphological and structural changes at the Merapi lava dome monitored in 2012–15 using unmanned aerial vehicles (UAVs). *J Volcanol Geotherm Res* 349:256–267. <https://doi.org/10.1016/j.jvolgeores.2017.11.006>
- De Beni E, Cantarero M, Messina A (2019) UAVs for volcano monitoring: a new approach applied on an active lava flow on Mt. Etna (Italy), during the 27 February–02 March 2017 eruption. *J Volcanol Geotherm Res* 369:250–262. <https://doi.org/10.1016/j.jvolgeores.2018.12.001>
- de Saint Jean B (2008) Étude et développement d'un système de gravimétrie mobile. Ph.D. thesis, Observatoire de Paris
- Deffontaines B, Chang K-J, Champenois J et al (2017) Active interseismic shallow deformation of the Pingting terraces (Longitudinal Valley—Eastern Taiwan) from UAV high-resolution topographic data combined with InSAR time series. *Geomat Nat Hazards Risk* 8:120–136. <https://doi.org/10.1080/19475705.2016.1181678>
- Delacourt C, Allemand P, Berthier E et al (2007) Remote-sensing techniques for analysing landslide kinematics: a review. *Bull Soc Géol France* 178:89–100. <https://doi.org/10.2113/gssgfbull.178.2.89>
- Dering GM, Micklethwaite S, Thiele ST et al (2019) Review of drones, photogrammetry and emerging sensor technology for the study of dykes: Best practises and future potential. *J Volcanol Geotherm Res* 373:148–166. <https://doi.org/10.1016/j.jvolgeores.2019.01.018>
- Derrien A, Villeneuve N, Peltier A, Beauducel F (2015) Retrieving 65 years of volcano summit deformation from multitemporal structure from motion: the case of Piton de la Fournaise (La Réunion Island). *Geophys Res Lett* 42:6959–6966. <https://doi.org/10.1002/2015GL064820>
- Domenghetti A, Schumann GJ-P, Tarpanelli A (2019) Preface: remote sensing for flood mapping and monitoring of flood dynamics. *Remote Sens* 11:943. <https://doi.org/10.3390/rs11080943>
- Duarte D, Nex F, Kerle N, Vosselman G (2018) Multi-resolution feature fusion for image classification of building damages with convolutional neural networks. *Remote Sens* 10:1636. <https://doi.org/10.3390/rs10101636>
- Edenhofer O, Pichs-Madruga R, Sokona Y et al (2014) Summary for policymakers. In: *Climate change 2014: mitigation of climate change*. IPCC Working Group III Contribution to AR5. Cambridge University Press
- Eker R, Aydın A, Hübl J (2018) Unmanned aerial vehicle (UAV)-based monitoring of a landslide: Gallenzerkogel landslide (Ybbs-Lower Austria) case study. *Environ Monit Assess.* <https://doi.org/10.1007/s10661-017-6402-8>
- Eltner A, Sardemann H, Grundmann J (2020) Flow velocity and discharge measurement in rivers using terrestrial and unmanned-aerial-vehicle imagery. *Hydrol Earth Syst Sci.* <https://doi.org/10.5194/hess-24-1429-2020>
- Erdelj M, Natalizio E, Chowdhury KR, Akyildiz IF (2017) Help from the sky: leveraging UAVs for disaster management. *IEEE Pervasive Comput* 16:24–32. <https://doi.org/10.1109/MPRV.2017.11>
- Everaerts J (2008) The use of unmanned aerial vehicles (UAVs) for remote sensing and mapping. *Int Arch Photogramm Remote Sens Sp Inf Sci* 37(2008):1187–1192
- Fahlstrom P, Gleason T (2012) *Introduction to UAV systems*. Wiley, Hoboken
- Favalli M, Fornaciari A, Nannipieri L et al (2018) UAV-based remote sensing surveys of lava flow fields: a case study from Etna's 1974 channel-fed lava flows. *Bull Volcanol* 80:29
- Feng Q, Liu J, Gong J (2015) Urban flood mapping based on unmanned aerial vehicle remote sensing and random forest classifier—a case of Yuyao, China. *Water* 7:1437–1455. <https://doi.org/10.3390/w7041437>
- Fernandez Galarreta J, Kerle N, Gerke M (2015) UAV-based urban structural damage assessment using object-based image analysis and semantic reasoning. *Nat Hazards Earth Syst Sci* 15:1087–1101. <https://doi.org/10.5194/nhess-15-1087-2015>
- Fernandes O, Murphy R, Adams J, Merrick D (2018) quantitative data analysis: CRASAR small unmanned aerial systems at hurricane Harvey. In: *2018 IEEE international symposium on safety, security, and rescue robotics (SSRR)*. IEEE, Philadelphia, PA, pp 1–6

- Fu G, Liu C, Zhou R et al (2017) Classification for high resolution remote sensing imagery using a fully convolutional network. *Remote Sens* 9:498. <https://doi.org/10.3390/rs9050498>
- Funaki M, Higashino S-I, Sakanaka S et al (2014) Small unmanned aerial vehicles for aeromagnetic surveys and their flights in the South Shetland Islands, Antarctica. *Polar Sci* 8:342–356. <https://doi.org/10.1016/j.polar.2014.07.001>
- Gablrik P (2015) The use of direct georeferencing in aerial photogrammetry with micro UAV. *IFAC-PapersOnLine* 48:380–385. <https://doi.org/10.1016/j.ifacol.2015.07.064>
- Gailler L, Kauahikaua J (2017) Monitoring the cooling of the 1959 Kīlauea Iki lava lake using surface magnetic measurements. *Bull Volcanol*. <https://doi.org/10.1007/s00445-017-1119-7>
- Gailler L-S, Lénat J-F, Blakely RJ (2016) Depth to Curie temperature or bottom of the magnetic sources in the volcanic zone of la Réunion hot spot. *J Volcanol Geotherm Res* 324:169–178. <https://doi.org/10.1016/j.jvolgeores.2016.06.005>
- Gao M, Xu X, Klinger Y et al (2017) High-resolution mapping based on an Unmanned Aerial Vehicle (UAV) to capture paleoseismic offsets along the Altyn-Tagh fault, China. *Sci Rep* 7:1–11
- Gebrehiwot A, Hashemi-Beni L, Thompson G et al (2019) Deep convolutional neural network for flood extent mapping using unmanned aerial vehicles data. *Sensors* 19:1486. <https://doi.org/10.3390/s19071486>
- Giletycz SJ, Chang C-P, Lin AT-S et al (2017) Improved alignment of the Hengchun Fault (southern Taiwan) based on fieldwork, structure-from-motion, shallow drilling, and levelling data. *Tectonophysics* 721:435–447. <https://doi.org/10.1016/j.tecto.2017.10.018>
- Giordan D, Hayakawa Y, Nex F et al (2018) The use of remotely piloted aircraft systems (RPASs) for natural hazards monitoring and management. *Nat Hazards Earth Syst Sci* 18:1079–1096. <https://doi.org/10.5194/nhess-18-1079-2018>
- Giordan D, Adams MS, Aicardi I et al (2020) The use of unmanned aerial vehicles (UAVs) for engineering geology applications. *Bull Eng Geol Environ*. <https://doi.org/10.1007/s10064-020-01766-2>
- Girardeau-Montaut D, Roux M, Marc R, Thibault G (2005) Change detection on points cloud data acquired with a ground laser scanner. *Int Arch Photogramme Remote Sens Spat Inf Sci* 36:W19
- Gomez C, Kennedy B (2018) Capturing volcanic plumes in 3D with UAV-based photogrammetry at Yasur Volcano—Vanuatu. *J Volcanol Geotherm Res* 350:84–88. <https://doi.org/10.1016/j.jvolgeores.2017.12.007>
- Gomez C, Purdie H (2016) UAV-based photogrammetry and geocomputing for hazards and disaster risk monitoring—a review. *Geoenviron Disasters*. <https://doi.org/10.1186/s40677-016-0060-y>
- Gonçalves JA, Henriques R (2015) UAV photogrammetry for topographic monitoring of coastal areas. *ISPRS J Photogramm Remote Sens* 104:101–111. <https://doi.org/10.1016/j.isprsjprs.2015.02.009>
- Gong J, Wang D, Li Y et al (2010) Earthquake-induced geological hazards detection under hierarchical stripping classification framework in the Beichuan area. *Landslides* 7:181–189. <https://doi.org/10.1007/s10346-010-0201-4>
- Gonzalez Toro F, Tsourdos A (2018) UAV or drones for remote sensing applications. MDPI Books, Basel
- Gori S, Falcucci E, Galadini F et al (2018) Surface faulting caused by the 2016 central Italy seismic sequence: field mapping and LiDAR/UAV imaging. *Earthq Spectra* 34:1585–1610. <https://doi.org/10.1193/111417EQS236MR>
- Görüm T (2019) Landslide recognition and mapping in a mixed forest environment from airborne LiDAR data. *Eng Geol* 258:105155. <https://doi.org/10.1016/j.enggeo.2019.105155>
- Graff K, Lissak C, Thiery Y et al (2019) Analysis and quantification of potential consequences in multirisk coastal context at different spatial scales (Normandy, France). *Nat Hazards* 99:637–664. <https://doi.org/10.1007/s11069-019-03763-5>
- Guilbert V, Antoine R, Heinkele C et al (2020) Fusion of thermal and visible point clouds : application to the Vaches Noires landslide, Normandy, France. In: Accepted for the international archives of the photogrammetry, remote sensing and spatial information sciences (ISPRS Archives). Nice, France, p 6
- Harris AJL, Baloga SM (2009) Lava discharge rates from satellite-measured heat flux. *Geophys Res Lett*. <https://doi.org/10.1029/2009GL039717>
- Harris AJL, Stevenson DS (1997) Thermal observations of degassing open conduits and fumaroles at Stromboli and Vulcano using remotely sensed data. *J Volcanol Geotherm Res* 76:175–198. [https://doi.org/10.1016/S0377-0273\(96\)00097-2](https://doi.org/10.1016/S0377-0273(96)00097-2)
- Harris A, Dehn J, Patrick M et al (2005) Lava effusion rates from hand-held thermal infrared imagery: an example from the June 2003 effusive activity at Stromboli. *Bull Volcanol* 68:107–117. <https://doi.org/10.1007/s00445-005-0425-7>

- Hastaoğlu KÖ, Gül Y, Poyraz F, Kara BC (2019) Monitoring 3D areal displacements by a new methodology and software using UAV photogrammetry. *Int J Appl Earth Obs Geoinf* 83:101916. <https://doi.org/10.1016/j.jag.2019.101916>
- Hervo M, Quennehen B, Kristiansen NI et al (2012) Physical and optical properties of 2010 Eyjafjallajökull volcanic eruption aerosol: ground-based, Lidar and airborne measurements in France. *Atmos Chem Phys* 12:1721–1736. <https://doi.org/10.5194/acp-12-1721-2012>
- Hungr O, Leroueil S, Picarelli L (2014) The Varnes classification of landslide types, an update. *Landslides* 11:167–194. <https://doi.org/10.1007/s10346-013-0436-y>
- Imam R, Pini M, Marucco G et al (2019) Data from GNSS-based passive radar to support flood monitoring operations. In: 2019 international conference on localization and GNSS (ICL-GNSS). IEEE, Nuremberg, Germany, pp 1–7
- Jaboyedoff M, Oppikofer T, Abellán A et al (2012) Use of LIDAR in landslide investigations: a review. *Nat Hazards* 61:5–28. <https://doi.org/10.1007/s11069-010-9634-2>
- James MR, Robson S, Pinkerton H, Ball M (2006) Oblique photogrammetry with visible and thermal images of active lava flows. *Bull Volcanol* 69:105–108. <https://doi.org/10.1007/s00445-006-0062-9>
- James MR, Carr B, D'Arcy F et al (2020) Volcanological applications of unoccupied aircraft systems (UAS): developments, strategies, and future challenges. *Volcanica* 3:67–114
- Jiang H, Su Y, Jiao Q et al (2014) Typical geologic disaster surveying in Wenchuan 8.0 earthquake zone using high resolution ground LiDAR and UAV remote sensing. In: Lidar remote sensing for environmental monitoring XIV. International Society for Optics and Photonics, p 926219
- Johnson K, Nissen E, Saripalli S et al (2014) Rapid mapping of ultrafine fault zone topography with structure from motion. *Geosphere* 10:969–986. <https://doi.org/10.1130/GES01017.1>
- Jones RR, Kokkalas S, McCaffrey KJW (2009) Quantitative analysis and visualization of nonplanar fault surfaces using terrestrial laser scanning (LIDAR)—The Arkitsa fault, central Greece, as a case study. *Geosphere* 5:465–482
- Kakooei M, Baleghi Y (2017) Fusion of satellite, aircraft, and UAV data for automatic disaster damage assessment. *Int J Remote Sens* 38:2511–2534. <https://doi.org/10.1080/01431161.2017.1294780>
- King S, Leon J, Mulcahy M et al (2017) Condition survey of coastal structures using UAV and photogrammetry. *Australasian Coasts & Ports 2017: Working with Nature* 704
- Kitonsa H, Kruglikov SV (2018) Significance of drone technology for achievement of the United Nations sustainable development goals. *R-Economy* 4(3):115–120. <https://doi.org/10.15826/recon.2018.4.3.016>
- Klemas V (2015) Remote sensing of floods and flood-prone areas: an overview. *J Coast Res* 31:1005–1013. <https://doi.org/10.2112/JCOASTRES-D-14-00160.1>
- Koutalakis P, Tzoraki O, Zaimis G (2019) UAVs for hydrologic scopes: application of a low-cost UAV to estimate surface water velocity by using three different image-based methods. *Drones* 3:14. <https://doi.org/10.3390/drones3010014>
- Kreye C, Hein GW, Zimmermann B (2006) Evaluation of airborne vector gravimetry using GNSS and SDINS observations. In: Flury J, Rummel R, Reigber C et al (eds) *Observation of the earth system from space*. Springer, Berlin, pp 447–461
- Labazuy P (2015) Unmanned aerial vehicles (UAVs)-based remote sensing applications for studying and monitoring volcanic environments
- Labazuy P, Gouhier M, Harris A et al (2012) Near real-time monitoring of the April-May 2010 Eyjafjallajökull ash cloud: an example of a web-based, satellite data-driven, reporting system. *Int J Environ Pollut* 48:262. <https://doi.org/10.1504/IJEP.2012.049673>
- Lague D, Brodu N, Leroux J (2013) Accurate 3D comparison of complex topography with terrestrial laser scanner: application to the Rangitikei canyon (N-Z). *ISPRS J Photogramm Remote Sens* 82:10–26. <https://doi.org/10.1016/j.isprsjprs.2013.04.009>
- Lahousse T, Chang KT, Lin YH (2011) Landslide mapping with multi-scale object-based image analysis—a case study in the Baichi watershed, Taiwan. *Nat Hazards Earth Syst Sci* 11:2715–2726. <https://doi.org/10.5194/nhess-11-2715-2011>
- Lang S, Füreder P, Rogenhofer E (2018) Earth observation for humanitarian operations. In: Al-Ekabi C, Ferretti S (eds) *Yearbook on space policy 2016*. Springer, Cham, pp 217–229
- Langhammer J, Bernsteinová J, Miřijovský J (2017) Building a high-precision 2D hydrodynamic flood model using UAV photogrammetry and sensor network monitoring. *Water* 9:861. <https://doi.org/10.3390/w9110861>
- Lee S, Har D, Kum D (2016) Drone-assisted disaster management: finding victims via infrared camera and lidar sensor fusion. In: 2016 3rd Asia-Pacific world congress on computer science and engineering (APWC on CSE), pp 84–89

- Leitão JP, Moy de Vitry M, Scheidegger A, Rieckermann J (2016) Assessing the quality of digital elevation models obtained from mini unmanned aerial vehicles for overland flow modelling in urban areas. *Hydrol Earth Syst Sci* 20:1637–1653. <https://doi.org/10.5194/hess-20-1637-2016>
- Li S, Tang H, He S et al (2015) Unsupervised detection of earthquake-triggered roof-holes from UAV images using joint color and shape features. *IEEE Geosci Remote Sens Lett* 12:1823–1827. <https://doi.org/10.1109/LGRS.2015.2429894>
- Lin C-Y, Lo H-M, Chou W-C, Lin W-T (2004) Vegetation recovery assessment at the Jou-Jou Mountain landslide area caused by the 921 Earthquake in Central Taiwan. *Ecol Model* 176:75–81. <https://doi.org/10.1016/j.ecolmodel.2003.12.037>
- Lindner G, Schraml K, Mansberger R, Hübl J (2016) UAV monitoring and documentation of a large landslide. *Appl Geomat* 8:1–11. <https://doi.org/10.1007/s12518-015-0165-0>
- Lissak C, Gomez C, Shimizu M et al (2019) Drifted wood distribution in Asakura (Kyushu) following the 2017 rain-triggered Debris-flows and Landslides. In: *Geophysical research abstracts*
- Lowe DG (1999) Object recognition from local scale-invariant features. In: *Proceedings of the seventh IEEE international conference on computer vision*, pp 1150–1157
- Lowe DG (2004) Distinctive image features from scale-invariant keypoints. *Int J Comput Vis* 60:91–110. <https://doi.org/10.1023/B:VISI.0000029664.99615.94>
- Lucieer A, de Jong SM, Turner D (2014) Mapping landslide displacements using Structure from Motion (SfM) and image correlation of multi-temporal UAV photography. *Progress Phys Geogr Earth Environ* 38:97–116. <https://doi.org/10.1177/0309133313515293>
- Magee C, Stevenson CTE, Ebmeier SK et al (2018) Magma plumbing systems: a geophysical perspective. *J Petrol* 59:1217–1251. <https://doi.org/10.1093/petrology/egy064>
- Marshall DM, Barnhart RK, Shappee E, Most MT (2015) *Introduction to unmanned aircraft systems*. CRC Press, Boca Raton
- Mavroulis S, Andreadakis E, Spyrou N-I et al (2019) UAV and GIS based rapid earthquake-induced building damage assessment and methodology for EMS-98 isoseismal map drawing: the June 12, 2017 Mw 6.3 Lesvos (Northeastern Aegean, Greece) earthquake. *Int J Disaster Risk Reduct* 37:101–169. <https://doi.org/10.1016/j.ijdrr.2019.101169>
- Menegoni N, Meisina C, Perotti C, Crozi M (2018) Analysis by UAV digital photogrammetry of folds and related fractures in the Monte Antola Flysch Formation (Ponte Organasco, Italy). *Geosciences* 8:299. <https://doi.org/10.3390/geosciences8080299>
- Mezaal M, Pradhan B, Rizeei H (2018) Improving landslide detection from airborne laser scanning data using optimized Dempster–Shafer. *Remote Sens* 10:1029. <https://doi.org/10.3390/rs10071029>
- Mian O, Lutes J, Lipa G et al (2015) Direct georeferencing on small unmanned aerial platforms for improved reliability and accuracy of mapping without the need for ground control points. *ISPRS Int Arch Photogramm Remote Sens Spat Inf Sci XL-1/W4:397–402*. <https://doi.org/10.5194/isprsarchives-XL-1-W4-397-2015>
- Michael N, Shen S, Mohta K et al (2014) Collaborative mapping of an earthquake damaged building via ground and aerial robots. In: Yoshida K, Tadokoro S (eds) *Field and service robotics: results of the 8th international conference*. Springer, Berlin, pp 33–47
- Middlemiss RP, Samarelli A, Paul DJ et al (2016) Measurement of the Earth tides with a MEMS gravimeter. *Nature* 531:614–617. <https://doi.org/10.1038/nature17397>
- Millington SC, Saunders RW, Francis PN, Webster HN (2012) Simulated volcanic ash imagery: a method to compare NAME ash concentration forecasts with SEVIRI imagery for the Eyjafjallajökull eruption in 2010. *J Geophys Res Atmos*. <https://doi.org/10.1029/2011JD016770>
- Mokhtar MRM, Matori AN, Yusof KW et al (2014) Assessing UAV landslide mapping using unmanned aerial vehicle (UAV) for landslide mapping activity. *Appl Mech Mater* 567:669–674. <https://doi.org/10.4028/www.scientific.net/AMM.567.669>
- Moosavi V, Talebi A, Shirmohammadi B (2014) Producing a landslide inventory map using pixel-based and object-oriented approaches optimized by Taguchi method. *Geomorphology* 204:646–656. <https://doi.org/10.1016/j.geomorph.2013.09.012>
- Mori T, Hashimoto T, Terada A et al (2016) Volcanic plume measurements using a UAV for the 2014 Mt. Ontake eruption. *Earth Planets Space* 68:49. <https://doi.org/10.1186/s40623-016-0418-0>
- Morsdorf F, Eck C, Zraggen C et al (2017) UAV-based LiDAR acquisition for the derivation of high-resolution forest and ground information. *Lead Edge* 36:566–570. <https://doi.org/10.1190/le36070566.1>
- Murphy R, Dufek J, Sarmiento T et al (2016) Two case studies and gaps analysis of flood assessment for emergency management with small unmanned aerial systems. In: *2016 IEEE international symposium on safety, security, and rescue robotics (SSRR)*, pp 54–61
- Nedjati A, Izbirak G, Vizvari B, Arkat J (2016) Complete coverage path planning for a multi-UAV response system in post-earthquake assessment. *Robotics* 5:26. <https://doi.org/10.3390/robotics5040026>

- Nex F, Duarte D, Steenbeek A, Kerle N (2019) Towards real-time building damage mapping with low-cost UAV solutions. *Remote Sens* 11:287. <https://doi.org/10.3390/rs11030287>
- Niethammer U, James MR, Rothmund S et al (2012) UAV-based remote sensing of the Super-Sauze landslide: evaluation and results. *Eng Geol* 128:2–11. <https://doi.org/10.1016/j.enggeo.2011.03.012>
- Nikolakopoulos K, Kyriou A, Koukouvelas I et al (2019) Combination of aerial, satellite, and UAV photogrammetry for mapping the diachronic coastline evolution: the case of Lefkada Island. *ISPRS Int J Geo-Inf* 8:489. <https://doi.org/10.3390/ijgi8110489>
- Pajares G (2015) Overview and current status of remote sensing applications based on unmanned aerial vehicles (UAVs). *Photogramm Eng Remote Sens* 81:281–330. <https://doi.org/10.14358/PERS.81.4.281>
- Pallister JS, Diefenbach AK, Burton WC et al (2013) The Chaitén rhyolite lava dome: eruption sequence, lava dome volumes, rapid effusion rates and source of the rhyolite magma. *Andean Geol*. <https://doi.org/10.5027/andgeoV40n2-a06>
- Patrick M, Orr T, Fisher G et al (2017) Thermal mapping of a pāhoehoe lava flow, Kīlauea Volcano. *J Volcanol Geotherm Res* 332:71–87. <https://doi.org/10.1016/j.jvolgeores.2016.12.007>
- Patrick MR, Younger EF, Tollett W (2019) Lava level and crater geometry data during the 2018 lava lake draining at Kīlauea Volcano, Hawaii. U.S. Geological Survey data release. <https://doi.org/10.5066/P9MJY24N>
- Peltier A, Fontaine FJ, Finizola A et al (2018) Volcano destabilizations: from observations to an integrated model of active deformation. In: AGU fall meeting abstracts, p 23
- Perks MT, Russell AJ, Large ARG (2016) Advances in flash flood monitoring using UAVs. *Hydrol Earth Syst Sci* 20:4005–4015. <https://www.hydrol-earth-syst-sci.net/20/4005/2016/doi:10.5194/hess-20-4005-2016>
- Peternel T, Kumelj Š, Oštir K, Komac M (2017) Monitoring the Potoška planina landslide (NW Slovenia) using UAV photogrammetry and tachymetric measurements. *Landslides* 14:395–406. <https://doi.org/10.1007/s10346-016-0759-6>
- Petley DN, Crick WD, Hart AB (2002) The use of satellite imagery in landslide studies in high mountain areas. In: Proceedings of the 23rd Asian conference on remote sensing (ACRS 2002), Kathmandu
- Picard D, Attoui M, Sellegri K (2019) B3010: a boosted TSI 3010 condensation particle counter for airborne studies. *Atmos Measur Tech*. <https://doi.org/10.5194/amt-12-2531-2019>
- Piégay H, Arnaud F, Belletti B et al (2020) Remotely sensed rivers in the Anthropocene: state of the art and prospects. *Earth Surf Processes Landf* 45:157–188. <https://doi.org/10.1002/esp.4787>
- Pieri D, Ma C, Simpson JJ et al (2002) Analyses of in situ airborne volcanic ash from the February 2000 eruption of Hekla Volcano, Iceland. *Geophys Res Lett* 29:191–194. <https://doi.org/10.1029/2001GL013688>
- Popescu D, Ichim L, Stoican F (2017) Unmanned aerial vehicle systems for remote estimation of flooded areas based on complex image processing. *Sensors* 17:446. <https://doi.org/10.3390/s17030446>
- Rathje EM, Franke K (2016) Remote sensing for geotechnical earthquake reconnaissance. *Soil Dyn Earthq Eng* 91:304–316. <https://doi.org/10.1016/j.soildyn.2016.09.016>
- Rau JY, Jhan JP, Lo CF, Lin YS (2012) Landslide mapping using imagery acquired by a fixed-wing UAV. *ISPRS Int Arch the Photogramm Remote Sens Spat Inf Sci XXXVIII-1/C22:195–200*. <https://doi.org/10.5194/isprsarchives-XXXVIII-1-C22-195-2011>
- Ridolfi E, Manciola P (2018) Water level measurements from drones: a pilot case study at a dam site. *Water* 10:297. <https://doi.org/10.3390/w10030297>
- Rinaldi P, Larrabide I, D'Amato JP (2019) Drone based DSM reconstruction for flood simulations in small areas: a pilot study. In: Rocha Á, Adeli H, Reis LP, Costanzo S (eds) *New knowledge in information systems and technologies*. Springer, Cham, pp 758–764
- Rossi G, Nocentini M, Lombardi L et al (2016) Integration of multicopter drone measurements and ground-based data for landslide monitoring. In: Aversa et al. (eds) *Landslides and engineered slopes. Experience, theory and practice*, Rome, Italy, p 6
- Rossi G, Tanteri L, Tofani V et al (2018) Multitemporal UAV surveys for landslide mapping and characterization. *Landslides* 15:1045–1052. <https://doi.org/10.1007/s10346-018-0978-0>
- Rothmund S, Vouillamoz N, Joswig M (2017) Mapping slow-moving alpine landslides by UAV—opportunities and limitations. *Lead Edge* 36:571–579. <https://doi.org/10.1190/tle36070571.1>
- Rüdiger J, Tirititz J-L, de Moor JM et al (2018) Implementation of electrochemical, optical and denuder-based sensors and sampling techniques on UAV for volcanic gas measurements: examples from Masaya, Turrialba and Stromboli volcanoes. *Atmos Measur Tech*. <https://doi.org/10.5194/amt-11-2441-2018>
- Rupnik E, Daakir M, Pierrot Deseilligny M (2017) MicMac—a free, open-source solution for photogrammetry. *Open Geospat Data Softw Stand*. <https://doi.org/10.1186/s40965-017-0027-2>

- Saggiani G, Ceruti A, Amici S et al (2006) UAV systems volcano monitoring: first test on Stromboli on October 2004. In: Geophysical research abstracts. Munich, Germany, p 1
- Saito H, Korup O, Uchida T et al (2014) Rainfall conditions, typhoon frequency, and contemporary landslide erosion in Japan. *Geology* 42:999–1002. <https://doi.org/10.1130/G35680.1>
- Sandvik KB, Lohne K (2014) The rise of the humanitarian drone: giving content to an emerging concept. *Millennium* 43:145–164. <https://doi.org/10.1177/0305829814529470>
- Sanyal J, Lu XX (2004) Application of remote sensing in flood management with special reference to monsoon Asia: a review. *Nat Hazards* 33:283–301. <https://doi.org/10.1023/B:NHAZ.0000037035.65105.95>
- Sanz-Ablanedo E, Chandler JH, Rodríguez-Pérez JR, Ordóñez C (2018) Accuracy of unmanned aerial vehicle (UAV) and SfM photogrammetry survey as a function of the number and location of ground control points used. *Remote Sens* 10:1606. <https://doi.org/10.3390/rs10101606>
- Saroglou C, Asteriou P, Zekkos D et al (2018) UAV-based mapping, back analysis and trajectory modeling of a coseismic rockfall in Lefkada island, Greece. *Nat Hazards Earth Syst Sci* 18:321–333. <https://doi.org/10.5194/nhess-18-321-2018>
- Scaioni M, Longoni L, Melillo V, Papini M (2014) Remote sensing for landslide investigations: an overview of recent achievements and perspectives. *Remote Sens* 6:9600–9652. <https://doi.org/10.3390/rs6109600>
- Schneider DJ, Vallance JW, Logan M et al (2005) Airborne thermal infrared imaging of the 2004–2005 eruption of Mount St. Helens. In: AGU fall meeting abstracts 24
- Schumann GJ-P, Domeneghetti A (2016) Exploiting the proliferation of current and future satellite observations of rivers. *Hydrol Processes* 30:2891–2896. <https://doi.org/10.1002/hyp.10825>
- Scott JE, Scott CH (2019) Models for drone delivery of medications and other healthcare items. In: *Unmanned aerial vehicles: breakthroughs in research and practice*. IGI Global, pp 376–392
- Smith LC (1997) Satellite remote sensing of river inundation area, stage, and discharge: a review. *Hydrol Processes* 11:1427–1439. [https://doi.org/10.1002/\(SICI\)1099-1085\(199708\)11:10%3c1427:AID-HYP473%3e3.0.CO;2-S](https://doi.org/10.1002/(SICI)1099-1085(199708)11:10%3c1427:AID-HYP473%3e3.0.CO;2-S)
- Spampinato L, Calvari S, Oppenheimer C, Boschi E (2011) Volcano surveillance using infrared cameras. *Earth-Sci Rev* 106:63–91. <https://doi.org/10.1016/j.earscirev.2011.01.003>
- Stumpf A, Kerle N (2011) Combining Random Forests and object-oriented analysis for landslide mapping from very high resolution imagery. *Procedia Environ Sci* 3:123–129. <https://doi.org/10.1016/j.proenv.2011.02.022>
- Stumpf A, Malet J-P, Kerle N et al (2013) Image-based mapping of surface fissures for the investigation of landslide dynamics. *Geomorphology* 186:12–27. <https://doi.org/10.1016/j.geomorph.2012.12.010>
- Stumpf A, Malet J-P, Allemand P et al (2015) Ground-based multi-view photogrammetry for the monitoring of landslide deformation and erosion. *Geomorphology* 231:130–145. <https://doi.org/10.1016/j.geomorph.2014.10.039>
- Sui H, Tu J, Song Z et al (2014) A novel 3D building damage detection method using multiple overlapping UAV images. *ISPRS Int Arch Photogramm Remote Sens Spat Inf Sci XL-7*:173–179. <https://doi.org/10.5194/isprsarchives-XL-7-173-2014>
- Tang C, Tanyas H, van Westen CJ et al (2019) Analysing post-earthquake mass movement volume dynamics with multi-source DEMs. *Eng Geol* 248:89–101. <https://doi.org/10.1016/j.enggeo.2018.11.010>
- Tanteri L, Rossi G, Tofani V et al (2017) Multitemporal UAV survey for mass movement detection and monitoring. In: Mikos M, Tiwari B, Yin Y, Sassa K (eds) *Advancing culture of living with landslides*. Springer, Cham, pp 153–161
- Tauro F, Porfiri M, Grimaldi S (2016) Surface flow measurements from drones. *J Hydrol* 540:240–245. <https://doi.org/10.1016/j.jhydrol.2016.06.012>
- Techy L, Schmale DG, Woolsey CA (2010) Coordinated aerobiological sampling of a plant pathogen in the lower atmosphere using two autonomous unmanned aerial vehicles. *J Field Robot* 27:335–343. <https://doi.org/10.1002/rob.20335>
- Terada A, Morita Y, Hashimoto T et al (2018) Water sampling using a drone at Yugama crater lake, Kusatsu-Shirane volcano, Japan. *Earth Planets Space*. <https://doi.org/10.1186/s40623-018-0835-3>
- Thiebes B, Tomelleri E, Mejia Aguilar A et al (2016) Assessment of the 2006 to 2015 Corvara landslide evolution using a UAV-derived DSM and orthophoto. CRC Press, Boca Raton, pp 1897–1902
- Thiele ST, Varley N, James MR (2017) Thermal photogrammetric imaging: A new technique for monitoring dome eruptions. *J Volcanol Geotherm Res* 337:140–145. <https://doi.org/10.1016/j.jvolgeores.2017.03.022>
- Tofani V, Segoni S, Agostini A et al (2013) Technical note: use of remote sensing for landslide studies in Europe. *Natural Hazards Earth Syst Sci* 13:299–309. <https://doi.org/10.5194/nhess-13-299-2013>

- Torrero L, Seoli L, Molino A et al (2015) The use of micro-UAV to monitor active landslide scenarios. In: Lollino G, Manconi A, Guzzetti F et al (eds) *Engineering geology for society and territory* -, vol 5. Springer, Cham, pp 701–704
- Tournadre V, Pierrot-Deseilligny M, Faure PH (2014) UAV photogrammetry to monitor dykes-calibration and comparison to terrestrial lidar. *ISPRS Int Arch Photogramm Remote Sens Spat Inf Sci XL-3/W1*:143–148. <https://doi.org/10.5194/isprsarchives-XL-3-W1-143-2014>
- Turner D, Lucieer A, Wallace L (2014) Direct georeferencing of ultrahigh-resolution UAV imagery. *IEEE Trans Geosci Remote Sens* 52:2738–2745. <https://doi.org/10.1109/TGRS.2013.2265295>
- Turner D, Lucieer A, de Jong S (2015) Time series analysis of landslide dynamics using an unmanned aerial vehicle (UAV). *Remote Sens* 7:1736–1757. <https://doi.org/10.3390/rs70201736>
- Valkaniotis S, Papathanassiou G, Ganas A (2018) Mapping an earthquake-induced landslide based on UAV imagery; case study of the 2015 Okeanos landslide, Lefkada, Greece. *Eng Geol* 245:141–152. <https://doi.org/10.1016/j.enggeo.2018.08.010>
- Van Den Eeckhaut M, Kerle N, Poesen J, Hervás J (2012) Object-oriented identification of forested landslides with derivatives of single pulse LiDAR data. *Geomorphology* 173–174:30–42. <https://doi.org/10.1016/j.geomorph.2012.05.024>
- Vetrivel A, Gerke M, Kerle N et al (2018) Disaster damage detection through synergistic use of deep learning and 3D point cloud features derived from very high resolution oblique aerial images, and multiple-kernel-learning. *ISPRS J Photogramm Remote Sens* 140:45–59. <https://doi.org/10.1016/j.isprsjprs.2017.03.001>
- Villa T, Gonzalez F, Miljevic B et al (2016) An overview of small unmanned aerial vehicles for air quality measurements: present applications and future perspectives. *Sensors* 16:1072. <https://doi.org/10.3390/s16071072>
- Voigt S, Giulio-Tonolo F, Lyons J et al (2016) Global trends in satellite-based emergency mapping. *Science* 353:247–252. <https://doi.org/10.1126/science.aad8728>
- Vollgger SA, Cruden AR (2016) Mapping folds and fractures in basement and cover rocks using UAV photogrammetry, Cape Liptrap and Cape Paterson, Victoria, Australia. *J Struct Geol* 85:168–187. <https://doi.org/10.1016/j.jsg.2016.02.012>
- Wallemacq P, Below R, McLean D (2018) UNISDR and CRED report: economic losses, poverty & disasters (1998–2017). Centre for Research on the Epidemiology of Disasters – CRED. https://urldefense.proofpoint.com/v2/url?u=https-3A__www.cred.be_unisdr-2Dand-2Dcred-2Dreport-2Deconomic-2Dlosses-2Dpoverty-2Ddisasters-2D1998-2D2017&d=DwIDaQ&c=vh6FgFnduejNhPPDofl_yRaSfZy8CWbWnIf4XJhSqx8&r=r2aSgYn6PHMQXXmeBiKsnvfFG9T9U5fmdQ67xEVmgo0&m=ktrJ0pKA6VD69oYCBwKuReprks4SwDgXCLbHGC58tXE&s=nllLeOALPXPx1QXrUvFduk1NN9dxWEFl_0H4nHiDH4&e=
- Walter M, Niethammer U, Rothmund S, Joswig M (2009) Joint analysis of the Super-Sauze (French Alps) mudslide by nanoseismic monitoring and UAV-based remote sensing. *Near Surf Geosci* 27:8
- Walter TR, Jousset P, Allahbakhshi M et al (2020) Underwater and drone based photogrammetry reveals structural control at Geysir geothermal field in Iceland. *J Volcanol Geotherm Res* 391:106282. <https://doi.org/10.1016/j.jvolgeores.2018.01.010>
- Watts AC, Ambrosia VG, Hinkley EA (2012) Unmanned aircraft systems in remote sensing and scientific research: classification and considerations of use. *Remote Sens* 4:1671–1692. <https://doi.org/10.3390/rs4061671>
- Weintrit B, Bakula K, Jedryka M et al (2018) Emergency rescue management supported by UAV remote sensing data. *ISPRS Int Arch Photogramm Remote Sens Spat Inf Sci XLII-3/W4*:563–567. <https://doi.org/10.5194/isprs-archives-XLII-3-W4-563-2018>
- Wessels RL, Vaughan RG, Patrick MR, Coombs ML (2013) High-resolution satellite and airborne thermal infrared imaging of precursory unrest and 2009 eruption at Redoubt Volcano, Alaska. *J Volcanol Geotherm Res* 259:248–269. <https://doi.org/10.1016/j.jvolgeores.2012.04.014>
- Westoby MJ, Brasington J, Glasser NF et al (2012) ‘Structure-from-Motion’ photogrammetry: a low-cost, effective tool for geoscience applications. *Geomorphology* 179:300–314. <https://doi.org/10.1016/j.geomorph.2012.08.021>
- Wu C (2011) VisualSFM: a visual structure from motion system. <http://www.cs.washington.edu/homes/ccwu/vsfm>
- Wu C (2013) Towards linear-time incremental structure from motion. In: 2013 International conference on 3D vision. IEEE, Seattle, WA, USA, pp 127–134
- Xu Z, Wu L, Zhang Z (2018) Use of active learning for earthquake damage mapping from UAV photogrammetric point clouds. *Int J Remote Sens* 39:5568–5595. <https://doi.org/10.1080/01431161.2018.1466083>

- Yalcin E (2018) Generation of high-resolution digital surface models for urban flood modelling using UAV imagery. In: WIT transactions on ecology and the environment, WIT Press. Lightning Source, UK, Great Britain, pp 357–366
- Yamazaki F, Liu W (2016) Remote sensing technologies for post-earthquake damage assessment: a case study on the 2016 Kumamoto earthquake. Philippines, Cebu City
- Yang W, Wang M, Shi P (2013) Using MODIS NDVI time series to identify geographic patterns of landslides in vegetated regions. *IEEE Geosci Remote Sens Lett* 10:707–710. <https://doi.org/10.1109/LGRS.2012.2219576>
- Yu M, Huang Y, Zhou J, Mao L (2017) Modeling of landslide topography based on micro-unmanned aerial vehicle photography and structure-from-motion. *Environ Earth Sci*. <https://doi.org/10.1007/s12665-017-6860-x>
- Zarco-Tejada PJ, González-Dugo V, Berni JAJ (2012) Fluorescence, temperature and narrow-band indices acquired from a UAV platform for water stress detection using a micro-hyperspectral imager and a thermal camera. *Remote Sens Environ* 117:322–337. <https://doi.org/10.1016/j.rse.2011.10.007>
- Zekkos D, Clark M, Cowell K, Medwedeff W, Manousakis J, Saroglou H, Tsiambaos G (2017) Satellite and UAV-enabled mapping of landslides caused by the November 17th 2015 Mw 6.5 Lefkada earthquake. In *Proc. 19th Int. Conference on soil mechanics and geotechnical engineering*, pp. 17–22
- Zhang J (2010) Multi-source remote sensing data fusion: status and trends. *Int J Image Data Fusion* 1:5–24. <https://doi.org/10.1080/19479830903561035>
- Zhou Y (2019) 100% automatic metrology with UAV photogrammetry and embedded GPS and its application in dike monitoring. PhD thesis, Université Paris-Est

Publisher's Note Springer Nature remains neutral with regard to jurisdictional claims in published maps and institutional affiliations.

6 Démarche scientifique

Cette section est dédiée à la présentation de ma démarche scientifique, qui constitue la colonne vertébrale de mon travail de chercheur. Après avoir décrit ma formation initiale, mon parcours de recherche est présenté en le positionnant dans le contexte de mon établissement. Ce parcours est guidé par un questionnement scientifique dont je décris l'ensemble des aspects, ainsi que les axes de recherche que j'ai mis en place pour y répondre. Enfin, mon positionnement scientifique est exposé au regard de cette activité.

6.1 Une formation initiale conjuguant physique et géologie

Après trois années d'études en mathématiques et physique, je me suis tourné vers les sciences de la Terre et l'exploration planétaire. J'ai intégré la Licence 3 de sciences de la Terre et de l'Univers de l'Université de Toulouse en 2002, au sein de laquelle j'ai acquis des connaissances en géologie et planétologie. Mon contact avec la recherche a été initié lors de mon stage de Master 1. J'ai ainsi participé à une mission de terrain financée par mes soins sur le volcan Piton de la Fournaise à l'île de la Réunion, dans le cadre du programme ACI CATNAT³³. Cette première expédition scientifique, qui demeure un souvenir fabuleux et formateur, fut le point de départ de mon parcours scientifique, forgé par diverses expériences en France et au Japon :

- En 2003-2004 : un stage de Master 1 dans lequel j'ai travaillé sur les données thermiques issus de thermocouples implantés dans le sol volcanique de la Plaine des Sables (Piton de la Fournaise, île de La Réunion) ;
- En 2004-2005 : un stage de Master 2 sur l'étude locale des circulations d'air et d'eau dans le sol d'un cône volcanique inactif du Piton de la Fournaise (Formica Leo). J'ai découvert la modélisation numérique des processus de convection en milieu poreux dans ce stage ;
- En 2006-2009 : une thèse en co-direction entre l'Université Paul Sabatier et l'Université de La Réunion. Celle-ci étend l'étude des écoulements convectifs d'air et d'eau à l'ensemble du Piton de la Fournaise et à une zone volcanique récente de la planète Mars à partir d'observations optiques, géophysiques et de la modélisation numérique des circulations en milieu poreux ;
- En 2008 : un séjour d'un mois à l'Université de Tokyo en tant que bénéficiaire d'une bourse internationale de l'Université de Toulouse. Ce séjour a permis d'initier mes relations avec l'Université de Tokyo (professeur Kei Kurita) ;
- En 2009-2011 : deux années de post-doctorat à l'Earthquake Research Institute de l'Université de Tokyo sur invitation du professeur Kei Kurita en tant que lauréat du programme franco-japonais CNRS-JSPS³⁴. J'y ai étudié la dynamique de la convection en milieu poreux en conditions expérimentales.

6.2 Contexte de mon poste et positionnement scientifique

6.2.1 Contexte de mon poste

En 2011, j'ai réussi le concours de chargé de recherche en géophysique appliquée du Ministère de la Transition Écologique et Solidaire (MTES) et affecté au CETE³⁵ Normandie-Centre, devenu Cerema³⁶ en 2014. Il s'agit d'un établissement tourné vers l'appui scientifique et technique aux politiques publiques, placé sous la double tutelle du MTES et du Ministère de la cohésion des territoires et des relations avec les collectivités territoriales. Le Cerema est issu de la fusion de plusieurs centres d'ingénierie

33. Programme Actions Concertées Incitatives 1999-2004 "Prévention des catastrophes Naturelles"

34. Japan Society for the Promotion of Science

35. Centre d'Étude Technique de l'Équipement

36. Centre d'Études et d'Expertise sur les Risques, l'Environnement, la Mobilité et l'Aménagement

publique (CETE, CERTU³⁷, CETMEF³⁸ et SETRA³⁹). Bien qu'étant un centre tourné vers l'ingénierie, l'établissement a été reconnu acteur de la recherche nationale par la loi de programmation de la recherche en 2021. L'équipe ENDSUM⁴⁰ a été créée au 1er janvier 2018. Son objectif principal est le développement de méthodes de caractérisation et de diagnostic non destructives des sols et des ouvrages. En effet, les techniques actuelles (tels que les forages) ne délivrent souvent que des résultats ponctuels, onéreux et destructifs des structures et matériaux impliqués. L'enjeu est donc de mettre à disposition des gestionnaires des techniques et outils de diagnostic et de contrôle non invasifs, si possible à grand rendement, à faibles coûts et améliorant l'efficacité des procédures d'inspection et de suivi.

Au sein d'ENDSUM, j'ai poursuivi le développement de mon projet initié en thèse en tentant de répondre à la question scientifique suivante : **Peut-on caractériser le sous-sol et les structures du génie civil en combinant données d'imagerie optiques, géophysiques et modélisation numérique** ? Je me focalise notamment sur l'étude du lien entre phénomènes de surface et profonds (notamment hydrodynamiques), en utilisant une combinaison originale de données associant données de terrain (méthodes électriques, radar géologique, potentiels spontanés), aéroportés (infrarouge thermique, visible), satellitaires (infrarouge thermique, visible, accélérométriques) et modélisation (transferts de chaleur et de masse en milieu poreux, inversion électrique). Cette question centrale m'a amené à construire un parcours qui repose sur l'étude d'objets et de processus variés et qui ont des échelles spatiales et temporelles très différentes. Au Cerema, mes applications se sont enrichies en s'étendant au génie civil, à l'archéologie ou aux sciences pour l'ingénieur. J'ai pu analyser les données de nombreux capteurs, qu'ils soient embarqués depuis l'orbite, aéroportés ou déployés au sol (caméras, matériels géophysiques). La diversité et le volume important de ces observations m'a poussé à faire évoluer ma méthodologie initiale, en développant des outils permettant de combiner ou fusionner ces données spatialisées et les modèles. Cette approche s'est avérée très efficace au fil des années pour 1) mieux comprendre les phénomènes hydrogéologiques ou électriques en jeu dans les sols, 2) mieux contraindre certains traitements géométriques ou géophysiques (inversion...) et 3) fournir des outils de visualisation et d'analyse intuitifs. Mes recherches posent des questions diverses, qu'elles soient de nature scientifique ou technique, qui sont liées :

- au domaine spectral étudié. Peut-on utiliser l'infrarouge thermique, afin de caractériser des écoulements souterrains ou des structures dans les sols ? Cela sous-entend notamment de comprendre 1) comment l'eau circule dans les milieux et 2) comment se font les échanges aéro-hydro-thermiques entre la subsurface et l'atmosphère.
- au volume d'observations acquises. Quelles méthodes utiliser pour combiner/fusionner des données de télédétection, géophysiques et géométriques afin de faciliter et d'enrichir l'interprétation des données ?
- à l'avènement de nouveaux modes d'observation. Peut-on utiliser les drones comme vecteurs d'observation fiables, robustes et à bas coût pour des auscultations à grand rendement ?

Afin de répondre à ces questions, mes recherches sont structurées selon les trois axes de recherche d'ENDSUM, nourris par les remontées de terrain du Cerema, ainsi que par mes interactions avec des établissements et universités au niveau national et international : 1) la caractérisation physique et géométrique des milieux (section 3.1) ; 2) le développement de méthodologies d'observation et de traitement de données (section 3.2) et 3) le développement de prototypes et de moyens de mesure (section 3.3).

37. Centre d'études sur les réseaux, les transports, l'urbanisme et les constructions publiques

38. Centre d'études techniques, maritimes et fluviales

39. Service d'études sur les transports, les routes et leurs aménagements

40. Évaluation Non Destructive des Structures et des Matériaux

6.2.2 Positionnement scientifique

A l'interface entre la physique et les sciences de la Terre, mon investissement est à l'image de ce que j'aime faire :

- réaliser/analyser des observations et concevoir des modèles pour comprendre des phénomènes physiques ;
- Explorer des domaines scientifiques variés et créer de la connaissance pluridisciplinaire ;
- Développer des méthodologies ayant vocation à irriguer l'ingénierie ;
- en étant au Cerema, pouvoir réaliser des expertises pour les collectivités, au plus proche des besoins des concitoyens ;
- pouvoir interagir quotidiennement en relation avec des techniciens et ingénieurs de disciplines diverses.

Mon positionnement scientifique me semble relativement singulier dans le paysage international. De ma formation initiale en physique et géologie a découlé une thèse en géophysique et télédétection appliquée à la volcanologie planétaire, et une carrière en cohérence avec cette orientation pluridisciplinaire. Ce profil me permet de communiquer avec des scientifiques de plusieurs communautés, voire d'être de plus en plus en mesure de les fédérer (géologie, géotechnique, géophysique, télédétection, mathématiques appliquées). Les contributions personnelles issues de ces collaborations sont diversifiées, allant du pilotage de la collecte de données (en géophysique de subsurface ou en télédétection) à la réalisation de modèles numériques permettant d'expliquer les observations (modélisation directe hydro-thermique ou inversion électrique). Mon expérience dans les processus de convection en milieu poreux me permet par ailleurs de développer des idées originales faisant le lien entre températures de surface, phénomènes géophysiques et hydrogéologiques. Du point de vue thématique, mes publications scientifiques peuvent donc aussi bien traiter d'interactions sol-atmosphère, de phénomènes de subsurface, que d'interactions fluide-roche. Enfin, étant télépilote de drone depuis 2016, je maîtrise l'ensemble de la chaîne acquisition-traitement-interprétation pour les observations issues de ce vecteur. A titre d'exemple, cette compétence me permet aujourd'hui de participer au programme de gestion du littoral Ouest Africain (WACA⁴¹) afin de faire monter en compétence les équipes africaines sur l'usage des drones pour l'observation du littoral.

6.3 Des collaborations nationales et internationales

La diversité de mes thématiques de recherche fait que de nombreuses collaborations se sont développées au niveau national et international, donnant lieu à une participation à des projets et/ou à des publications scientifiques communes. D'abord, j'ai toujours su garder le réseau issu de ma thèse, constitué du GET⁴² (Michel Rabinowicz), de l'IPGP⁴³ (Fabrice Fontaine), le Laboratoire Géosciences Réunion (Anthony Finizola) et le laboratoire Magma et Volcans de l'Université Clermont-Auvergne (Lydie Gailler). Ces partenariats ont donné lieu à divers projets CNES (projets TOSCA), ANR (projet Slide4Volc), européens (7^{em}e PCRD Medsurv) et internationaux (Huayruro) et à l'encadrement de Cécile Mézon et de Téodolina Lopez en tant que doctorante et post-doctorante pendant plusieurs années. Avec mon intégration au Cerema, mes liens avec d'autres établissements se sont développés comme avec l'UGE⁴⁴ (Yannick Fargier, Sergio Palma Lopes et Jean-Luc Sorin) et l'ENPC⁴⁵ (Yu-Jun Cui). Ces collaborations ont donné lieu à plusieurs travaux publiés, ainsi qu'au projet FUI national Didro (2016-2019). Ce projet a marqué le début de la montée en compétence de l'équipe ENDSUM Rouen sur les drones et m'a permis d'encadrer Marion Tanguy en tant que post-doctorante. Au niveau régional, je

41. <https://www.wacaprogram.org/fr>

42. Laboratoire Géosciences Environnement Toulouse

43. Institut de Physique du Globe de Paris

44. Université Gustave Eiffel

45. Ecole des Ponts Paris Tech

possède des liens étroits avec le laboratoire M2C⁴⁶ (Fayçal Rejiba et Abdel Jardani), le laboratoire IDEES⁴⁷ de Caen (Olivier Maquaire et Stéphane Costa), le Laboratoire de Mathématique de l'INSA de Rouen (Carole Le Guyader) et le Laboratoire de Mathématiques Raphaël Sale (LMRS) de l'Université de Rouen Normandie. Ces liens ont donné lieu à deux projets régionaux sur l'observation des falaises (TéléDÉTAC et Defhy3geo), à la thèse d'Azziz Saley, de Georges EDDE et à l'encadrement de trois post-doctorants : Imen Hassen, Sam Taoum et Thomas Junique.

Enfin, mes relations internationales ont été initiées grâce à mon post-doctorat à l'Université de Tokyo. Mes liens avec Anthony Finizola de l'Université de la Réunion ont permis une collaboration de plusieurs années avec Tullio Ricci de l'INGV⁴⁸ dans le cadre de la thèse de Cécile Mézon, mais aussi dans le cadre des projets d'imagerie électrique grande profondeur du Vésuve et de l'Etna (projet Medsurv). Par ailleurs, j'ai réalisé quatre séjours à l'Ingemmet⁴⁹ au Pérou entre 2015 et 2018 avec Anthony Finizola, soit un total cumulé de 6 mois en tant que chercheur invité dans le cadre du projet archéologique Huayruro⁵⁰. Depuis ma thèse en 2009, j'ai donc passé 2 ans et demi dans des instituts étrangers afin de mener des travaux collaboratifs. Enfin, depuis 2020, nous avons formé un consortium franco-chinois avec l'ENPC, la Northwest Agriculture and Forestry University (Heijun Hu), Zhengzhu University (Weikang Song), Cardiff University (Ni An) et le pôle "applications satellitaires" du Cerema (Téodolina Lopez) afin de d'étudier le lien entre données satellitaires, données géotechniques et géophysiques en milieu aride. Plusieurs articles sont en cours de rédaction sur cette thématique.

6.4 Une activité portant sur l'ensemble des facettes du métier de chercheur

Cet investissement constant dans plusieurs domaines me permet aujourd'hui de présenter à l'Habilitation à Diriger des Recherches un dossier attestant de diverses facettes du métier de chercheur qui seront détaillées en section 2 :

- 26 publications en premier auteur ou co-auteur en revues internationales à comité de lecture, donnant un h-index de 8 (référencement Scopus),
- deux chapitres d'ouvrage,
- quatre conférences invitées,
- 45 congrès internationaux avec actes,
- 15 communications avec actes en congrès national,
- 13 rapports de recherche,
- neuf rapports d'expertise.

J'ai co-encadré quatre thèses et ai participé à l'encadrement de quatre chercheurs post-doctoraux et de nombreux étudiants, du niveau prépa/DUT au niveau Master 2. Je porte actuellement un projet pour la Région Normandie en 2022, ainsi qu'un contrat d'expertise pour la ville de La Rochelle. J'ai été responsable de workpackages dans un projet industriel (FUI) et un projet international (franco-péruvien). Enfin, j'ai participé à 12 projets régionaux, nationaux ou internationaux.

En terme d'activité collective, je suis responsable-adjoint de l'équipe ENDSUM du Cerema Normandie-Centre (1DR, 1CR, 4 chargés d'études, 1 à 4 thèses ou post-doctorats par an et 1 à 5 stagiaires par an). Je m'investis pour ma communauté scientifique depuis 2014 en tant qu'élu à la Comeval⁵¹ et membre de son bureau national. Il s'agit de l'équivalent du CoNRS au MTES. Depuis 2022, je suis nommé au Conseil Scientifique du Patrimoine Naturel de Normandie du fait de mes travaux en hydrogéologie. Enfin, mes travaux sont ponctués par une valorisation très importante à destination de la po-

46. Laboratoire de Morphodynamique Continentale et Côtière de l'Université Rouen Normandie

47. Laboratoire Identité et Différenciation de l'Espace, de l'Environnement et des Sociétés

48. Istituto Nazionale di Geofisica e Vulcanologia

49. Instituto Geológico, Minero y Metalúrgico

50. Acronyme du projet franco-péruvien "Las civilizaciones olvidadas del volcan HUAYnaputina y les grand Retos del futURO"

51. COMmission nationale d'EVALuation des Chercheurs du Ministère de l'écologie

pulation, sous forme d'articles, d'interviews ou de films réalisés en collaboration avec la société de production 4scienceprod et les médias locaux/nationaux.

Après avoir présenté mon Curriculum Vitae détaillé dans la section suivante, mon mémoire se focalisera sur mes différents axes de recherche, afin de présenter les points saillants de mon activité scientifique. Finalement, je terminerai par le développement de mon projet de recherche pour les années à venir.

7 Projet de recherche

Fort de l'expérience acquise suite à ces travaux ancrés dans la communauté académique et la recherche appliquée, j'envisage les thématiques suivantes afin de continuer à promouvoir l'utilisation conjointe de données optiques, géophysiques et de modélisation à toutes les échelles.

7.0.1 Caractérisation physique des milieux

Je souhaite poursuivre mes investigations sur l'origine des anomalies thermiques dans les bassins sédimentaires. Un sujet qui me tient particulièrement à cœur est l'accès à l'eau. A l'échelle mondiale, les eaux souterraines constituent le principal réservoir d'eau douce disponible (96,7 %). Les événements hydro-météorologiques extrêmes associés au changement climatique, telles que les sécheresses et les inondations, deviennent plus fréquents et affectent la disponibilité de l'eau. En conséquence, 38 % de la population mondiale sera exposée au stress hydrique en 2025, contre 9 % en 2008. À l'échelle régionale, l'épuisement des eaux souterraines a de graves répercussions sur la société, l'économie et l'environnement [20]. L'impact de la sécheresse sur les régions (semi-)arides est considérable : accès limité aux eaux souterraines propres, problèmes sanitaires et instabilités sociales notamment pour les aquifères transfrontaliers. En effet, les régions (semi-)arides représentent ≈ 30 % de la surface de la Terre où les nappes constituent une ressource importante en eau douce ; faiblement renouvelable car l'apport en eau est souvent très localisé, mais exploitable (e.g., [19]). Le Programme des Nations unies pour le développement (PNUE) prévoit une diminution des précipitations de 5 à 15 % dans la plupart des zones désertiques du monde. Étant donné l'importance croissante de ces ressources en eau spécifiques dans le monde, il est essentiel que tous les efforts soient faits pour trouver, gérer et préserver ces ressources fragiles. Le développement de méthodologies permettant de déterminer la présence de nappe dans ces zones et de suivre son évolution est donc fondamental pour la stabilité des zones arides. Ce projet vise à explorer la présence de la nappe et à étudier son évolution en utilisant une combinaison de données satellitaires, de mesures *in situ* et de modélisation numérique. Nos principales hypothèses de recherche sont les suivantes : 1) les nouvelles avancées dans la recherche satellitaire et les études d'interaction sol-atmosphère montrent qu'une nappe phréatique peut influencer l'hydrologie et le comportement thermique de la surface dans certaines zones arides [36] et 2) étant donné la première hypothèse, la combinaison des mesures *in situ* avec les données satellitaires peut aider à explorer l'aquifère.

Les mesures seront effectuées dans le désert de Badain Jaran (BJD) en Mongolie intérieure (figure 21), qui possède les plus hautes dunes immuables du monde (jusqu'à 400 m) et où la présence d'un système aquifère dans les sédiments sableux du Quaternaire et les grès du Néogène-Crétacé est bien décrite [24]. Cet aquifère s'exprime en surface par la présence de lacs permanents entre les dunes, mais la teneur en eau peut encore être très élevée à une altitude de 100 m sur les dunes. Les fluctuations saisonnières du lac sont inférieures à 0,5 m, en raison de la décharge quasi-stable des eaux souterraines (et probablement d'une alimentation permanente). De nombreux travaux ont été réalisés pour caractériser l'origine des eaux souterraines alimentant les lacs, la connexion hydrologique entre le BJD et le bassin de la rivière Heihe (HRB), la recharge par infiltration et les caractéristiques géochimiques des eaux. Récemment, un effet d'îlot de chaleur a été décrit par [26] sur la région des lacs. Ils proposent que cet excès de chaleur atmosphérique est principalement lié à la chaleur transportée par l'aquifère profond. Les nouvelles observations satellitaires Landsat et ASTER recueillies par notre équipe soutiennent clairement cette hypothèse en révélant la présence d'anomalies thermiques de surface à grande échelle, quotidiennes et saisonnières, sur le BJD, où les régions autour des lacs sont $\approx 5^\circ\text{C}$ plus chaudes le jour et la nuit (figure 22). Ces observations suggèrent que la nappe phréatique affecte la température du sol. Elles font du BJD un laboratoire original à grande échelle adapté à l'utilisation de données

satellites et *in situ* pour étudier le lien entre la nappe phréatique et la surface. Ce projet fait l'objet d'une soumission à l'ANR et fait intervenir l'ENPC (Yu-Jun Cui), l'IGN (Pierre-Louis Frison) et le Cerema (Téodolina Lopez).



FIGURE 21 – Photographie du désert du Badain Jaran avec vue sur les dunes immuables et les lacs permanents (crédit photo ©chinadiscovery.com).

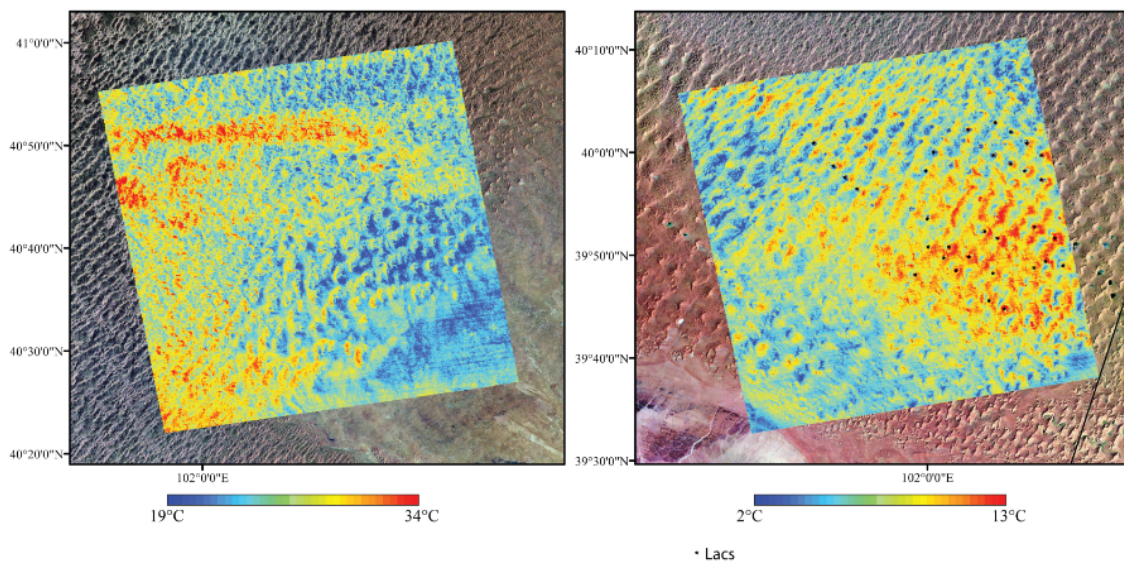


FIGURE 22 – Carte de température de jour et de nuit de la zone désertique du Badain Jaran. Certaines zones sableuses sont chaudes de jour comme de nuit et probablement associées à la nappe présente dans les sables du quaternaire, alimentée par des eaux profondes. Les lacs sont signalés par des étoiles.

Au Sahel, [36] a montré qu'une anomalie thermique peut être générée par des circulations convectives d'eau sous le Lac Tchad du fait de variations spatiales de conductivité thermique dans le bassin sédimentaire et de la présence de topographie dans les couches sédimentaires. Il est aussi bien connu que des anomalies de température

peuvent apparaître juste avant des séismes importants à l'aplomb de certains bassins sédimentaires [14]. Ces anomalies thermiques chaudes pouvant couvrir une superficie allant jusqu'à 100 000 km² ont été observées depuis une vingtaine d'années avant des séismes de magnitude supérieure à 5. Nous nous attachons plus particulièrement à étudier les anomalies thermiques qui se sont développées environ 20 jours avant le séisme de Boumerdès qui a touché l'Algérie le 21 Mai 2003 ($M_w \approx 6,9$), comme le montre la figure 23. Le but de l'étude est de comprendre les processus hydro-tectoniques à l'oeuvre pour générer de telles anomalies avant un séisme, en tenant compte du contexte géologique particulier de la région algérienne. En reposant sur les hypothèses déjà existantes, nous proposons que le développement des anomalies thermiques avant le séisme de Boumerdès est induit par un relâchement catastrophique d'eau souterraine vers la surface. Ce relâchement est contrôlé par la combinaison d'un phénomène de compaction des argiles et du cycle de déshydratation-hydratation d'une couche épaisse et profonde d'argile (un mélange de smectite et d'illite) [42]. Cette combinaison de phénomènes provoque des changements dans 1) la perméabilité verticale de la séquence sédimentaire et 2) la quantité d'eau arrivant en surface et apportant de l'énergie par condensation dans la zone. La combinaison originale d'analyse de séries temporelles de température de surface (obtenues par les capteurs thermiques à bord des satellites MODIS - Moderate Resolution Imaging Spectroradiometer), des données de précipitations (TRMM) et des estimations du stock d'eau continental (GRACE) avec des données géologiques et géophysiques (gravimétrie et tomographie sismique) permettrait de proposer une vision alternative d'un sujet peu étudié jusqu'alors. Ce sujet pourrait avoir un impact fort sur la compréhension de la physique des séismes lents et donc permettre d'améliorer la compréhension 1) de l'évolution des bassins sédimentaires en contexte de compression tectonique et 2) proposer dans le futur un outil de détection pour les très gros séismes à partir des données gratuites américaines telles que les données MODIS mais aussi en reposant sur les nouvelles constellations Copernicus comme les données Sentinel-3, la nouvelle mission TRISHNA et la future mission LSTM (Land Surface Temperature Monitoring). Ces travaux sont réalisés en collaboration avec Téodolina Lopez du Cerema de Toulouse et Michel Rabinowicz du GET.

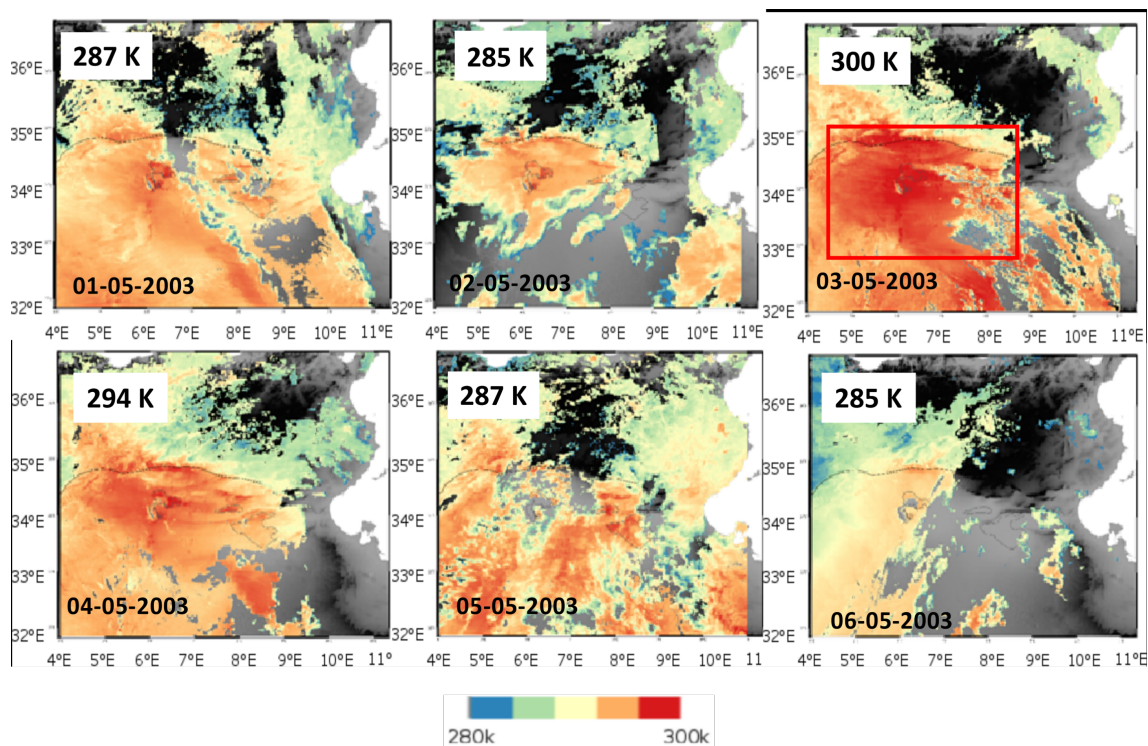


FIGURE 23 – Évolution de la température de nuit quelques jours avant le séisme de Bourmedès qui a eu lieu le 21 mai 2003. Noter le réchauffement important de la zone le 03 mai 2003. L'objectif de ce projet est d'expliquer comment une telle anomalie thermique peut être générée dans une zone aride avant un séisme.

L'eau joue un rôle prépondérant dans l'érosion des falaises. A l'ouest du bassin sédimentaire parisien, les falaises de craie et de marnes de Normandie subissent une ablation continue avec des conséquences pouvant être importante pour le bâti littoral. Si les caractéristiques mécaniques des falaises littorales de Normandie sont connues, les interactions falaises/eaux continentales/eaux marines (dont la connaissance est primordiale pour les études de stabilité) sont moins bien décrites. En particulier, les mécanismes de transfert de l'eau météorique à travers la falaise depuis le plateau limoneux jusqu'au platier carbonaté restent à préciser. Le projet Région Normandie Defhy3geo qui a commencé au 1^{er} janvier 2022 vise à établir un modèle hydrologique de certaines falaises de Normandie (badlands littorales des Vaches Noires et falaise de craie de Sainte-Marguerite-sur-Mer) à partir de données optiques, géophysiques, géologiques et la modélisation numérique. Le projet implique un consortium constitué des Laboratoire M2C, IDEES, le LMI et le Cerema. Dans ce cadre, les premiers modèles des Vaches Noires combinant modèle infrarouge (obtenu avant le lever du soleil en hiver) et imagerie électriques 3D (obtenue grâce au code PYLGRIM) ont pu être réalisés, comme le montre la figure 24. Le calcul d'inversion 3D incorporant six profils électriques longitudinaux et transversaux a été fait en donnant plus de poids aux variations verticales de résistivité, ce qui permet de bien décrire le milieu tabulaire composé de marnes, d'argile et de calcaire constituant le glissement des Vaches Noires. Ces résultats montrent bien le lien entre la présence de zones conductrices à l'intérieur de la structure (soulignées par des tirets blancs sur la figure 24) et des sorties d'eau (11-12°C observées en hiver) à deux altitudes différentes sur le glissement. Dans ce cas, l'eau est détectée par la caméra thermique, car la température du sol est proche de 0°C en février. La végétation est de même plus chaude que le sol au petit matin (mais à peu près à la même température que les sorties d'eau), du fait de l'arrêt de l'évapotranspiration pendant la nuit. Ces zones de résurgences sont localisées dans des cassures de pentes de la falaise et sont le lieu de

coulées de boue importantes, dont la mise en place semble à certains moments décorrélée des épisodes de précipitations [56]. Je souhaite m'investir dans la compréhension de la génération de ces coulées de boue, événements qui conditionnent l'érosion du littoral des Vaches Noires et le recul du trait de côte dans cette région. En particulier, le lien entre les écoulements et le comportement rhéologique des marnes (constitué d'argiles et de calcaire) à l'intérieur du plateau en dehors des événements dits saisonniers me paraît intéressant à investiguer. Il est connu que la rhéologie des argiles dépend du volume de liquide interstitiel dans les pores. Lorsque ce volume atteint un certain seuil (appelé seuil de consolidation allant de 26% à 47%, dépendant du type d'argile), les grains ne sont plus en contact, peuvent glisser dans la suspension boueuse et s'écouler au niveau du glissement [42]. Les mécanismes à l'origine de la migration, de la concentration de l'eau et de la séparation de la boue de ces argiles (générées par la compaction) restent à décrire et c'est ce que je veux m'atteler à faire dans les années à venir. Si ce mécanisme est présent dans le plateau, l'extraction de boue devrait alors se traduire par une subsidence locale. Des travaux récents de TU Delph montrent qu'il semble possible de détecter des variations verticales associées au retrait-gonflement des argiles à partir de données InSAR ([17], [22]). Je souhaite donc tester l'apport potentiel de données interférométriques fournies par le satellite Sentinel 1 pour répondre aux questions suivantes 1) Peut-on observer des variations verticales de hauteur saisonnière du plateau du fait de l'humidification/compaction des argiles dans le milieu?; 2) Peut-on détecter des phénomènes de subsidence du fait de l'expulsion de matière à l'intérieur du plateau? et 3) si oui, existe-t-il des phénomènes de subsidence intra-saisonniers non corrélés aux événements pluvieux? Ces données disponibles via l'European Ground Motion Service (<https://egms.land.copernicus.eu/>) seront complétées par des mesures réalisées au GPS et photogrammétriques, des observations infrarouge, des mesures *in situ* de teneur en eau jusqu'à 1 m de profondeur dans le sol, des mesures géophysiques et météorologiques.

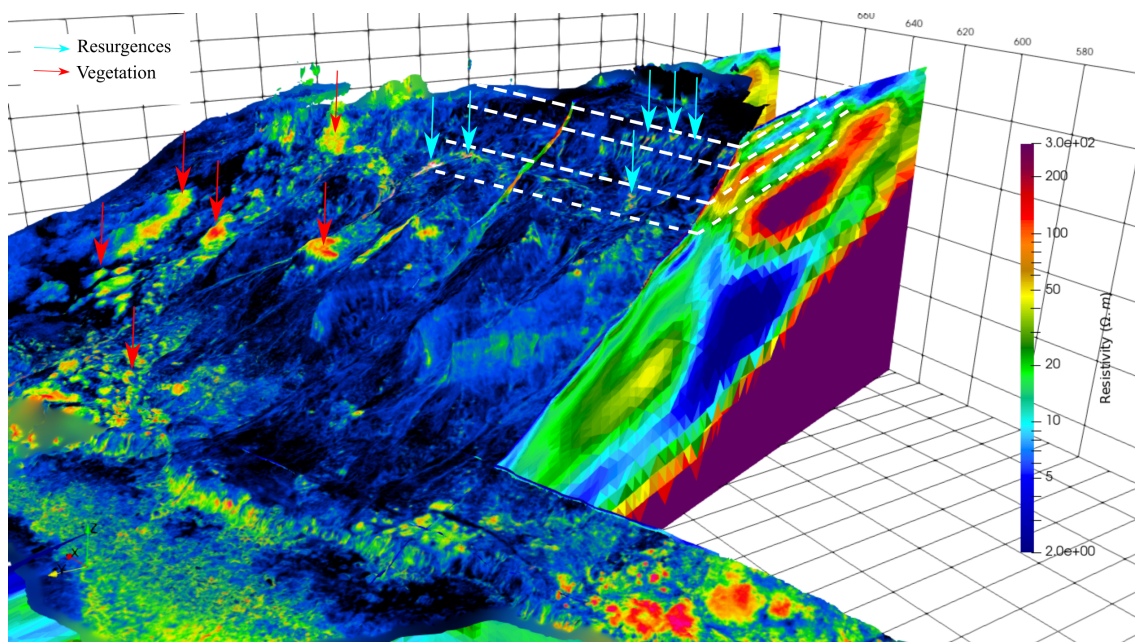


FIGURE 24 – Modèle de température 3D des Vaches Noires obtenu en hiver combiné au résultats d'imagerie électrique pour six profils inversés ensemble. Les flèches rouges et vertes localisent les résurgences d'eau et la végétation, respectivement.

Enfin, à petite échelle, je souhaite continuer à promouvoir l'utilisation de l'infrarouge thermique pour les risques associés aux cavités. Les déstabilisations des cavités souter-

raines constituent un aléa important pour l'aménagement du territoire. En Normandie, des dizaines de milliers de cavités anthropiques (appelées marnières) ont été creusées (au XIXe siècle) pour l'extraction de la craie servant à l'amendement des sols. Celles-ci se distinguent d'autres cavités artificielles par un volume réduit par rapport à leur profondeur (jusqu'à 50 m) et par le fait qu'elles sont souvent oubliées, ignorées ou mal localisées. Les marnières sont reliées à la surface par un puits de diamètre métrique souvent mal rebouché et recouvert de sol agraire (figure 25). L'effondrement de ces objets, souvent brutal et parfois léthal, est un réel problème en Normandie et constitue une préoccupation majeure pour les pouvoirs publics et les citoyens [25]. Leur détection est donc primordiale, en particulier du fait du réchauffement climatique, dont les manifestations de plus en plus fréquentes peuvent accélérer les effondrements. Dans les années 2000, des données thermiques aériennes ont permis de détecter la signature thermique de surface de puits de plusieurs marnières (figure 26), faisant apparaître cette méthode comme prometteuse, mais sans en comprendre les mécanismes à l'origine de ces observations [12].

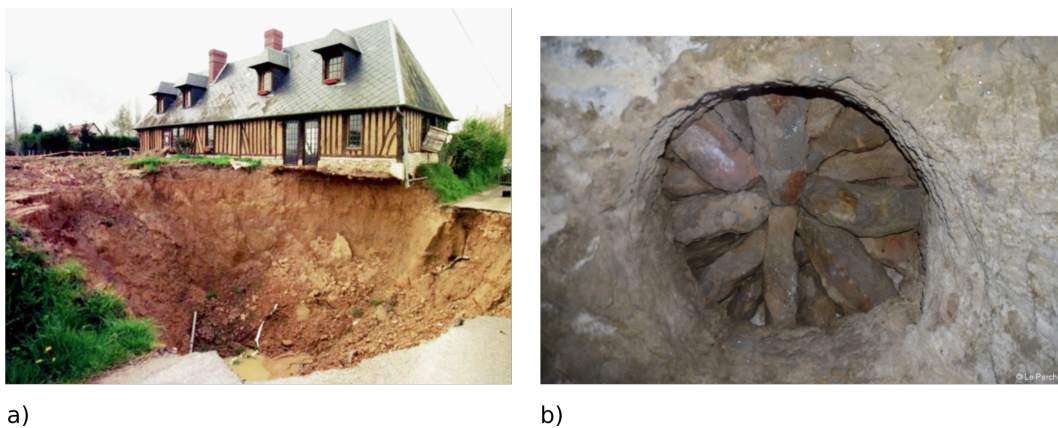


FIGURE 25 – a) Photographie d'un effondrement de marnière en Normandie et b) Photographie d'un puits bouché par des galets prise de l'intérieur de la marnière et montrant une perméabilité très importante.

Les travaux que j'ai menés sur les cavités souterraines à partir de 2015 mettent en évidence le lien potentiel entre températures et déformations de surface [49]. Ces subsidences sont souvent générées à un stade avancé de la migration de la cavité vers la surface [49]. Je souhaite donc me focaliser sur leur détection précoce, en me basant sur la caractérisation quantitative des échanges d'air et d'eau entre les marnières et l'atmosphère. L'objectif est de modéliser les circulations convectives et les transferts de chaleur en 3D dans ces objets pour comprendre comment sont générées les anomalies thermiques observées en surface. Pour un milieu fluide (e.g. vide), le nombre de Rayleigh Ra donnant la vigueur de la convection est donnée par la formule suivante :

$$Ra = \frac{g\alpha H^3 \Delta T}{\nu \kappa} \quad (2)$$

avec g , l'accélération de la gravité (9.81 m s^{-2}); α le coefficient d'expansion thermique du fluide ($3.7 \cdot 10^{-4} \text{ K}^{-1}$); H la hauteur de la cavité (2 m), ΔT la différence de température entre le haut et le bas de la cavité (1 K); ν la viscosité du fluide ($2 \cdot 10^{-5} \text{ Pa s}$) et κ la diffusivité thermique du fluide ($2 \cdot 10^{-5} \text{ m}^2 \text{ s}$). Ainsi, en prenant en compte ces valeurs pour une cavité totalement vide, le nombre de Rayleigh Ra est d'environ $3 \cdot 10^9$, donc très largement au dessus du nombre de Rayleigh critique (10^3). Cette valeur montre que la convection peut être extrêmement active dans ce milieu avec la création de plusieurs cellules comme l'atteste les résultats obtenus pour la marnière de Barcq (figure 26). La topographie réaliste de la cavité a été obtenue par photogrammétrie avec des photos

acquises par le groupe Risques Naturels du Cerema de Rouen. Il est à noter que cette valeur calculée de Ra constitue plutôt un maximum pour les modèles, car les marnières intègre un milieu poreux, qui diminue drastiquement ce nombre. Nous comparerons ces modèles aux observations thermiques et géophysiques obtenues sur plusieurs sites en Normandie. La thèse de Georges EDDE qui débutera au dernier trimestre 2022 portera sur cette thématique. La thèse permettra de répondre aux questions suivantes :

- Quelles doivent être les caractéristiques du sol pour que de la convection d'air se déclenche dans des cavités souterraines et interagissent avec l'atmosphère ?
- Comment se font les interactions entre le rayonnement de surface, par définition évolutif, et le système convectif ?
- Quelles sont les anomalies de température générées en surface par ces circulations d'air ?
- Quelles sont les modifications du champ thermique lorsque de l'eau est ajoutée au système ?

Le projet sera réalisé en collaboration avec Ionut Danaila de l'Université de Rouen Normandie. Le code 3D du LMRS écrit en éléments finis est capable de décrire des phénomènes de convection en milieu "fluide" (vide) et en milieu poreux. Il permettra donc de s'adapter aux configurations géologiques complexes rencontrées dans ces marnières. Une collaboration pourra être par ailleurs développée avec le BRGM qui possède des données géophysiques récentes de plusieurs sites en Normandie.

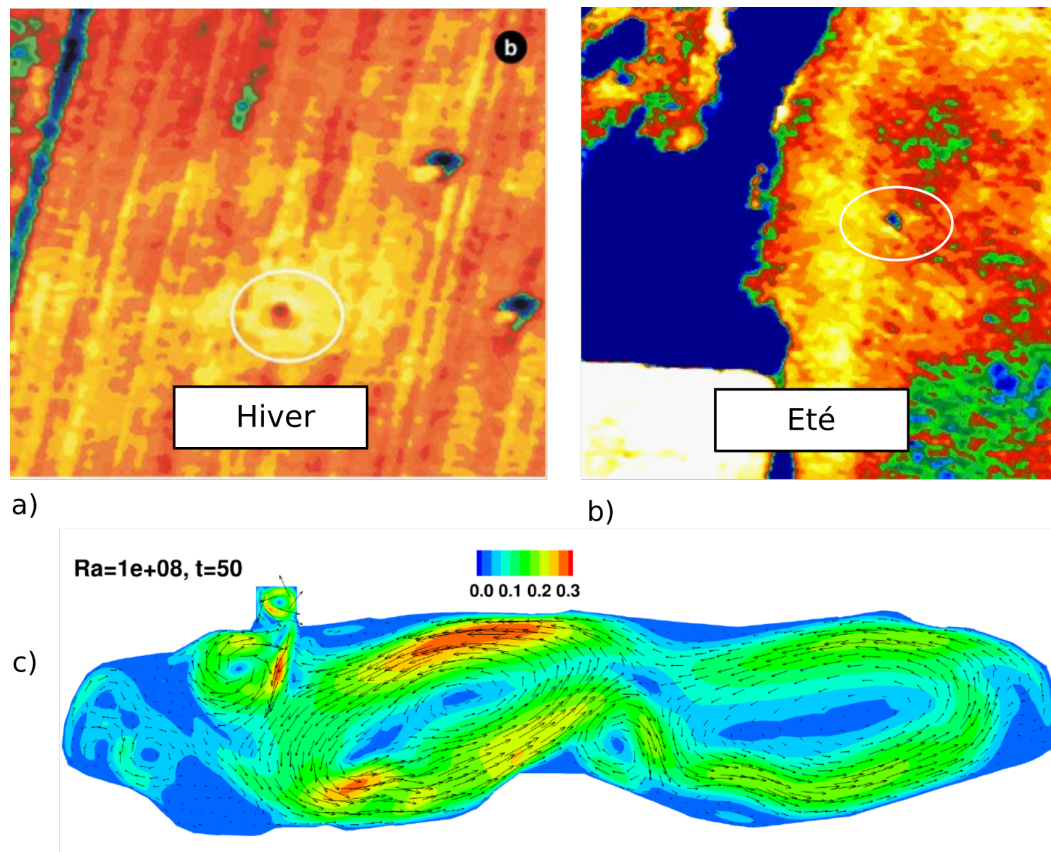


FIGURE 26 – a) Anomalie thermique au droit d'un puits invisible en surface générée en hiver (contraste de 2 à 4°C entre le puits et l'encaissant), b) anomalie thermique induite en été (même type de contraste) et c) Champ de vitesse 2D adimensionné de l'air issu du couplage entre l'équation de Navier-Stokes et de la chaleur pour un nombre de Rayleigh de 10^8 sous FreeFEM++. Il montre la formation de plusieurs cellules de convection dans une marnière refroidie par le haut et ayant un puits non bouché (connecté à l'atmosphère). La cavité est la marnière de Barcq. Sa morphologie est réaliste, ayant été obtenue par photogrammétrie. Résultats obtenus pendant le stage de Georges EDDE.

7.0.2 Développement de méthodologie d'observations et de traitement de données

Le développement d'outils de détection des puits de marnières me semble particulièrement primordial pour la région Normandie. La thèse de Georges EDDE se concentrera sur la compréhension du comportement thermique des structures grâce à la modélisation numérique et à la confrontation de ces modèles à des observations thermiques, géologiques et géophysiques (disponibles dans la bibliographie historique des laboratoires des Ponts et Chaussées et plus récemment suite à nos mesures). Elle décrira les configurations optimales géologiques, météorologiques et temporelles favorisant la génération des anomalies thermiques, mettra en exergue les avantages et les limitations de l'infrarouge thermique et finalement permettra de définir les premiers contours d'une méthodologie de détection. Il n'existe en ce moment aucune méthode à grand rendement capable de détecter ces petits objets, notamment en contexte de couverture argileuse. La micro-gravimétrie, seul outil capable de détecter des défauts de masse dans les sols a certes fait de gros progrès (sensibilité multipliée par 10 en 20 ans), mais elle n'est pas adaptée pour le grand rendement du fait des temps d'acquisition longs en chaque point. Le drone (et l'avion) sont des outils capables de faire du grand rendement (10 min/Ha pour le drone) et permettent de plus l'emport de plusieurs capteurs complémentaires.

Même si la thèse menait à une capacité de détection de 10 % à 20 % des marnières grâce à l'infrarouge thermique, cela constituerait une avancée considérable et un vivier de plusieurs dizaines de milliers de cavités à traiter. Enfin, les résultats obtenus dans ce cadre pourront servir à d'autres types de cavités comme les catiches du Nord de la France, les carrières possédant des fontis ou même les dolines naturelles interagissant avec l'atmosphère.

La détection visuelle de singularités thermiques, qu'elles soient associées à des puits de cavités souterraines ou à des circulations d'eau est très fastidieuse, sinon impossible à réaliser lorsque l'on parcourt des surfaces importantes. Dans toutes nos études, la détection de ces signaux nécessite l'intervention humaine, en comparant données acquises dans l'infrarouge, le visible et des observations météorologiques. Elle requiert souvent une analyse dynamique (saisonnnière et/ou journalière) afin de détecter l'anomalie à proprement dit. Dans les prochaines années, je souhaite m'investir dans la détection de ces signaux à partir de méthodologies de classification automatiques. Les falaises des Vaches Noires constituent un terrain de jeu idéal pour tester différentes méthodes de détection des résurgences d'eau. Un premier stage réalisé en 2021 en collaboration avec Philippe Foucher (Endsum Strasbourg) a permis de montrer qu'il est tout à fait possible de détecter automatiquement les anomalies thermiques associées aux sorties d'eau sans végétation présentées sur la figure 24. Cette détection se base sur le fait que les sorties d'eau et la végétation sont chauds par rapport au sol en hiver. L'orthoimage thermique possède donc deux classes qui sont les zones chaudes et froides. Pour supprimer la contribution thermique de la végétation et ne détecter que les sorties d'eau, on effectue une classification de la végétation et du sol nu sur les données visibles (obtenue à partir du nuage de point dense). La soustraction des deux orthoimages classifiées fournit alors la localisation des résurgences d'eau, comme le montre la figure 27.

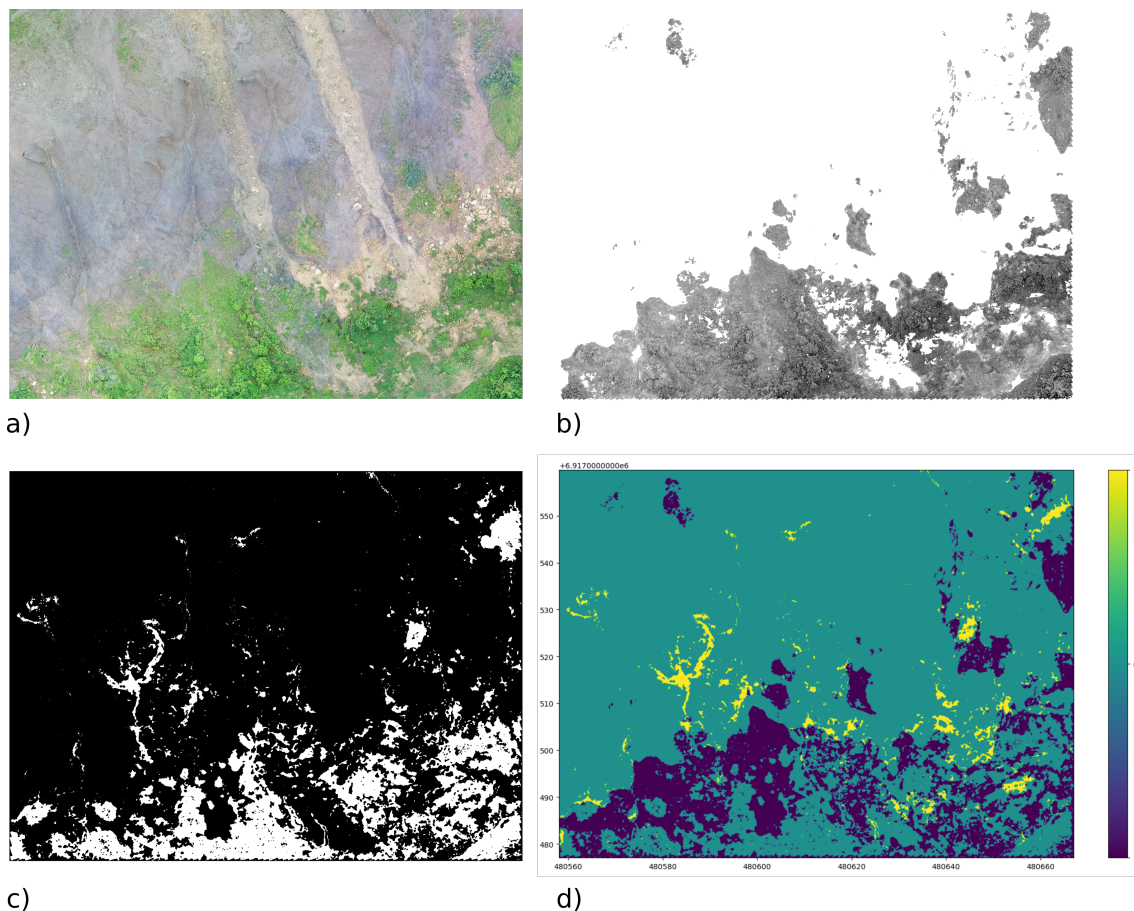


FIGURE 27 – a) orthophoto visible d'une zone des Vaches Noires ; b) classification de la végétation sur l'orthophoto visible ; c) orthophoto binarisée montrant les zones chaudes et froides sur l'orthophoto thermique et d) résultat de la soustraction entre les orthophotos thermiques et visible classifiées. Le chiffre 1 (jaune) signifie qu'on a de l'eau chaude s'écoulant sur un sol nu ; le chiffre 0 (vert) signifie que la végétation est chaude ou que le sol nu est froid et le chiffre -1 (violet) signifie qu'une partie de la végétation est froide. La détection se fait donc grâce à la localisation de la valeur 1.

7.0.3 Développement de prototypes et de moyen de recueil de données

Si les caméras sont classiquement utilisées sur les drones, j'envisage pour les années à venir de m'investir dans l'emploi de l'imagerie géophysique embarquée. Le matériel géophysique est par définition relativement fastidieux à mettre en oeuvre notamment dans les zones avec de la topographie marquée. Par conséquent, les observations géophysiques réalisées grâce à un drone obéissant à un plan de vol automatisé sont en plein développement et prennent de l'ampleur. Les méthodes magnétiques [28], électromagnétiques basse fréquence [23] et géoradar [30] sont maintenant commercialisées sur ces systèmes et de nouvelles méthodologies comme la gravimétrie quantique embarquée sont en cours de développement [29]. Dans le cadre de Defhy3geo, j'ai fait l'acquisition d'un radar géologique embarqué possédant trois fréquences (75 MHz, 120 MHz, 200 MHz) et présenté sur la figure 28. Celui-ci est couplé à un système d'asservissement laser maintenant le drone à une hauteur constante par rapport au sol, ce qui facilite le traitement de l'arrivée directe de l'onde dans l'air. Cette combinaison d'outils permettra de réaliser des mesures radar dans des environnements inaccessibles pour un opérateur. Elle ouvrira une nouvelle voie de recherche exploitant ce type de données dans des environnements divers (infrastructures, piles de ponts, digues, etc...) et apportera

son lot de nouvelles méthodologies pour les équipes opérationnelles du Cerema. Nous prévoyons par exemple des essais de faisabilité au droit des falaises verticales de craie de Sainte-Marguerite-sur-Mer qui font entre dix et vingt mètres de hauteur. La profondeur d'investigation pour un tel matériau avoisine les dix mètres de profondeur. Dans le cas de ce type de scans verticaux, un des challenges majeurs réside dans le fait de localiser correctement la mesure sur la paroi. C'est l'objectif de la thèse de Diego Navarro démarrée fin 2021 dans le cadre du Défi INRIA-Cerema en collaboration avec Ezio Malis de l'équipe ACENTAURI de l'INRIA. Celle-ci permettra de fournir une méthodologie de positionnement du drone et de la mesure (notamment lorsque les données GPS sont manquantes) grâce à la fusion de données multi-modales issues 1) de la centrale inertielle de navigation (IMU) permettant d'avoir les accélérations de l'appareil ; 2) d'une ou plusieurs caméras par odométrie visuelle et 3) d'un LiDAR grâce à la technique du Simultaneous Localisation and Mapping - SLAM). Les résultats de cette thèse permettront d'envisager à l'avenir des investigations géophysiques sur parois d'ouvrages (piles de ponts par exemple) jusqu'ici très difficiles à exécuter et finalement d'enrichir le diagnostic de ces objets.



FIGURE 28 – Photographie du nouveau drone DJI M300 RTK embarquant un radar RADSYS Zond Aero Low Frequency disponible à ENDSUM Rouen (crédits photo UGCS).

7.0.4 Perspectives stratégiques et scientifiques

Ce mémoire présente mon parcours académique et de recherche. Il montre comment j'ai adapté les connaissances acquises à l'environnement de travail du Cerema qui possède une forte spécificité appliquée. Il montre aussi finalement les fortes interactions entre tous mes domaines d'études et c'est ce qui explique mon intérêt pour toutes les échelles d'observations et la pluri-disciplinarité depuis le début de ma carrière. Ma pluri-disciplinarité s'est forgée grâce à un réseau solide de laboratoires et d'écoles que j'ai su développé et pérenniser depuis mon recrutement. Ces expériences m'ont permis d'intégrer de nombreux projets de recherche nationaux et internationaux permettant des investissements importants, de me former à de nouvelles techniques ou de travailler avec de jeunes chercheurs. Cette implication se concrétise par des publications de rang A, une stabilité de l'équipe et de ses personnels permanents et par une attracti-

tivité croissante pour des chercheurs de disciplines différentes (origines des doctorant(e)s et postdoctorant(e)s variée e.g. géophysiciens, géologues, automaticiens et mathématiciens). L'obtention de l'HDR me permettra de m'impliquer dans des directions de thèses et de rayonner plus largement au niveau national/international. Ce diplôme sera par ailleurs une grande reconnaissance de mon travail et de ma persévérance qui me permet aujourd'hui de présenter un dossier équilibré entre production scientifique, activité d'encadrement/formation, de valorisation et collective. La création de l'équipe ENDSUM est le fruit d'un travail en commun que peu de chercheurs de ma génération vivent. Cet exercice à la fois exigeant et motivant doit permettre de pérenniser l'équipe et ses thématiques de recherche, tout en offrant un cadre de travail adéquat aux jeunes chercheurs et aux personnels permanents. Je souhaite que l'obtention de l'HDR puisse contribuer à son renforcement et à son développement dans les années à venir.

Du point de vue scientifique, mes études montrent bien que les échanges sol-atmosphère sont rencontrés dans divers contextes géologiques (et même planétaires) et peuvent être caractérisés en utilisant les outils que je développe depuis une dizaine d'années. Ces échanges influencent de façon fondamentale la couche limite atmosphérique via les transferts hydriques et thermiques, ce qui affecte la circulation atmosphérique. Ces interactions jouent donc un rôle important dans la modélisation météorologique. Dans les années à venir, je souhaite porter cette thématique et les enseignements issus de mes travaux au niveau international. Cette activité pourrait prendre la forme de la création d'un groupement de recherche rassemblant les acteurs de différents domaines disciplinaires (géologues, géophysiciens, atmosphériciens...) et travaillant sur la compréhension, la modélisation et la prédiction des interactions sol-atmosphère en lien avec les phénomènes météorologiques.

Références

- [1] M. E. CHASE, « Airborne remote sensing for groundwater studies in Prairie environment, » *Canadian Journal of Earth Sciences*, t. 6, n° 4, p. 737-741, 1969. DOI : [10.1139/e69-068](https://doi.org/10.1139/e69-068). adresse : <https://doi.org/10.1139/e69-068>.
- [2] P. WIERENGA, R. M. HAGAN et D. NIELSEN, « Soil temperature profiles during infiltration and redistribution of cool and warm irrigation water, » *Water Resources Research*, t. 6, n° 1, p. 230-238, 1970.
- [3] K. CARTWRIGHT, « Tracing shallow groundwater systems by soil temperatures, » *Water Resources Research*, t. 10, n° 4, p. 847-855, 1974. DOI : <https://doi.org/10.1029/WR010i004p00847>. eprint : <https://agupubs.onlinelibrary.wiley.com/doi/pdf/10.1029/WR010i004p00847>. adresse : <https://agupubs.onlinelibrary.wiley.com/doi/abs/10.1029/WR010i004p00847>.
- [4] C. D. WHITEMAN, K. J. ALLWINE, L. J. FRITSCHEN, M. M. ORGILL et J. R. SIMPSON, « Deep valley radiation and surface energy budget microclimates. Part I : Radiation, » *Journal of applied meteorology and climatology*, t. 28, n° 6, p. 414-426, 1989.
- [5] R. DUBAYAH et V. VAN KATWIJK, « The topographic distribution of annual incoming solar radiation in the Rio Grande river basin, » *Geophysical Research Letters*, t. 19, n° 22, p. 2231-2234, 1992.
- [6] B. ROSS, S. AMTER et N. LU, « Numerical studies of rock-gas flow in Yucca Mountain, » Sandia National Labs., rapp. tech., 1992.
- [7] A. ROSE et W. GUO, « Thermal convection of soil air on hillsides, » *Environmental Geology*, t. 25, n° 4, p. 258-262, 1995.
- [8] N. LU, Y. ZHANG et B. ROSS, « Onset of gas convection in a moist porous layer with the top boundary open to the atmosphere, » *International Communications in Heat and Mass Transfer*, t. 26, n° 1, p. 33-44, 1999, ISSN : 0735-1933. DOI : [https://doi.org/10.1016/S0735-1933\(98\)00119-5](https://doi.org/10.1016/S0735-1933(98)00119-5). adresse : <https://www.sciencedirect.com/science/article/pii/S0735193398001195>.
- [9] S. OHSAWA, Y. YUSA, K. OUE et K. AMITA, « Entrainment of atmospheric air into the volcanic system during the 1995 phreatic eruption of Kuju Volcano, Japan, » *Journal of Volcanology and Geothermal Research*, t. 96, n° 1, p. 33-43, 2000, ISSN : 0377-0273. DOI : [https://doi.org/10.1016/S0377-0273\(99\)00134-1](https://doi.org/10.1016/S0377-0273(99)00134-1). adresse : <https://www.sciencedirect.com/science/article/pii/S0377027399001341>.
- [10] E. P. WEEKS, « Effect of topography on gas flow in unsaturated fractured rock : Concepts and observations, » *Washington DC American Geophysical Union Geophysical Monograph Series*, t. 42, p. 53-59, jan. 2001. DOI : [10.1029/GM042p0053](https://doi.org/10.1029/GM042p0053).
- [11] M. LEBLANC, M. RAZACK, D. DAGORNE, L. MOFOR et C. JONES, « Application of Meteosat thermal data to map soil infiltrability in the central part of the Lake Chad basin, Africa., » *Geophysical Research Letters*, t. 30, n° 19, 2003. DOI : <https://doi.org/10.1029/2003GL018094>.
- [12] C. FAUCHARD, P. POTHÉRAT, P. CÔTE et M. MUDET, « Détection de cavités souterraines par méthodes géophysiques., » Laboratoire Central des Ponts et Chaussées., rapp. tech., 2004.
- [13] R. DELALOYE et C. LAMBIEL, « Evidence of winter ascending air circulation throughout talus slopes and rock glaciers situated in the lower belt of alpine discontinuous permafrost (Swiss Alps), » *Norsk Geografisk Tidsskrift-Norwegian Journal of Geography*, t. 59, n° 2, p. 194-203, 2005.
- [14] S. PANDA, S. CHOUDHURY, A. K. SARAF et J. D. DAS, « MODIS land surface temperature data detects thermal anomaly preceding 8 October 2005 Kashmir earthquake, » *International Journal of Remote Sensing*, t. 28, n° 20, p. 4587-4596, 2007.

- [15] P. REIFFSTECK, B. DORBANI, E. HAZA-ROZIER et J. J. FRY, « A new hydraulic profiling tool including cpt measurements, » in *Proceedings of the 2nd International Symposium on Cone Penetration Testing (CPT'10)*, 2010.
- [16] T. SCHUETZ et M. WEILER, « Quantification of localized groundwater inflow into streams using ground-based infrared thermography, » *Geophysical Research Letters*, t. 38, n° 3, 2011. DOI : <https://doi.org/10.1029/2010GL046198>.
- [17] B. t. BRAKE, R. F. HANSSSEN, M. J. van der PLOEG et G. H. de ROOIJ, « Satellite-based radar interferometry to estimate large-scale soil water depletion from clay shrinkage : Possibilities and limitations, » *Vadose Zone Journal*, t. 12, n° 3, p. 1-13, 2013.
- [18] X. KUANG, J. J. JIAO et H. LI, « Review on airflow in unsaturated zones induced by natural forcings, » *Water Resources Research*, t. 49, n° 10, p. 6137-6165, 2013. DOI : <https://doi.org/10.1002/wrcr.20416>. eprint : <https://agupubs.onlinelibrary.wiley.com/doi/pdf/10.1002/wrcr.20416>. adresse : <https://agupubs.onlinelibrary.wiley.com/doi/abs/10.1002/wrcr.20416>.
- [19] J. MARGAT et J. VAN DER GUN, *Groundwater around the world : a geographic synopsis*. Crc Press, 2013.
- [20] J. S. FAMIGLIETTI, « The global groundwater crisis, » *Nature Climate Change*, t. 4, n° 11, p. 945-948, 2014.
- [21] G. E. CUSHING, C. H. OKUBO et T. N. TITUS, « Atypical pit craters on Mars : New insights from THEMIS, CTX, and HiRISE observations, » *Journal of Geophysical Research : Planets*, t. 120, n° 6, p. 1023-1043, 2015. DOI : <https://doi.org/10.1002/2014JE004735>. eprint : <https://agupubs.onlinelibrary.wiley.com/doi/pdf/10.1002/2014JE004735>. adresse : <https://agupubs.onlinelibrary.wiley.com/doi/abs/10.1002/2014JE004735>.
- [22] B. te BRAKE, *Estimation of soil water storage change from clay shrinkage using satellite radar interferometry*. Wageningen University et Research, 2017.
- [23] R. ERÖSS, B. TEZKAN, J. B. STOLL et R. BERGERS, « Interpretation of Very Low Frequency Measurements Carried Out with an Unmanned Aerial System by 2D Conductivity Models, » *Journal of Environmental and Engineering Geophysics*, t. 22, n° 1, p. 83-94, 2017. DOI : [10.2113/JEEG22.1.83](https://doi.org/10.2113/JEEG22.1.83). adresse : <https://doi.org/10.2113/JEEG22.1.83>.
- [24] X.-S. WANG et Y. ZHOU, « Investigating the mysteries of groundwater in the Badain Jaran Desert, China, » *Hydrogeology Journal*, t. 26, n° 5, p. 1639-1655, 2018.
- [25] P. GUIGNARD et J.-P. MORETAU, « La gestion des risques engendrés par les marnières abandonnées., » Commissariat Général au Développement Durable., rapp. tech., 2020.
- [26] X. LIANG, L. ZHAO, Z. NIU, X. XU, N. MENG et N. WANG, « Warm Island Effect in the Badain Jaran Desert Lake Group Region Inferred from the Accumulated Temperature, » *Atmosphere*, t. 11, n° 2, p. 153, 2020.
- [27] Á. TÓTH, A. GALSA et J. MÁDL-SZŐNYI, « Significance of basin asymmetry and regional groundwater flow conditions in preliminary geothermal potential assessment – Implications on extensional geothermal plays, » *Global and Planetary Change*, t. 195, p. 103344, 2020, ISSN : 0921-8181. DOI : <https://doi.org/10.1016/j.gloplacha.2020.103344>. adresse : <https://www.sciencedirect.com/science/article/pii/S0921818120302356>.
- [28] L. GAILLER, P. LABAZUY, E. RÉGIS et al., « Validation of a new UAV magnetic prospecting tool for volcano monitoring and geohazard assessment, » *Remote Sensing*, t. 13, n° 5, p. 894, 2021.

- [29] L. EARL, J. VOVROSH, M. WRIGHT et al., « Demonstration of a Compact Magneto-Optical Trap on an Unstaffed Aerial Vehicle, » *Atoms*, t. 10, n° 1, 2022, ISSN : 2218-2004. DOI : [10.3390/atoms10010032](https://doi.org/10.3390/atoms10010032). adresse : <https://www.mdpi.com/2218-2004/10/1/32>.
- [30] J. KARUŠS, K. LAMSTERS, J. JEŠKINS, I. SOBOTA et P. DŽERIŃŠ, « UAV and GPR Data Integration in Glacier Geometry Reconstruction : A Case Study from Irenebreen, Svalbard, » *Remote Sensing*, t. 14, n° 3, p. 456, 2022.

Articles dans des revues à comité de lecture répertoriés

- [31] R. ANTOINE, D. BARATOUX, M. RABINOWICZ et al., « Thermal infrared image analysis of a quiescent cone on Piton de la Fournaise volcano : Evidence of convective air flow within an unconsolidated soil, » *Journal of Volcanology and Geothermal Research*, t. 183, n° 3-4, p. 228-244, 2009. DOI : <https://doi.org/10.1016/j.jvolgeores.2008.12.003>.
- [32] R. ANTOINE, T. LOPEZ, D. BARATOUX, M. RABINOWICZ et K. KURITA, « Thermal analysis of fractures at Cerberus Fossae, Mars : Detection of air convection in the porous debris apron, » *Icarus*, t. 214, n° 2, p. 433-446, 2011. DOI : <https://doi.org/10.1016/j.icarus.2010.12.025>.
- [33] T. LOPEZ, R. ANTOINE, D. BARATOUX, M. RABINOWICZ, K. KURITA et L. D'USTON, « Thermal anomalies on pit craters and sinuous rilles of Arsia Mons : Possible signatures of atmospheric gas circulation in the volcano, » *Journal of Geophysical Research : Planets*, t. 117, n° E9, 2012. DOI : <https://doi.org/10.1029/2012JE004050>.
- [34] C. FAUCHARD, R. ANTOINE, F. BRETAR et al., « Assessment of an ancient bridge combining geophysical and advanced photogrammetric methods : Application to the Pont De Coq, France, » *Journal of Applied Geophysics*, t. 98, p. 100-112, 2013. DOI : <https://doi.org/10.1016/j.jappgeo.2013.08.009>.
- [35] R. ANTOINE, C. FAUCHARD, Y. FARGIER et E. DURAND, « Detection of leakage areas in an earth embankment from GPR measurements and permeability logging, » *International Journal of Geophysics*, t. 2015, 2015. DOI : <https://doi.org/10.1155/2015/610172>.
- [36] T. LOPEZ, R. ANTOINE, Y. KERR et al., « Subsurface hydrology of the Lake Chad Basin from convection modelling and observations, » *Remote Sensing and Water Resources*, p. 281-312, 2016. DOI : [10.1007/s10712-016-9363-5](https://doi.org/10.1007/s10712-016-9363-5).
- [37] A. D. SALEY, A. JARDANI, A. S. AHMED, R. ANTOINE et J.-P. DUPONT, « Hamiltonian Monte Carlo algorithm for the characterization of hydraulic conductivity from the heat tracing data, » *Advances in Water Resources*, t. 97, p. 120-129, 2016. DOI : [10.1016/j.advwatres.2016.09.004](https://doi.org/10.1016/j.advwatres.2016.09.004).
- [38] R. ANTOINE, A. FINIZOLA, T. LOPEZ et al., « Electric potential anomaly induced by humid air convection within Piton de La Fournaise volcano, La Réunion Island, » *Geothermics*, t. 65, p. 81-98, 2017. DOI : <https://doi.org/10.1016/j.geothermics.2016.01.003>.
- [39] Y. FARGIER, R. ANTOINE, L. DORE, S. P. LOPES et C. FAUCHARD, « 3D assessment of an underground mine pillar by combination of photogrammetric and geoelectric methods, » *Geophysics*, t. 82, n° 4, E143-E153, 2017. DOI : <https://doi.org/10.1190/geo2016-0274.1>.
- [40] G. BERGER, D. BEAUFORT et R. ANTOINE, « Clay minerals related to the late magmatic activity of the Piton des Neiges (Réunion Island) : consequence for the primitive crusts, » *Clay Minerals*, t. 53, n° 4, p. 675-690, 2018. DOI : <https://doi.org/10.1180/clm.2018.51>.

- [41] C. FAUCHARD, A. D. SALEY, C. CAMERLYNCK, Y. FARGIER, R. ANTOINE et P.-F. THÉRAIN, « Discovery of the Romanesque church of the Abbey of our lady of Bec (Le Bec-Hellouin, Normandy, France) by means of geophysical methods, » *Archaeological Prospection*, t. 25, n° 4, p. 315-328, 2018. DOI : <https://doi.org/10.1002/arp.1711>.
- [42] T. LOPEZ, R. ANTOINE, J. DARROZES, M. RABINOWICZ et D. BARATOUX, « Development and evolution of the size of polygonal fracture systems during fluid-solid separation in clay-rich deposits, » *Journal of Earth Science*, t. 29, n° 6, p. 1319-1334, 2018. DOI : <https://doi.org/10.1007/s12583-017-0814-9>.
- [43] T. LOPEZ, G. RAMILLIEN, R. ANTOINE, J. DARROZES, Y.-J. CUI et Y. KERR, « Investigation of short-term evolution of soil characteristics over the Lake Chad basin using GRACE data, » *Remote Sensing*, t. 10, n° 6, p. 924, 2018. DOI : <https://doi.org/10.3390/rs10060924>.
- [44] M. MEDJKANE, O. MAQUAIRE, S. COSTA et al., « High-resolution monitoring of complex coastal morphology changes : Cross-efficiency of SfM and TLS-based survey (Vaches-Noires cliffs, Normandy, France), » *Landslides*, t. 15, n° 6, p. 1097-1108, 2018. DOI : <https://doi.org/10.1007/s10346-017-0942-4>.
- [45] C. MEZON, V. MOURZENKO, J.-F. THOVERT et al., « Thermal convection in three-dimensional fractured porous media, » *Physical Review E*, t. 97, n° 1, p. 013 106, 2018. DOI : <https://doi.org/10.1103/PhysRevE.97.013106>.
- [46] S. COSTA, O. MAQUAIRE, P. LETORTU et al., « Sedimentary Coastal cliffs of Normandy : modalities and quantification of retreat, » *Journal of Coastal Research*, t. 88, n° SI, p. 46-60, 2019. DOI : <https://doi.org/10.2112/SI88-005.1>.
- [47] R. ANTOINE, T. LOPEZ, M. TANGUY et al., « Geoscientists in the sky : unmanned aerial vehicles responding to geohazards, » *Surveys in Geophysics*, t. 41, n° 6, p. 1285-1321, 2020. DOI : <https://doi.org/10.1007/s10712-020-09611-7>.
- [48] R. ANTOINE, I. CIOTIR, S. COSTA et al., « Coastline Erosion Study via UAV Drone Remote Sensing Using Python Modelling Electrical Resistivity Imaging (PyMERI), » in *IGARSS 2020 IEEE International Geoscience and Remote Sensing Symposium*, IEEE, 2020, p. 441-444. DOI : [10.1109/IGARSS39084.2020.9323414](https://doi.org/10.1109/IGARSS39084.2020.9323414).
- [49] R. ANTOINE, C. FAUCHARD, J.-F. OEHLER et P. JOIGNANT, « Permeability and voids influence on the thermal signal, as inferred by multitemporal UAV-based infrared and visible images, » *Journal of Hydrology*, t. 587, p. 124 907, 2020. DOI : <https://doi.org/10.1016/j.jhydrol.2020.124907>.
- [50] V. GUILBERT, R. ANTOINE, C. HEINKELE et al., « Fusion of thermal and visible point clouds : Application to the Vaches Noires landslide, Normandy, France, » *ISPRS-International Archives of the Photogrammetry, Remote Sensing and Spatial Information Sciences*, t. 43, p. 227-232, 2020. DOI : <https://doi.org/10.5194/isprs-archives-XLIII-B2-2020-227-2020>.
- [51] R. ANTOINE, C. FAUCHARD, V. GUILBERT et al., « Geophysical and Uav-Based Observations Over a Flood Defense Structure : Application to the POLDER2C'S Experimental Dike, » *ISPRS-International Archives of the Photogrammetry, Remote Sensing and Spatial Information Sciences*, t. 43, p. 237-242, 2021. DOI : [10.5194/isprs-archives-XLIII-B3-2021-237-2021](https://doi.org/10.5194/isprs-archives-XLIII-B3-2021-237-2021).
- [52] I. HASSEN, C. FAUCHARD, R. ANTOINE et al., « 3D geological modelling of a coastal area : case study of the Vaches Noires Cliffs, Normandy, France, » *Bull Eng Geol Environ*, t. 80, n° 2, p. 1375-1388, 2021. DOI : <https://doi.org/10.1007/s10064-020-01955-z>.
- [53] J. MARIÑO, K. CUEVA, J.-C. THOURET et al., « Multidisciplinary Study of the Impacts of the 1600 CE Huaynaputina Eruption and a Project for Geosites and Geo-touristic Attractions, » *Geoheritage*, t. 13, n° 3, p. 1-29, 2021. DOI : <https://doi.org/10.1007/s12371-021-00577-5>.

- [54] C. FAUCHARD, V. GUILBERT, R. ANTOINE et al., « Diachronic study of coastal badlands with UAV and geophysical methods in the context of accelerated erosion processes, » *Accepté dans la revue Landslide*, 2022.
- [55] P. LETORTU, N. LE DANTEC, E. AUGEREAU et al., « Experimental field study on the fatigue and failure mechanisms of coastal chalk cliffs : Implementation of a multi-parameter monitoring system (Sainte-Marguerite-sur-Mer, France), » *Geomorphology*, p. 108211, 2022, ISSN : 0169-555X. DOI : <https://doi.org/10.1016/j.geomorph.2022.108211>.
- [56] T. ROULLAND, O. MAQUAIRE, S. COSTA et al., « Seasonal activity quantification of coast badlands by TLS monitoring over five years at the "Vaches Noires" cliffs (Normandy, France), » *Geomorphology*, p. 108083, 2022. DOI : <https://doi.org/10.1016/j.geomorph.2021.108083>.
- [57] W. SONG, T. LOPEZ, Y.-J. CUI et R. ANTOINE, « Investigation on the relationship between ground clay particle distribution and microclimate in the Lake Chad zone using satellite data and climate reanalysis, » *To be submitted to Journal of Hydrology*, 2022.
- [58] A. TONNOIR, Y. FARGIER, R. ANTOINE et C. FAUCHARD, « PyLGRIM : Modelling 3D-ERI with infinite elements in complex topography context, » *To be submitted to Geophysical Journal International*, 2022.

Articles dans des revues à comité de lecture non répertoriés

- [59] M. GUYOT, P.-F. THÉRAIN, R. ANTOINE et C. MAISONNAVE, *Ménéval, Saumont-la-Poterie-Le Pont de Coq. Fouille programmée (2014)*, 2021.

Chapitres d'ouvrage

- [60] C. FAUCHARD, J. LACOGNE et R. ANTOINE, « De l'utilisation de mesures géophysiques pour connaître un site, » in *Le pont de Coq : histoires d'une restauration*, P.-F. T. et l'Association de SAUVEGARDE DU PONT DE COQ, éd., Rouen : Éditions Point de vues, DL 2017, 2017, chap. 10, p. 79-91.
- [61] R. ANTOINE et T. LOPEZ, « Télédétection dans l'infrarouge thermique, » in *Manuel de mécanique des roches tome 5-Thermomécanique des roches*, M. GASC, V. MERRIEN-SOUKATCHOFF et P. BERREST, éd., Presses de l'école des Mines, 2018, chap. 10, p. 266-290.

Conférences internationales

- [62] R. ANTOINE, D. BARATOUX, M. RABINOWICZ et al., « Convective Gas Flow in Terrestrial and Martian Volcanic Soils : Implications for the Interpretation of THEMIS-IR Data, » in *Seventh International Conference on Mars*, t. 1353, 2007, p. 3097.
- [63] R. ANTOINE, D. BARATOUX, M. RABINOWICZ et al., « Thermography of volcanic areas on Piton de la Fournaise, Reunion Island : Mapping surface properties and possible detection of convective air flow within volcanic debris, » in *AGU Fall Meeting Abstracts*, t. 2007, 2007, p. V11D-0813.
- [64] T. LOPEZ, D. BARATOUX, M. RABINOWICZ, R. ANTOINE, F. AYOUB et L. D'USTON, « What Does Control the Thermal Behaviour of the Pits Near Arsia Mons? » in *Lunar and Planetary Science Conference*, 2009, p. 1912.

- [65] R. ANTOINE, T. L. GONZALEZ, D. BARATOUX et al., « Abnormally high night temperatures in pit craters and collapsed sinuous rilles on Arsia Mons' flanks. Interpretations in terms of subsurface air circulation along slopes., » in *EGU General Assembly 2010*, 2010.
- [66] R. ANTOINE et K. KURITA, « Thermal plumes and electric potentials generation in a porous medium locally heated from below, » in *AGU Fall Meeting Abstracts*, t. 2010, 2010, V21E-2357.
- [67] T. LOPEZ GONZALEZ, D. BARATOUX, M. RABINOWICZ, R. ANTOINE, F. AYOUB et L. D'USTON, « Abnormally high night temperatures in pit craters and collapsed sinuous rilles on Arsia Mons' flanks. Interpretations in terms of subsurface air circulation along slopes., » in *EGU General Assembly Conference Abstracts*, 2010, p. 6640.
- [68] R. ANTOINE et C. FAUCHARD, « Revealing the hidden structures of an historical bridge by high resolution geophysical methods : A case study of Pont de Coq, France, » in *EGU General Assembly Conference Abstracts*, 2012, p. 12 781.
- [69] R. ANTOINE, N. GESHI, K. KURITA et al., « Air-cooled volcanoes? New insights on convective airflow process within Miyakejima and Piton de la Fournaise volcanoes, » in *EGU General Assembly Conference Abstracts*, 2012, p. 11 421.
- [70] T. LOPEZ, D. BARATOUX, R. ANTOINE et al., « Formation of Mud Volcanoes, Giant Polygons and Chaotic Terrains on Mars as the Result of Compaction and Convection of Thick Altered Pyroclastic Deposit, » in *AGU Fall Meeting Abstracts*, t. 2013, 2013, p. V53C-2815.
- [71] R. ANTOINE, D. BARATOUX, J. LACOGNE et al., « First 3D thermal mapping of an active volcano using an advanced photogrammetric method, » in *EGU General Assembly Conference Abstracts*, 2014, p. 14 597.
- [72] R. ANTOINE, C. FAUCHARD, B. BEAUCAMP et V. GUILBERT, « Using a new multichannel GPR and ERT method for high resolution archaeological mapping : application to a buried Gallo-Roman site in Normandy, France, » in *EGU General Assembly Conference Abstracts*, 2014, p. 14 067.
- [73] R. DUVAL, C. FAUCHARD et R. ANTOINE, « Topographic effect on Radio-Magnetotelluric and Slingram signals : application to a levee along the Loire river, France., » in *EGU General Assembly Conference Abstracts*, 2014, p. 14 861.
- [74] A. FINIZOLA, T. RICCI, M. PORET et al., « Fluid circulation at Somma-Vesuvius volcanic complex inferred by electrical resistivity tomography, self-potential, temperature and soil degassing, » in *MED-SUV 1th year meeting, Nicolosi (catania)*, 2014, p. 7-9.
- [75] P. GENTHON, T. LOPEZ, R. ANTOINE et al., « Detection of Groundwater from Space-Based IR Data : Application to the Lake Chad Basin., » in *AGU Fall Meeting Abstracts*, t. 2014, 2014, H43C-0975.
- [76] T. LOPEZ, R. ANTOINE, P. GENTHON et al., « Detection of groundwater from space-based IR data : application to the Lake Chad basin., » in *EGU General Assembly Conference Abstracts*, 2014, p. 9976.
- [77] T. LOPEZ, D. BARATOUX, R. ANTOINE et al., « Formation of mud volcanoes, giant polygons and chaotic terrains on Mars as the result of compaction and convection of altered pyroclastic deposits., » in *EGU General Assembly Conference Abstracts*, 2014, p. 10 260.
- [78] P. ADLER, C. MEZON, V. MOURZENKO, J. THOVERT, R. ANTOINE et A. FINIZOLA, « Natural thermal convection in fractured porous media, » in *AGU Fall Meeting Abstracts*, t. 2015, 2015, H21L-04.

- [79] Y. FARGIER, L. DORE, R. ANTOINE et al., « Contribution of SFM and ERI Methods to Assess an Underground Quarry Pillar, » in *Near Surface Geoscience 2015-21st European Meeting of Environmental and Engineering Geophysics*, European Association of Geoscientists & Engineers, t. 2015, 2015, p. 1-5.
- [80] T. LOPEZ, R. ANTOINE, M. RABINOWICZ et al., « Formation of polygonal fault systems as a result of hydrodynamical instabilities in clay-rich deposits., » in *EGU General Assembly Conference Abstracts*, 2015, p. 11 637.
- [81] C. MEZON, V. MOURZENKO, J.-F. THOVERT, R. ANTOINE, A. FINIZOLA et P. M. ADLER, « Natural thermal convection in fractured porous media, » in *2015 AGU Fall Meeting*, 2015.
- [82] F. ANTHONY, R. TULLIO, D. ERIC et al., « The summit part of Mount Etna revealed by High Resolution DC Electrical Resistivity Tomography coupled with complementary geophysical and soil gas techniques, » in *MED-SUV Final Meeting*, 2016.
- [83] S. ARAUJO, L. DELBREILH, R. ANTOINE, E. DARGENT et C. FAUCHARD, « Study of the dielectric properties of weathered granite, basalt and quartzite by means of broadband dielectric spectroscopy over a wide range of frequency and temperature., » in *EGU General Assembly Conference Abstracts*, 2016, EPSC2016-14 232.
- [84] Y. FARGIER, L. DORE, R. ANTOINE, S. PALMA LOPES et C. FAUCHARD, « Combination of photogrammetric and geoelectric methods to assess 3d structures associated to natural hazards, » in *EGU General Assembly Conference Abstracts*, 2016, EPSC2016-8628.
- [85] A. FINIZOLA, T. RICCI, R. ANTOINE et al., « The summit part of Mount Etna revealed by High Resolution DC Electrical Resistivity Tomography coupled with complementary geophysical and soil gas techniques, » in *EGU General Assembly Conference Abstracts*, 2016, EPSC2016-12 963.
- [86] C. MEZON, V. MOURZENKO, J. FRANÇOIS THOVERT et al., « 3D convection in a fractured porous medium : influence of fracture network parameters and comparison to homogeneous approach., » in *EGU General Assembly Conference Abstracts*, 2016, EPSC2016-4561.
- [87] R. TULLIO, G. MARCEAU, V. JEAN et al., « Hydrothermal fluid flow structures at Solfatara volcano, Somma-Vesuvius volcanic complex and Mt. Etna., » in *MED-SUV Final Meeting*, 2016.
- [88] L. DORE, Y. FARGIER, S. PALMA-LOPES, R. ANTOINE et C. FAUCHARD, « Contribution of ERI, Photogrammetry and Surface Resistivity Probe Methods for Assessing an Underground Mine Pillar, » in *23rd European Meeting of Environmental and Engineering Geophysics*, European Association of Geoscientists & Engineers, t. 2017, 2017, p. 1-5.
- [89] A. JARDANI, A. SOUEID AHMED, A. RAPHAEL, J. P. DUPONT et al., « Hamiltonian Monte Carlo algorithm for the characterization of hydraulic conductivity from the heat tracing data, » in *EGU General Assembly Conference Abstracts*, 2017, p. 9138.
- [90] T. LOPEZ, R. ANTOINE, D. BARATOUX et M. RABINOWICZ, « Contribution of thermal infrared images on the understanding of the subsurface/atmosphere exchanges on Earth., » in *EGU General Assembly Conference Abstracts*, 2017, p. 11 811.
- [91] T. LOPEZ, G. RAMILLIEN, R. ANTOINE et M. RABINOWICZ, « Influence of the surface permeability on the GRACE water mass variations. Case of the Lake Chad basin., » in *EGU General Assembly Conference Abstracts*, 2017, p. 11 769.
- [92] R. ANTOINE, C. FAUCHARD, J.-F. OEHLER et P. JOIGNANT, « Characterising the surface temperatures and the deformations of a civil engineering structure by drone : application to a harbor dock, » in *EGU General Assembly Conference Abstracts*, 2018, p. 14 342.

- [93] C. FAUCHARD, Y. FARGIER, O. MAQUAIRE et al., « Combination of aerial and near surface geophysical data : Badlands case study of " Les Vaches Noires" cliffs, Normandy, France., » in *Geophysical Research Abstracts*, t. 20, 2018.
- [94] T. LOPEZ, D. LEROUX, R. ANTOINE, Y. CUI et G. RAMILLIEN, « Space-based study of the mechanisms of surface fluids exchanges in the arid region of Badain Jaran., » in *EGU General Assembly Conference Abstracts*, 2018, p. 12 586.
- [95] A. PELTIER, F. J. FONTAINE, A. FINIZOLA et al., « Volcano destabilizations : from observations to an integrated model of active deformation, » in *AGU Fall Meeting Abstracts23*, 2018.
- [96] R. ANTOINE, M. TANGUY, S. PALMA LOPES et J.-L. SORIN, « Didro-An Innovative Multi-Sensor UAV System for Routine and Crisis Monitoring of Dikes, » in *AGU Fall Meeting Abstracts*, t. 2019, 2019, EP11C-2123.
- [97] C. FAUCHARD, R. ANTOINE, S. TAOUM et al., « Erosion and Deposition Volumes Estimation Using a Drone and Near Surface Geophysics Methods in Coastal Badlands Context., » in *AGU Fall Meeting Abstracts*, t. 2019, 2019, H14A-01.
- [98] T. L. GONZALEZ, R. ANTOINE, D. REMY, M. GERBAULT et M. RABINOWICZ, « Thermal infrared observation of pre-seismic vertical permeability changes. The Boumerdes-Zemmouri (M= 6.8) case, » in *21st EGU General Assembly*, 2019.
- [99] R. GUÉRIN, L. BODET, M. DANGEARD et al., « Characterization of the vadose zone above an abandoned underground quarry of Chalk, using different geophysical tools., » in *Geophysical Research Abstracts*, t. 21, 2019.
- [100] T. LOPEZ, R. ANTOINE, D. RÉMY, M. GERBAULT et M. RABINOWICZ, « Thermal infrared observation of pre-seismic vertical permeability changes. The Boumerdes-Zemmouri (M= 6.8) case., » in *Geophysical Research Abstracts*, t. 21, 2019.
- [101] O. MAQUAIRE, S. COSTA, C. LISSAK et al., « Combination of aerial and near surface methods. Application at two different types of coast and landslides (Normandy cliffs, France), » in *International workshop on fluidized landslide*, 2019.
- [102] O. MAQUAIRE, S. COSTA, C. LISSAK et al., « RICOCHET project : multi-Risk assessment on Coastal territory in a global CHange context, » in *First China-France Symposium on Transportation Geotechnics*, 2019.
- [103] T. ROULLAND, O. MAQUAIRE, S. COSTA et al., « High-resolution monitoring of the " Vaches Noires" cliffs by multi-method analysis : characterization of hydrogravity processes and induced dynamics (Normandy, France)., » in *Geophysical Research Abstracts*, t. 21, 2019.
- [104] T. LOPEZ, H. HU, Y. CUI, R. ANTOINE et N. AN, « Analysis of the space-based surface temperature distribution in Badain Jaran Desert, » in *EGU General Assembly Conference Abstracts*, 2020, p. 17 910.
- [105] Y. FARGIER, T. DEZERT, R. ANTOINE, A. TONNOIR et C. FAUCHARD, « Impact of the Dems Resolution on 2d and 3d-Eri Common Practice, » in *NSG2021 2nd Conference on Geophysics for Infrastructure Planning, Monitoring and BIM*, European Association of Geoscientists & Engineers, t. 2021, 2021, p. 1-5.
- [106] C. FAUCHARD, L. AILLAUD, A. LEGRAND et al., « Transept Foundations of a 12th Century Chapel Revealed by Geophysical and Photogrammetric Prospection, » in *NSG2021 2nd Conference on Geophysics for Infrastructure Planning, Monitoring and BIM*, European Association of Geoscientists & Engineers, t. 2021, 2021, p. 1-5.
- [107] R. ANTOINE, F. CEREMA-DTERNC, J. BERNARD et F. LMV-CLERMONT-FERRAND, « Multidisciplinary investigation (ERT, CO₂, SP and T) reveals fluid circulation at Somma-Vesuvius. »
- [108] A. FINIZOLA, T. RICCI, A. SCIARRA et al., « Geochemical characterization of a High Resolution DC Electrical Resistivity Tomography crossing the summit craters of Mt Etna. »

Conférences nationales

- [109] R. ANTOINE, C. FAUCHARD, E. DURAND et B. BEAUCAMP, « Apport du radar géologique à l'imagerie interne des digues, » in *Digues maritimes et fluviales de protection contre les submersions-2e colloque national-Digues 2013*, Lavoisier, 2013, p. 353.
- [110] V. MOURZENKO, C. MEZON, J.-F. THOVERT et al., « 3D convection in a fractured porous medium : influence of fracture network parameters, » in *13èmes Journées d'études des Milieux Poreux 2016*, 2016.
- [111] C. FAUCHARD, V. GUIBERT, R. ANTOINE et al., « Mesures combinées d'imagerie de résistivité électrique et de photogrammétrie : étude des falaises des Vaches Noires, » in *SFPT ENSG*, 2017.
- [112] T. ROULLAND, O. MAQUAIRE, S. COSTA et al., « Suivi de l'évolution des processus hydrogravitaires des falaises des Vaches Noires par analyse multi-méthodes (Calvados, Normandie, France), » in *Journées Aléas Gravitaires*, 2017.
- [113] D. BOGGIO, J. SORIN, M. PIERROT-DESEILLIGNY et al., « DIDRO, un outil intégré pour l'auscultation des digues par drone, » in *Digues maritimes et fluviales de protection contre les inondations-3e colloque-Digues 2019*, 2019, p. 6.
- [114] T. ROULLAND, O. MAQUAIRE, S. COSTA et al., « Caractérisation des processus hydrogravitaires et des dynamiques saisonnières des falaises des Vaches Noires par photogrammétrie, télémétrie laser terrestre et mesure in situ, » in *Journées Aléas Gravitaires*, 2019.
- [115] R. ANTOINE, J. LACOGNE, F. BRETAR et al., « Comment obtenir des informations topographiques à partir de données d'imagerie thermique infrarouge ? Le cas du Piton de la Fournaise.. »
- [116] D. BOGGIO, J. SORIN, M. PIERROT-DESEILLIGNY et al., « DIDRO, un outil intégré pour lauscultation des digues par drone DIDRO, an integrated tool for levees survey by drone. »

Rapports de recherche

- [117] R. ANTOINE, D. BARATOUX et M. RABINOWICZ, « Détection d'anomalies thermiques par méthode infrarouge thermique sur le cone Formica Leo, » rapp. tech., 2008.
- [118] R. ANTOINE, A. FINIZOLA, D. BARATOUX et M. RABINOWICZ, « Anomalies thermiques générées par une circulation convective d'air humide dans le cône Formica Leo, » rapp. tech., 2009.
- [119] R. ANTOINE, G. SARACCO, D. BARATOUX et M. RABINOWICZ, « Anomalies de potentiels électriques générées par une circulation d'air et d'eau dans le Piton de la Fournaise, » rapp. tech., 2010.
- [120] C. FAUCHARD et R. ANTOINE, *Mesures thermiques et géophysique sur les quais Joannes Couvert du Grand Port Maritime du Havre*, 2014.
- [121] C. FAUCHARD, R. ANTOINE, P.-F. THÉRAIN, J. LACOGNE, F. BRETAR et M. PIERROT-DESEILLIGNY, « Apport de la photogrammétrie pour la restitution de mesures géophysiques : application pour la sauvegarde du Pont De Coq, Ménéval (76), » rapp. tech., 2014.
- [122] C. FAUCHARD et R. ANTOINE, *Mesures photogrammétriques et infrarouge thermiques sur les quais Joannes Couvert du Grand Port Maritime du Havre*, 2016.
- [123] D. JACQUELINE, R. ANTOINE et E. KASSA, « Deliverable D3. 3, » rapp. tech., 2017.
- [124] R. ANTOINE et J. L. SORIN, « Validation de puces GPS de type U-Blocs pour le suivi de cible dérivantes en contexte de crise, » rapp. tech., 2018.

- [125] R. ANTOINE, G. RABATEL et J. L. SORIN, « Observations thermiques, visibles et Lidar sur ouvrage hydraulique : application à la digue de BOU dans le Loiret, » rapp. tech., 2019.
- [126] R. ANTOINE et J. L. SORIN, « Combinaison de données thermiques et visible sur un ouvrage hydraulique expérimental : application à la digue du CER dans de cadre du Projet Didro, » rapp. tech., 2019.
- [127] —, « Observations multispectrales appliquées à DIDRO : considérations finales, » rapp. tech., 2019.
- [128] A. SILLA, A. VIRTANEN, E. LEHTONEN et al., « Results of the evaluation of pilot tests. Deliverable D4. 4 of the SAFER-LC project, » rapp. tech., 2020.

Rapports d'expertise

- [129] R. ANTOINE et B. BEAUCAMP, *Mesures radar sur le canal latéral à la Loire : application à la digue en terre de Saint-Firmin-sur-Loire (Loiret, 45)*, 2012.
- [130] R. ANTOINE, V. GUILBERT, B. BEAUCAMP et C. FAUCHARD, *Caractérisation géophysique d'un théâtre gallo-romain (Arnières Sur Iton, 27) par radar 3D et Tomographie de Résistivité Electrique (2013)*, 2013.
- [131] R. ANTOINE, *Mesures géophysique sur le terril en combustion interne de Haveluy (59)*, 2014.
- [132] R. ANTOINE et V. GUILBERT, *Observations dans infrarouge thermiques de la tranchée couverte RFF, Rive Gauche de la Ville de Rouen*, 2014.
- [133] R. ANTOINE et C. FAUCHARD, *Mesures géophysiques complémentaires (en tomographie de résistivité électrique) sur le Pont de Coq, Pays de Bray*, 2015.
- [134] C. FAUCHARD et R. ANTOINE, *Observations radar sur la digue du Val d'Orléans*, 2015.
- [135] C. FAUCHARD, V. GUILBERT, B. BEAUCAMP et R. ANTOINE, *Mesures radar 3D et imagerie électrique sur l'abbaye du Bec Hellouin*, 2015.
- [136] L. AUBIN et R. ANTOINE, *Mesures photogrammétriques sur l'épi de Port Neuf, Ville de la Rochelle*, 2021.